



Aalborg Universitet

AALBORG UNIVERSITY
DENMARK

Field-induced Dissociation of Excitons in Mono- and Bilayer Structures

Kamban, Høgni Carlsson

DOI (link to publication from Publisher):
[10.54337/aau473637858](https://doi.org/10.54337/aau473637858)

Publication date:
2022

Document Version
Publisher's PDF, also known as Version of record

[Link to publication from Aalborg University](#)

Citation for published version (APA):
Kamban, H. C. (2022). *Field-induced Dissociation of Excitons in Mono- and Bilayer Structures*. Aalborg Universitetsforlag. <https://doi.org/10.54337/aau473637858>

General rights

Copyright and moral rights for the publications made accessible in the public portal are retained by the authors and/or other copyright owners and it is a condition of accessing publications that users recognise and abide by the legal requirements associated with these rights.

- Users may download and print one copy of any publication from the public portal for the purpose of private study or research.
- You may not further distribute the material or use it for any profit-making activity or commercial gain
- You may freely distribute the URL identifying the publication in the public portal -

Take down policy

If you believe that this document breaches copyright please contact us at vbn@aub.aau.dk providing details, and we will remove access to the work immediately and investigate your claim.

FIELD-INDUCED DISSOCIATION OF EXCITONS IN MONO- AND BILAYER STRUCTURES

**BY
HØGNI C. KAMBAN**

DISSERTATION SUBMITTED 2022



AALBORG UNIVERSITY
DENMARK

Field-induced Dissociation of Excitons in Mono- and Bilayer Structures

Ph.D. Dissertation
Høgne C. Kamban

Dissertation submitted April, 2022

Dissertation submitted: April, 2022

PhD supervisor: Professor Thomas G. Pedersen
Aalborg University

PhD committee: Professor Kjeld Pedersen (chair)
Aalborg University, Denmark

Professor Kirill Bolotin
Freie Universität Berlin, Germany

Professor Nikolaj T. Zinner
Aarhus University, Denmark

PhD Series: Faculty of Engineering and Science, Aalborg University

Department: Department of Materials and Production

ISSN (online): 2446-1636
ISBN (online): 978-87-7573-917-2

Published by:
Aalborg University Press
Kroghstræde 3
DK – 9220 Aalborg Ø
Phone: +45 99407140
aauf@forlag.aau.dk
forlag.aau.dk

© Copyright: Høgni C. Kamban

Printed in Denmark by Stibo Complete, 2022

English abstract

The focus of this thesis is to study electric-field-induced dissociation of excitons in material structures based on both monolayer materials and bilayer heterostructures. Excitons are quasi-particles found in semiconductors and insulators. When an electron is excited from the valence band, typically by absorbing a photon, it leaves behind a vacancy in this band. This vacancy behaves like a positively charged particle and is referred to as a hole. The excited electron and hole are attracted to one another via the Coulomb force due to their opposite electric charge. They may therefore form a bound state, and it is this bound state that is known as an exciton. Excitons in bulk semiconductors are usually weakly bound, and thermal agitation is sufficient to dissociate them into free electrons and holes. This is not the case for mono- and bilayer structures, however. As the number of layers composing the material structure reduces, the screening of the interaction between electrons and holes also reduces. This leads to a stronger interaction between electron-hole pairs, and exciton binding energies therefore become larger. Such strongly bound excitons are thermally stable, and it is therefore interesting to see if one may assist the dissociation process by applying in-plane electric fields to the excitons.

A recent experiment showed that the photoresponse rate of a WSe₂ monolayer increases as a static electric field is applied to the excitons. The field-induced increase in photoresponse rate at weak fields was well described by a Wannier exciton dissociation model. However, it proved difficult to obtain theoretical predictions of exciton dissociation rates when the electric fields were sufficiently weak. One of the goals of the present thesis was to find a numerical method capable of efficiently computing these weak field dissociation rates. This method has subsequently been used to compute exciton dissociation rates in monolayer transition metal dichalcogenides (TMDs), phosphorene, and bilayer TMD heterostructures. The results indicate an exponential dependence on field strength, particularly in weak electric fields. The exciton binding energy is, furthermore, found to be the dominating parameter determining exciton dissociation rates, but reduced masses and substrate screening also have an im-

pact. This is made clear by deriving an analytical weak field approximation in which all of these parameters are included.

Dissociation induced by THz pulses is also considered for excitons in monolayer TMDs. The results are obtained using a fully time-dependent Wannier model and indicate that realistic THz pulses are able to dissociate a substantial amount of excitons in realistic semiconductors.

Danish abstract

Formålet med denne afhandling er at studere elektrisk-felt-induceret eksiton dissociation i materielle strukturer, der består af et- og tolags materialer. Eksitoner er kvasi-partikler, der findes i halvledere og isolatorer. Når en elektron eksiteres fra valensbåndet, typisk ved at absorbere en foton, efterlader den et hul. Dette hul opfører sig som en positivt ladet partikel. Da de to partikler har modsat ladning, vil den eksiterede elektron og hullet tiltrække hinanden ved hjælp af Coulomb kraften. De kan derfor danne bundne tilstande, og det er præcis sådan en bunden tilstand, vi kalder en eksiton. Eksitoner i almindelige halvledere er typisk svagt bundne, og termiske rystelser er derfor nok til at dissociere dem, således at de omdannes til frie elektroner og huller. Dette er ikke tilfældet i et- og tolags strukturer. Som antallet af lag, der opbygger den materielle struktur, reduceres, reduceres screeningen af interaktionen mellem elektronerne og hullerne også. Dette fører til en stærkere interaktion mellem elektron-hul par, og eksiton bindingsenergien bliver derfor også større. Disse stærkt bundne eksitoner er termisk stabile, og det er derfor interessant at se, om det er muligt at hjælpe dissocieringsprocessen ved at gøre brug af elektriske felter.

Fornylig blev et eksperiment udført, hvor fotostrømmen i et WSe_2 lag blev målt. Her fandt man, at fotostrømmen voksede, når et elektrisk felt blev sat hen over eksitonerne. Den felt-inducerede vækst kunne forklares ved hjælp af en Wannier model. Det viste sig dog at være svært at forudsige, hvad dissociationsraterne skulle være teoretisk, hvis felterne blev meget små. Et af målene i denne afhandling var at finde en numerisk metode, der effektivt kunne regne disse svagfelts dissociationsrater. Denne metode blev sidenhen brugt til at regne eksiton dissociations rater i etlags overgangsmetal dikalkogenider (TMDe), phosphoren og tolags heterostrukturer. Resultaterne viser, at dissociationsraterne afhænger eksponentielt af feltstyrken, specielt for svage felter. Bindingsenergien er det dominerende parameter, der afgør størrelsen af eksiton dissociations raterne, men den reducerede masse og screening fra omgivelserne spiller også en rolle. Dette ses tydeligt ved at udlede en svagfelts

approximation, hvori disse parametre indgår.

Dissociation induceret af THz pulser bliver også undersøgt for eksitoner i etlags TMDer. Resultaterne er regnede med en tidsafhængig Wannier model og indikerer, at realistiske THz pulser kan dissociere en stor del af eksitoner i realistiske halvledere.

Contents

English abstract	iii
Danish abstract	v
List of publications	ix
Preface	xi
1 Introduction	1
1.1 Excitons	3
1.2 This work	4
2 Theoretical Formalism	9
2.1 Wannier exciton model	10
2.1.1 Excitons in monolayer transition metal dichalcogenides	11
2.1.2 Excitons in bilayer van der Waals heterostructures . . .	13
2.1.3 Excitons in phosphorene	18
2.2 Exciton dissociation by static electric fields	21
2.2.1 Complex scaling	23
2.2.2 Exterior complex scaling	26
2.3 Solving the two-dimensional Schrödinger equation using a finite element approach	28
2.3.1 Implementing exterior complex scaling	35
2.4 Exciton dissociation by dynamic electric fields	37
2.4.1 Numerical procedure	39
3 Summary of Results	41
3.1 Binding energies and parameters	41
3.2 Exciton dissociation by static in-plane electric fields in monolayers	47
3.2.1 Monolayer TMDs	47

Contents

3.2.2	Phosphorene	54
3.3	Exciton dissociation by static in-plane electric fields in bilayer structures	58
3.4	THz induced exciton dissociation in TMD monolayers	61
4	Conclusion	67
	References	69
	Publications	85
A	Field-induced dissociation of two-dimensional excitons in transition metal dichalcogenides	87
B	Finite-difference time-domain simulation of strong-field ionization: a perfectly matched layer approach	97
C	Interlayer excitons in van der Waals heterostructures: Binding energy, Stark shift, and field-induced dissociation	109
D	Analytical quantitative semiclassical approach to the Lo Surdo-Stark effect and ionization in two-dimensional excitons	121
E	Anisotropic Stark shift, field-induced dissociation, and electroabsorption of excitons in phosphorene	131
F	Calculation of the nonlinear response functions of intra-exciton transitions in two-dimensional transition metal dichalcogenides	147
G	Efficient ionization of two-dimensional excitons by intense single-cycle terahertz pulses	159

List of publications

This thesis is based on the following papers:

- Paper A:** *Field-induced dissociation of two-dimensional excitons in transition metal dichalcogenides*,
Høgni C. Kamban and Thomas G. Pedersen,
Phys. Rev. B **100**, 045307 (2019)
- Paper B:** *Finite-Difference Time-Domain Simulation of Strong-Field Ionization: A Perfectly Matched Layer Approach*,
Høgni C. Kamban, Sigurd S. Christensen, Thomas Søndergaard, and Thomas G. Pedersen,
Phys. Stat. Sol. B **257**, 1900467 (2020)
- Paper C:** *Interlayer excitons in van der Waals heterostructures: Binding energy, Stark shift, and field-induced dissociation*,
Høgni C. Kamban and Thomas G. Pedersen,
Sci. Rep. **10**, 5537 (2020)
- Paper D:** *Analytical quantitative semiclassical approach to the Lo Surdo–Stark effect and ionization in two-dimensional excitons*,
J. C. G. Henriques, **Høgni C. Kamban**, Thomas G. Pedersen, and N. M. R. Peres,
Phys. Rev. B **102**, 035402 (2020)
- Paper E:** *Anisotropic Stark shift, field-induced dissociation, and electroabsorption of excitons in phosphorene*,
Høgni C. Kamban, Thomas G. Pedersen, and N. M. R. Peres,
Phys. Rev. B **102**, 115305 (2020)
- Paper F:** *Calculation of the nonlinear response functions of intra-exciton transitions in two-dimensional transition metal dichalcogenides*,
J. C. G. Henriques, **Høgni C. Kamban**, Thomas G. Pedersen, and N.

List of publications

M. R. Peres,
Phys. Rev. B **103**, 235412 (2021)

Paper G: *Efficient ionization of two-dimensional excitons by intense single-cycle terahertz pulses*,
Høgne C. Kamban and Thomas G. Pedersen,
Phys. Rev. B **104**, 235305 (2021)

This thesis has been submitted for assessment in partial fulfillment of the PhD degree. The thesis is based on the published scientific papers which are listed above. As part of the assessment, co-author statements have been made available to the assessment committee and are also available at the Faculty.

Preface

The present thesis is the result of the work I have conducted as a Ph.D. student at the Department of Materials and Production at Aalborg University during the period 2018 – 2021.

I remember my years as an undergraduate student when the semester containing quantum mechanics on its curriculum was approaching. It had a reputation of being a difficult course among the students, and a natural curiosity of the subject arose. While some topics turned out to be more difficult than others, all of them turned out to be profoundly interesting. Of course, the contagious enthusiasm of the instructor, Professor Thomas Garm Pedersen, did not hurt either. I remember walking into Thomas’ office as the course was ending, to ask if he could recommend a book for me to further study the topic during the summer holidays. He quickly found a book in his office and let me borrow it. This readiness to guide the curious student, his open-door policy, his passion for physics and mathematical reasoning, and his eagerness to discuss interesting topics (whether they are directly related to the research topic or not) are just a few of the reasons that I am grateful of having had Professor Thomas Garm Pedersen as my Ph.D. supervisor.

I would also like to express my gratitude towards Nuno Peres who made my visits at the University of Minho and INL (International Iberian Nanotechnology Laboratory) in Braga a wonderful experience. Not only did we have many interesting work-related discussions, but he took time out of his day to show me around in Portugal, for which I am grateful. Unfortunately, my physical presence in Braga was cut short due to the pandemic. Aalborg University called for all of its employees located abroad to come home as a safety precaution. Fortunately, our collaboration could continue unhindered with the help of online tools.

I would also like to thank the other Ph.D. students and postdocs at Aalborg University for creating a pleasant atmosphere. In particular, I would like to thank Pawel Cielecki, Jonas Have, and Enok Skjølstrup for engaging conversations, and for organizing entertaining activities outside of academia.

Preface

Finally, I would like to thank my friends and family. In particular, I would like to thank my parents for their continuous support without which reaching this point would have been ever more challenging. I would like to thank Katrin for her support during the time of writing this thesis. I also owe a thank you to my daughter, Gunnvør, for her patience and understanding even when her father has absent-mindedly been thinking about the topics of this thesis.

Høgni C. Kamban
Aalborg University, April 4, 2022

Chapter 1

Introduction

Two-dimensional (2D) materials have attracted a lot of attention in recent years. These materials consist of a single to a few layers of atoms confined to the plane. Early theoretical considerations [1–4] led to the conclusion that such materials could not exist in a stable form. However, this did not stop Novoselov and Geim from successfully exfoliating graphene, a single layer of carbon atoms, in 2004 [5, 6]; an action that has since sparked a tremendous research interest in 2D materials.

Graphene has been intensely studied due to its remarkable properties [7] and potential for nanoscale electronic applications [4, 7–9]. Examples include high-speed electronics [10, 11] that exploit the exceptionally high electron mobility of about $200000 \text{ cm}^2\text{V}^{-1}\text{s}^{-1}$ [9, 12], and bendable electronics that utilize its flexibility [7]. Interestingly, graphene had been isolated years prior to its rediscovery in 2004 by a German group [13, 14] already in the early 1960s by reduction of graphite oxide. This method produces comparatively poor quality samples to those produced by the Scotch-tape method used by Novoselov and Geim. Perhaps this is one of the reasons that researchers only took notice once graphene was rediscovered.

Although graphene has many desirable properties, its electronic and optoelectronic applications are limited by the absence of a band gap. While a band gap may be induced in graphene by, e.g., introducing a periodic array of circular holes to the sheet [15–17], or by applying an electric field to graphene bilayers [18], it is advantageous to find alternative semiconducting 2D materials [19, 20]. A particularly interesting group is the so-called transition metal dichalcogenides (TMDs). In their 2D form, these materials consist of a single hexagonal layer of transition-metal atoms (such as Mo and W) that are sandwiched between two layers of chalcogen atoms (such as S, Se, and Te) [21].

Both graphene and TMDs exist as layered materials in nature. That is, their bulk (3D) structure consists of stacked monolayers that are attracted to one another by relatively weak forces. This structure is the reason that it is easy to peel these materials layer by layer and produce isolated monolayers. Some of the most studied TMDs are MoS_2 , MoSe_2 , WS_2 , and WSe_2 , and these are also the TMDs that will be considered in the present thesis. A remarkable feature of these TMDs is how the band gap transitions from an indirect to a direct band gap as they transition from their bulk to monolayer form [22–30,30,31], making them very attractive for optoelectronic devices [32–35]. As examples, excitonic LEDs [36–44], photodetectors [45–50], and lasers [51–53] built using monolayer TMDs are expected to be efficient. They also show potential applications in solar cells [54–56].

One of the newer members of the 2D family is phosphorene (a single layer of black phosphorous) [57–62]. Unlike TMDs, it is a direct band gap semiconductor regardless of the number of layers [63–65]. The size of the gap evolves from around 0.3 eV in its bulk form to around 2 eV in monolayers [57, 60, 66–68]. The ability to tune the direct band gap by controlling the number of layers is one of the features that make phosphorene such an attractive material for applications [35]. It is also a highly anisotropic material, which suggests further tunability of its physical properties [69–77] by rotating the crystal as one sees fit.

While 2D materials are profoundly interesting from a fundamental point of view, the real potential for applications lies not with isolated monolayers but with artificially stacked structures. The idea is quite simple, take a monolayer material and place it on top of another monolayer or few-layer structure. Continue by adding layers of your choosing on top of this structure. Such structures are referred to as van der Waals heterostructures (vdWHs) [78], and were experimentally realized for the first time in 2011 [79] and several examples have since been constructed [46, 80–83]. Whereas the motivation behind many of the 2D materials that are being studied is to correct for the weaknesses of graphene [19, 20, 27, 84–86], stacked vdWHs form an endless array of artificial structures for which the physical parameters may be tuned by carefully selecting the monolayers that compose these structures [78].

Many of the extraordinary properties of 2D materials are due to the strongly bound excitons in these materials. As these excitons are precisely the focus of the present thesis, a somewhat detailed description is warranted.

1.1 Excitons

In solid-state physics, the electronic band structure of a material describes the allowed energy states that an electron may occupy in said material. Semiconductors and insulators have a gap in the band structure, the so-called band gap, whereas metals do not. The lower band is referred to as the valence band and the higher one as the conduction band. Due to the gap, electrons in semiconductors and insulators must absorb a finite amount of energy to be excited from the valence band into the conduction band, where they can contribute to an electrical current. Consider for a moment a semiconductor in its ground state. That is, where the valence band is full and the conduction band is empty. If we subject the semiconductor to light of the proper frequency, an electron in the valence band may be excited into the conduction band by absorbing a photon. The excited electron leaves behind a vacancy in the valence band. This vacancy behaves like a positively charged particle and is referred to as a hole. Due to their opposite charge, the electron and hole interact via the attractive Coulomb force, and they may therefore form bound states. It is these bound states that we call excitons. Since the electron and hole win a small amount of energy by forming a bound state, an exciton may be formed by the electron absorbing an amount of energy that is a bit lower than the band gap.

Frenkel was the first to introduce the concept of excitons in 1931 [87, 88] when studying how light transforms into heat in semiconductors. The excitons introduced by Frenkel have small radii (distance between electron and hole) and large binding energies. Both the electron and hole are therefore typically located on a single molecule in the crystal. Wannier [89] and Mott [90] later considered excitons where the radius was much larger than the crystal lattice vector. They were therefore able to construct a model in which the lattice potential is taken into account via the effective mass method. The resulting model is very simple and is mathematically similar to that of the hydrogen atom. Wannier-Mott excitons are mostly observed in semiconductors with narrow band gaps and large dielectric constants [91]. Early experimental evidence of Wannier-Mott excitons was obtained by Gross and Yacobson [92, 93] where they observed spectra near the band gap absorption edge resembling those of hydrogen.

Frenkel and Wannier-Mott excitons are two extreme cases of the excitonic phenomenon with small and large radii, respectively. It is natural to ask if intermediate cases exist and if it is possible to construct a joint theory of these concepts. Indeed it is, and it is the so-called Bethe-Salpeter equation (BSE) [94] that one must use. This equation was derived by E. E. Salpeter and H. A. Bethe in 1951 in a different context. Later, Sham and Rice showed that

it is precisely this equation that describes excitons, and that the Wannier-Mott equation is an approximation to this equation in the relevant region of small binding energy and large spatial extent [95]. The BSE is used when one wishes to compute excitonic properties from first principles. The process is laid out in Ref. [96]. Typically the single-particle properties are first calculated using density functional theory. Then these properties are corrected using a GW approximation [97]. Finally, the excitonic properties are computed via the BSE and taking the GW corrected band structure as input. This type of calculation has proven accurate for many materials, such as carbon nanotubes [98], transition metal dichalcogenides (TMDs) [99], and phosphorene [67]. The downside of this method is that it is quite complicated and very computationally demanding. Hence, it is useful to apply the Wannier-Mott model when applicable.

Exciton binding energies in bulk (3D) semiconductors are typically just a few meV [100–103]. Temperature-induced crystal vibrations (thermal agitation) are therefore typically enough to dissociate the excitons into free electrons and holes. The contribution of these excitons to, e.g., the optical absorption can therefore often be neglected. This is not the case for 2D materials, however. Here, the reduced screening brings with it a stronger interaction between the electron and hole, and thus the binding energies will be much larger and can often reach several hundred meV [68, 104–108]. The stronger interaction between the electron and hole in 2D materials may intuitively be understood by drawing electric field lines between the particles. In a bulk semiconductor, the field lines are dampened by the large dielectric constant of the semiconductor itself. However, many of the field lines between electrons and holes in 2D materials travel in the surrounding media that typically has a much lower dielectric constant, hence less dampening occurs (see Fig. 1.1 for a visual demonstration). Excitons in these materials are therefore resistant to thermal dissociation and dominate the optical spectra below the band gap. As many optoelectronic applications (such as photodetectors and solar cells) require free electrons and holes to operate, it is natural to ask if we can somehow induce dissociation of these strongly bound excitons. As we shall see in the present thesis, this may be achieved by applying electric fields to the excitons.

1.2 This work

The main focus of the present thesis is to study electric-field-induced dissociation of excitons in monolayer materials and bilayer vdWHs. Subjecting excitons to external fields is of tremendous fundamental interest, as it is a method of collecting information about their characteristic behavior. An undisturbed exciton does not show all of its properties. As an example, external magnetic fields

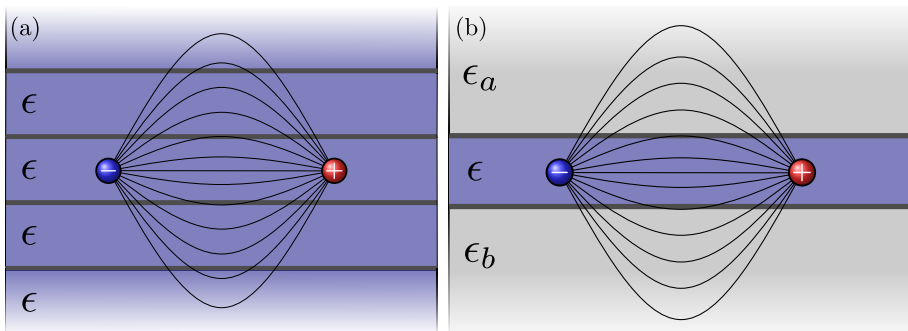


Fig. 1.1: Sketch of electron-hole pair in a bulk (a) and a monolayer (b) structure. The interaction between the electron-hole pair is represented by the field lines drawn between them. The bulk structure consists of many monolayers with dielectric constant ϵ stacked on top of one another, whereas the monolayer structure consists of a single layer surrounded by media with dielectric constants ϵ_a and ϵ_b above and below the layer, respectively. Typically, $\epsilon_{a/n} \ll \epsilon$.

have been used to probe the spatial extent and mass of excitons in monolayer materials [109–111]. Electric fields, on the other hand, shift the exciton energy levels (exciton Stark effect) [112–118] which in turn shifts the absorption peaks of the semiconducting material. Sufficiently strong fields are able to completely dissociate the excitons [113–117] which in turn modifies the photoresponse rate of materials [116]. This ability to dynamically control the excitonic properties in semiconducting devices is of tremendous practical interest. As mentioned above, many practical applications rely on the conversion of photons into electrical current. Efficient conversion of photons into electrical current requires dissociation of excitons. It is a four-step process: (i) a photon is absorbed and an exciton is created, (ii) the exciton is dissociated into a free electron and hole, (iii) the charge carriers are transported through the material in order to (iv) be collected at the attached contacts. While thermal agitation is sufficient for point (ii) in most bulk semiconductors, it is typically not the case for the strongly bound excitons in 2D semiconductors at low temperatures.

Prior to this work, Stark shifts and dissociation rates in 2D materials had been computed for excitons in MoS_2 [113, 114] and WSe_2 [116] monolayers. Massicotte et al. [116] performed a systematic experimental study where they measured the photoresponse rate of WSe_2 as a function of applied field strength. They found that for weak fields ($\lesssim 15 \text{ V}/\mu\text{m}$), the photoresponse rate is limited by field-induced exciton dissociation. Obtaining theoretical predictions for dissociation rates at such weak fields turned out to be difficult using the standard method of complex scaling. The rates were therefore obtained by fitting to a functional form motivated by the 2D hydrogen atom. Figuring out how

to obtain these weak field exciton dissociation rates was one of the goals in the present thesis. This was achieved by using a slightly different numerical approach based on exterior complex scaling. Using this method, we have computed exciton Stark shifts and dissociation rates for monolayer MoS_2 , MoSe_2 , WS_2 , and WSe_2 in various dielectric environments. The results were reported in Paper A. While this method is more stable for weak electric fields, it turns out that any numerical method with finite precision arithmetic breaks down when the fields become sufficiently weak. For this reason, a general analytical weak-field approximation that bridges the gap between dissociation rates for moderate and extremely weak electric fields was derived. To determine the coefficient of this expression, the exciton wave function must be known with high numerical accuracy. The aim of Paper D was to see if this coefficient could also be approximated such that a fully analytical approximation may be derived.

An interesting experimental study was published during the time that this thesis was taking shape. Merkl et al. [119] measured exciton binding energies of interlayer excitons in bilayer vdWHs WSe_2/WS_2 . This sparked an interest in both binding energies and field-induced dissociation rates for interlayer excitons in bilayer structures. Interlayer excitons, in contrast to intralayer excitons, are excitons where the electron and hole reside in two different monolayers. The exciton dynamics in bilayer vdWHs turned out to be profoundly interesting. Hong et al. [56], for instance, found that photoexcited excitons in the MoS_2 layer of a MoS_2/WS_2 structure are transformed from intra- to interlayer excitons remarkably fast. In particular, they found that the hole tunnels from the MoS_2 layer into the WS_2 layer within 50 fs. It is therefore likely that conversion from photons to current in these structures involves the additional step of forming an interlayer exciton. In Paper C, we computed binding energies, Stark shifts, and dissociation rates for interlayer excitons in the six bilayer combinations of MoS_2 , MoSe_2 , WS_2 , and WSe_2 that form a type-II band alignment (where the conduction band minimum and the valence band maximum reside in different layers).

As discussed before, one of the newer members of the 2D family is phosphorene. This material is different from the TMDs above due to its highly anisotropic nature. Previous studies have analyzed exciton Stark shifts in phosphorene [120, 121], but little attention was given to exciton dissociation. Due to the anisotropic nature of this material, one expects both Stark shifts and dissociation rates to depend on the direction of the in-plane electric field. The aim of Paper E was to study this dependence, and in the paper we present shifts, rates, as well as absorption spectra under the influence of external electric fields.

From a practical perspective, it is not very convenient to apply static elec-

tric fields to excitons in 2D materials. For instance, Massicotte et al. [116] introduced their electric fields by incorporating buried electrical contacts with a tiny gap in their sample. Using a different type of electric field, say, a laser, may be more convenient as little to no modifications need to be made to the sample. With the rapid progression of THz technology, THz pulses are a natural candidate. In Paper G, we therefore study exciton dissociation induced by THz pulses. This paper was, in part, motivated by the experimental study performed by Shi et al. [122] in 2020. They measured the absorption spectrum of a MoS₂ sample during the influence of a THz pulse. The authors found that the broadening of their absorption peaks was well explained by a Franz-Keldysh model, rather than exciton dissociation. As it is well known that exciton dissociation also broadens the absorption peaks, it is interesting to compute just how much broadening is introduced by dissociation.

Finally, we note that the results of Papers B and F will not be discussed in the present thesis. This is done in order to keep the main text as coherent as possible.

Chapter 1. Introduction

Chapter 2

Theoretical Formalism

In the published works, only the most important details of the theoretical methods and models used are given. This condensed form with only the essential details to allow reproduction of the results is common for journal papers. With the goal of making this thesis as self-consistent as possible, detailed descriptions of the theory will be provided here.

The first section introduces the Wannier exciton model used throughout the published works. Here, the unperturbed exciton problem in the different material structures considered is described in detail. The next section describes how an electric field may be incorporated into the model, and how both exciton dissociation rates and Stark shifts may be obtained from the resulting equations. The method of complex scaling is used, and the focus of this section is on both the mathematical formalism and physical intuition behind it. The third section then describes how this formalism may be implemented in a numerical method. This is done by expanding the wave function in a finite element basis. The final section in the present chapter describes how excitonic processes induced by time-dependent electric fields may be computed within the Wannier exciton model.

2.1 Wannier exciton model

The state-of-the-art for describing excitonic effects from first principles is the many-body Bethe-Salpeter equation (BSE) [94,96,123,124]. Unfortunately, the BSE is complicated to solve and is computationally demanding even for simple systems. Fortunately, however, excitons may be modeled as electron-hole pairs whose behavior is governed by the much simpler Wannier equation when the exciton radius is large compared to the lattice constant of the semiconducting crystal [95,125]. Excellent agreement between binding energies from the BSE and the Wannier model have repeatedly been demonstrated [105,126–130]. The Wannier model [89,131] makes use of the two-band, effective mass approximation, and the equation reads

$$H_0\psi(\mathbf{r}) = E_0\psi(\mathbf{r}), \quad (2.1)$$

where the H_0 is the Hamilton operator, ψ the wave function, E_0 the binding energy, and $\mathbf{r} = \mathbf{r}_e - \mathbf{r}_h$ the relative electron-hole coordinate. The Hamiltonian for an electron-hole pair is given by

$$H_0 = -\frac{1}{2\mu}\nabla^2 + V(\mathbf{r}), \quad (2.2)$$

where $\mu = m_em_h/(m_e + m_h)$ is the reduced exciton mass, and V describes the electrostatic interaction between the electron and hole. Here, m_e and m_h are the effective electron and hole masses, respectively. Equation (2.1) is identical to the Schrödinger equation for a two-particle system. It is the correct form for both 2D and 3D problems [125]. One simply has to use the appropriate differential and position operators. That is

$$\mathbf{r} = x\mathbf{e}_x + y\mathbf{e}_y + z\mathbf{e}_z \quad (2.3)$$

$$\nabla^2 = \frac{\partial^2}{\partial x^2} + \frac{\partial^2}{\partial y^2} + \frac{\partial^2}{\partial z^2}, \quad (2.4)$$

where \mathbf{e} are the unit vectors, and the z terms are omitted for 2D problems. Equation (2.1) contains the two material dependent quantities μ and V . The reduced mass μ may be obtained either from first principle calculations or from experiments, whereas the interaction potential may be estimated by solving the Poisson equation for the relevant system. For an electron and hole located at (x, y, z) and $(0, 0, z')$, respectively, it reads

$$\nabla \cdot [\boldsymbol{\epsilon} \cdot \nabla V(x, y, z, z')] = 4\pi\delta(x)\delta(y)\delta(z - z'), \quad (2.5)$$

where δ is the Dirac delta function, and $\boldsymbol{\epsilon}$ is the dielectric tensor of the material structure. In the present thesis, we will study three distinct types of material structures. These are monolayer TMDs, phosphorene, and bilayer vdWHs. A more detailed discussion of Wannier excitons in these materials follows.

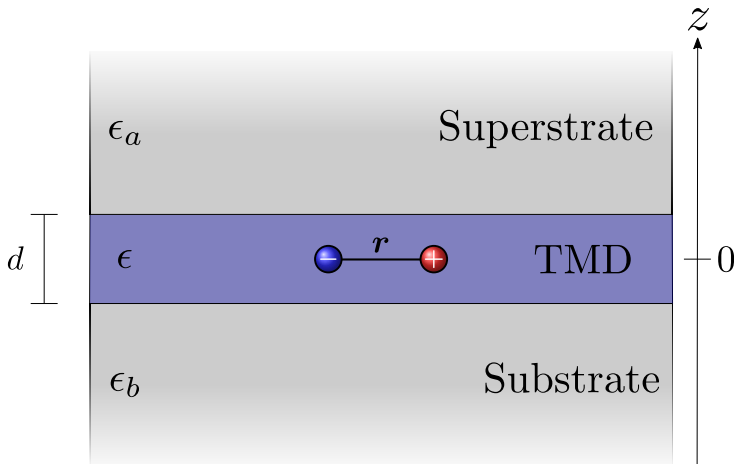


Fig. 2.1: Model of a TMD monolayer with thickness d and dielectric constant ϵ surrounded by a sub- and superstrate with dielectric constants ϵ_a and ϵ_b , respectively. The relative electron-hole coordinate is denoted by \mathbf{r} .

2.1.1 Excitons in monolayer transition metal dichalcogenides

Monolayer TMDs are usually either placed on a substrate or fully encapsulated by some media when studied experimentally. Typically the surrounding media is much thicker than the monolayer itself. Such a structure may therefore be modeled as a sheet of thickness d with dielectric constant ϵ surrounded by sub- and superstrates that extend to infinity with dielectric constants ϵ_a and ϵ_b , respectively. The geometry is sketched in Fig. 2.1. The interaction potential between two charges in such a structure when $d \rightarrow 0$ was derived by Rytova [132] and later rediscovered by Keldysh [133]. The Rytova-Keldysh (RK) potential reads [132–134]

$$V(\mathbf{r}) = -\frac{\pi}{2r_0} \left[H_0\left(\frac{\kappa r}{r_0}\right) - Y_0\left(\frac{\kappa r}{r_0}\right) \right], \quad (2.6)$$

where r_0 is the so-called screening length, $\kappa = (\epsilon_a + \epsilon_b)/2$ is the average of the dielectric constants of the sub- and superstrates, and H_0 and Y_0 are the Struve and Bessel functions of zeroth order, respectively [135]. Note that if the surrounding media have different in- (\parallel) and out-of-plane (\perp) dielectric constants, then $\epsilon_a = \sqrt{\epsilon_a^{(\parallel)} \epsilon_a^{(\perp)}}$. The two constants κ and r_0 describe the extent to which the interaction is screened by the surrounding media and the sheet itself, respectively. Larger values lead to weaker interactions. The screening length may be related to the 2D polarizability of the sheet α_{2D} by $r_0 = 2\pi\alpha_{2D}$

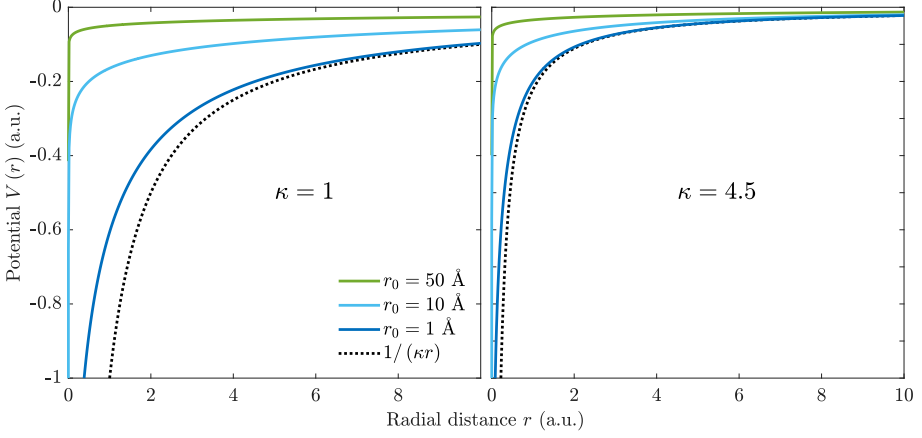


Fig. 2.2: Rytova-Keldysh potential for various screening lengths r_0 in two different dielectric surroundings. The left panel corresponds to freely suspended materials ($\kappa = 1$), and the right to hBN encapsulated materials ($\kappa = 4.5$). The dotted line shows the screened Coulomb potential $-1/(\kappa r)$.

[126]. A series expansion of Eq. (2.6) for large arguments may be obtained [135]

$$\begin{aligned}
 & -\frac{\pi}{2r_0} \left[H_0 \left(\frac{\kappa r}{r_0} \right) - Y_0 \left(\frac{\kappa r}{r_0} \right) \right] \\
 & = \sum_{k=0}^{m-1} \frac{\Gamma(1/2 + k)(2r_0)^{2k}}{\Gamma(1/2 - k)(\kappa r)^{2k+1}} + O \left(\frac{|r_0|^{2m}}{|\kappa r|^{2m+1}} \right). \quad (2.7)
 \end{aligned}$$

From this expansion, it is immediately clear that the RK potential behaves as the simple screened Coulomb potential $-1/(\kappa r)$ when either r is very large or r_0 very small. This behavior is confirmed in Fig. 2.2, where the RK potential is plotted for various screening lengths in two distinct dielectric surroundings. From Fig. 2.2 it is also clear that the RK potential diverges slower than the Coulomb potential as r tends to zero. In fact, it diverges only logarithmically [126].

The RK potential exhibits central symmetry. Analogous to the 2D hydrogen atom [136], the differential equation may therefore be separated into an angular and a radial part and, as a result, the eigenstates are of the form $\psi_{mn}(\mathbf{r}) = R_n(r) \exp(im\theta)$, where $n = 1, 2, 3, \dots$ and $|m| = 0, 1, 2, \dots, n-1$ are the principal quantum number and angular momentum, respectively. Excitons in TMDs are therefore usually referred to by their principal quantum number and angular momentum quantum number [112, 137–139]. We note that angular momentum quantum numbers are often denoted by letters such that $|m| = \{0, 1, 2, 3, 4, 5, 6, 7, \dots\}$ are labeled by $\{s, p, d, f, g, h, i, k, \dots\}$ [140]. The

ground state exciton is therefore referred to as $1s$, where the quantum numbers are $n = 1$ and $m = 0$.

While there are many similarities between Wannier excitons and the 2D hydrogen atom, the eigenenergies exhibit different qualitative behaviors. The energies for hydrogen only depend on the principal quantum number. They are therefore degenerate with respect to m , which is a special case for the simple atom. The degeneracy is often referred to as an accidental degeneracy, as there is no obvious symmetry that results in it. It can, however, be traced back to a 2D form of the Runge-Lenz vector [141]. This degeneracy is not present for 2D excitons.

2.1.2 Excitons in bilayer van der Waals heterostructures

By artificially stacking a number of distinct monolayers, one may construct an endless array of structures with different physical properties [78]. In this section, we will focus on bilayer vdWHs formed by stacking two monolayers. In a similar manner as discussed in the previous section, this bilayer structure would then be encapsulated by some surrounding media. We model this structure as a four-layer structure: two slabs of thickness d_1 and d_2 with dielectric constants ϵ_1 and ϵ_2 , respectively, surrounded by super- and substrates with dielectric constants ϵ_a and ϵ_b , respectively. The model structure can be seen in Fig. 2.3. Bilayer vdWHs support both intra- and interlayer excitons. These are excitons for which both the electron and hole reside in the same (intra) or different (inter) layers, and they are shown in Fig. 2.3. Whether the ground-state exciton is an intra- or interlayer exciton depends on how the band structures of the two monolayers align. Here, we will focus on TMD monolayers that form a type-II band alignment when brought together. This type of band alignment leads to the valence band maximum and the conduction band minimum residing in two different layers. The result is that electrons and holes in a type-II bilayer would prefer to be located in different monolayers. If the loss in exciton binding energy is smaller than the energy gained by the band offset, the ground state exciton is an interlayer exciton. This is the case for all structures considered in the present thesis.

Interlayer excitons have been intensely studied in recent years (see, e.g., Refs. [56, 119, 143–147]). A particularly interesting experiment was performed by Hong et al. [56], where they observed that the hole of a photoexcited intralayer exciton in the MoS_2 layer of an MoS_2/WS_2 bilayer tunneled into the WS_2 layer within 50 fs after excitation. This ultrafast transition from intra- to interlayer excitons, along with the long lifetime of interlayer excitons due to the small overlap of the electron and hole wave functions [144, 148–151], means

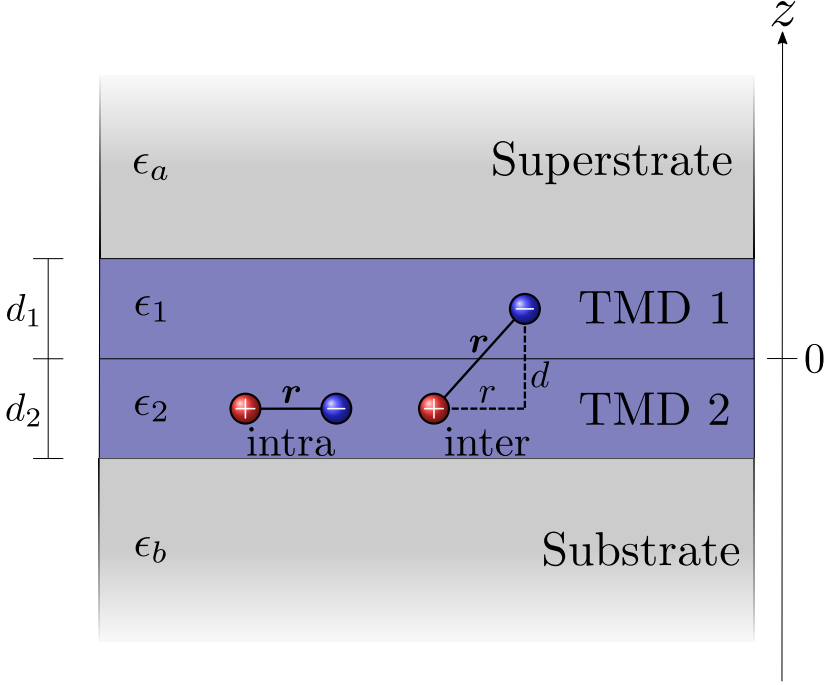


Fig. 2.3: Model of bilayer vdWH surrounded by a super- and substrate with dielectric constant ϵ_a and ϵ_b , respectively. The first (second) monolayer has thickness d_1 (d_2) and dielectric constant ϵ_1 (ϵ_2). Two distinct types of excitons are shown, namely an intralayer and an interlayer exciton. This figure is a modified version of the figure in Paper C [142].

that interlayer excitons play a major role in the optoelectronic properties of these structures.

In what follows, we will refer to the bilayer vdWHs as TMD1/TMD2, where the conduction band minimum is located in TMD1 and the valence band maximum in TMD2. For all the structures considered in the present thesis, the loss in exciton binding energy is smaller than the energy gained from the electron and hole residing in the first and second layers, respectively. This results in the many-body exciton ground state being an interlayer exciton. The Wannier equation may be used to describe excitons in this structure as well. However, we must include an additional parameter $d = |z_e - z_h|$ that describes the vertical distance between the electron and hole. We consider the particles as confined to move in the middle of a particular monolayer. The vertical distance therefore becomes $d_{\text{inter}} = (d_1 + d_2)/2$ and $d_{\text{intra}} = 0$ for the inter- and intralayer excitons, respectively. To estimate the potential interaction between an electron-hole pair in this structure, we turn to the Poisson equation. This was done in Paper C, where we found that the interaction between an electron

2.1. Wannier exciton model

in the first TMD and a hole in the second is given by

$$V_{\text{inter}}(r) = - \int_0^\infty \frac{e^{-dq} J_0(qr)}{\epsilon_{\text{inter}}(q)} dq, \quad (2.8)$$

where $d = (d_1 + d_2)/2$. The effective dielectric function describes the screening of the interaction, and is given by $\epsilon_{\text{inter}}(q) = A_{\text{inter}}(q)/B_{\text{inter}}(q)$ where

$$A_{\text{inter}}(q) = (\epsilon_1^2 \gamma_+ + \epsilon_a \epsilon_2 \gamma_-) Y_-^{2d_1} + (\epsilon_a \epsilon_1 \gamma_+ + \epsilon_1 \epsilon_2 \gamma_-) Y_+^{2d_1} \quad (2.9)$$

$$B_{\text{inter}}(q) = 2 \left(\epsilon_a Y_-^{d_1} + \epsilon_1 Y_+^{d_1} \right) \left(\epsilon_2 Y_+^{d_2} + \epsilon_b Y_-^{d_2} \right) \quad (2.10)$$

and, to simplify notation, we have defined

$$Y_\pm^x = 1 \pm e^{-xq} \quad (2.11)$$

$$\gamma_\pm = \epsilon_2 Y_\pm^{2d_2} + \epsilon_b Y_\mp^{2d_2}. \quad (2.12)$$

The effective dielectric function tends to the average sub and superstrate dielectric constant $\kappa = (\epsilon_a + \epsilon_b)/2$ when $q \rightarrow 0$, and to the average of the two layers $(\epsilon_1 + \epsilon_2)/2$ when $q \rightarrow \infty$, as expected due to the inverse relationship between q and r . The interaction for intralayer excitons is given by

$$V_{\text{intra}}(r) = - \int_0^\infty \frac{J_0(qr)}{\epsilon_{\text{intra}}^{(j)}(q)} dq, \quad (2.13)$$

where the parameter $j = \{1, 2\}$ indicates whether both particles reside in the first or second layer. The effective dielectric functions are given by $\epsilon_{\text{intra}}^{(j)}(q) = A_{\text{intra}}^{(j)}(q)/B_{\text{intra}}^{(j)}(q)$ where

$$A_{\text{intra}}^{(1)}(q) = \epsilon_1 \left\{ (\epsilon_1^2 \gamma_+ + \epsilon_2 \epsilon_a \gamma_-) Y_-^{2d_1} + \epsilon_1 Y_+^{2d_1} \left[(\epsilon_2^2 + \epsilon_a \epsilon_b) Y_-^{2d_2} + \epsilon_2 (\epsilon_a + \epsilon_b) Y_+^{2d_2} \right] \right\} \quad (2.14)$$

$$B_{\text{intra}}^{(1)}(q) = \left[Y_-^{2d_2} \left(\epsilon_2^2 Y_-^{d_1} + \epsilon_1 \epsilon_b Y_+^{d_1} \right) + \epsilon_2 Y_+^{2d_2} \left(\epsilon_1 Y_+^{d_1} + \epsilon_b Y_-^{d_1} \right) \right] \times \left(\epsilon_1 Y_+^{d_1} + \epsilon_a Y_-^{d_1} \right) \quad (2.15)$$

$$A_{\text{intra}}^{(2)}(q) = \epsilon_2 \left\{ (\epsilon_1^2 \gamma_+ + \epsilon_2 \epsilon_a \gamma_-) Y_-^{2d_1} + \epsilon_1 Y_+^{2d_1} \left[(\epsilon_2^2 + \epsilon_a \epsilon_b) Y_-^{2d_2} + \epsilon_2 (\epsilon_a + \epsilon_b) Y_+^{2d_2} \right] \right\} \quad (2.16)$$

$$B_{\text{intra}}^{(2)}(q) = \left[Y_-^{2d_1} \left(\epsilon_1^2 Y_-^{d_2} + \epsilon_2 \epsilon_a Y_+^{d_2} \right) + \epsilon_1 Y_+^{2d_1} \left(\epsilon_2 Y_+^{d_2} + \epsilon_a Y_-^{d_2} \right) \right] \times \left(\epsilon_2 Y_+^{d_2} + \epsilon_b Y_-^{d_2} \right). \quad (2.17)$$

The limits for the intralayer functions are ϵ_1 and ϵ_2 for the first and second layer, respectively, when $q \rightarrow \infty$ and $\kappa = (\epsilon_a + \epsilon_b)/2$ when $q \rightarrow 0$.

It is convenient to obtain an approximation for these interaction potentials in the form of simple analytical functions. Fogler et al. [148] proposed a bare-Coulomb-type interaction with a correction term as an approximation. More commonly, the RK potential is used with the distance replaced by $\sqrt{r^2 + d^2}$ [152–154]. However, simply substituting $r \rightarrow \sqrt{r^2 + d^2}$ in the monolayer RK potential does not take into account the additional screening at small distances contributed by the second TMD layer. The result is an interaction that is too strong compared to the full result of the Poisson equation [155]. To deal with this, we proposed in Paper C that one substitutes $r_0 \rightarrow r_0^{(1)} + r_0^{(2)}$ as well, where $r_0^{(1)}$ and $r_0^{(2)}$ are the screening lengths of the first and second monolayer, respectively. This is further motivated by the fact that the screening length is proportional to the thickness of the structure [133, 134]. These substitutions lead to the bilayer Keldysh (BLK) interaction

$$V_{\text{BLK}}(r) = -\frac{\pi}{2(r_0^{(1)} + r_0^{(2)})} \left[H_0 \left(\frac{\kappa \sqrt{r^2 + d^2}}{r_0^{(1)} + r_0^{(2)}} \right) - Y_0 \left(\frac{\kappa \sqrt{r^2 + d^2}}{r_0^{(1)} + r_0^{(2)}} \right) \right], \quad (2.18)$$

where d is the vertical distance between the electron and hole. This form also tends to the expected large radii behavior $-1/(\kappa \sqrt{r^2 + d^2})$.

While the BLK form does not follow simply from the full solution to the Poisson equation, the intralayer form may be motivated by expanding the intralayer dielectric function to first order in q . That is

$$\epsilon_{\text{intra}}^{(1)} \approx \kappa + \left(\frac{d_1 \epsilon_1}{2} + \frac{d_2 \epsilon_2}{2} - \frac{d_1 \epsilon_a^2}{4\epsilon_1} - \frac{d_1 \epsilon_b^2}{4\epsilon_1} - \frac{d_2 \epsilon_b^2}{2\epsilon_2} \right) q \quad (2.19)$$

$$\approx \kappa + \left(\frac{d_1 \epsilon_1}{2} + \frac{d_2 \epsilon_2}{2} \right) q \quad (2.20)$$

$$\approx \kappa + (r_0^{(1)} + r_0^{(2)}) q \quad (2.21)$$

$$\epsilon_{\text{intra}}^{(2)} \approx \kappa + \left(\frac{d_1 \epsilon_1}{2} + \frac{d_2 \epsilon_2}{2} - \frac{d_2 \epsilon_a^2}{4\epsilon_2} - \frac{d_2 \epsilon_b^2}{4\epsilon_2} - \frac{d_1 \epsilon_a^2}{2\epsilon_1} \right) q \quad (2.22)$$

$$\approx \kappa + \left(\frac{d_1 \epsilon_1}{2} + \frac{d_2 \epsilon_2}{2} \right) q \quad (2.23)$$

$$\approx \kappa + (r_0^{(1)} + r_0^{(2)}) q \quad (2.24)$$

2.1. Wannier exciton model

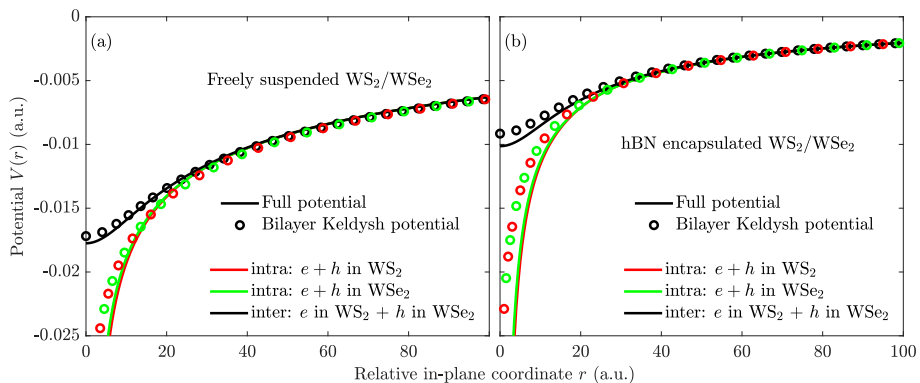


Fig. 2.4: Interaction potential for excitons in a freely suspended (a) and hBN encapsulated (b) WS_2/WSe_2 bilayer vdWH. The black solid line corresponds to the interlayer interaction between an electron and hole in the WS_2 and WSe_2 layer, respectively, and is given by Eq. (2.8). The red and green lines correspond to the intralayer interaction where both particles reside in the WS_2 or WSe_2 layer, respectively, and is given by Eq. (2.13). The circles correspond to the bilayer Keldysh approximation. Panel (a) is a reproduction of the figure in Paper C [142]. [Note that the intralayer interactions in Paper C have been mislabeled]

where the the approximations are justified because the dielectric constants of the TMDs are typically much larger than those of the surrounding media, and the screening length for layer j is $r_0^{(j)} \approx d_j \epsilon_j / 2$ [106]. Using these approximations in Eq. (2.13) leads to an interaction on the Keldysh form with the usual monolayer r_0 replaced by the sum of the two screening lengths of the respective monolayers. Note that the approximate intralayer potentials are identical regardless of which layer the two particles reside. Unfortunately, the integral in Eq. (2.8) does not have a closed form expression even with a linearized dielectric function. Nevertheless, the interlayer BLK approximation is justified by good agreement with Eq. (2.8). A graphical comparison is made in Fig. 2.4 for a WS_2/WSe_2 structure in free space and hBN encapsulation. The parameters used in the calculations are the screening lengths from Olsen et al. [128], the dielectric constants from Laturia et al. [156], and the TMD widths used are half of the vertical lattice constants from He et al. [157]. As may be seen in Fig. 2.4, the interlayer potential is finite at the origin and behaves as $a + b^2$ where a and b are constants for small r . This behavior becomes clear from the expansion of the Bessel function

$$J_0(qr) = 1 - \left(\frac{qr}{2}\right)^2 + O(r^4). \quad (2.25)$$

For this reason, a harmonic oscillator model is sometimes used to analyze interlayer excitons [147,153]. We did not find good agreement between such a model

and the full Poisson equation. The results in the present thesis are therefore computed using the BLK potential.

2.1.3 Excitons in phosphorene

Phosphorene consists of a single layer of black phosphorous [57–60, 62]. Unlike the TMDs above, it is an anisotropic material. Phosphorene has seen a lot of attaction, both experimentally [158, 159] and theoretically [66, 160–165]. The research interest in phosphorene has been on a remarkable growth rate ever since it was isolated, even more so than graphene [61]. Whereas TMDs only have a direct band gap when in their monolayer form [22], black phosphorous is a direct band gap semiconductor regardless of the number of layers [63–65, 163]. The size of the gap transforms from about 0.3 eV in its bulk form to around 2 eV in monolayers [57, 60, 66–68]. The band gap of few-layer black phosphorous is therefore extremely tunable. That is, one may choose the number of layers such that the band gap has the optimized size for the application at hand. The anisotropic nature of phosphorene is observed in nearly all of its physical properties, such as its electrical [69, 70], magneto-optical [71–73], thermal [74, 75], and mechanical [76] properties. Particular examples of anisotropic quantities are the conductivity [77], absorption [62], and photoluminescence [68]. Both monolayer and bilayer phosphorene show strong absorption peaks [57, 159] that are attributed to strongly bound excitons [67, 166–168].

In order to study these excitons using the Wannier model, we must solve the Wannier equation while taking into account the anisotropic nature of phosphorene. It reads

$$\left[-\frac{1}{2\mu_x} \frac{\partial^2}{\partial x^2} - \frac{1}{2\mu_y} \frac{\partial^2}{\partial y^2} + V(\mathbf{r}) \right] \psi(\mathbf{r}) = E\psi(\mathbf{r}), \quad (2.26)$$

where V is the electron-hole interaction, E is the energy, and

$$\mu_{x/y} = \frac{m_e^{(x/y)} m_h^{(x/y)}}{m_e^{(x/y)} + m_h^{(x/y)}} \quad (2.27)$$

is the reduced mass with $m_e^{(x/y)}$ and $m_h^{(x/y)}$ being the direction-specific electron and hole effective masses, respectively. The superscript shows which axis the effective mass belongs to. The results in the present thesis have been obtained using the reduced masses from Choi et al. [169] $\mu_x = 0.1533$ and $\mu_y = 0.6605$. The directions in phosphorene are often referred to as armchair and zigzag directions [75, 76, 170–174]. To be consistent with the literature [67, 161, 166], we take the x - and y -axis along the armchair and zigzag directions, respectively.

2.1. Wannier exciton model

Asahina and Morita [64] calculated the dielectric constant of bulk black phosphorous and found $\epsilon_x = 12.5$ and $\epsilon_y = 10.2$. Rodin et al. [166] have since computed the polarizabilities of phosphorene to be $\chi_{xx} = 4.20\text{\AA}$ and $\chi_{yy} = 3.97\text{\AA}$. These lead to the screening lengths $r_{0x} = 26.39\text{\AA}$ and $r_{0y} = 24.94\text{\AA}$, respectively. The interaction between the electron and hole may again be estimated from the Poisson equation. This was done in Paper E, and the approximate interaction (using a linearized dielectric function) may be written as

$$V(r, \theta) = - \int_0^\infty \frac{J_0(qr)}{\sqrt{\epsilon_y \epsilon_x}} dq - 2 \int_0^\infty \sum_{k=1}^\infty (-1)^k \left(\frac{\sqrt{\epsilon_y - \epsilon_x}}{\sqrt{\epsilon_y} + \sqrt{\epsilon_x}} \right)^{2k} \frac{J_{2k}(qr)}{\sqrt{\epsilon_y \epsilon_x}} \cos(2k\theta) dq, \quad (2.28)$$

where $\epsilon_x(q) = \kappa + r_{0x}q$ and $\epsilon_y(q) = \kappa + r_{0y}q$. [Note that this is a corrected version of the expression in Paper E. The error does not impact the results of Paper E, as the expression is not used in the final calculations.] As the screening lengths in phosphorene are quite close, the higher order terms may be neglected as a first approximation. By also expanding $\sqrt{\epsilon_x \epsilon_y}$ and retaining only up to first order in q , i.e. $\sqrt{\epsilon_x \epsilon_y} \approx \kappa + (r_{0x} + r_{0y})q/2$, we find

$$V(r, \theta) \approx V_{\text{RK}}(r) = -\frac{\pi}{2r_0} \left[H_0\left(\frac{\kappa r}{r_0}\right) - Y_0\left(\frac{\kappa r}{r_0}\right) \right], \quad (2.29)$$

where $r_0 = (r_{0x} + r_{0y})/2$. This is the RK potential with the screening length replaced by the average of the two direction-specific screening lengths. This approximation was also used by Rodin et al. [166] to study excitons in phosphorene.

For numerical computations, it is convenient to switch the coordinate system so that the kinetic energy becomes isotropic. This may be done by introducing the coordinates [166]

$$X = \sqrt{\frac{\mu_x}{2\mu}} x, \quad Y = \sqrt{\frac{\mu_y}{2\mu}} y, \quad \mu = \frac{\mu_x \mu_y}{\mu_x + \mu_y}. \quad (2.30)$$

Excitons in phosphorene may then be described by

$$\left\{ -\frac{1}{4\mu} \nabla^2 + V_{\text{RK}} \left[R \sqrt{1 + \beta \cos 2\Theta} \right] - E \right\} \psi(\mathbf{R}) = 0, \quad (2.31)$$

where $\beta = (\mu_y - \mu_x)/(\mu_y + \mu_x)$ is a measure of the anisotropy, and R and Θ are the polar representation of the XY -plane. The Laplacian in Eq. (2.31) should be taken with respect to these new coordinates. The anisotropic part has thus been passed from the kinetic term to the potential interaction. This is

more convenient numerically, and it allows for a more intuitive understanding of the eigenstates. The potential in Eq. (2.31) is even in Θ and invariant if one shifts $\Theta \rightarrow \Theta + \pi$. As was pointed out by Rodin et al. [166], the eigenstates therefore fall into four distinct groups. In Paper E, we write these as

$$\psi_{ce} = \sum_{m=0}^{\infty} \varphi_m^{(ce)}(R) \cos(2m\Theta), \quad (2.32)$$

$$\psi_{co} = \sum_{m=0}^{\infty} \varphi_m^{(co)}(R) \cos[(2m+1)\Theta], \quad (2.33)$$

$$\psi_{se} = \sum_{m=1}^{\infty} \varphi_m^{(se)}(R) \sin(2m\Theta), \quad (2.34)$$

$$\psi_{so} = \sum_{m=0}^{\infty} \varphi_m^{(so)}(R) \sin[(2m+1)\Theta], \quad (2.35)$$

where the subscript *c/s* indicates whether the trigonometric function is a cosine or sine, and *e/o* indicates whether the angular momentum parity is even or odd. Symmetry observations about the states are summarized in Tbl. II of Paper E. As the *co* and *so* states have nodes along the *Y* and *X* axes, respectively, they are slightly deformed versions of the familiar p_x and p_y orbitals. The *se* states have nodes along both the *X* and the *Y* axes, and therefore resemble deformed d_{xy} orbitals.

2.2 Exciton dissociation by static electric fields

Consider for a moment an isolated exciton in a semiconducting crystal. If an electric field is applied to this exciton, the electron and hole will be pulled apart in opposite directions. A sufficiently strong electric field will be able to overcome the attractive Coulomb interaction and completely dissociate the exciton into a free electron and hole. This process is quite akin to that of a hydrogen atom in an electric field, which has been studied extensively in three [175–179], two [136, 180, 181], and fractional dimensional space [181]. Exciton dissociation is an important concept in many practical applications that require free electrons and holes, such as solar cells and photodetectors. As mentioned before, exciton binding energies in bulk semiconductors are typically low enough that thermal agitation is sufficient to ionize the excitons. However, binding energies in 2D materials are considerably larger, which makes them thermally stable even at room temperature. It is therefore of great interest to see if electric fields may be used to assist dissociation in these materials.

While field-induced exciton dissociation is interesting from a device perspective, it is also interesting on a fundamental level. Ionization of atoms has been studied for decades, and excitons in 2D materials provide a solid-state scene to test some of the already known ideas. Of course, the exciton is a much more complicated entity than an atom, and there are many other phenomena at play in a realistic semiconductor. Disentangling field-induced dissociation from other mechanisms can therefore be difficult. There are, however, promising experiments that may be performed. To see this, consider a source of light that continuously generates excitons in a semiconducting crystal. Due to loss mechanisms (such as recombination, defect-assisted recombination [182], and exciton-exciton annihilation [183, 184]), the exciton density reaches a stable equilibrium after a certain amount of time. If an electric field is then rapidly switched on, one expects to see a rise in number of free carriers and a decrease in exciton density. Such a change should, in principle, be measurable by observing changes in free carrier absorption, or by collecting charges via biased contacts. The latter was performed in the wonderful systematic experimental study led by Massicotte [116]. The group measured changes in the photoreponse rate as a function of the strength of an applied electric field. These changes were in good agreement with exciton dissociation rates predicted by the Wannier model for weak electric fields.

As is common for atoms [136, 175–181] and has also been done for excitons [114–116], we would like to use the Stark Hamiltonian

$$H = -\frac{1}{2\mu}\nabla^2 + V(\mathbf{r}) + \mathcal{E} \cdot \mathbf{r} \quad (2.36)$$

to model exciton dissociation, where \mathcal{E} is the static electric field. Before proceeding, however, it is important to note that dissociation is an inherently time-dependent concept. One may imagine an exciton generated at time $t = t_0$ that immediately begins the dissociation processes due to the applied field. Such a time-dependent problem should, in principle, be tackled by the time-dependent Schrödinger equation. However, if the electric field is sufficiently weak, the exciton will survive for many atomic periods $2\pi/|E_0|$ before eventually dissociating. Such long-lived resonance states are often referred to as quasistationary states [185], and may be *associated* with solutions to the stationary Schrödinger equation

$$\left[-\frac{1}{2\mu}\nabla^2 + V(\mathbf{r}) + \mathcal{E} \cdot \mathbf{r} \right] \psi(\mathbf{r}) = E\psi(\mathbf{r}). \quad (2.37)$$

It is well known that stationary states vary in time as $\exp(-iEt)$, and that (for real energies) the probability density is therefore independent of time. This is not the behavior we expect from a dissociating electron-hole pair. Rather, the probability of finding the exciton in a bound state is expected to decrease. Such a decreasing probability may be realized by allowing the energy to be complex

$$|\Psi(\mathbf{r}, t)|^2 = |\psi(\mathbf{r})e^{-iEt}|^2 = |\psi(\mathbf{r})|^2 e^{2\text{Im}(E)t} = |\psi(\mathbf{r})|^2 e^{-\Gamma t}, \quad (2.38)$$

where $\Gamma = -2\text{Im}(E)$ is referred to as the dissociation rate.

It is worth pausing for a moment to consider what is physically expected from dissociating states. An electron-hole pair subjected to an electric field is pulled apart in opposite directions. The relative radial coordinate should therefore be increasing with time. This implies that the states have a positive (real) radial momentum. That this immediately leads to complex energies may be seen by an insightful relation that is simple to derive. Multiplying Eq. (2.36) by ψ^* and subtracting the resulting equation and its complex conjugate from one another, we find

$$-\frac{1}{2\mu}[\psi^*\nabla^2\psi - \psi\nabla^2\psi^*] = -\frac{1}{2\mu}\nabla \cdot [\psi^*\nabla\psi - \psi\nabla\psi^*] = i2\text{Im}(E)|\psi|^2. \quad (2.39)$$

One may then integrate over a circle with area A and boundary S to find

$$-\frac{1}{\mu}\text{Re} \int_S (\psi^* p \psi) \cdot \mathbf{e}_r dS = 2\text{Im}(E) \int_A |\psi|^2 dA, \quad (2.40)$$

where $p = -i\nabla$ is the momentum operator, \mathbf{e}_r the radial unit vector, and we have made use of the divergence theorem. Evidently a non-zero (real) radial momentum results in a non-zero imaginary part of the energy. In particular,

it is seen that a negative $\text{Im}(E)$ is related to a net positive radial flux flowing out of the circle, as expected from dissociating states.

Using stationary states to describe dissociation has an important implication. It is implicitly assumed that probability flux has always been leaking out of a circle of arbitrary radius. The result is that the eigenfunctions describing dissociating states are exponentially increasing in space [186, 187]. This is the reason that these states are not found using traditional methods of quantum mechanics, such as expanding the wave function in a square integrable basis.

While the idea of using complex energies to describe states with a finite lifetime has been around for decades (in fact, Gamow associated the imaginary part of the energy of a resonance state with the lifetime of that state in his famous 1928 paper on α decay of atomic nuclei [188]), a question that often arises is how complex energies can arise from the Hamiltonian, usually a hermitian operator. The reason is, of course, that the operator itself is only hermitian with regards to a special set of functions. Recall that the condition for the Hamiltonian H (or any operator for that matter) to be hermitian may be written as (see e.g. Dahl [189])

$$\langle \psi_a | H | \psi_b \rangle = \langle H \psi_a | \psi_b \rangle . \quad (2.41)$$

Consider, for simplicity, the Hamiltonian describing the 1D Stark problem

$$H = -\frac{1}{2} \frac{d^2}{dx^2} + V(x) + \mathcal{E}x . \quad (2.42)$$

The last two terms are trivially hermitian as these are real quantities, but the first is only hermitian if

$$\left[\psi_a^* \frac{d}{dx} \psi_b - \psi_b \frac{d}{dx} \psi_a^* \right]_{-\infty}^{\infty} = 0 , \quad (2.43)$$

where we have used integration by parts. This is certainly true for bound states that tend to zero as $x \rightarrow \pm\infty$. However, it is (generally) not true for states that are exponentially increasing in space, which are exactly the states we seek.

Dealing with these exponentially increasing states numerically is exceptionally difficult. A convenient method for circumventing this behavior is to rotate the radial coordinate into the complex plane, thereby transforming the exponentially increasing functions into decreasing functions. This procedure is known as complex scaling, and it allows us to use a traditional basis consisting of square integrable functions to resolve the resonance states.

2.2.1 Complex scaling

As is evident from the discussion above, resonance states are described by eigenfunctions that are exponentially increasing in the asymptotic region. They are

therefore not square integrable, and traditional expansion methods may not be used to resolve them. Complex scaling is a method used to force these states into the square integrable domain [190–192]. In its simplest form, complex scaling corresponds to a rotation of the coordinates from the real axis into the complex plane by an angle ϕ , i.e. $x \rightarrow xe^{i\phi}$. If ϕ is chosen appropriately, it may overcome the exponentially increasing behavior of the resonance states and turn them into exponentially decreasing functions. Take the simple 1D function e^{ikx} representing a particle traveling to the right as an example. For a complex energy with $\text{Im}(E) < 0$ we may write $k = \sqrt{2E} = |k|e^{-i\beta}$ where $\beta > 0$. Under the complex scaling transformation, this function becomes $\exp[i|k|\cos(\beta - \phi)x + |k|\sin(\beta - \phi)x]$ which is exponentially decreasing if the angle of rotation is chosen such that $\beta < \phi < \beta + \pi$.

While the idea is incredibly simple, it has a lot of mathematical rigorous theory behind it [191, 193–197]. We shall begin by discussing how such a transformation alters the spectrum of the Hamiltonian. For simplicity, let us begin by considering the Schrödinger equation for the 2D hydrogen atom

$$\left[-\frac{1}{2}\nabla^2 - \frac{1}{r} \right] \psi(\mathbf{r}) = E\psi(\mathbf{r}). \quad (2.44)$$

The ground state is $\psi_0 \propto e^{-2r}$ [136]. If this equation is analytically continued into the complex plane $r \rightarrow re^{i\phi}$, it reads

$$\left[-\frac{e^{-i2\phi}}{2}\nabla^2 - \frac{e^{-i\phi}}{r} \right] \psi(e^{i\phi}\mathbf{r}) = E\psi(e^{i\phi}\mathbf{r}). \quad (2.45)$$

This transformation does not alter the functional form of the solutions, nor does it change the corresponding eigenvalues. As an example, the ground state function becomes $\psi_0 \propto \exp(-2e^{i\phi}r)$, and one can easily verify by substituting into Eq. (2.45) that the eigenvalue is still -2 regardless of the value of ϕ . Note, however, that the state is no longer square integrable if $|\phi| \geq \pi/2$. Thus, we conclude that the complex scaling procedure merely alters which functions in the spectrum of the Hamiltonian are square integrable, without changing the corresponding eigenvalues. For practical calculations, one usually expands the function $\psi(e^{i\phi}\mathbf{r})$ in a basis of square integrable functions that are zero either at some finite boundary or as $r \rightarrow \infty$. Therefore, if we still want to find the original bound state eigenvalues using such an expansion, we must choose $|\phi| < \pi/2$.

The old continuum states are rotated out of the square integrable domain by the introduction of a complex coordinate. At the same time, a new set of continuum states is rotated into the square integrable space, and the eigenvalues of these state fall on a continuum rotated down into the complex plane such that

the imaginary part is negative. In complex scaling literature, one often reads that complex scaling rotates the continuum eigenvalues down into the complex plane [198]. As should be clear from the discussion above, this is not strictly speaking true. Complex scaling does not alter the eigenvalues. Rather, it is a new set of eigenfunctions that enters the square integrable domain. Another new category of states that enters the square integrable domain is the resonance states discussed previously, and it is here our interest in the method lies.

The complex scaled exciton Stark Hamiltonian reads

$$H^\phi = -\frac{1}{2\mu}e^{-2i\phi}\nabla^2 + V(\mathbf{r}e^{i\phi}) + e^{i\phi}\boldsymbol{\mathcal{E}} \cdot \mathbf{r}, \quad (2.46)$$

and it is of this Hamiltonian we seek the eigenvalues. We mention in passing that in order to use complex scaling, the potential must be dilation analytic [193, 194, 196, 199]. This is not a severe restriction, however, as nearly all physically sensible potentials are. Nevertheless, the field term arising in the Hamiltonian is not dilation analytic [200, 201], and would pose a problem had not Herbst and Simon [202] extended the rigorous theory of complex scaling to include problems with a constant field. For a hydrogen atom in a constant electric field, they state that H^ϕ has a purely discrete spectrum which lies in the lower half of the complex plane, and the spectrum is independent of ϕ so long as $0 < \phi < \pi/3$ [202]. One then defines the resonance energy $E_n^\phi(\mathcal{E})$ of state ψ_n^ϕ as the eigenvalue that satisfies $E_n^\phi(\mathcal{E}) \rightarrow E_n^\phi(0)$ when $\mathcal{E} \rightarrow 0$, where we recall that the bound state energies $E_n^\phi(0)$ are real. Most of the results in the present thesis have been obtained using $\phi = 0.4$.

As shown by Bengtsson et al. [203]

$$\int \psi^*(\mathbf{r})O\psi(\mathbf{r})dA = \int [\psi^{-\phi}(\mathbf{r})]^* O^\phi \psi^\phi(\mathbf{r})dAe^{2i\phi}, \quad (2.47)$$

where O is an arbitrary operator, and the superscripts show in which direction the states have been rotated. Thus, all physical quantities obtainable from hermitian mechanics may be obtained from the complex scaled wave functions. If the unrotated states are purely real, then any imaginary part in the rotated states stems from the rotation itself, and $[\psi^{-\phi}(\mathbf{r})]^* = \psi^\phi(\mathbf{r})$. This is why the "left" state is usually not complex conjugated in inner products within non-hermitian quantum mechanics [191, 203–208].

In the numerical procedure, we expand the eigenstate of Eq. (2.46) in a basis of square integrable functions. In practice, it is convenient to use real basis functions to expand the states, and simply let the expansion coefficients handle the complex part. This method has been used to compute ionization rates by static electric fields in, e.g., Refs. [116, 209–211], where the focus was hydro-

gen atoms, multielectron atoms, relativistic hydrogen-like ions, and excitons, respectively.

2.2.2 Exterior complex scaling

While the above procedure is formally exact, numerical difficulties may be encountered when the fields become extremely weak. The reason for this is related to the fact that the imaginary parts of the resonance energies depend exponentially on the field strength for weak electric fields. Thus, the numerical differences in the wave function of a resonance state $\psi_n^\phi(\Delta\mathcal{E})$ (where $\Delta\mathcal{E}$ is small) compared to the unperturbed state $\psi_n^\phi(0)$ are so insignificant that they are considered the same states numerically within rounding errors. This led to difficulties in, e.g., Ref. [116], where exciton dissociation rates for fields below 15 V/ μm were needed. Fortunately, it turns out that a related method performs far better numerically for weak fields. This is the so-called exterior complex scaling (ECS) method. Instead of rotating the radial coordinate into the complex plane uniformly, one rotates it only outside of a finite radius R_0 . That is

$$r \rightarrow \begin{cases} r & \text{for } r < R_0, \\ R_0 + (r - R_0)e^{i\phi} & \text{for } r > R_0. \end{cases} \quad (2.48)$$

Early applications of such a contour were documented in Refs. [212, 213], where diverging integrals were transformed into converging integrals by integrating along a complex contour instead of along the real line. Simon [214] later formulated it as an extension of the complex scaling method. The motivation was to be able to apply complex scaling to study resonances for potentials that were only dilation analytic in a region $r > R_0$. ECS is often implemented as an absorbing boundary when solving the time-dependent Schrödinger equation to reduce spurious reflections [215–218]. It has also been used to analyze electron impact ionization [219–222], scattering problems [223], and photoionization [224–227]. In Refs. [228, 229] it was used to compute resonance energies, which is our goal as well. We mention that when both uniform complex scaling (UCS) and ECS are applicable, they formally lead to identical eigenvalues. However, numerical differences may apply, and this is where ECS is useful for the present problem. ECS leaves the wave functions unrotated in the interior region $r < R_0$. These states are therefore not decaying as quickly as the UCS states, and it becomes easier to retain enough numerical information to compute resonance energies for weaker fields.

The ECS transformed Hamiltonian is different in the two regions of space. For $r < R_0$, the usual unrotated Hamiltonian is used. For $r > R_0$, on the

2.2. Exciton dissociation by static electric fields

other hand, the Hamiltonian corresponding to the contour in Eq. (2.48) must be used. That is,

$$H^\phi = \begin{cases} -\frac{1}{2\mu}\nabla^2 + V(r, \theta) + \mathcal{E}r[\cos \alpha \cos \theta + \sin \alpha \sin \theta] & r < R_0 \\ -\frac{e^{-i2\phi}}{2\mu}\nabla^2 + V(\tilde{r}, \theta) + \mathcal{E}\tilde{r}[\cos \alpha \cos \theta + \sin \alpha \sin \theta] & r > R_0 \end{cases} \quad (2.49)$$

where $\tilde{r} = R_0 + (r - R_0)e^{i\phi}$. Here, we have made the dependence on the (real) polar coordinates r and θ more explicit by expanding the field term such that its angle α to the x -axis is explicitly shown. To solve the resulting differential equation, we must partition the radial domain in some way. This can be done efficiently by implementing a finite element approach.

2.3 Solving the two-dimensional Schrödinger equation using a finite element approach

One of the most common methods of solving the Schrödinger equation when no analytical solutions are available is to expand the wave function in a basis consisting of simple analytical functions. The choice of said functions is governed mostly by convergence speed and simplicity. Gaussian functions are frequently used, because the integrals that must be evaluated can often be done analytically, which speeds up computations. Such exponentially decaying functions are useful for describing bound state solutions to the Schrödinger equation. On the other hand, oscillating functions such as sines and cosines are often used to resolve the continuous spectrum. Common for these functions is that they expand the entire physical space considered. It is difficult to use such functions to resolve a function that behaves differently on certain parts of the spatial domain.

The computational method used in Papers A, C, D, E, and G consists of expanding the radial part of the wave function in a so-called finite element (FE) basis. Unlike the previously discussed functions, these functions are non-zero only on a specific part of the radial domain. Such an approach is incredibly flexible, as the functions on one segment need not be influenced by the behavior on the next (other than continuity of the wave function must be ensured). One of the major advantages of this approach is that it makes implementing ECS easy. We shall begin by considering how the standard hermitian Schrödinger equation may be solved using this method, as implementing complex scaling only slightly alters the scheme.

The basic idea is quite simple. The two-dimensional xy -plane is represented in polar coordinates, and a maximum simulation radius R is chosen outside of which Dirichlet (zero) boundary conditions are enforced. As R is an artificial boundary, one must ensure that it is chosen large enough such that it does not impact the results. The radial domain $r \in [0, R]$ is then divided into N segments $[r_{n-1}, r_n]$ with $N+1$ nodes r_n . This is illustrated in Fig. 2.5. On each radial segment, a set of p_n localized radial basis functions $f_i^{(n)}(r)$ is defined that are nonzero only on their respective segments. The FE ansatz reads

$$\psi(\mathbf{r}) = \sum_{m=-M}^M \varphi_m(r) Y_m(\theta) \quad (2.50)$$

where M is the maximum angular momentum included in the expansion. The angular functions Y_m may be chosen as, e.g., exponential functions or sines and cosines. Here, we opt for the latter and use the following normalized angular

2.3. Solving the two-dimensional Schrödinger equation using a finite element approach

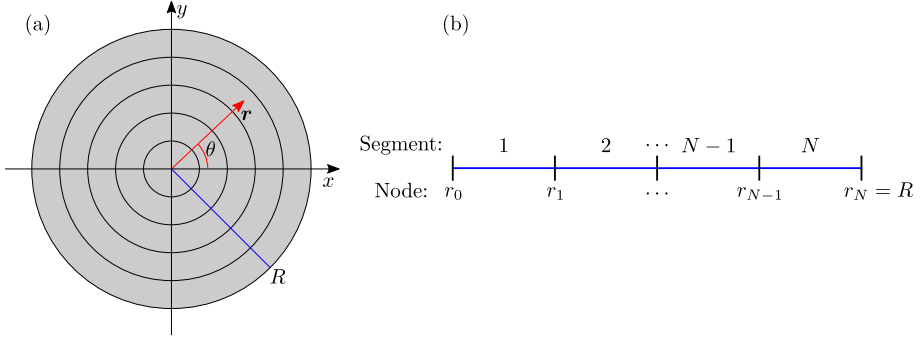


Fig. 2.5: Illustration of the partitioning of the radial domain. (a) Top view of the xy -plane. The black circles indicated the beginning (and end) of each radial segment. The position vector \mathbf{r} has been drawn in red with the polar angle denoted by θ . The maximum radius used in the simulations is denoted by R . (b) A one dimensional illustration of the blue line in (a), with nodes r_0, \dots, r_N and segments $n = 1, \dots, N$ indicated.

functions:

$$Y_m(\theta) = \frac{1}{\sqrt{\pi(1 + \delta_{m,0})}} \times \begin{cases} \sin(m\theta), & m > 0 \\ \cos(m\theta), & m \leq 0, \end{cases} \quad (2.51)$$

where δ is the Kronecker delta. The radial functions φ_m are expanded in the FE basis

$$\varphi_m(r) = \sum_{n=1}^N \sum_{i=q_m}^{p_n} c_i^{(m,n)} f_i^{(n)}(r), \quad (2.52)$$

where $c_i^{(m,n)}$ are the expansion coefficients, and $q_m = 2 - \delta_{m,0}$ ensures that states with $m \neq 0$ are zero at $r = 0$ (explained below). So far the procedure is not much different than any other expansion approach to solving the Schrödinger equation. However, continuity of the wave function does not come trivially with the FE approach.

To ensure continuity, we choose the $f_i^{(n)}$ functions so that they satisfy

$$\begin{aligned} f_i^{(n)}(r_{n-1}) &= f_i^{(n)}(r_n) = 0, \quad i = 2, \dots, p_n - 1 \\ f_1^{(n)}(r_{n-1}) &= f_{p_n}^{(n)}(r_n) = 1. \end{aligned} \quad (2.53)$$

That is, all functions on segment n are zero at the segment boundaries apart from the first and last functions, which are equal unity at the segment start and end, respectively. With the conditions in Eq. (2.53) satisfied, continuity across segment boundaries is guaranteed by demanding that the expansion coefficient of the last function on segment $n - 1$ is equal to that of the first function on

segment n , i.e.

$$c_{p_{n-1}}^{(n-1)} = c_1^{(n)}. \quad (2.54)$$

Dirichlet boundary conditions at R may be implemented by omitting the last function of the final segment, and at $r = 0$ by omitting the first (hence, the lower limit on the sum in Eq. (2.52) for $m \neq 0$). A technical discussion of the transformations needed to arrive at Eq. (2.53) from an initial set of functions $h_i^{(n)}$ may be found in Ref. [218]. Here, we choose the initial functions as the Legendre polynomials $h_i^{(n)} = P_{i-1}[y_n(r)]$, where y_n maps $[r_{n-1}, r_n]$ onto $[-1, 1]$. Explicitly

$$y_n(r) = \frac{2r - r_n - r_{n-1}}{r_n - r_{n-1}}. \quad (2.55)$$

The resulting functions may be written compactly as

$$\begin{aligned} f_i^{(n)}(r) &= \frac{1}{2}[1 - y_n(r)]\delta_{i,1} + \frac{1}{2}[1 + y_n(r)]\delta_{i,p_n} \\ &+ \frac{1}{2}\left\{2P_i[y_n(r)] + (-1)^{i+1}[1 - y_n(r)] - [1 + y_n(r)]\right\}(1 - \delta_{i,1} - \delta_{i,p_n}). \end{aligned} \quad (2.56)$$

As an example, the basis functions on the first two segments are shown in Fig. 2.6. In this example, three and four functions are used on the first and second segment, respectively. For most of the results in the present thesis, 30 functions have been used on each radial segment.

Equation (2.54) may be ensured by grouping the first and last function on each segment such that they form a single basis function. That is, define the new set of $p_n - 1$ functions on each segment

$$\begin{aligned} g_i^{(1)} &= f_i^{(1)}, & i &= 1, \dots, p_1 - 1 \\ g_{p_1}^{(1)} &= f_{p_1}^{(1)} + f_1^{(2)}, & i &= p_1 \\ g_i^{(1 < n < N)} &= f_{i+1}^{(n)}, & i &= 1, \dots, p_n - 2 \\ g_{p_n-1}^{(1 < n < N)} &= f_{p_n}^{(n)} + f_1^{(n+1)}, & i &= p_n - 1 \\ g_i^{(N)} &= f_{i+1}^{(N)}, & i &= 1, \dots, p_N - 2. \end{aligned} \quad (2.57)$$

The notable exceptions on the first and last segment arise because the first function on the first segment must be included, as the wave function is not necessarily zero at the origin, and the final function on the final segment must be omitted to implement Dirichlet boundary conditions. The expansion in Eq. (2.50) with Eq. (2.54) enforced then reads

$$\psi(\mathbf{r}) = \sum_{m=-M}^M \sum_{n=1}^N \sum_{i=q_n}^{Q_n} c_i^{(m,n)} g_i^{(n)}(r) Y_m(\theta) \quad (2.58)$$

2.3. Solving the two-dimensional Schrödinger equation using a finite element approach

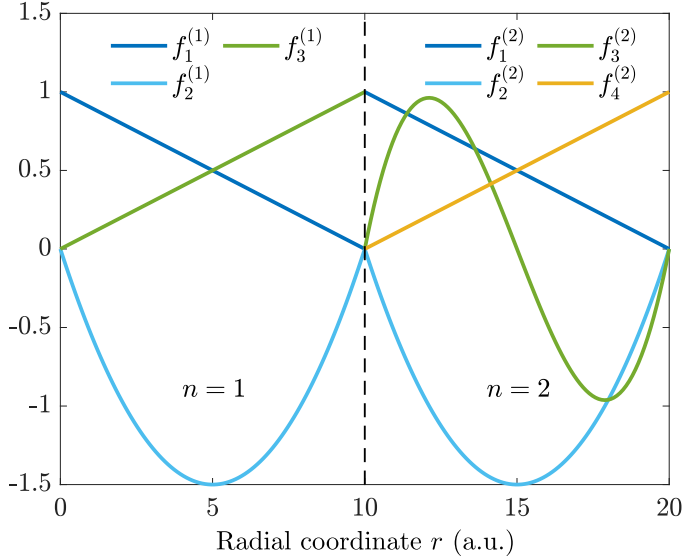


Fig. 2.6: Example FE basis with three and four basis functions on the first and second radial segment, respectively. Each of the two segments are 10 a.u. wide.

where, as before, $q_m = 2 - \delta_{m,0}$ and $Q_n = p_n - 1 + \delta_{n,1} - \delta_{n,N}$. Using this expansion, the Schrödinger equation may now be transformed into a generalized eigenvalue problem that may be solved by any standard procedure

$$\mathbf{H}\mathbf{c} = E\mathbf{S}\mathbf{c}, \quad (2.59)$$

where \mathbf{c} is a vector containing the expansion coefficients, and \mathbf{H} and \mathbf{S} are the Hamilton and overlap matrices, respectively. That is,

$$c_{\lambda,1} = c_i^{(m,n)} \quad (2.60)$$

$$H_{\lambda',\lambda} = \langle g_{i'}^{(n')} Y_{m'} | H | g_i^{(n)} Y_m \rangle \quad (2.61)$$

$$S_{\lambda',\lambda} = \langle g_{i'}^{(n')} Y_{m'} | g_i^{(n)} Y_m \rangle, \quad (2.62)$$

where λ is an index that takes on values $\lambda = 1, 2, 3, \dots$ for the different combinations of (m, n, i) . The size of the matrices depend on the maximum angular momentum M , the number of radial segments N , and the number of FE functions on the different segments p_n .

Fortunately, one does not need to explicitly define the basis in Eq. (2.57) to construct the Hamilton and overlap matrices in practice. We shall give a recipe for constructing the Hamilton matrix here, as the overlap matrix is obtained using the same steps and replacing H by unity. We begin by defining the segmentwise Hamilton matrices with elements

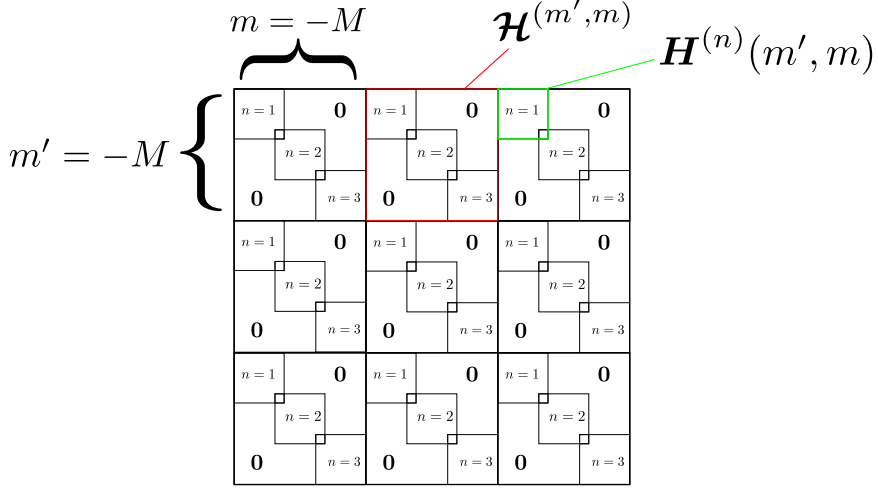


Fig. 2.7: Structure of the Hamiltonian matrix within the finite element approach. The segmentwise matrices $\mathbf{H}^{(n)}(m', m)$ are collected in the angular momentum block $\mathcal{H}_{m', m}$ by overlapping the last row and column of $\mathbf{H}^{(n-1)}(m', m)$ with the first row and column of $\mathbf{H}^{(n)}(m', m)$.

$$H_{ij}^{(n)}(m', m) = T_{i,j}^{(n)}(m', m) + V_{i,j}^{(n)}(m', m), \quad n = 1, \dots, N \quad (2.63)$$

where T and V denote the kinetic and potential matrix elements, respectively. The segmentwise potential and kinetic matrix elements are given by

$$V_{ij}^{(n)}(m', m) = \int_0^{2\pi} \int_{r_{n-1}}^{r_n} Y_{m'}(\theta) f_i^{(n)}(r) V(\mathbf{r}) f_j^{(n)}(r) Y_m(\theta) r dr d\theta, \quad (2.64)$$

and

$$T_{ij}^{(n)}(m', m) = \frac{\delta_{m', m}}{2\mu} \int_{r_{n-1}}^{r_n} \left[\frac{df_i^{(n)}(r)}{dr} \frac{df_j^{(n)}(r)}{dr} r - \frac{m^2}{r} f_i^{(n)}(r) f_j^{(n)}(r) \right] dr, \quad (2.65)$$

respectively. If an electric field is included in the Hamiltonian, it may be treated similarly to the potential in Eq. (2.64). Note that it is important that the kinetic matrix elements are computed as in Eq. (2.65) due to the nature of an FE basis (discussed below). These segmentwise matrices are then collected in an angular momentum block $\mathcal{H}_{m', m}$, and Eq. (2.54) is ensured by overlapping the last row and column of $\mathbf{H}^{(n-1)}(m', m)$ with the first row and column of $\mathbf{H}^{(n)}(m', m)$. It should be mentioned that when collecting the segmentwise

2.3. Solving the two-dimensional Schrödinger equation using a finite element approach

$$\begin{bmatrix} \ddots & & & & & \\ & \ddots & & & & \\ & & H_{p_{n-1}-1, p_{n-1}}^{(n-1)} & 0 & \cdots & 0 \\ \cdots & H_{p_{n-1}, p_{n-1}}^{(n-1)} + H_{1,1}^{(n)} & H_{1,2}^{(n)} & \cdots & H_{1, p_n}^{(n)} & 0 \\ 0 & H_{2,1}^{(n)} & \cdots & \cdots & H_{2, p_n}^{(n)} & 0 \\ \vdots & \vdots & \cdots & \cdots & \vdots & \vdots \\ \vdots & H_{p_n,1}^{(n)} & H_{p_n,2}^{(n)} & \cdots & H_{p_n, p_n}^{(n)} + H_{1,1}^{(n+1)} & H_{1,2}^{(n+1)} \\ 0 & 0 & 0 & 0 & H_{2,1}^{(n+1)} & \ddots \\ \vdots & \vdots & \vdots & \vdots & \vdots & \ddots \end{bmatrix}$$

Fig. 2.8: Structure of the Hamiltonian matrix angular momenta blocks in the finite element approach. The last row and column of the segmentwise matrix $\mathbf{H}^{(n-1)}(m', m)$ are overlapped with the first row and column of $\mathbf{H}^{(n)}(m', m)$. Note that the dependence on angular momentum quantum numbers has been omitted in the matrix to simplify notation.

matrices, one excludes the first row and column of $H^{(1)}$ for $m \neq 0$, and the last row and column of $H^{(N)}$ for all m . As discussed earlier, this is to ensure zero boundary conditions at the end of the domain, as well as on the start for relevant states.

Fig. 2.7 is a visual representation of the structure of the full Hamiltonian matrix, and Fig. 2.8 shows an explicit example of how an angular momenta block is constructed by collecting the segmentwise matrices. As is apparent from these figures, the matrix is quite sparse due to FE functions only overlapping on a single radial segment. Furthermore, the off-diagonal momenta blocks reduce to zero if the potential does not depend on θ . In this case, most of the segmentwise integrals are identical, and very few integrals need to be evaluated. Once the overlap matrix is constructed in a similar manner the eigenvalue problem in Eq. (2.59) may be solved numerically. The procedure above is incredibly flexible and efficient even for problems in standard Hermitian quantum mechanics, as the basis functions may resolve nearly any shape of wave function with relatively few finite element functions.

As mentioned, it is important that the kinetic matrix elements are computed as in Eq. (2.65). The reason is that while the FE basis functions are continuous on segment boundaries, they do not have a continuous first derivative. The kinetic energy must therefore be defined with care. Scrinzi and Elander [229] pointed out that the derivative of the wave function does not need to be continuous for the kinetic energy to be correctly defined. Rescigno

and McCurdy [223] also derived the correct kinetic energy following Scrinzi's and Elander's arguments. The remainder of this section is devoted to deriving the correct form of the kinetic energy in the FE basis and may be skipped if the technical details are not of interest. Following Refs. [223, 229], let us begin by considering the radial kinetic matrix elements involving derivatives of the wave function in Eq. (2.58). That is

$$-\frac{1}{2\mu} \int \psi^*(\mathbf{r}) \left[\frac{\partial^2}{\partial r^2} + \frac{1}{r} \frac{\partial}{\partial r} \right] \psi(\mathbf{r}) r dr d\theta. \quad (2.66)$$

Focusing on the second order derivative first, and using the expansion of ψ in Eq. (2.58), we have

$$-\frac{1}{2\mu} \int \varphi_m^*(r) \frac{\partial^2}{\partial r^2} \sum_{n=1}^N \sum_{i=q_n}^{Q_n} c_i^{(m,n)} g_i^{(n)}(r) r dr, \quad (2.67)$$

where φ_m is given by Eq. (2.52) (which is related to the g basis via Eqs. (2.54) and (2.57)). The g functions do not have continuous derivatives at the nodes r_n , and we may write

$$\frac{\partial g_i^{(n)}}{\partial r}(r) = Q_1(r) \Theta(r_n - r) + Q_2(r) \Theta(r - r_n), \quad (2.68)$$

where $\Theta(x)$ is a step function equal to unity for $x > 0$ and zero for $x < 0$, and Q_1 and Q_2 are two functions describing the derivative in the respective regions. The second order derivative may then be written as

$$\begin{aligned} \frac{\partial^2 g_i^{(n)}}{\partial r^2}(r) &= Q_1'(r) \Theta(r_n - r) + Q_2'(r) \Theta(r - r_n) \\ &\quad + [Q_2(r) - Q_1(r)] \delta(r - r_n), \end{aligned} \quad (2.69)$$

where the prime represents the derivative with respect to r . Using this in Eq. (2.67) leads to

$$\begin{aligned} \lim_{\epsilon \rightarrow 0} \left\{ \left[-\frac{1}{2\mu} \sum_{n=1}^N \int_{r_{n-1}+\epsilon}^{r_n-\epsilon} \varphi_m^*(r) \sum_{i=q_n}^{Q_n} c_i^{(m,n)} \frac{\partial^2 g_i^{(n)}(r)}{\partial r^2} r dr \right] \right. \\ \left. - \frac{1}{2\mu} \int_0^\infty \varphi_m^*(r) \sum_{n=1}^N \sum_{i=q_n}^{Q_n} c_i^{(m,n)} \delta(r - r_n) \right. \\ \left. \times \left[\frac{\partial g_i^{(n)}(r)}{\partial r} \right]_{r_n+\epsilon} - \left[\frac{\partial g_i^{(n)}(r)}{\partial r} \right]_{r_n-\epsilon} \right] r dr \Big\}. \end{aligned} \quad (2.70)$$

2.3. Solving the two-dimensional Schrödinger equation using a finite element approach

The term inside the square brackets may be expressed as

$$\begin{aligned}
& -\frac{1}{2\mu} \sum_{n=1}^N \varphi_m^*(r) \sum_{i=q_n}^{Q_n} c_i^{(m,n)} \frac{\partial g_i^{(n)}(r)}{\partial r} r \Bigg|_{r_{n-1}+\epsilon}^{r_n-\epsilon} \\
& + \frac{1}{2\mu} \sum_{n=1}^N \int_{r_{n-1}+\epsilon}^{r_n-\epsilon} \left[\varphi_m^*(r) + r \frac{\partial \varphi_m^*(r)}{\partial r} \right] \sum_{i=q_n}^{Q_n} c_i^{(m,n)} \frac{\partial g_i^{(n)}(r)}{\partial r} dr, \quad (2.71)
\end{aligned}$$

from which we see that the surface terms cancel the δ -function terms in Eq. (2.70), and we are left with

$$\lim_{\epsilon \rightarrow 0} \frac{1}{2\mu} \sum_{n=1}^N \int_{r_{n-1}+\epsilon}^{r_n-\epsilon} \left[\varphi_m^*(r) + r \frac{\partial \varphi_m^*(r)}{\partial r} \right] \sum_{i=q_n}^{Q_n} c_i^{(m,n)} \frac{\partial g_i^{(n)}(r)}{\partial r} dr. \quad (2.72)$$

Using this in Eq. (2.66), we find that the radial part of the kinetic energy reduces to

$$\lim_{\epsilon \rightarrow 0} \frac{1}{2\mu} \sum_{n=1}^N \int_{r_{n-1}+\epsilon}^{r_n-\epsilon} \frac{\partial \varphi_m^*(r)}{\partial r} \sum_{i=q_n}^{Q_n} c_i^{(m,n)} \frac{\partial g_i^{(n)}(r)}{\partial r} r dr, \quad (2.73)$$

which in turn leads to Eq. (2.65).

2.3.1 Implementing exterior complex scaling

The FE approach above is efficient for solving many problems within quantum mechanics, and, as an added bonus, it is simple to modify it such that ECS is implemented. One begins by choosing the ECS radius R_0 in Eq. (2.48) to coincide with a node $R_0 = r_{n'}$. All matrix elements corresponding to segments $[r_{n-1}, r_n]$ with $r_n \leq r_{n'} = R_0$ are unchanged, and the segmentwise matrices are therefore identical to the ones constructed in the previous section. On the other hand, the transformed version of the Hamiltonian Eq. (2.49) must be used for segments that fall outside of R_0 . The segmentwise integrals in Eqs. (2.64) and (2.65) for $r_{n-1} \geq R_0$ therefore become

$$V_{ij}^{(n \geq n')}(m', m) = \int_0^{2\pi} \int_{r=r_{n-1}}^{r=r_n} Y_{m'}(\theta) f_i^{(n)}(r) V(\tilde{\mathbf{r}}) f_j^{(n)}(r) Y_m(\theta) \tilde{r} d\tilde{r} d\theta, \quad (2.74)$$

and

$$\begin{aligned}
& T_{i,j}^{(n \geq n')}(m', m) = \\
& \frac{\delta_{m',m}}{2\mu} \int_{r=r_{n-1}}^{r=r_n} \left[\frac{df_i^{(n)}(r)}{d\tilde{r}} \frac{df_j^{(n)}(r)}{d\tilde{r}} \tilde{r} - \frac{m^2}{\tilde{r}} f_i^{(n)}(r) f_j^{(n)}(r) \right] d\tilde{r}, \quad (2.75)
\end{aligned}$$

where we integrate along the contour in Eq. (2.48) [recall that $\tilde{r} = R_0 + (r - R_0)e^{i\phi}$]. It is convenient to integrate with respect to the real coordinate r instead, which is simple to do since $d\tilde{r}/dr = e^{i\phi}$. We find,

$$V_{ij}^{(n \geq n')}(m', m) = \int_0^{2\pi} \int_{r_{n-1}}^{r_n} Y_{m'}(\theta) f_i^{(n)}(r) V(\tilde{r}) f_j^{(n)}(r) Y_m(\theta) \tilde{r} dr e^{i\phi} d\theta, \quad (2.76)$$

and

$$T_{i,j}^{(n \geq n')}(m', m) = \frac{\delta_{m',m}}{2\mu} \int_{r_{n-1}}^{r_n} \left[\frac{df_i^{(n)}(r)}{dr} \frac{df_j^{(n)}(r)}{dr} \tilde{r} e^{-i2\phi} - \frac{m^2}{\tilde{r}} f_i^{(n)}(r) f_j^{(n)}(r) \right] dr e^{i\phi}. \quad (2.77)$$

The field term in Eq. (2.49) may be treated similarly to the potential in Eq. (2.76). The complex scaled version of the generalized eigenvalue problem in Eq. (2.59) may therefore be set up by constructing the Hamilton and overlap matrix as laid out in the previous section, and simply replacing the segmentwise matrices outside of R_0 with the complex scaled version. The generalized eigenvalue problem may then be solved to obtain the complex energies E of the resonance states. The dissociation rate of the k th state is obtained by tracing $E_k(\mathcal{E})$ as the field strength is increased, starting from the bound state energy E_k at $\mathcal{E} = 0$. It is convenient to use eigenvalue algorithms that exploit the sparse nature of the matrix, such as inverse iteration. Computational software, such as MATLAB, usually have these functions in their standard function library.

2.4 Exciton dissociation by dynamic electric fields

From a device perspective, applying static fields to excitons in monolayer materials can be tricky. As mentioned before, the authors of the systematic experimental study in Ref. [116] applied a field to the excitons by incorporating buried electrical contacts with a tiny gap into their sample. This requires constructing a sample that is particularly designed for these types of measurements. On the other hand, if, say, a laser pulse was used to probe the excitons, one could use the same TMD sample (e.g. MoS_2 in hBN) to study excitonic behavior induced by different field shapes and sizes without the need to modify the sample itself. A particularly interesting type of dynamic perturbation is a THz pulse. Unlike the static fields discussed in the previous sections, such pulses apply an electric field to the excitons only for a finite amount of time. If the field is sufficiently strong (and the pulse duration long enough), one would still expect such a pulse to be able to dissociate excitons. Previous studies have analyzed exciton dissociation induced by THz pulses in, for example, bulk germanium [230] and GaAs [231], and GaAs based quantum-wells [232,233]. However, THz-induced dissociation probabilities for excitons in 2D materials had not been computed prior to the publication of Paper G.

A method of measuring THz-induced ionization in atomic physics is to count the number of ions produced in gaseous samples [234,235]. Unfortunately, such a method cannot be implemented in the solid-state case. Within solid-state physics, exciton dissociation is often discussed in electroabsorption experiments [230–232]. Here, one measures the absorption of a sample while a THz pulse propagates through it. One finds that exciton absorption peaks are shifted and broadened while the THz pulse is present, and a stronger pulse leads to more pronounced effects. It is well known that exciton dissociation contributes to the broadening of the absorption peaks. However, detailed experimental studies performed on both MoS_2 [122] and carbon nanotubes [236] suggest that the broadening induced by dissociation is negligible compared to other effects. It is therefore difficult to disentangle exciton dissociation from other effects in traditional electroabsorption experiments. However, if the pulse is capable of dissociating a substantial amount of excitons, one should, in principle, observe changes in the free-carrier absorption that may be related to exciton dissociation. Alternatively, one may collect free carriers via biased contacts, as was done for a static field in Ref. [116]. These are examples of interesting experiments that have yet to be performed.

We now turn to theoretically estimating exciton dissociation probabilities induced by such THz pulses. In Sec. 2.2, a time-independent formalism was used. This was possible as the applied fields were static in nature. On the other

hand, a pulse applies an electric field only for a finite amount of time. We must therefore use a time-dependent formalism to analyze such a perturbation. To this end, we employ a time-dependent version of the Wannier (or Schrödinger) equation for the exciton Stark problem. It reads

$$-i\frac{\partial}{\partial t}\Psi(\mathbf{r},t) = H\Psi(\mathbf{r},t), \quad (2.78)$$

where

$$H = -\frac{1}{2\mu}\nabla^2 + V(r) + \mathcal{E}(t)x. \quad (2.79)$$

Here, V is the RK potential (see Eq. (2.6)) and $\mathcal{E}(t)$ is the time-dependent electric field taken to be along the x -axis. We seek to expand the wave function in eigenstates of the unperturbed Hamiltonian

$$H_0\varphi_{mn}(\mathbf{r}) = E_{mn}\varphi_{mn}(\mathbf{r}), \quad (2.80)$$

where H_0 is given by Eq. (2.79) with $\mathcal{E} = 0$. Here, m and n refer to the angular momentum and principal quantum number. Note that angular momentum is a good quantum number as the potential is centrally symmetric. It is computationally convenient to make the continuum discrete by truncating the radial domain by introduce an infinite barrier at $r = R$ where we require $\varphi = 0$. As long as R is chosen large enough, the wave function $\Psi(\mathbf{r},t)$ should be well described within this limit for the relevant period of time. We write

$$\Psi(\mathbf{r},t) = \sum_{m=0}^M \sum_{n=0}^N d_{mn}(t)\varphi_{mn}(\mathbf{r})e^{-iE_{mn}t}. \quad (2.81)$$

To obtain a complete set of functions, one should, in principle, let M and N tend to infinity, but in practical calculations we keep them finite and gradually increase them until the results are converged. The probability of finding the exciton in state $\varphi_{n'm'}$ may then be obtained as

$$P_{m'n'}(t) = |\langle\varphi_{m'n'}(\mathbf{r})|\Psi(\mathbf{r},t)\rangle|^2 = |d_{m'n'}|^2, \quad (2.82)$$

where the final equality follows from the orthogonality of the eigenstates. In particular, the probability of the exciton being dissociated is

$$P_{\text{diss}}(t) = 1 - \sum_{m,n \text{ bound}} P_{m'n'}(t), \quad (2.83)$$

where the sum runs over all bound states, i.e. states for which $E_{mn} < 0$. Substituting the expansion into Eq. (2.78) and taking the inner product with $\varphi_{m'n'}$, one finds

$$\frac{d}{dt}d_{m'n'}(t) = -i \sum_{mn} d_{mn}(t)\mathcal{E}(t) \langle\varphi_{m'n'}|x|\varphi_{mn}\rangle e^{-i(E_{mn}-E_{m'n'})t}, \quad (2.84)$$

2.4. Exciton dissociation by dynamic electric fields

which lets us propagate the expansion coefficients in time, and thereby obtain the dissociation probability in Eq. (2.83) at any desirable time. Equation (2.84) may be written compactly as

$$\frac{d\mathbf{d}(t)}{dt} = -i\mathcal{E}(t)e^{i\mathbf{E}t}\mathbf{U}[e^{-i\mathbf{E}t}\mathbf{d}(t)], \quad (2.85)$$

where \mathbf{E} is a matrix with energies E_{mn} on the diagonal, \mathbf{d} the (column) vector containing the expansion coefficients, and \mathbf{U} has elements

$$U_{m'n',mn} = \langle \varphi_{m'n'} | x | \varphi_{mn} \rangle. \quad (2.86)$$

2.4.1 Numerical procedure

The eigenstates of the unperturbed Hamiltonian are not known analytically for the RK potential. We therefore expand them in an FE basis as in Eq. (2.58). That is,

$$\varphi_{mn}(\mathbf{r}) = \sum_{k=1}^K \sum_{i=q_n}^{Q_n} c_i^{(k)}(m, n) g_i^{(k)}(r) Y_m(\theta). \quad (2.87)$$

Note that m and n refer to the eigenstate here, and that k and i refer to the segment and FE basis function, respectively. Due to central symmetry, only a single angular function is needed to resolve the state. The Hamilton matrix may then be constructed in the exact same manner as laid out in Sec. 2.3, and one obtains the vector $\mathbf{c}(m, n)$ with FE coefficients describing state (m, n) by solving the resulting eigenvalue problem. Substituting Eq. (2.87) into Eq. (2.86), one may express the entire \mathbf{U} matrix as

$$\mathbf{U} = \mathbf{C}^T \mathbf{P} \mathbf{C}, \quad (2.88)$$

where \mathbf{C} is a matrix with the vectors $\mathbf{c}(m, n)$ on its columns, and \mathbf{P} is the finite element representation of the Stark matrix. That is, the matrix constructed as the Hamilton matrix in the FE section, but with H replaced by x . One may therefore construct the entire propagation matrix as a single matrix product. The scheme laid out above also makes it possible to apply exterior complex scaling at the ends of the domain to reduce spurious reflections from the boundary if desired. One must be careful doing so, however, as ECS can become unstable when applied in the length gauge (see, e.g. [215, 217, 218]). This is particularly true for long (low frequency) pulses, and so most of the low-frequency results have been obtained by the standard hermitian procedure above without implementing ECS.

There are many methods for attacking the differential equation in Eq. (2.85). The standard fourth order Runge-Kutta method approximates

$$\mathbf{d}(t + \Delta t) \approx \mathbf{d}(t) + \frac{\Delta t}{6}(\mathbf{k}_1 + 2\mathbf{k}_2 + 2\mathbf{k}_3 + \mathbf{k}_4), \quad (2.89)$$

where

$$\mathbf{k}_1 = -i\mathcal{E}(t)e^{i\mathbf{E}t}\mathbf{U}[e^{-i\mathbf{E}t}\mathbf{d}(t)] \quad (2.90)$$

$$\mathbf{k}_2 = -i\mathcal{E}\left(t + \frac{\Delta t}{2}\right)e^{i\mathbf{E}(t+\Delta t/2)}\mathbf{U}\left\{e^{-i\mathbf{E}(t+\Delta t/2)}\left[\mathbf{d}(t) + \frac{\Delta t\mathbf{k}_1}{2}\right]\right\} \quad (2.91)$$

$$\mathbf{k}_3 = -i\mathcal{E}\left(t + \frac{\Delta t}{2}\right)e^{i\mathbf{E}(t+\Delta t/2)}\mathbf{U}\left\{e^{-i\mathbf{E}(t+\Delta t/2)}\left[\mathbf{d}(t) + \frac{\Delta t\mathbf{k}_2}{2}\right]\right\} \quad (2.92)$$

$$\mathbf{k}_4 = -i\mathcal{E}(t + \Delta t)e^{i\mathbf{E}(t+\Delta t)}\mathbf{U}\left\{e^{-i\mathbf{E}(t+\Delta t)}[\mathbf{d}(t) + \Delta t\mathbf{k}_3]\right\}. \quad (2.93)$$

However, it is much more convenient to absorb the time-dependent exponential function into $\mathbf{b} = e^{-i\mathbf{E}t}\mathbf{d}$ to improve stability. This is particularly true if complex scaling is used, as it is difficult to repeatedly compute the exponential with complex energies to sufficient numerical accuracy. It may then be recast as

$$\mathbf{b}(t + \Delta t) \approx e^{-i\mathbf{E}\Delta t}\mathbf{b}(t) + \frac{\Delta t}{6}\left[e^{-i\mathbf{E}\Delta t}\boldsymbol{\kappa}_1 + 2e^{-i\mathbf{E}\Delta t/2}(\boldsymbol{\kappa}_2 + \boldsymbol{\kappa}_3) + \boldsymbol{\kappa}_4\right]. \quad (2.94)$$

where

$$\boldsymbol{\kappa}_1 = -i\mathcal{E}(t)\mathbf{U}\mathbf{b}(t) \quad (2.95)$$

$$\boldsymbol{\kappa}_2 = -i\mathcal{E}\left(t + \frac{\Delta t}{2}\right)\mathbf{U}\left\{e^{-i\mathbf{E}\Delta t/2}\left[\mathbf{b}(t) + \frac{\Delta t\boldsymbol{\kappa}_1}{2}\right]\right\} \quad (2.96)$$

$$\boldsymbol{\kappa}_3 = -i\mathcal{E}\left(t + \frac{\Delta t}{2}\right)\mathbf{U}\left\{e^{-i\mathbf{E}\Delta t/2}\mathbf{b}(t) + \frac{\Delta t\boldsymbol{\kappa}_2}{2}\right\} \quad (2.97)$$

$$\boldsymbol{\kappa}_4 = -i\mathcal{E}(t + \Delta t)\mathbf{U}\left\{e^{-i\mathbf{E}\Delta t}\mathbf{b}(t) + \Delta t e^{-i\mathbf{E}\Delta t/2}\boldsymbol{\kappa}_3\right\}. \quad (2.98)$$

While the RK4 method performs well, it lacks an adaptive step size procedure. The results in Paper G were obtained using an adaptive step-size eight-order Dormand-Prince Runge-Kutta method with embedded fifth- and third-order methods for error control [237], which improves the method considerably. For centrally symmetric problems, it is also more efficient to dissect the matrix products used in the time-propagation scheme into their angular momentum blocks.

Chapter 3

Summary of Results

This chapter contains a summary and discussion of selected results from the published papers, as well as some previously unpublished results. The purpose of the first section is to give an estimate of exciton binding energies in 2D materials. This is an important quantity when discussing exciton dissociation. Here, we also discuss the impact that the parameters in the Wannier model have on the exciton binding energies. One often finds different estimates of the parameters in the literature, so it is worth pointing out that most of the results will only be qualitatively accurate. The next section summarizes the results on exciton dissociation in monolayers induced by static electric fields. The results for monolayer TMDs are from Paper A, while the results for phosphorene are from Paper E. The third section then summarizes similar results for bilayer heterostructures. These results have been published in Paper C. Finally, exciton dissociation in monolayer TMDs induced by THz pulses is discussed in the fourth section.

3.1 Binding energies and parameters

As discussed in Sec. 2.1, Wannier excitons in 2D materials are modeled as electron-hole pairs whose interaction is screened by the surrounding media, as well as the 2D material itself. For TMD monolayers, the approximate interaction is given by the RK potential (see Eq. (2.6)). This model contains three parameters that completely define the exciton binding energy within the Wannier model. Values for the reduced mass μ and screening length r_0 are often obtained from first principle calculations based on density functional theory (DFT). The screening from the surrounding media is then taken into account via the average dielectric constant κ . Such a procedure was, for example, used

in Ref. [106] where good agreement was found between the Wannier model and the first principle BSE approach. We have collected the binding energies from Ref. [106], as well as other theoretically predicted values in Table 3.1. The first column shows the (approximate) average dielectric constant of the surrounding media. Two aspects are immediately clear from this table. First, most of the results are for freely suspended monolayers, as incorporating substrate screening yields more complex calculations. Second, the predicted binding energies span a remarkable range with many of the highest predictions being more than twice the lowest ones. Some of the discrepancies may be traced back to different convergence criteria used. Nevertheless, it is clear that accurately determining exciton binding energies is not such a simple task. This problem is further complicated, as values for reduced masses and screening lengths predicted by these calculations also vary [104, 106, 107, 128, 238–241], and it is therefore not so clear which values should be used in the Wannier model.

An alternative approach to determine exciton binding energies is based on

Table 3.1: Theoretically predicted binding energies for excitons in various TMD monolayers. The first column shows the average dielectric screening of the surrounding media κ . Energies are given in meV. Computational methods are given alongside the references at the bottom of the table.

κ	MoS ₂	MoSe ₂	WS ₂	WSe ₂
1	500 ^a , 501 ^b , 527 ^c , 540 ^d , 540 ^e , 860 ^f , 897 ^g , 960 ^h , 1040 ⁱ , 1100 ^j	465 ^b , 470 ^e , 477 ^c , 650 ^k , 780 ^j , 910 ⁱ	500 ^e , 510 ^c , 540 ^d , 543 ^b , 700 ^l , 1040 ⁱ	450 ^e , 456 ^c , 494 ^b , 900 ⁱ
2	349 ^c	323 ^c	323 ^c	295 ^c
2.4	455 ^f			

^a Reference [242]: BSE with GW band structure.

^b Reference [128]: BSE with DFT band structure.

^c Reference [243]: DFT and path integral Monte Carlo approach.

^d Reference [244]: BSE with GW band structure.

^e Reference [106]: Wannier model parameterized by DFT and RPA.

^f Reference [245]: Density matrix formalism.

^g Reference [240]: Hydrogen expression with input from GW band structure.

^h Reference [107]: BSE with GW band structure.

ⁱ Reference [104]: BSE with GW band structure.

^j Reference [246]: BSE with GW band structure.

^k Reference [99]: BSE with GW band structure.

^l Reference [247]: BSE with GW band structure.

3.1. Binding energies and parameters

experiments. The exciton binding energy is defined as the difference between the optical and electronic band gap of a material. Here, the optical band gap refers to the lowest photon energy for which we find an absorption peak (i.e. the energy of the A exciton). By measuring the difference between these values, the binding energy may be determined. This procedure was done in Ref. [248] where the authors used photocurrent spectroscopy to determine the two band gaps. They found that the exciton binding energy in a freely suspended MoS₂ monolayer is at least 570 meV. While the value is not very precise, it does agree with the theoretical predictions in Table 3.1. Refs. [99, 249] also compared the electronic and optical band gaps for excitons in MoSe₂ on bilayer graphene and MoS₂ on graphite, respectively. The first group found a value of 550 meV, and the latter group a value of 220 meV (or 420 meV if a second threshold was used).

A promising alternative method is to perform absorption spectroscopy on a sample during the application of strong magnetic fields. Such measurements may be used to determine the 1s exciton diamagnetic shift coefficient σ , which may be expressed as $\sigma = \langle r^2 \rangle / (8\mu)$, where $\langle r^2 \rangle$ is the average value of the squared exciton radius. By using a value for μ from DFT calculations and a κ inferred from the bulk dielectric constants of the surrounding media, Stier et al. [109] were able to fix r_0 by computing the average squared exciton radius using the Wannier model, and demanding that the resulting σ matched the experimentally measured values. This, in turn, fixes the exciton binding energy. The sample used in the experiments was a WSe₂ monolayer in various surroundings. These values (among others) are collected in Table 3.2.

Importantly, by fixing the reduced mass and computing κ from the bulk values of the surrounding media, Stier et al. [109] find that a different r_0 best fits the experimentally measured data for their WSe₂ sample in various dielectric surroundings. This is not how one typically thinks of the Wannier model. The screening length r_0 is typically fixed from the polarizability of the 2D material, regardless of the surrounding screening. A discrepancy is, of course, to be expected, as the Wannier model with the RK potential is too simple to capture the complex dependence on substrate screening. Stier et al. [109], furthermore, show by fixing r_0 and μ and varying κ that the Wannier model with the RK potential underestimates the dependence of the binding energies on κ .

Goryca et al. [111] performed a similar experiment on various TMD monolayers encapsulated by hBN. Whereas Stier et al. used a reduced mass from DFT calculations, Goryca et al. inferred the reduced mass by measuring the energy shifts of excited (*ns*) excitons as a function of (strong) applied magnetic fields. The idea is that the shifts of weakly bound excitons in strong fields depend primarily on μ and are virtually independent of κ and r_0 . Thus, μ may be

predicted by comparing the measured energy shifts of these excitons to those from the Wannier model including the magnetic field term $B^2 r^2 / (8\mu)$, where B is the magnetic field (see Ref. [111] or, e.g. [189] for more information). Once the reduced mass is fixed, r_0 and κ may be fixed by demanding that the eigenvalues of the Wannier model agree with the measured shifts for the lower-lying excitons. In this manner, they determine all parameters needed to use the Wannier model for excitons in TMD monolayers encapsulated by hBN from experiment. They find that slightly different κ best fit the different TMDs, even if the same hBN encapsulation is used. The ranges span from 4.35 – 4.5, depending on the TMD. This is in line with the discussion above. Only varying κ when the surrounding dielectric screening changes is not sufficient to capture the complex dependence on surrounding screening.

The results in the published papers have been obtained by the standard method used for Wannier excitons. Namely, fixing μ and r_0 for the specific monolayer, and then varying κ based on the substrate screening. While this may not be the most accurate method, it does give a qualitative understanding of how binding energies and other parameters behave as the substrate screening is changed. In Papers A, C, and D, reduced masses and screening lengths

Table 3.2: Experimentally obtained binding energies for excitons in various TMD monolayers. The first column shows the (approximate) average dielectric screening of the surrounding media κ . Energies are given in meV. Note that two values are obtained in Ref. [109] due to the use of two different reduced masses, and that the experiment in Ref. [248] predicted an exciton binding energy of at least 570 meV.

κ	MoS ₂	MoSe ₂	WS ₂	WSe ₂
1	$\geq 570^a$			
1.55				362 (482) ^b
2.25				270 (351) ^b
2.4	440 ^c		320 ^c , 320 ^d	370 ^e
3.3				180(211) ^b
4.5	221 ^f	231 ^f	180 ^f	167 ^g

^a Ref. [248]

^b Ref. [109]

^c Ref. [250]

^d Ref. [241]

^e Ref. [251]

^f Ref. [111]

^g Ref. [252]

3.1. Binding energies and parameters

were obtained from the first principle calculations made by Olsen et al. [128]. These parameters were obtained for freely suspended materials. In Paper G, the experimentally determined parameters from Goryca et al. [111] were used. Both sets of parameters may be found in Table 3.3. The difference between the reduced masses of the molybdenum and tungsten-based materials is larger for the experimentally determined parameters. In addition, the screening lengths are lower than those obtained from Olsen et al. We show the binding energies predicted by the Wannier model using these parameters while varying κ in Fig. 3.1. The binding energies in Fig. 3.1(a) are identical to the ones computed by Pedersen [112], as the same parameters were used. Evidently, the parameters lead to binding energies that behave quite differently. In particular, the molybdenum-based materials have considerably larger binding energies than the tungsten-based materials when using the experimental parameters [111]. Additionally, they are more spread than those obtained by using the first principle parameters from Ref. [128]. One may expect that the parameters by Olsen et al. that have been computed for freely suspended structures are more accurate for monolayers where $\kappa \approx 1$, and that those by Goryca et al. are more accurate in the vicinity $\kappa \approx 4.5$.

Table 3.3: Reduced masses μ and screening lengths r_0 for four TMDs. The parameters by Olsen et al. have been computed from first principles, whereas the parameters by Goryca et al. have been determined from experiments. Goryca et al. find slightly different κ to best describe hBN encapsulation for the various TMDs. These values are also given in the table below.

	Olsen et al. [128]		Goryca et al. [111]		
	μ	r_0	μ	r_0	κ (hBN)
MoS ₂	0.28	44	0.28	34	4.45
MoSe ₂	0.27	51	0.35	39	4.4
WS ₂	0.22	40	0.18	34	4.35
WSe ₂	0.23	46	0.20	45	4.5

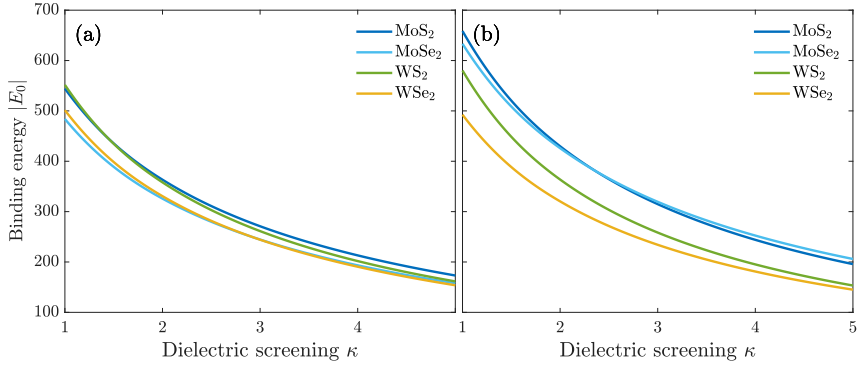


Fig. 3.1: Exciton binding energies in four TMDs as a function of surrounding dielectric screening. The binding energies in (a) and (b) have been computed using the parameters by Olsen et al. [128] and Goryca et al. [111], respectively.

3.2 Exciton dissociation by static in-plane electric fields in monolayers

Applying a static electric field to an exciton shifts its energy levels (the exciton Stark shift) and may eventually lead to dissociation. The main focus of Paper A was to study these processes for excitons in TMD monolayers. How exciton Stark shifts and dissociation rates change with substrate screening and field strength were of particular interest. One of the goals of Paper A was also to demonstrate that the ECS formalism implemented via an FE approach was more efficient than the traditionally used methods for obtaining field-induced dissociation rates for weak electric fields. An analytical weak-field approximation to these rates has also been derived in order to better understand the parameters involved, as well as to make weak-field dissociation rates easily available to researchers. The weak-field approximation consists of an analytical form with a numerically determined coefficient. The aim of Paper D was to find an analytical approximation for this coefficient as well, thereby obtaining a fully analytical approximation. Armed with the method of Paper A, we turned to implement it to study Stark shifts and exciton dissociation rates in phosphorene in Paper E. Phosphorene is different from the TMDs in that it is an anisotropic material. Exciton shifts and rates in phosphorene will therefore depend on the direction of the electric field. It was interesting to see the extent of this dependence. We will discuss the results of these papers below.

3.2.1 Monolayer TMDs

In Paper A, we modeled excitons as electron-hole pairs described by the 2D Wannier equation [see Eqs. (2.1) and (2.6)]. We then applied an external electric field to the excitons [see Eq. (2.37)], and used ECS to compute the dissociation rates (see Sec. 2.2). One of the main focuses of this paper was to obtain exciton dissociation rates for extremely weak fields. This had not been done before, as the methods used prior were difficult to get to converge for weak fields. Another focus of the paper was to obtain an analytical approximation to the dissociation rates for weak fields. There are three major reasons why such an expression is useful. First, dissociation rates for extremely weak fields remain unobtainable due to numerical difficulties, even with the efficient method laid out in Paper A. An analytical expression valid for extremely weak fields therefore bridges the gap between numerically obtainable rates and rates obtained when the field strength tends to zero. Second, an analytical expression is convenient for researchers to get a quick estimate of the rates without the need of performing numerical computations. Third, an analytical expression helps

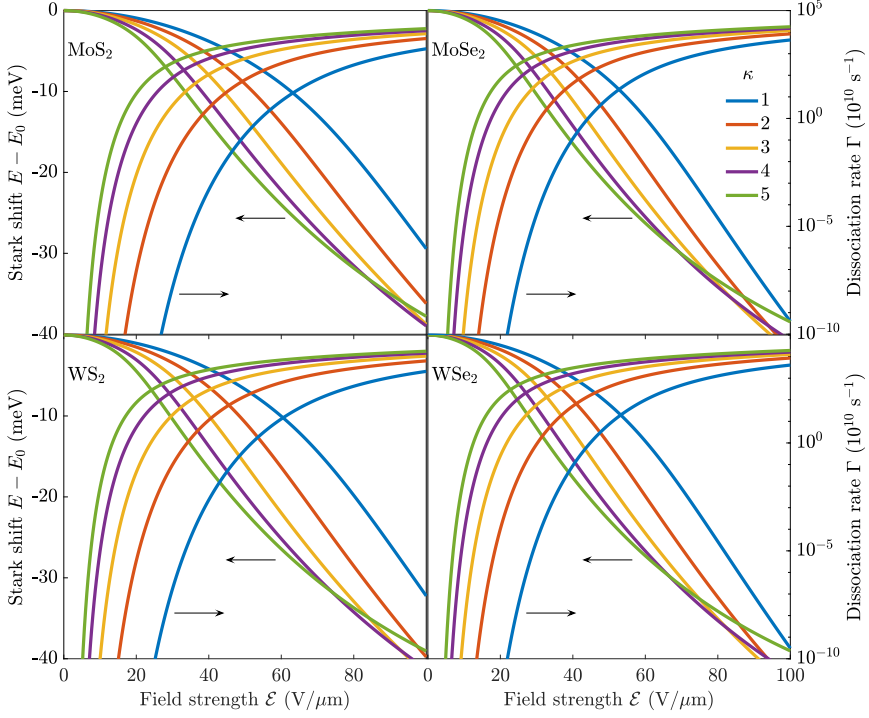


Fig. 3.2: Exciton Stark shift and dissociation rate of the ground-state exciton for four important TMD materials in various dielectric environments. Screening lengths and reduced masses used in calculation are from [128]. This figure is a reproduction of the figure in Paper A [117].

us understand how dissociation rates depend on material parameters, such as substrate screening.

In Fig. 3.2, we show Stark shifts (left axis) and dissociation rates (right axis) of the exciton ground state in four TMDs predicted by the Wannier model parameterized by the first principle parameters from Olsen et al. [128]. Different color curves correspond to different values of the average dielectric constant of the surrounding media κ . A very sensitive dependence on field strength is found for the dissociation rates, in particular. The behavior of the shifts and rates is qualitatively similar across the different TMDs, both as a function of substrate screening and field strength. There are substantial quantitative differences between them, however. To make this clear, we have collected dissociation rates for experimentally relevant field strengths in Table 3.4. The exponential dependence on the field strength for weak electric fields is immediately clear, with rates increasing by as much as a factor of 30 when going from 10 to 20 V/ μm . The rates also grow rapidly as the screening is increased. This is a

3.2. Exciton dissociation by static in-plane electric fields in monolayers

direct result of the reducing binding energy [see Fig. 3.1(a)].

A common material used for encapsulation is hBN with an average dielectric constant of about $\kappa \approx 4.5$ [111]. Evidently, encapsulation by hBN causes the dissociation rates to increase by several orders of magnitude over the freely suspended materials. As was discussed in the previous section, the Wannier model tends to underestimate the impact of substrate screening when fixed μ and r_0 are used, and κ is varied [109]. Goryca et al. [111] have experimentally determined the optimal parameters to describe excitons in hBN encapsulated TMDs. It is interesting to see the difference between dissociation rates that the two sets of parameters (found in Table 3.3) lead to. To this end, we compute rates using the theoretically predicted μ and r_0 from Olsen et al. [128], as well as the experimentally determined parameters from Goryca et al. [111] for hBN encapsulated materials. The values for κ used for both sets of parameters are obtained from Goryca et al. (see Table 3.3). Results using both parameters are in qualitative agreement for all TMDs considered. Interestingly, however, the experimental parameters predicted lower and higher dissociation rates for the molybdenum and tungsten-based materials, respectively. This behavior is consistent with the binding energies predicted by the two sets of parameters (see Fig. 3.1), which are $\{193, 178, 186, 171\}$ and $\{220, 232, 179, 161\}$ for MoS_2 , MoSe_2 , WS_2 , WSe_2 for the theoretical and experimental parameters, respectively. That is, the experimentally determined parameters lead to larger and lower binding energies for the molybdenum and tungsten-based materials for $\kappa \approx 4.5$, respectively.

As was mentioned in Sec. 2.2, excitons in realistic semiconductors have finite lifetimes due to loss mechanisms such as recombination, defect-assisted recombination [182], and exciton-exciton annihilation [183,184]. Exciton dissociation

Table 3.4: Exciton dissociation rates in various TMD monolayers induced by static electric fields of 10 and 20 V/ μm . Encapsulating media with average dielectric constants in the range $\kappa = [1, 5]$ are considered. Dissociation rates are given in units of s^{-1} . Numbers in parenthesis represent powers of 10, such that $a(b) = a \times 10^b$. Values with an asterisk have been obtained using the analytical weak-field approximation in Paper A, whereas the other values have been obtained using the numerical procedure.

κ	MoS_2		MoSe_2		WS_2		WSe_2	
	$\mathcal{E} = 10$	$\mathcal{E} = 20$	$\mathcal{E} = 10$	$\mathcal{E} = 20$	$\mathcal{E} = 10$	$\mathcal{E} = 20$	$\mathcal{E} = 10$	$\mathcal{E} = 20$
1	5.3(-38)*	6.1(-8)*	5.6(-27)*	1.5(-2)*	2.7(-33)*	4.9(-6)*	1.9(-26)*	1.5(-2)*
2	4.8(-14)*	8.4(2)	2.1(-8)	4.3(5)	3(-10)*	3.5(4)	2.6(-7)*	1.0(6)
3	9.9(-4)	2.4(7)	2.7	1.0(9)	9.3(-1)	4.4(8)	3.2(1)	2.5(9)
4	4.4(2)	5.8(9)	7.9(4)	6.3(10)	9.6(4)	5.4(10)	7.0(5)	1.4(11)
5	1.1(6)	1.4(11)	4.2(7)	6.6(11)	8.3(7)	7.4(11)	2.7(8)	1.2(12)

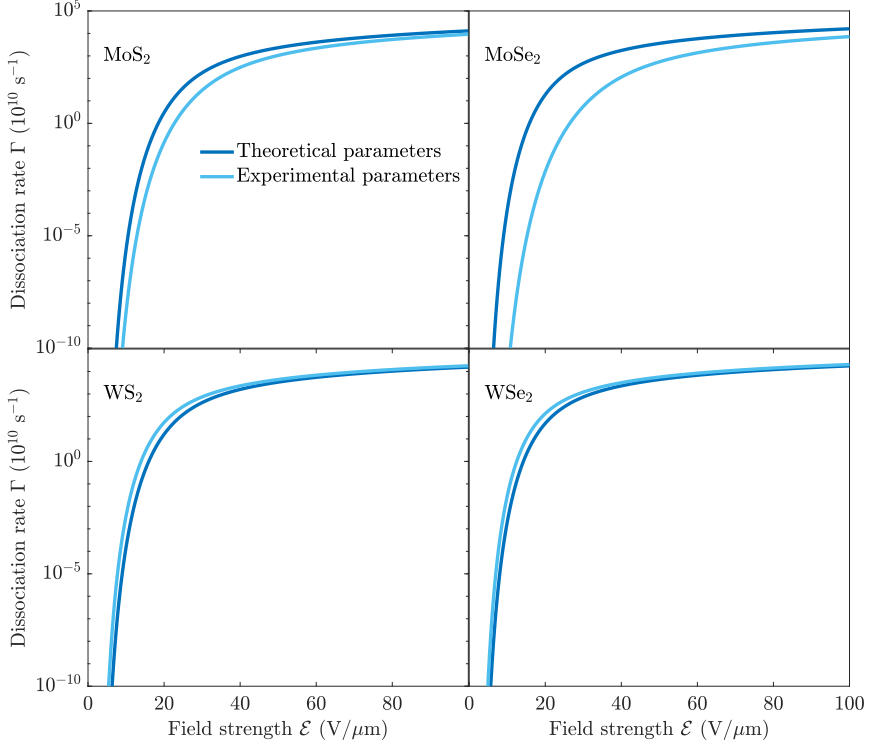


Fig. 3.3: Exciton dissociation rates for the ground state exciton in four TMD monolayer encapsulated by hBN. The dark blue curves have been computed using theoretically predicted μ and r_0 from Olsen et al. [128], whereas the light blue curves have been computed using the experimentally obtained parameters from Goryca et al. [111]. For both sets of parameters, average dielectric constants of $\kappa = \{4.45, 4.4, 4.35, 4.5\}$ have been used to describe hBN encapsulated MoS₂, MoSe₂, WS₂, and WSe₂, respectively.

is in direct competition with these processes. For an electric field to be able to dissociate a substantial amount of excitons, the field must be sufficiently strong such that excitons are dissociated before they recombine or are otherwise annihilated. In order to get an idea of how large fields are required, we may compare the dissociation rates to the field-free lifetimes. At low densities and (very) low temperatures, radiative recombination dominates, leading to an exciton lifetime of about 200 fs [138,253,254] in MoS₂, and similar values are found for the other TMDs [253]. Furthermore, due to the low temperature, thermal dissociation is expected to be negligible. A lifetime of 200 fs corresponds to a decay rate of about $5 \times 10^{12} \text{ s}^{-1}$. Comparing to Fig. 3.2 and Table 3.4, we see that reasonably strong fields are required to dissociate these excitons. In particular, if a substrate screening of $\kappa \approx 5$ is considered, a field strength of $\gtrsim 30$ is needed to overcome the radiative recombination. As the temperature increases to room

3.2. Exciton dissociation by static in-plane electric fields in monolayers

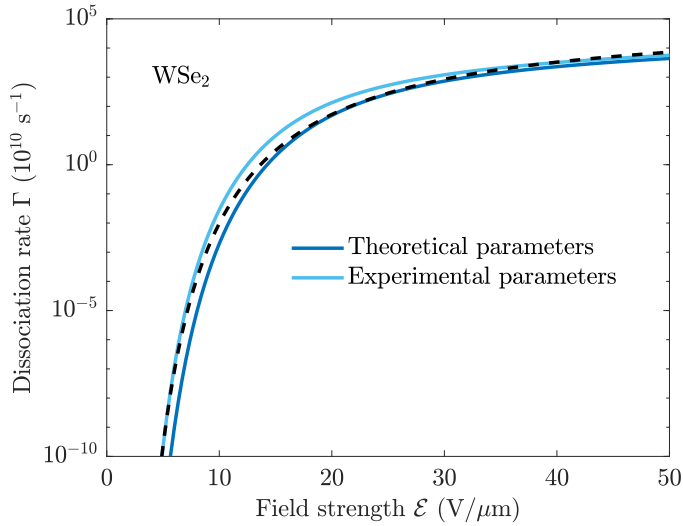


Fig. 3.4: Dissociation rate for excitons in hBN encapsulated WSe₂ (same as in Fig. 3.2). The dark and light blue curves are obtained using the theoretical and experimental parameters, respectively. The black dashed curve shows the exponential fit in Ref. [116].

temperature, recombination times increase to about 1 ns [182, 253, 255]. The much shorter characteristic lifetime of defect-assisted recombination of about 4 ps therefore starts to dominate [182, 256, 257]. This corresponds to a decay rate of $2.5 \times 10^{11} \text{ s}^{-1}$, and a slightly weaker field of $\gtrsim 20 \text{ V}/\mu\text{m}$ becomes sufficient. Note also that at room temperature, field-induced dissociation is assisted by thermal agitation, which is expected to further reduce the strength of the required field. As a final remark, we mention that the analysis performed here is qualitative. As is evident from Fig. 3.3, a slight change in the values of the parameters can lead to dissociation rates that differ by several orders of magnitude. This makes it difficult to obtain quantitatively accurate dissociation rates, which in turn makes it difficult to compare to exciton lifetimes.

Prior to the publication of Paper A, only few results on exciton dissociation in monolayer materials had been published [113, 114, 116]. Haastrup et al. [114] had computed rates for freely suspended MoS₂ as well as MoS₂ on an hBN substrate or encapsulated by hBN. Their results were for fields larger than $50 \text{ V}/\mu\text{m}$. At $\mathcal{E} \approx 50 \text{ V}/\mu\text{m}$ they find a dissociation rate of $\Gamma \approx 3 \times 10^{11} \text{ s}^{-1}$ for MoS₂ encapsulated by two hBN monolayers. Using the experimental and theoretical parameters discussed above, we find similar rates at $\mathcal{E} \approx 30$ and $\mathcal{E} \approx 24 \text{ V}/\mu\text{m}$, respectively. The model used in Ref. [114] uses the polarizability of the structure hBN/MoS₂/hBN, rather than introducing the constant κ .

The experimental study made by Massicotte et al. [116] on hBN encapsu-

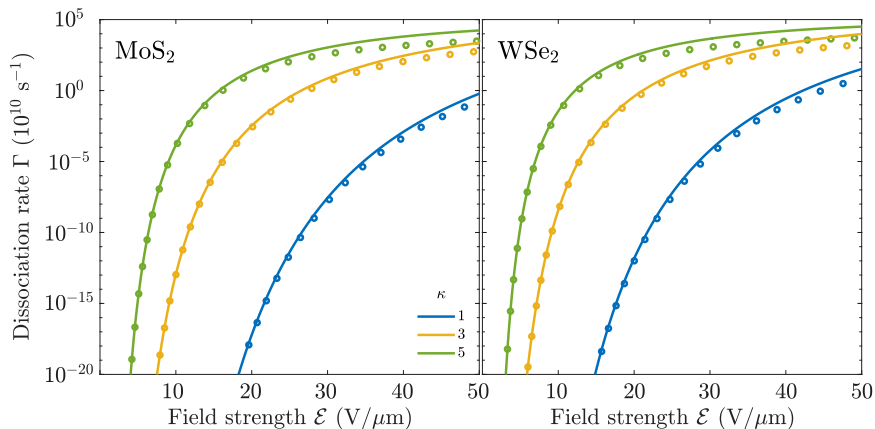


Fig. 3.5: Exciton dissociation rates for MoS₂ (upper) and WSe₂ (lower) encapsulated by various dielectric media. The circles are the numerically exact results obtained by the ECS method. The solid lines correspond to the analytical weak-field formula. The parameters from Olsen et al. [128] have been used. This figure is a reproduction of the figure in Paper A [117].

lated WSe₂ indicated that exciton dissociation rates were the limiting factor in photocurrent generation for fields weaker than 15 V/μm. Their theoretical predictions were obtained by using the theoretical parameters above together with the UCS approach discussed in Sec. 2.2. Here, it was noted that this approach is inefficient for weak electric fields, and the results in Ref. [116] for weak fields were therefore obtained by fitting to an exponential form motivated by the 2D hydrogen atom. That is $a\mathcal{E}^{-1/2} \exp(b/\mathcal{E})$, where a and b are constants. These results turned out to accurately reproduce the measured photoresponse for fields of $\mathcal{E} \lesssim 13$ V/μm. In Fig. 3.4, we compare this fit to the results for hBN encapsulated WSe₂. Evidently, the weak-field fit that reproduces the experimental values in Ref. [116] tends to the results obtained using the experimentally predicted parameters by Goryca et al. [111] for weak fields.

The difficulty with predicting dissociation rates for weak fields using numerical methods is known within atomic physics [178]. Trinh et al. [178] argued that any numerical method with finite precision arithmetic will fail for sufficiently weak fields. They proceeded by implementing a multiple-precision method for predicting ionization rates of the hydrogen atom for extremely weak fields. The reason that this is possible for the hydrogen atom is that the computation of Γ may be formulated such that it only involves basic arithmetic operations. This traces back to the fact that the Coulomb potential is separable in parabolic coordinates. While the RK potential does not satisfy this condition, it does have a Coulomb tail. This lets us derive a weak-field approximation to the

3.2. Exciton dissociation by static in-plane electric fields in monolayers

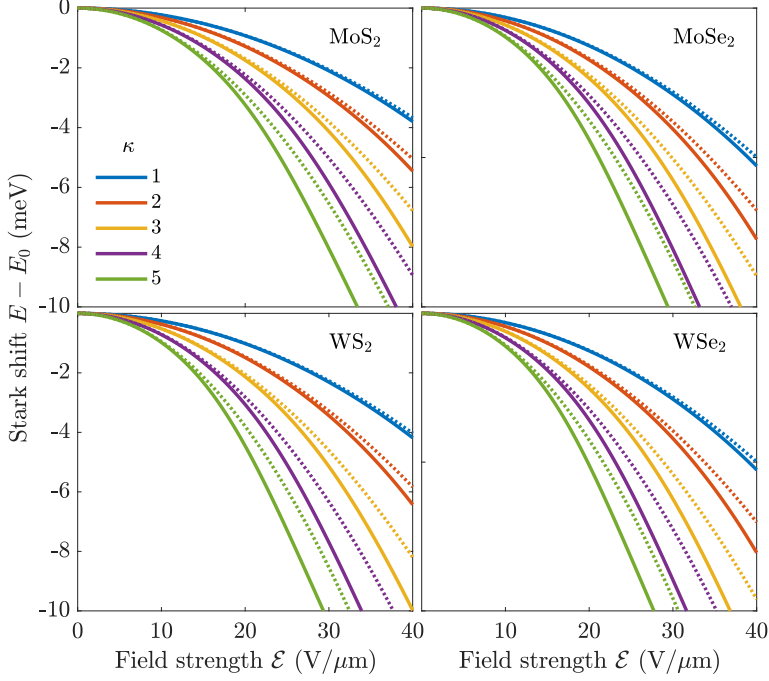


Fig. 3.6: Exciton Stark shift for four important TMDs in various dielectric environments. The solid lines correspond to the real part of the resonance energy, while the dotted lines show the shift predicted by perturbation theory. This figure is a reproduction of the figure in Paper A [117].

dissociation rates (see Paper A). It has the form

$$\Gamma \approx a \mathcal{E}^{1/2-2\mu/(\kappa k)} \exp\left(-\frac{2k^3}{3\mu\mathcal{E}}\right), \quad (3.1)$$

where a is a constant defined in Paper A, and $k = \sqrt{2\mu E_b}$ with $E_b = -E_0$ being the exciton binding energy. The approximate rates are compared to the ECS results in Fig. 3.5. Evidently, a good agreement is found between the analytical weak-field approximation (circles) and the exact rates (lines) for weak electric fields, making the expression useful for quick estimates. As expected, the agreement becomes better as the field strength decreases. The binding energy of the 2D hydrogen atom is 2 a.u., which simplifies the field-dependent front factor in Eq. (3.1) to $\mathcal{E}^{-1/2}$.

As a check that the Stark shifts produced by the complex scaling calculation are in agreement with what one expects, we may compare them to the well-known perturbation result for weak electric fields. For a potential that exhibits central symmetry, we have $E - E_0 \approx -\alpha \mathcal{E}^2/2$, where α is the exciton

polarizability. The comparison may be found in Fig. 3.6, where the dotted lines show the perturbation series result and the solid lines show the exact results (see Paper A for computation of α). The numerical Stark shifts are seen to agree with the quadratic perturbation result for weak electric fields.

3.2.2 Phosphorene

Phosphorene differs from the TMDs discussed above, as it is anisotropic in the plane. Thus, the excitonic response will depend on the direction of the applied electric field. Studying this dependence was the aim of Paper E. The computational procedure is again the FE-ECS method described in Secs. 2.2 and 2.3. However, as the potential (in the transformed coordinates) is no longer centrally symmetric, the sine and cosine blocks no longer decouple. The calculations are therefore more computationally demanding than for the TMDs.

To better understand the role of the anisotropy, we show the exciton Stark shifts (left axis) and dissociation rates (right axis) in Fig. 3.7. Here, phosphorene in three different dielectric surroundings is considered, namely, freely suspended $\kappa = 1$ (top), on an SiO_2 substrate $\kappa = 2.4$ (middle), and encapsulated by hBN (bottom) $\kappa = 4.5$. The different colors correspond to an external in-plane field with an angle α to the x -axis, and we recall that the x - and y -axis are taken along the armchair and zigzag directions, respectively. Evidently, we find that it is easier to dissociate the excitons along the armchair axis. This is in good agreement with what one expects from the direction-specific material quantities $\epsilon_{x,y} = \{12.5, 10.2\}$ [64], $\chi_{xx,yy} = \{4.20, 3.97\} \text{\AA}$ [166], $\mu_{x,y} = \{0.1533, 0.6605\}$ [169]. The dissociation rates decrease by several orders of magnitude by rotating the field from the x -axis to the y -axis, and a substantial difference is also found in the Stark shifts. This direction dependence provides an additional degree of freedom to consider in device design, as the Stark shifts and dissociation rates may be tuned by rotating the electric field. For practical applications, phosphorene will mostly be encapsulated by, e.g., hBN. Similar to the TMDs, we find that the dielectric surroundings greatly influence both dissociation rates and Stark shifts, due to the reducing binding energy. For hBN, in particular, we find that the rates increase by several orders of magnitude over both the freely suspended and SiO_2 substrate cases.

As before, it is useful to obtain an analytical weak-field approximation. The approximation derived in Paper A was generalized to the anisotropic case in Paper E. It has the form

$$\Gamma \approx a(\alpha) \tilde{\mathcal{E}}^{1/2-2Z/k} \exp\left(-\frac{2k^3}{3\tilde{\mathcal{E}}}\right), \quad (3.2)$$

3.2. Exciton dissociation by static in-plane electric fields in monolayers

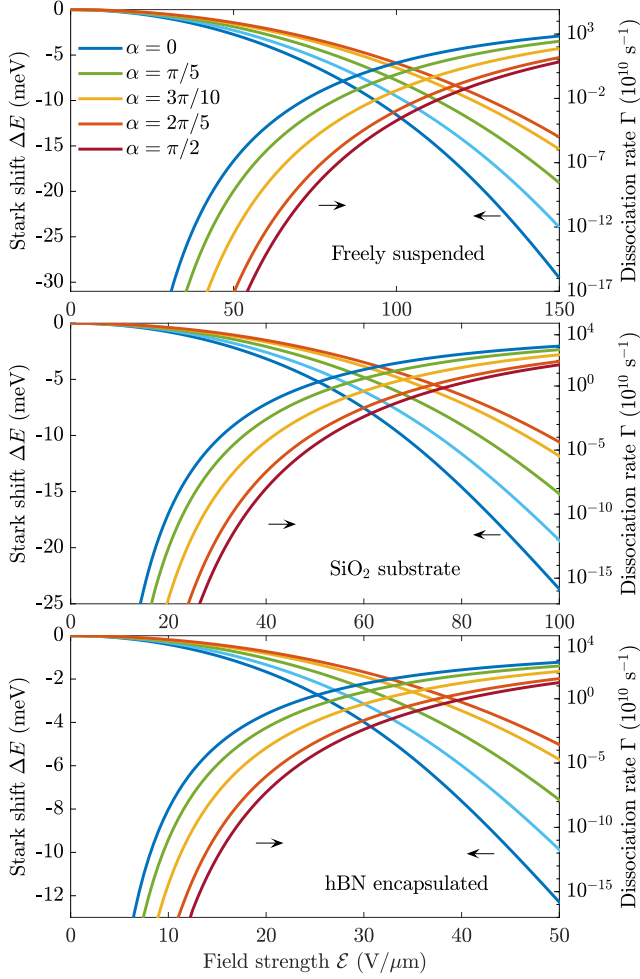


Fig. 3.7: Stark shifts $\Delta E = \text{Re}(E - E_0)$ (left axis) and dissociation rates $\Gamma = -2\text{Im} E$ (right axis) of excitons in phosphorene that is freely suspended (top), on an SiO₂ substrate (middle), or encapsulated by hBN (bottom). For each of the three cases, electric fields with an angle to the x -axis α ranging from 0 to $\pi/2$ are considered. The figure is from Paper E [258].

where $k = \sqrt{2|E_0|}$,

$$\tilde{\mathcal{E}}(\alpha) = \mathcal{E} \sqrt{\frac{\cos^2 \alpha}{\mu_x} + \frac{\sin^2 \alpha}{\mu_y}}, \quad (3.3)$$

$$Z(\alpha) = \frac{1}{\kappa} \sqrt{\frac{2\mu(\mu_y \cos^2 \alpha + \mu_x \sin^2 \alpha)}{(1 + \beta)\mu_y \cos^2 \alpha + (1 - \beta)\mu_x \sin^2 \alpha}}, \quad (3.4)$$

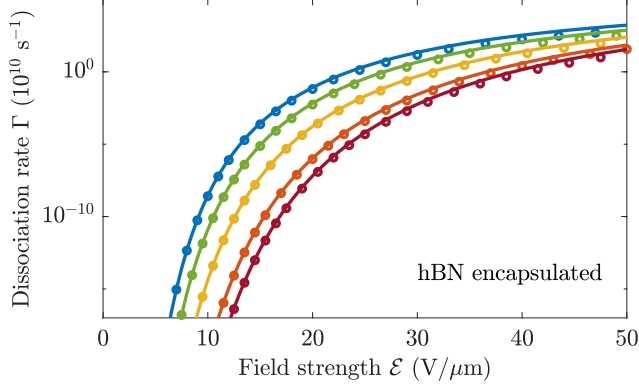


Fig. 3.8: Comparison between the analytical weak-field expression (circles) and the numerically exact results (lines). The figure is a reproduction of the figure in Paper E [258].

and $\beta = (\mu_y - \mu_x)/(\mu_y + \mu_x)$ and $\mu = \mu_x\mu_y/(\mu_x + \mu_y)$ were defined in Sec. 2.1.3. The (direction dependent) coefficients are given in Paper E. This form is similar to that of Eq. (3.1) but the quantities now depend on the field direction. A comparison between the approximation (circles) and the numerically exact rates (lines) can be seen in Fig. 3.8 for hBN encapsulated phosphorene. Clearly the weak-field approximation captures the angular dependence of the dissociation rates at weak electric fields. While only the hBN case is shown here, the approximation is also accurate for freely suspended phosphorene and phosphorene on an SiO₂ substrate (see Paper E). This expression will therefore be useful to obtain quick estimates of dissociation rates induced by weak electric fields. Note also that if $\mu_x = \mu_y$, it reduces to the form in Eq. (3.1).

It is also interesting to see how the anisotropic exciton polarizability may predict the Stark shifts from a second-order perturbation expression. As described in Paper E, the second-order energy correction depends on the direction-specific exciton polarizabilities. These have been computed for the five lowest energy states in phosphorene in the different dielectric surroundings. The results are shown in Tbl. IV of Paper E. A comparison between the second-order perturbation series and the numerically exact Stark shifts in freely suspended phosphorene is shown in Fig. 3.9. The form of the eigenstates was given in Sec. 2.1.3. The three panels correspond to fields pointing in three different directions. The top panel is for a field along the x -axis, the middle panel at an intermediate angle, and the bottom panel along the y -axis. The five lowest energy states are shown and are indicated by color. Evidently, the perturbation

3.2. Exciton dissociation by static in-plane electric fields in monolayers

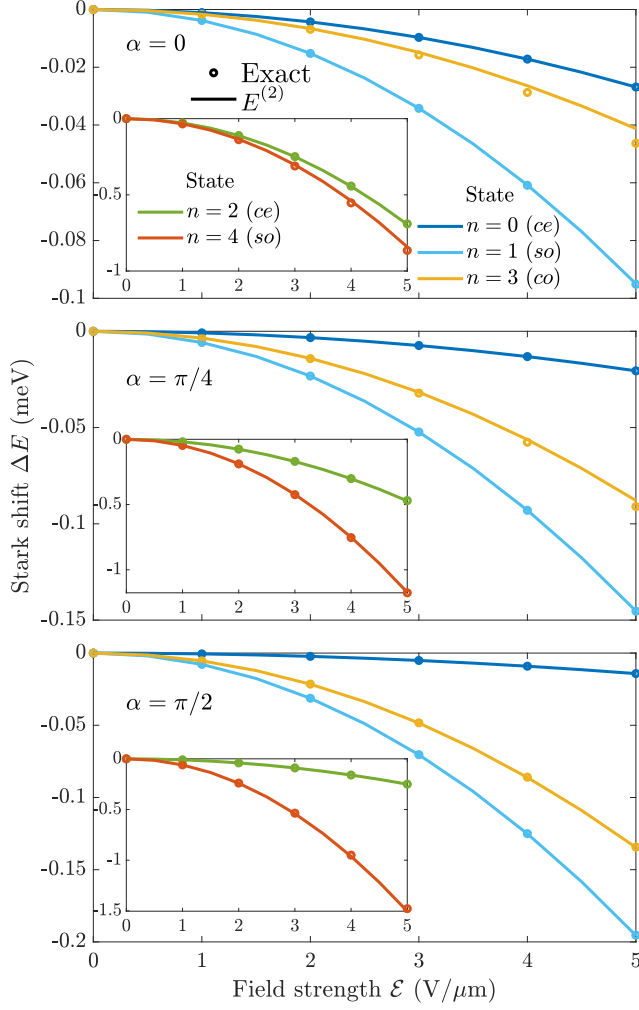


Fig. 3.9: Comparison between the second-order perturbation expression (circles) and the numerically exact Stark shifts (lines). The figure is from Paper E ([258]).

approximation agrees with the numerical results for (extremely) weak fields, and the angular dependence is captured by the exciton polarizability.

3.3 Exciton dissociation by static in-plane electric fields in bilayer structures

Certain bilayer configurations from a so-called type-II band alignment, where the conduction band minimum and the valence band maximum reside in different layers. Electrons and holes in such a structure will therefore prefer to reside in separate layers. Excitons consisting of a bound electron-hole pair where the particles reside in different layers are referred to as interlayer excitons. Whether the ground-state exciton is an interlayer or intralayer exciton depends on whether the energy won by the band offset is larger than the loss in binding energy. This is the case for the bilayer structures considered here, and the ground-state exciton is therefore an interlayer exciton. This means that excitons that are generated in one of the monolayers will quickly transform into interlayer excitons. Depending on the structure, this transformation may occur incredibly fast. For instance, as was mentioned before, Hong et al. [56] found that the hole of an exciton generated in the MoS₂ layer of a MoS₂/WS₂ structure tunneled into the WS₂ layer within 50 fs. As we shall see, this rate is much larger than the field-induced dissociation rates at moderate fields. We, therefore, expect dissociation rates of interlayer excitons to be the limiting factor in photocurrent generation in such bilayer structures. Recall that we refer to the bilayer structures as TMD1/TMD2, such that the conduction band minimum and valence band maximum are located in TMD1 and TMD2, respectively. The electron and hole will therefore prefer to reside in TMD1 and TMD2, respectively.

Using the model laid out in Sec. 2.1.2, the Stark shifts and dissociation rates for six different structures have been computed in Paper C. The results for these structures can be seen in Fig. 3.10. An interesting feature of interlayer excitons is the relatively large Stark shifts. We find that the polarizabilities for the interlayer excitons are substantially larger than the excitons in their monolayer counterparts. As an example, the interlayer exciton in hBN encapsulated MoS₂/WSe₂ has a polarizability of $\alpha_{\text{MoS}_2/\text{WSe}_2}^{(\kappa=4.9)} = 116 \times 10^{-18} \text{ eV(m/V)}^2$ [142] whereas in their single monolayer counterparts they are $\alpha_{\text{MoS}_2}^{(\kappa=4.9)} = 14.2 \times 10^{-18} \text{ eV(m/V)}^2$ and $\alpha_{\text{WSe}_2}^{(\kappa=4.9)} = 20.8 \times 10^{-18} \text{ eV(m/V)}^2$ [112]. The reason for this large difference is twofold. First, excitons in a bilayer structure experience more screening than in a monolayer structure. Second, interlayer excitons are separated by a vertical distance, which reduces the attractive Coulomb force. We mention in passing that the average dielectric constant of hBN was taken as $\kappa = 4.9$ in Paper C, rather than the ≈ 4.5 used in Papers E and G, as well as the hBN encapsulated results in Sec. 3.2.1. The

3.3. Exciton dissociation by static in-plane electric fields in bilayer structures

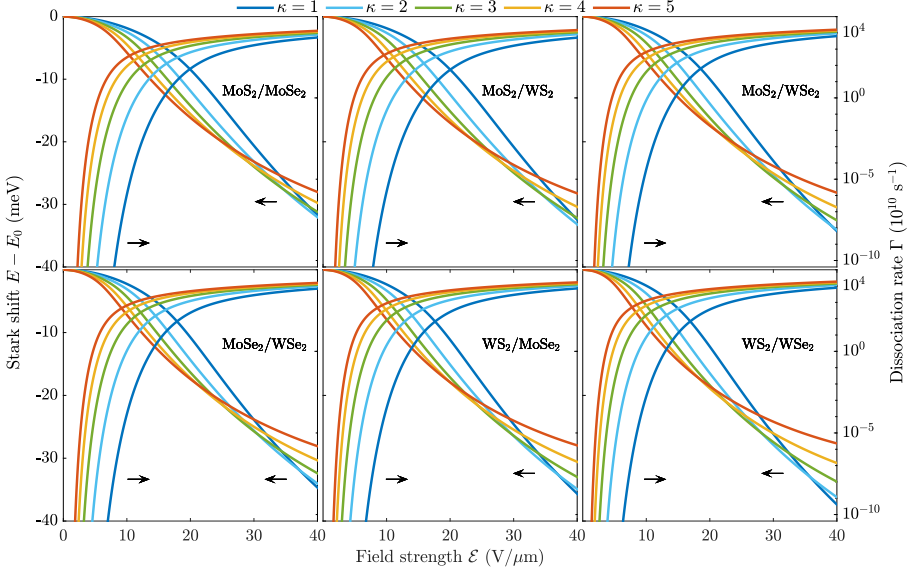


Fig. 3.10: Exciton Stark shifts (left axis) and dissociation rates (right axis) for interlayer excitons in six different bilayer structures in various dielectric environments. Reduced masses and screening lengths for the individual monolayers have been obtained from Olsen et al. [128]. The figure is from Paper C [258].

change to ≈ 4.5 was motivated by the experimental study performed by Goryca et al. [111] published around the same time.

Considering freely suspended MoS_2/WS_2 , the interlayer excitons have a dissociation rate of around $\Gamma \approx 1.7 \times 10^4 \text{ s}^{-1}$ already at $\mathcal{E} = 10 \text{ V}/\mu\text{m}$ [142]. The monolayer counterparts have $\Gamma \approx 5.3 \times 10^{-38} \text{ s}^{-1}$ and $\Gamma \approx 2.7 \times 10^{-33} \text{ s}^{-1}$ for monolayer MoS_2 and WS_2 , respectively, at this field strength [117]. This significant difference is due to the exponential dependence on binding energy for weak fields. Comparing now the dissociation rates for interlayer excitons in a bilayer structure to intralayer excitons in the same structure, we find $\Gamma \approx 2.1 \times 10^{-3} \text{ s}^{-1}$ and $\Gamma \approx 2.9 \times 10^4 \text{ s}^{-1}$ for $\mathcal{E} = 10 \text{ V}/\mu\text{m}$ in the top and bottom layer of MoS_2/WS_2 , respectively [142]. The large difference between these two rates can be traced back to the reduced masses, which are $\mu = 0.2513$ and $\mu = 0.1543$ in the top and bottom layers, respectively. The time it takes to dissociate these excitons with the given field may be approximated as $\tau = 1/\Gamma \approx 476 \text{ s}$ and $\tau \approx 3.5 \times 10^{-5} \text{ s}$, respectively. In their experiment, Hong et al. found that the holes of photoexcited excitons in the MoS_2 layer of this structure tunneled into the WS_2 layer within 50 fs [56]. This is significantly faster than the intralayer excitons may be dissociated, and the limiting factor for photocurrent generation at weak fields in such a structure is therefore expected to be the interlayer

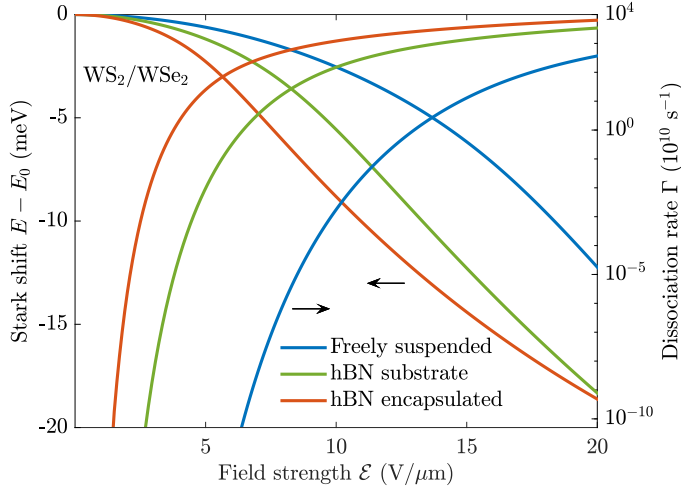


Fig. 3.11: Exciton Stark shifts (left axis) and dissociation rates (right axis) for interlayer excitons in WS_2/WSe_2 in three different dielectric surroundings. The figure is from Paper C [258].

dissociation rates.

Figure 3.10 suggests that both Stark shifts and dissociation rates can be tuned by carefully selecting the bilayer and substrate materials in the structure. This is very promising for device design and practical applications. As a final note, we show the technologically important case of hBN encapsulated WS_2/WSe_2 in Fig. 3.11. Here, the surroundings can again be seen to change the shifts and rates significantly.

3.4 THz induced exciton dissociation in TMD monolayers

So far we have discussed exciton dissociation induced by static in-plane electric fields. While many of the results are interesting, a significant downside to using static electric fields is that it requires making alterations to the sample. As mentioned, Massicotte et al. [116] used buried contacts in their sample to apply the electric field. This is by no means a trivial task to accomplish. On the other hand, if a THz pulse was used instead of a static electric field, then no alterations need to be made to the sample. This would therefore be a noninvasive method of inducing exciton dissociation. Estimating dissociation probabilities for these types of pulses was the aim of Paper G.

A schematic illustration of the setup can be seen in Fig. 3.12(a). Before the THz pulse is applied, the exciton may be found in its ground state. Once the THz pulse begins to reach its peak field strength, the exciton becomes polarized. The exciton is then in a superposition of bound and ionized states after the THz pulse subsides. That is, it has a certain probability of being dissociated or still being in a bound state. The actual pulse shape used in the simulations can be seen in Fig. 3.12(b). The black circles are the experimental THz pulse used in Ref. [122]. Pulses used in the present thesis are based on the shape of this pulse, in order to obtain realistic pulse shapes. For numerical convenience, and to make reproduction of the results easier, we fit the experimental pulse to a simple functional form (see Paper G). The fitted pulse may be seen as the red curve in Fig. 3.12(b).

The time-resolved dissociation probability, computed by the method in Sec. 2.4, can be seen in the left panel of Fig. 3.12(c). These results are for hBN encapsulated MoS_2 subjected to a THz pulse with a peak field strength of $37 \text{ V}/\mu\text{m}$. It is clear that almost all dissociation occurs in a very narrow time range close to the peak field strength. This is due to the exponential dependence on field strength, such that the contribution from the pulse tails is negligible. We furthermore see that the simulations based on the experimental and fitted pulses are in excellent agreement, hence the choice of said fitted pulse. It is furthermore observed that the ground-state depletion probability coincides with the dissociation probability after the pulse. This indicates that any transiently occupied excited states are completely ionized after the pulse.

Turning to the middle panel, we show the dissociation probability for three different peak field strengths as functions of the dielectric screening of the surrounding media. We again see the by now well-known exponential dependence. The inset shows the exciton binding energy for the relevant screening, and it can be seen to follow the same trend as the dissociation rates. The right panel

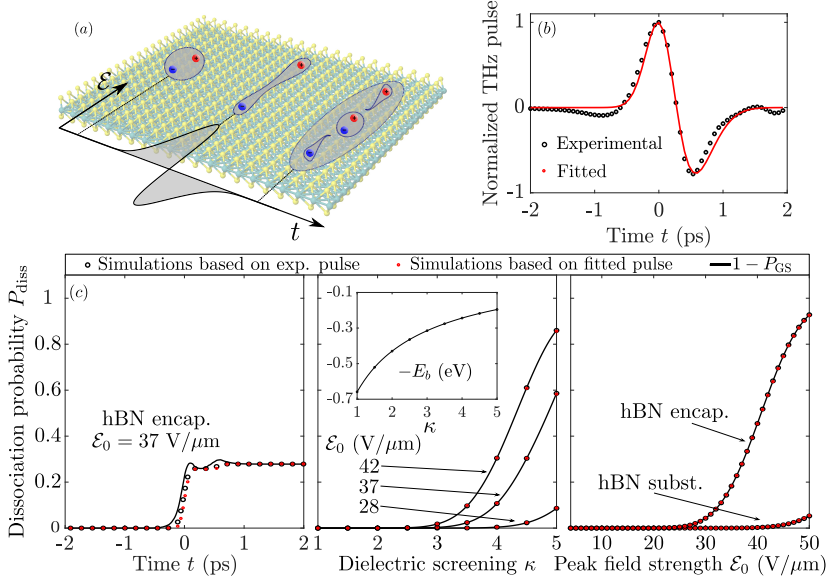


Fig. 3.12: (a) Schematic illustration of an exciton in a THz pulse. The initially bound exciton becomes polarized as a result of the pulse and is in a superposition of bound and ionized states as the pulse subsides. (b) The experimental pulse in Ref. [122] and the fitted pulse are shown as the black circles and red line, respectively. Figure (c) consists of three panels that summarize the results for a single non-interacting exciton in MoS₂ subjected to a THz pulse with the shape shown in (b). Here, the black and red circles correspond to simulations made with the experimental and fitted pulse, respectively. The solid black lines represent the ground-state depletion probability. (left) Time-resolved exciton dissociation probability during a THz pulse with a peak field strength of 37 V/ μm in hBN-encapsulated MoS₂. (middle) Exciton dissociation probabilities after the pulse has died out for three different field strengths as functions of the dielectric surroundings. The inset shows the corresponding binding energies. (right) Dissociation probabilities after the pulse has died out as functions of peak field strength for MoS₂ encapsulated by hBN as well as for MoS₂ on an hBN substrate. The results have been obtained using the experimental parameters in Ref. [111] (see Table 3.3). The figure is a reproduction of the figure from Paper G [259].

of Fig. 3.12(c) shows the dissociation probability for MoS₂ in two different dielectric surroundings as a function of peak field strength. Namely on an hBN substrate as well as hBN encapsulation. A significant difference in dissociation probability is observed. Even the largest peak field strength considered dissociates only a small fraction of the excitons in the substrate case. On the other hand, the probability of ionizing the exciton in hBN-encapsulated MoS₂ using the same pulse is almost unity.

In their experiment, the authors of Ref. [122] use a sapphire substrate for which they find a binding energy of about 240 meV [122]. They find a broadening of the exciton absorption peak of about 10.8 meV for a THz pulse with a peak field strength of 37 V/ μm . We are able to reproduce this binding energy in

our model by letting $\kappa \approx 4.1$ [259]. In this case, the middle panel of Fig. 3.12(c) indicates that around 14% of the excitons should be ionized. This is not a significant portion, and it therefore corroborates the conclusion reached by the authors of Ref. [122] that exciton dissociation does not contribute significantly to their results. We may estimate the contribution to the broadening from exciton dissociation by using the method for static electric fields. Computing the complex energy for a field strength of $37 \text{ V}/\mu\text{m}$, one finds a full width of around 0.6 meV [259], which is significantly less than the broadening found in the experiment. This further validates the assumption that the broadening is not caused by exciton dissociation in this particular case.

Note that the results of Fig. 3.12 should not be compared directly to the absorption measurements in Ref. [122]. The reason is that intricate interplay between excitons and free charge carriers is important in realistic semiconductors. This is not considered in Fig. 3.12, as we only wish to get an estimate of exciton dissociation probabilities here. Before we investigate this interplay, let us discuss the results for four well-known monolayer TMDs. Figure 3.13 shows the dissociation probabilities in (a) MoS_2 , (b) MoSe_2 , (c) WS_2 , and (d) WSe_2 as functions of peak field strength and dielectric surrounding. Panel (e) shows the exciton binding energy in these four materials in the relevant screening regions. The line color corresponds to the color of the chemical composition in panels (a)-(d). As expected, almost no dissociation occurs if either the field is too weak or the screening too low. As the field strength and screening increase, the dissociation probability increases rapidly. An interesting observation is that the tungsten materials have larger dissociation probabilities than the molybdenum based ones in the relevant regions for device components. This is caused by the lower exciton binding energies in the tungsten materials when using the parameters by Goryca et al. [111] (see Fig. 3.1). The dissociation probabilities follow what one would expect from the binding energies. Note that MoS_2 has a larger exciton binding energy than MoSe_2 for $\kappa \lesssim 2.5$, resulting in a crossing of the energy curves. This can be explained by the larger 2D polarizability of MoS_2 [111]. As the surrounding dielectric screening increases, however, the polarizability of the monolayers themselves become less important, and the larger reduced mass of the MoSe_2 exciton starts to dominate. This behavior can also be understood from the series expansion of the RK potential in Eq. (2.7). When κ becomes large, the leading term will be dominating, i.e. $V \sim 1/(\kappa r)$. Thus, the 2D polarizability (r_0) does no longer contribute significantly.

Let us now examine the impact of THz-induced dissociation on the carrier densities in a realistic semiconductor. To this end, we employ a model that takes into account the finite lifetime of excitons and free carriers, as well as the fact that free carriers may combine to form excitons (see Paper G for a more

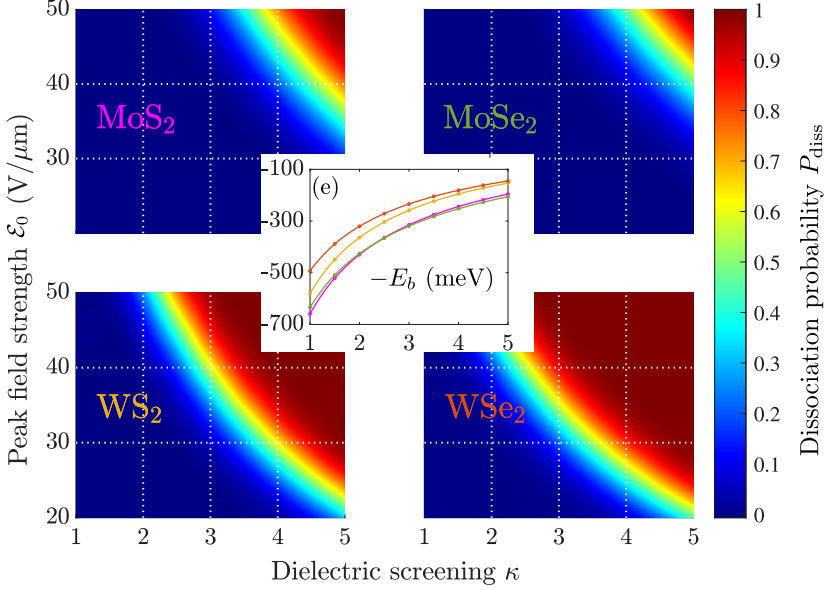


Fig. 3.13: Dissociation probability as a function of peak field strength and dielectric surroundings for the four TMDs (a) MoS₂, (b) MoSe₂, (c) WS₂, and (d) WSe₂. The exciton binding energies in the relevant screening are shown in panel (e), where the line color corresponds to a chemical composition in panels (a)-(d). The figure is a reproduction from the figure in Paper G [259].

detailed explanation). The time-resolved densities are shown in Fig. 3.14(a). The solid red and black curves show the exciton n_x and free carrier n densities, respectively, and with values indicated on the left axis. The dotted line shows the THz pulse with peak field strength 42 V/ μ m and duration $\tau = 2.1$ ps, and uses the right axis. The curves are shifted such that the peak field strength is reached at $t = 0$. Before the pulse runs through the TMD, the densities are in equilibrium at $n_x \approx 7 \times 10^{12} \text{ cm}^{-2}$ and $n \approx 3.5 \times 10^{10} \text{ cm}^{-2}$. A rapid increase in the free carrier density can be seen, and a peak of about $1.8 \times 10^{12} \text{ cm}^{-2}$ is observed when the pulse is close to its peak field strength. This is an increase by a factor of about 50. The densities quickly return to their equilibrium densities after the pulse subsides. Evidently, the densities are modified only when the THz pulse is present, in agreement with the results in Ref. [122]. These results indicate that THz pulses may be very useful for dynamically controlling carrier densities in TMDs, which is promising for applications such as THz modulators [260, 261]. Furthermore, it should be possible to measure exciton dissociation probabilities by correlating them to the free carrier absorption spectra.

The duration of the THz pulse discussed above is sufficiently long that an adiabatic calculation produced accurate results. This can be seen in Fig. 3.14,

3.4. THz induced exciton dissociation in TMD monolayers

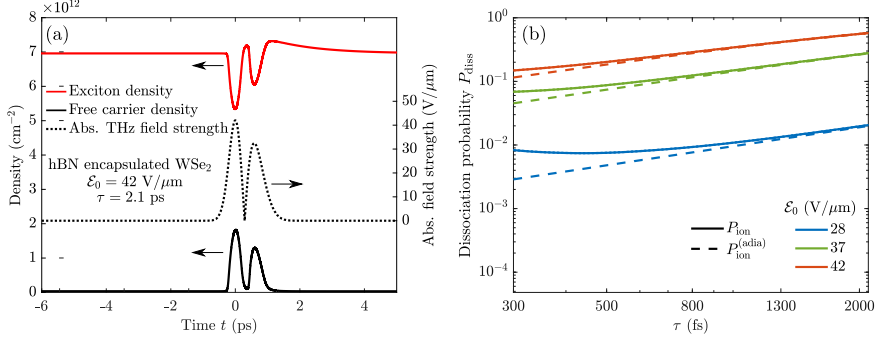


Fig. 3.14: (a) Exciton and free carrier densities in hBN-encapsulated WSe₂. The exciton n_x and free carrier n densities are shown as the red and black curve, respectively, and use the left axis. The THz pulse is shown as the dotted line and uses the right axis. (b) Dissociation probability as a function of pulse duration for different peak field strengths. The solid lines are computed by propagating the Wannier equation, while the dashed lines are an adiabatic approximation. The adiabatic probabilities are given by $P_{\text{ion}}^{(\text{adia})} = 1 - e^{-\tau\Gamma_1}$, where $\Gamma_1 = \{9.62, 154.24, 407.63\} \text{ ns}^{-1}$ for $\mathcal{E}_0 = \{28, 37, 42\} \text{ V}/\mu\text{m}$, respectively. The figure is a reproduction of the figure from Paper G [259].

where the pulse duration is varied. The solid and dashed lines correspond to the full numerical and adiabatic calculations (see Paper G for details), respectively. Different colors correspond to different peak field strengths. We find that the interaction ceases to be adiabatic as the pulse duration becomes sufficiently low. This is due to the rapid changes induced by shorter pulses.

Chapter 4

Conclusion

As a result of reduced screening, exciton binding energies in mono- and bilayer structures are significantly larger than in bulk semiconductors. While thermal agitation is typically sufficient to dissociate excitons in bulk semiconductors, excitons in few layer structures are stable even at room temperature. Efficient conversion of photons to electrical current in these structures therefore relies heavily on electric-field-induced dissociation. In the present thesis, field-induced dissociation of excitons in these types of structures has been studied. The monolayers that have been considered are phosphorene, as well as the four transition metal dichalcogenides (TMDs): MoS_2 , MoSe_2 , WS_2 , and WSe_2 . The bilayer structures considered are the combinations of these TMD monolayers that form a type-II band alignment. Dissociation induced by both static electric fields, as well as THz pulses has been analyzed for the TMD monolayers, whereas only static fields have been considered for phosphorene and bilayer structures.

Excitons in these structures have been modeled using the Wannier exciton model, in which the exciton states are solutions to an equation that is mathematically similar to the one describing the two-dimensional (2D) hydrogen atom. Dissociation by static fields has a particularly simple description, as the dissociating states may be associated with solutions of the time-independent Schrödinger equation. For THz pulses, on the other hand, a fully time-dependent theory must be used.

Focusing first on static fields, we have found that dissociation rates depend heavily on the strength of the applied field. This is particularly true for weak electric fields, where the dependence is shown to be exponential. For the technologically important cases of hBN encapsulated monolayer TMDs and phosphorene, this weak-field region corresponds to field strengths in the range

$\approx [0, 25] \text{ V}/\mu\text{m}$. As one would expect, excitons with large binding energies are more difficult to dissociate than weakly bound excitons. However, binding energies and field strengths alone do not uniquely define the dissociation rate. The reduced mass, substrate screening, and the 2D polarizability of the monolayer also play a role. This became particularly apparent when an analytical weak-field approximation was derived that included these parameters. This weak-field approximation was also extended to account for the anisotropic case of phosphorene, where a pronounced dependence on the direction of the applied field was found.

One of the goals in the present thesis was to find an efficient numerical method capable of computing these weak-field dissociation rates. This had proven difficult to do using the standard method of uniform complex scaling. This problem was only encountered recently for excitons, as dissociation rates at such weak fields had not been of interest earlier. The goal was reached with the implementation of exterior complex scaling in a finite element basis expansion of the wave function. This method has proven to be fruitful, and the majority of the results in the present thesis have been obtained using it.

The ground-state exciton in the bilayer structures analyzed is an interlayer exciton. That is, excitons in which the electron and hole reside in different layers. Field-induced dissociation of these types of excitons has been studied, and they are found to dissociate at faster rates than their monolayer counterparts, mostly due to the reduced binding energy. The exciton dynamics in these structures are exceptionally interesting, as photogenerated (intralayer) excitons in one of the two monolayers transform into interlayer excitons long before they are dissociated by the electric field. It is therefore dissociation of interlayer excitons that is expected to be the limiting factor in photocurrent generation in such structures.

Turning to dissociation induced by THz pulses, we find a strong dependence on the peak field strength of the pulse. This is expected due to the exponential dependence found on field strength for static fields. As a result, nearly all dissociation occurs around a narrow temporal region close to the peak field strength. The shape of the THz pulse used was motivated by a recent experiment, and it is therefore a realistic pulse. It was shown that such a pulse was capable of dissociating a substantial part of the excitons in monolayer TMDs, and these types of pulses are therefore promising for inducing exciton dissociation.

References

- [1] R. E. Peierls. *Ann. I. H. Poincaré* **5**, 177 (1935).
- [2] L. D. Landau. *Phys. Z. Sowjetunion* **11**, 26 (1937).
- [3] N. D. Mermin. *Phys. Rev.* **176**, 250 (1968).
- [4] A. K. Geim and K. S. Novoselov. *Nat. Mater.* **6**, 183 (2007).
- [5] K. S. Novoselov, A. K. Geim, S. V. Morozov, D. Jiang, Y. Zhang, S. V. Dubonos, I. V. Grigorieva and A. A. Firsov. *Science* **306**, 666 (2004).
- [6] K. S. Novoselov, D. Jiang, F. Schedin, T. J. Booth, V. V. Khotkevich, S. V. Morozov and A. K. Geim. *Proc. Natl. Acad. Sci.* **102**, 10451 (2005).
- [7] K. S. Novoselov, V. I. Fal'Ko, L. Colombo, P. R. Gellert, M. G. Schwab and K. Kim. *Nature* **490**, 192 (2012).
- [8] C. Berger *et al.* *J. Phys. Chem. B* **108**, 19912 (2004).
- [9] X. Du, I. Skachko, A. Barker and E. Y. Andrei. *Nat. Nanotechnol.* **3**, 491 (2008).
- [10] Y. M. Lin, K. A. Jenkins, V. G. Alberto, J. P. Small, D. B. Farmer and P. Avouris. *Nano Lett.* **9**, 422 (2009).
- [11] Y. M. Lin, C. Dimitrakopoulos, K. A. Jenkins, D. B. Farmer, H. Y. Chiu, A. Grill and P. Avouris. *Science* **327**, 662 (2010).
- [12] S. V. Morozov, K. S. Novoselov, M. I. Katsnelson, F. Schedin, D. C. Elias, J. A. Jaszczak and A. K. Geim. *Phys. Rev. Lett.* **100**, 016602 (2008).
- [13] H. P. Boehm, A. Clauss, G. O. Fischer and U. Hofmann. *Z. Naturforsch.* **17**, 150 (1962).
- [14] H. P. Boehm, A. Clauss, G. O. Fischer and U. Hofmann. *Z. Anorg. Allg.* **316**, 119 (1962).

References

- [15] T. G. Pedersen, C. Flindt, J. Pedersen, N. A. Mortensen, A. P. Jauho and K. Pedersen. *Phys. Rev. Lett.* **100**, 136804 (2008).
- [16] T. G. Pedersen, C. Flindt, J. Pedersen, A. P. Jauho, N. A. Mortensen and K. Pedersen. *Phys. Rev. B* **77**, 245431 (2008).
- [17] T. G. Pedersen, A. P. Jauho and K. Pedersen. *Phys. Rev. B* **79**, 113406 (2009).
- [18] E. V. Castro, K. S. Novoselov, S. V. Morozov, N. M. Peres, J. M. Dos Santos, J. Nilsson, F. Guinea, A. K. Geim and A. H. Neto. *Phys. Rev. Lett.* **99**, 216802 (2007).
- [19] M. Xu, T. Liang, M. Shi and H. Chen. *Chem. Rev.* **113**, 3766 (2013).
- [20] R. Mas-Ballesté, C. Gómez-Navarro, J. Gómez-Herrero and F. Zamora. *Nanoscale* **3**, 20 (2011).
- [21] J. A. Wilson and A. D. Yoffe. *Adv. Phys.* **18**, 193 (1969).
- [22] M. Chhowalla, H. S. Shin, G. Eda, L.-J. Li, K. P. Loh and H. Zhang. *Nat. Chem.* **5**, 263 (2013).
- [23] S. Lebègue and O. Eriksson. *Phys. Rev. B* **79**, 115409 (2009).
- [24] K. F. Mak, C. Lee, J. Hone, J. Shan and T. F. Heinz. *Phys. Rev. Lett.* **105**, 136805 (2010).
- [25] A. Splendiani, L. Sun, Y. Zhang, T. Li, J. Kim, C.-Y. Chim, G. Galli and F. Wang. *Nano Lett.* **10**, 1271 (2010).
- [26] C. Lee, H. Yan, L. E. Brus, T. F. Heinz, J. Hone and S. Ryu. *ACS Nano* **4**, 2695 (2010).
- [27] Q. H. Wang, K. Kalantar-Zadeh, A. Kis, J. N. Coleman and M. S. Strano. *Nat. Nanotechnol.* **7**, 699 (2012).
- [28] D. Xiao, G. B. Liu, W. Feng, X. Xu and W. Yao. *Phys. Rev. Lett.* **108**, 196802 (2012).
- [29] H. Zeng *et al.* *Sci. Rep.* **3**, 4908 (2013).
- [30] A. Arora, K. Nogajewski, M. Molas, M. Koperski and M. Potemski. *Nanoscale* **7**, 20769 (2015).
- [31] G. Frey and S. Elani. *Phys. Rev. B* **57**, 6666 (1998).

References

- [32] C. Gong, H. Zhang, W. Wang, L. Colombo, R. M. Wallace and K. Cho. *Appl. Phys. Lett.* **103**, 053513 (2013).
- [33] D. Jariwala, V. K. Sangwan, L. J. Lauhon, T. J. Marks and M. C. Hersam. *ACS Nano* **8**, 1102 (2014).
- [34] L. Kou, Y. Ma, S. C. Smith and C. Chen. *J. Phys. Chem. Lett.* **6**, 1509 (2015).
- [35] A. Carvalho, M. Wang, X. Zhu, A. S. Rodin, H. Su and A. H. Castro Neto. *Nat. Rev. Mater.* **1**, 16061 (2016).
- [36] J. S. Ross *et al.* *Nat. Nanotechnol.* **9**, 268 (2014).
- [37] R. S. Sundaram, M. Engel, A. Lombardo, R. Krupke, A. C. Ferrari and M. Steiner. *Nano Lett.* **13**, 1416 (2013).
- [38] Y. Ye, Z. Ye, M. Gharghi, H. Zhu, M. Zhao, Y. Wang, X. Yin and X. Zhang. *Appl. Phys. Lett.* **104**, 193508 (2014).
- [39] B. W. Baugher, H. O. Churchill, Y. Yang and P. Jarillo-Herrero. *Nat. Nanotechnol.* **9**, 262 (2014).
- [40] A. Pospischil, M. M. Furchi and T. Mueller. *Nat. Nanotechnol.* **9**, 257 (2014).
- [41] C. H. Lee *et al.* *Nat. Nanotechnol.* **9**, 676 (2014).
- [42] F. Withers *et al.* *Nat. Mater.* **14**, 301 (2015).
- [43] F. Withers *et al.* *Nano Lett.* **15**, 8223 (2015).
- [44] Y. J. Zhang, T. Oka, R. Suzuki, J. T. Ye and Y. Iwasa. *Science* **344**, 725 (2014).
- [45] M. Massicotte, P. Schmidt, F. Vialla, K. G. Schädler, A. Reserbat-Plantey, K. Watanabe, T. Taniguchi, K. J. Tielrooij and F. H. Koppens. *Nat. Nanotechnol.* **11**, 42–46 (2016).
- [46] L. Britnell *et al.* *Science* **335**, 947 (2012).
- [47] W. J. Yu, Y. Liu, H. Zhou, A. Yin, Z. Li, Y. Huang and X. Duan. *Nat. Nanotechnol.* **8**, 952 (2013).
- [48] M. S. Choi, D. Qu, D. Lee, X. Liu, K. Watanabe, T. Taniguchi and W. J. Yoo. *ACS Nano* **8**, 9332 (2014).

References

- [49] Y. Li, C. Y. Xu, J. Y. Wang and L. Zhen. *Sci. Rep.* **4**, 7186 (2014).
- [50] W. Zhang *et al.* *Sci. Rep.* **4**, 3826 (2014).
- [51] S. Wu *et al.* *Nature* **520**, 69 (2015).
- [52] Y. Ye, Z. J. Wong, X. Lu, X. Ni, H. Zhu, X. Chen, Y. Wang and X. Zhang. *Nat. Photonics* **9**, 733 (2015).
- [53] O. Salehzadeh, M. Djavid, N. H. Tran, I. Shih and Z. Mi. *Nano Lett.* **15**, 5302 (2015).
- [54] S. Wi, H. Kim, M. Chen, H. Nam, L. J. Guo, E. Meyhofer and X. Liang. *ACS Nano* **8**, 5270 (2014).
- [55] M. Bernardi, M. Palummo and J. C. Grossman. *Nano Lett.* **13**, 3664 (2013).
- [56] X. Hong, J. Kim, S.-F. Shi, Y. Zhang, C. Jin, Y. Sun, S. Tongay, J. Wu, Y. Zhang and F. Wang. *Nat. Nanotechnol.* **9**, 682 (2014).
- [57] H. Liu, A. T. Neal, Z. Zhu, Z. Luo, X. Xu, D. Tománek and P. D. Ye. *ACS Nano* **8**, 4033 (2014).
- [58] L. Li, Y. Yu, G. J. Ye, Q. Ge, X. Ou, H. Wu, D. Feng, X. H. Chen and Y. Zhang. *Nat. Nanotechnol.* **9**, 372 (2014).
- [59] S. P. Koenig, R. A. Doganov, H. Schmidt, A. H. Castro Neto and B. Özyilmaz. *Appl. Phys. Lett.* **104**, 103106 (2014).
- [60] A. Castellanos-Gomez *et al.* *2D Mater.* **1**, 025001 (2014).
- [61] A. Castellanos-Gomez. *J. Phys. Chem. Lett.* **6**, 4280 (2015).
- [62] F. Xia, H. Wang and Y. Jia. *Nat. Commun.* **5**, 4458 (2014).
- [63] R. W. Keyes. *Phys. Rev.* **92**, 580 (1953).
- [64] H. Asahina and A. Morita. *J. Phys. Condens. Matter* **17**, 1839 (1984).
- [65] A. Morita. *Appl. Phys. A* **39**, 227 (1986).
- [66] J. Qiao, X. Kong, Z.-X. Hu, F. Yang and W. Ji. *Nat. Commun.* **5**, 4475 (2014).
- [67] V. Tran, R. Soklaski, Y. Liang and L. Yang. *Phys. Rev. B* **89**, 235319 (2014).

References

- [68] X. Wang, A. M. Jones, K. L. Seyler, V. Tran, Y. Jia, H. Zhao, H. Wang, L. Yang, X. Xu and F. Xia. *Nat. Nanotechnol.* **10**, 517 (2015).
- [69] R. Fei and L. Yang. *Nano Lett.* **14**, 2884 (2014).
- [70] Y. Xu, J. Dai and X. C. Zeng. *J. Phys. Chem. Lett.* **6**, 1996 (2015).
- [71] X. Y. Zhou, R. Zhang, J. P. Sun, Y. L. Zou, D. Zhang, W. K. Lou, F. Cheng, G. H. Zhou, F. Zhai and K. Chang. *Sci. Rep.* **5**, 12295 (2015).
- [72] X. Zhou, W. K. Lou, F. Zhai and K. Chang. *Phys. Rev. B* **92**, 165405 (2015).
- [73] X. Zhou, W. K. Lou, D. Zhang, F. Cheng, G. Zhou and K. Chang. *Phys. Rev. B* **95**, 045408 (2017).
- [74] Z.-Y. Ong, Y. Cai, G. Zhang and Y.-W. Zhang. *J. Phys. Chem. C* **118**, 25272 (2014).
- [75] A. Jain and A. J. H. McGaughey. *Sci. Rep.* **5**, 8501 (2015).
- [76] Q. Wei and X. Peng. *Appl. Phys. Lett.* **104**, 251915 (2014).
- [77] F. Xia, H. Wang, D. Xiao, M. Dubey and A. Ramasubramaniam. *Nat. Photon.* **8**, 899 (2014).
- [78] A. K. Geim and I. V. Grigorieva. *Nature* **499**, 419 (2013).
- [79] L. A. Ponomarenko *et al.* *Nat. Phys.* **7**, 958 (2011).
- [80] S. J. Haigh, A. Gholinia, R. Jalil, S. Romani, L. Britnell, D. C. Elias, K. S. Novoselov, L. A. Ponomarenko, A. K. Geim and R. Gorbachev. *Nat. Mater.* **11**, 764 (2012).
- [81] C. Dean, A. F. Young, L. Wang, I. Meric, G. H. Lee, K. Watanabe, T. Taniguchi, K. Shepard, P. Kim and J. Hone. *Solid State Commun.* **152**, 1275 (2012).
- [82] R. V. Gorbachev *et al.* *Nat. Phys.* **8**, 896–901 (2012).
- [83] T. Georgiou *et al.* *Nat. Nanotechnol.* **8**, 100 (2013).
- [84] M. Osada and T. Sasaki. *Adv. Mater.* **24**, 210 (2012).
- [85] S. Z. Butler *et al.* *ACS Nano* **7**, 2898 (2013).

References

- [86] G. Fiori, F. Bonaccorso, G. Iannaccone, T. Palacios, D. Neumaier, A. Seabaugh, S. K. Banerjee and L. Colombo. *Nat. Nanotechnol.* **9**, 768 (2014).
- [87] J. Frenkel. *Phys. Rev.* **37**, 17 (1931).
- [88] J. Frenkel. *Phys. Rev.* **37**, 1276 (1931).
- [89] G. H. Wannier. *Phys. Rev.* **52**, 191 (1937).
- [90] N. F. Mott. *Trans. Faraday Soc.* **34**, 500–506 (1938).
- [91] V. V. Rumyantsev and K. V. Gumennyk. *J. Photonic Mater. Technol.* **1**, 1 (2015).
- [92] E. Gross and M. Yacobson. *Dokl. Akad. Nauk. SSSR* **102**, 485 (1955).
- [93] E. F. Gross. *Sov. Phys. Usp.* **5**, 195 (1962).
- [94] E. E. Salpeter and H. A. Bethe. *Phys. Rev.* **84**, 1232–1242 (1951).
- [95] L. J. Sham and T. M. Rice. *Phys. Rev.* **144**, 708–714 (1966).
- [96] M. Rohlfing and S. G. Louie. *Phys. Rev. Lett.* **81**, 2312–2315 (1998).
- [97] L. Hedin. *Phys. Rev.* **139**, A796 (1965).
- [98] C. D. Spataru, S. Ismail-Beigi, L. X. Benedict and S. G. Louie. *Phys. Rev. Lett.* **92**, 077402 (2004).
- [99] M. M. Ugeda *et al.* *Nat. Mater.* **13**, 1091 (2014).
- [100] A. R. Goi, A. Cantarero, K. Syassen and M. Cardona. *Phys. Rev. B* **41**, 10111 (1990).
- [101] A. Mang, K. Reimann, S. Rübenacke and M. Steube. *Phys. Rev. B* **53**, 16283 (1996).
- [102] W. Shan, B. Little, A. Fischer, J. Song and B. Goldenberg. *Phys. Rev. B* **54**, 16369 (1996).
- [103] M. Dvorak, S. H. Wei and Z. Wu. *Phys. Rev. Lett.* **110**, 016402 (2013).
- [104] A. Ramasubramaniam. *Phys. Rev. B* **86**, 115409 (2012).
- [105] S. Latini, T. Olsen and K. S. Thygesen. *Phys. Rev. B* **92**, 245123 (2015).
- [106] T. C. Berkelbach, M. S. Hybertsen and D. R. Reichman. *Phys. Rev. B* **88**, 045318 (2013).

References

- [107] D. Y. Qiu, da F. H. Jornada and S. G. Louie. *Phys. Rev. Lett.* **111**, 216805 (2013).
- [108] T. Galvani, F. Paleari, H. P. Miranda, A. Molina-Sánchez, L. Wirtz, S. Latil, H. Amara and F. Ducastelle. *Phys. Rev. B* **94**, 125303 (2016).
- [109] A. V. Stier, N. P. Wilson, G. Clark, X. Xu and S. A. Crooker. *Nano Lett.* **16**, 7054 (2016).
- [110] E. Liu, J. Van Baren, T. Taniguchi, K. Watanabe, Y. C. Chang and C. H. Lui. *Phys. Rev. B* **99**, 205420 (2019).
- [111] M. Goryca *et al.* *Nat. Commun.* **10**, 4172 (2019).
- [112] T. G. Pedersen. *Phys. Rev. B* **94**, 125424 (2016).
- [113] B. Scharf, T. Frank, M. Gmitra, J. Fabian, I. Žutić and V. Perebeinos. *Phys. Rev. B* **94**, 245434 (2016).
- [114] S. Haastrup, S. Latini, K. Bolotin and K. S. Thygesen. *Phys. Rev. B* **94**, 041401(R) (2016).
- [115] T. G. Pedersen, S. Latini, K. S. Thygesen, H. Mera and B. K. Nikolić. *New J. Phys.* **18**, 073043 (2016).
- [116] M. Massicotte *et al.* *Nat. Commun.* **9**, 1633 (2018).
- [117] H. C. Kamban and T. G. Pedersen. *Phys. Rev. B* **100**, 045307 (2019).
- [118] V. Perebeinos and P. Avouris. *Nano Lett.* **7**, 609–613 (2007).
- [119] P. Merkl *et al.* *Nat. Mater.* **18**, 691 (2019).
- [120] L. S. R. Cavalcante, da D. R. Costa, G. A. Farias, D. R. Reichman and A. Chaves. *Phys. Rev. B* **98**, 245309 (2018).
- [121] A. Chaves, T. Low, P. Avouris, D. Çakır and F. M. Peeters. *Phys. Rev. B* **91**, 155311 (2015).
- [122] J. Shi *et al.* *Nano Lett.* **20**, 5214 (2020).
- [123] G. Strinati. *Phys. Rev. B* **29**, 5718 (1984).
- [124] G. Onida, L. Reining and A. Rubio. *Rev. Mod. Phys.* **74**, 601 (2002).
- [125] H. Haug and S. W. Koch. *Quantum Theory of the Optical and Electronic Properties of Semiconductors* (World Scientific, Singapore, 2004), 4 edn.

References

- [126] P. Cudazzo, C. Attaccalite, I. V. Tokatly and A. Rubio. *Phys. Rev. Lett.* **104**, 226804 (2010).
- [127] P. Cudazzo, I. V. Tokatly and A. Rubio. *Phys. Rev. B* **84**, 085406 (2011).
- [128] T. Olsen, S. Latini, F. Rasmussen and K. S. Thygesen. *Phys. Rev. Lett.* **116**, 056401 (2016).
- [129] J. Have, G. Catarina, T. G. Pedersen and N. M. Peres. *Phys. Rev. B* **99**, 035416 (2019).
- [130] K. Andersen, S. Latini and K. S. Thygesen. *Nano Lett.* **15**, 4616 (2015).
- [131] F. L. Lederman and J. D. Dow. *Phys. Rev. B* **13**, 1633 (1976).
- [132] N. S. Rytova. *Moscow Univ. Phys. Bull.* **22**, 18 (1967).
- [133] L. V. Keldysh. *JETP Lett.* **29**, 658 (1979).
- [134] M. L. Trolle, T. G. Pedersen and V. Vénard. *Sci. Rep.* **7**, 39844 (2017).
- [135] M. Abramowitz and I. Stegun (eds.) *Handbook of Mathematical Functions, With Formulas, Graphs, and Mathematical Tables* (Dover, New York, 1972).
- [136] X. L. Yang, S. H. Guo, F. T. Chan, K. W. Wong and W. Y. Ching. *Phys. Rev. A* **43**, 1186 (1991).
- [137] S. Cha, J. H. Sung, S. Sim, J. Park, H. Heo, M. H. Jo and H. Choi. *Nat. Commun.* **7**, 10768 (2016).
- [138] C. Poellmann, P. Steinleitner, U. Leierseder, P. Nagler, G. Plechinger, M. Porer, R. Bratschitsch, C. Schüller, T. Korn and R. Huber. *Nat. Mater.* **14**, 889 (2015).
- [139] P. Steinleitner, P. Merkl, P. Nagler, J. Mornhinweg, C. Schüller, T. Korn, A. Chernikov and R. Huber. *Nano Lett.* **17**, 1455 (2017).
- [140] L. D. Landau and L. M. Lifshitz. *Quantum Mechanics: Non-Relativistic Theory* (Pergamon Press, Oxford, England, 1989), 3 edn.
- [141] D. G. Parfitt and M. E. Portnoi. *J. Math. Phys.* **43**, 4681 (2002).
- [142] H. C. Kamban and T. G. Pedersen. *Sci. Rep.* **10**, 5537 (2020).
- [143] H. Chen *et al.* *Nat. Commun.* **7**, 12512 (2016).

References

- [144] B. Miller, A. Steinhoff, B. Pano, J. Klein, F. Jahnke, A. Holleitner and U. Wurstbauer. *Nano Lett.* **17**, 5229 (2017).
- [145] J. Kunstmann *et al.* *Nat. Phys.* **14**, 801 (2018).
- [146] N. A. Asriyan, I. L. Kurbakov, A. K. Fedorov and Y. E. Lozovik. *Phys. Rev. B* **99**, 085108 (2019).
- [147] M. A. Semina. *Phys. Solid State* **61**, 2218 (2019).
- [148] M. M. Fogler, L. V. Butov and K. S. Novoselov. *Nat. Commun.* **5**, 4555 (2014).
- [149] P. Rivera *et al.* *Nat. Commun.* **6**, 6242 (2015).
- [150] P. Nagler *et al.* *2D Mater.* **4**, 025112 (2017).
- [151] C. Jin *et al.* *Science* **360**, 893 (2018).
- [152] O. L. Berman and R. Y. Kezerashvili. *Phys. Rev. B* **93**, 245410 (2016).
- [153] O. L. Berman and R. Y. Kezerashvili. *Phys. Rev. B* **96**, 094502 (2017).
- [154] M. N. Brunetti, O. L. Berman and R. Y. Kezerashvili. *J. Phys. Condens. Matter* **30**, 225001 (2018).
- [155] M. Van Der Donck and F. M. Peeters. *Phys. Rev. B* **98**, 115104 (2018).
- [156] A. Laturia, de M. L. Put and W. G. Vandenberghe. *NPJ 2D Mater. Appl.* **2**, 6 (2018).
- [157] J. He, K. Hummer and C. Franchini. *Phys. Rev. B* **89**, 075409 (2014).
- [158] L. Liang, J. Wang, W. Lin, B. G. Sumpter, V. Meunier and M. Pan. *Nano Lett.* **14**, 6400 (2014).
- [159] S. Zhang *et al.* *ACS Nano* **8**, 9590 (2014).
- [160] P. Li and I. Appelbaum. *Phys. Rev. B* **90**, 115439 (2014).
- [161] D. Çakır, C. Sevik and F. M. Peeters. *Phys. Rev. B* **92**, 165406 (2015).
- [162] Z. Dai *et al.* *Phys. Rev. Mater.* **1**, 074003 (2017).
- [163] A. N. Rudenko and M. I. Katsnelson. *Phys. Rev. B* **89**, 201408 (2014).
- [164] Y. Li, S. Yang and J. Li. *J. Phys. Chem. C* **118**, 23970 (2014).
- [165] Y. Du, C. Ouyang, S. Shi and M. Lei. *J. Appl. Phys.* **107**, 093718 (2010).

References

- [166] A. S. Rodin, A. Carvalho and A. H. Castro Neto. *Phys. Rev. B* **90**, 075429 (2014).
- [167] R. J. Hunt, M. Szyniszewski, G. I. Prayogo, R. Maezono and N. D. Drummond. *Phys. Rev. B* **98**, 075122 (2018).
- [168] J. C. Henriques and N. M. Peres. *Phys. Rev. B* **101**, 035406 (2020).
- [169] J. H. Choi, P. Cui, H. Lan and Z. Zhang. *Phys. Rev. Lett.* **115**, 066403 (2015).
- [170] J. Zhang, H. J. Liu, L. Cheng, J. Wei, J. H. Liang, D. D. Fan, J. Shi, X. F. Tang and Q. J. Zhang. *Sci. Rep.* **4**, 6452 (2014).
- [171] H. Guo, N. Lu, J. Dai, X. Wu and X. C. Zeng. *J. Phys. Chem. C* **118**, 14051 (2014).
- [172] W. Li, G. Zhang and Y. W. Zhang. *J. Phys. Chem. C* **118**, 22368 (2014).
- [173] C. Li, Z. Xie, Z. Chen, N. Cheng, J. Wang and G. Zhu. *Materials* **11**, 304 (2018).
- [174] X. Peng, Q. Wei and A. Copple. *Phys. Rev. B* **90**, 085402 (2014).
- [175] T. Yamabe, A. Tachibana and H. J. Silverstone. *Phys. Rev. A* **16**, 877 (1977).
- [176] R. J. Damburg and V. V. Kolosov. *J. Phys. B At. Mol. Phys.* **11**, 1921 (1978).
- [177] H. J. Silverstone, E. Harrell and C. Grot. *Phys. Rev. A* **24**, 1925 (1981).
- [178] V. H. Trinh, O. I. Tolstikhin, L. B. Madsen and T. Morishita. *Phys. Rev. A* **87**, 043426 (2013).
- [179] H. Mera, T. G. Pedersen and B. K. Nikolić. *Phys. Rev. Lett.* **115**, 143001 (2015).
- [180] K. Tanaka, M. Kobashi, T. Shichiri, T. Yamabe, D. M. Silver and H. J. Silverstone. *Phys. Rev. B* **35**, 2513 (1987).
- [181] T. G. Pedersen, H. Mera and B. K. Nikolić. *Phys. Rev. A* **93**, 013409 (2016).
- [182] H. Shi, R. Yan, S. Bertolazzi, J. Brivio, B. Gao, A. Kis, D. Jena, H. G. Xing and L. Huang. *ACS Nano* **7**, 1072 (2013).

References

- [183] D. Sun, Y. Rao, G. A. Reider, G. Chen, Y. You, L. Brézin, A. R. Harutyunyan and T. F. Heinz. *Nano Lett.* **14**, 5625 (2014).
- [184] S. Mouri, Y. Miyauchi, M. Toh, W. Zhao, G. Eda and K. Matsuda. *Phys. Rev. B* **90**, 155449 (2014).
- [185] A. J. Siegert. *Phys. Rev.* **56**, 750 (1939).
- [186] N. Hatano, K. Sasada, H. Nakamura and T. Petrosky. *Prog. Theor. Phys.* **119**, 187 (2008).
- [187] Nimrod Moiseyev. *Non-Hermitian Quantum Mechanics* (Cambridge University Press, Cambridge, 2011).
- [188] G. Gamow. *Z. Phys.* **51**, 204 (1928).
- [189] J. P. Dahl. *Introduction to the Quantum World of Atoms and Molecules* (World Scientific, Singapore, 2001).
- [190] J. N. Bardsley. *Int. J. Quantum Chem.* **14**, 343 (1978).
- [191] W. P. Reinhardt. *Ann. Rev. Phys. Chem.* **33**, 223 (1982).
- [192] B. R. Junker. *Adv. At. Mol. Phys.* **18**, 207 (1982).
- [193] E. Balslev and J. M. Combes. *Commun. Math. Phys.* **22**, 280 (1971).
- [194] J. Aguilar and J. M. Combes. *Commun. Math. Phys.* **22**, 269–279 (1971).
- [195] B. Simon. *Phys. Lett. A* **36**, 23 (1971).
- [196] B. Simon. *Commun. Math. Phys.* **27**, 1–9 (1972).
- [197] B. Simon. *Ann. Math.* **97**, 247–274 (1973).
- [198] Y. K. Ho. *Phys. Rep.* **99**, 1–68 (1983).
- [199] M. Reed and B. Simon. *Methods of Modern Mathematical Physics IV* (Academic Press, New York, 1982).
- [200] C. Cerjan, R. Hedges, C. Holt, W. P. Reinhardt, K. Scheibner and J. J. Wendoloski. *Int. J. Quantum Chem.* **14**, 393 (1978).
- [201] J. E. Avron and I. W. Herbst. *Commun. Math. Phys.* **52**, 239 (1977).
- [202] I. W. Herbst and B. Simon. *Phys. Rev. Lett.* **41**, 67–69 (1978).
- [203] J. Bengtsson, E. Lindroth and S. Selstø. *Phys. Rev. A* **78**, 032502 (2008).

References

- [204] N. Moiseyev, P. R. Certain and F. Weinhold. *Mol. Phys.* **36**, 1613 (1978).
- [205] N. Moiseyev. *Phys. Rep.* **302**, 202 (1998).
- [206] I. Gilary, A. Fleischer and N. Moiseyev. *Phys. Rev. A* **72**, 012117 (2005).
- [207] A. Fleischer and N. Moiseyev. *Phys. Rev. A* **72**, 032103 (2005).
- [208] I. Gilary, P. R. Kaprálová-Žd'ánská and N. Moiseyev. *Phys. Rev. A* **74**, 052505 (2006).
- [209] A. Maquet, S. I. Chu and W. P. Reinhardt. *Phys. Rev. A* **27**, 2946 (1983).
- [210] A. Scrinzi. *Phys. Rev. A* **61**, 041402(R) (2000).
- [211] I. A. Ivanov and Y. K. Ho. *Phys. Rev. A* **69**, 023407 (2004).
- [212] B. Gyarmati and T. Vertse. *Nucl. Physics, Sect. A* **160**, 523 (1971).
- [213] C. A. Nicolaides and D. R. Beck. *Phys. Lett. A* **65**, 11 (1978).
- [214] B. Simon. *Phys. Lett. A* **71**, 211 (1979).
- [215] C. W. McCurdy, C. K. Stroud and M. K. Wisinski. *Phys. Rev. A* **43**, 5980 (1991).
- [216] F. He, C. Ruiz and A. Becker. *Phys. Rev. A* **75**, 053407 (2007).
- [217] L. Tao, W. Vanroose, B. Reps, T. N. Rescigno and C. W. McCurdy. *Phys. Rev. A* **80**, 063419 (2009).
- [218] A. Scrinzi. *Phys. Rev. A* **81**, 053845 (2010).
- [219] C. W. McCurdy, T. N. Rescigno and D. Byrum. *Phys. Rev. A* **56**, 1958 (1997).
- [220] T. N. Rescigno, M. Baertschy, D. Byrum and C. W. McCurdy. *Phys. Rev. A* **55**, 4253 (1997).
- [221] T. N. Rescigno, M. Baertschy, W. A. Isaacs and C. W. McCurdy. *Science* **286**, 2474 (1999).
- [222] C. W. McCurdy, M. Baertschy and T. N. Rescigno. *J. Phys. B: At. Mol. Opt. Phys.* **37**, R137 (2004).
- [223] T. N. Rescigno and C. W. McCurdy. *Phys. Rev. A* **62**, 032706 (2000).
- [224] D. A. Horner, F. Morales, T. N. Rescigno, F. Martín and C. W. McCurdy. *Phys. Rev. A* **76**, 030701(R) (2007).

References

- [225] W. Vanroose, F. Martín, T. N. Rescigno and C. W. McCurdy. *Science* **310**, 1787 (2005).
- [226] W. Vanroose, D. A. Horner, F. Martín, T. N. Rescigno and C. W. McCurdy. *Phys. Rev. A* **74**, 052702 (2006).
- [227] D. A. Horner, C. W. McCurdy and T. N. Rescigno. *Phys. Rev. A* **78**, 043416 (2008).
- [228] C. A. Nicolaides, H. J. Gotsis, M. Chrysos and Y. Komninos. *Chem. Phys. Lett.* **168**, 570 (1990).
- [229] A. Scrinzi and N. Elander. *J. Chem. Phys.* **98**, 3866 (1993).
- [230] M. Stein, C. Lammers, J. T. Steiner, P. H. Richter, S. W. Koch, M. Koch and M. Kira. *J. Phys. B: At. Mol. Opt. Phys.* **51**, 154001 (2018).
- [231] Y. Murotani, M. Takayama, F. Sekiguchi, C. Kim, H. Akiyama and R. Shimano. *J. Phys. D: Appl. Phys.* **51**, 114001 (2018).
- [232] B. Ewers, N. S. Köster, R. Woscholski, M. Koch, S. Chatterjee, G. Khitrova, H. M. Gibbs, A. C. Klettke, M. Kira and S. W. Koch. *Phys. Rev. B* **85**, 075307 (2012).
- [233] M. J. Drexler, R. Woscholski, S. Lippert, W. Stolz, A. Rahimi-Iman and M. Koch. *Phys. Rev. B* **90**, 195304 (2014).
- [234] R. R. Jones, D. You and P. H. Bucksbaum. *Phys. Rev. Lett.* **70**, 1236 (1993).
- [235] S. Li and R. R. Jones. *Phys. Rev. Lett.* **112**, 143006 (2014).
- [236] T. Ogawa, S. Watanabe, N. Minami and R. Shimano. *Appl. Phys. Lett.* **97**, 041111 (2010).
- [237] William H. Press, S. A. Teukolsky, W. T. Vetterling and B. P. Flannery. *Numerical Recipes* (Cambridge University Press, New York, 2007), 3 edn.
- [238] A. Kormányos, G. Burkard, M. Gmitra, J. Fabian, V. Zólyomi, N. D. Drummond and V. Fal’Ko. *2D Mater.* **2**, 022001 (2015).
- [239] D. Wickramaratne, F. Zahid and R. K. Lake. *J. Chem. Phys.* **140**, 124710 (2014).
- [240] T. Cheiwchanchamnangij and W. R. Lambrecht. *Phys. Rev. B* **85**, 205302 (2012).

References

- [241] A. Chernikov, T. C. Berkelbach, H. M. Hill, A. Rigosi, Y. Li, O. B. Aslan, D. R. Reichman, M. S. Hybertsen and T. F. Heinz. *Phys. Rev. Lett.* **113**, 076802 (2014).
- [242] J. Feng, X. Qian, C. W. Huang and J. Li. *Nat. Photonics* **6**, 866 (2012).
- [243] I. Kylänpää and H.-P. Komsa. *Phys. Rev. B* **92**, 205418 (2015).
- [244] H. Shi, H. Pan, Y. W. Zhang and B. I. Yakobson. *Phys. Rev. B* **87**, 155304 (2013).
- [245] G. Berghäuser and E. Malic. *Phys. Rev. B* **89**, 125309 (2014).
- [246] H. P. Komsa and A. V. Krasheninnikov. *Phys. Rev. B* **86**, 241201(R) (2012).
- [247] Z. Ye, T. Cao, K. O'Brien, H. Zhu, X. Yin, Y. Wang, S. G. Louie and X. Zhang. *Nature* **513**, 214 (2014).
- [248] A. R. Klots *et al.* *Sci. Rep.* **4**, 6608 (2014).
- [249] C. Zhang, A. Johnson, C. L. Hsu, L. J. Li and C. K. Shih. *Nano Lett.* **14**, 2443 (2014).
- [250] H. M. Hill, A. F. Rigosi, C. Roquelet, A. Chernikov, T. C. Berkelbach, D. R. Reichman, M. S. Hybertsen, L. E. Brus and T. F. Heinz. *Nano Lett.* **15**, 2992 (2015).
- [251] K. He, N. Kumar, L. Zhao, Z. Wang, K. F. Mak, H. Zhao and J. Shan. *Phys. Rev. Lett.* **113**, 026803 (2014).
- [252] A. V. Stier, N. P. Wilson, K. A. Velizhanin, J. Kono, X. Xu and S. A. Crooker. *Phys. Rev. Lett.* **120**, 057405 (2018).
- [253] M. Palummo, M. Bernardi and J. C. Grossman. *Nano Lett.* **15**, 2794 (2015).
- [254] H. Wang, C. Zhang, W. Chan, C. Manolatou, S. Tiwari and F. Rana. *Phys. Rev. B* **93**, 045407 (2016).
- [255] M. O. Sauer, C. E. M. Nielsen, L. Merring-Mikkelsen and T. G. Pedersen. *Phys. Rev. B* **103**, 205404 (2021).
- [256] T. Korn, S. Heydrich, M. Hirmer, J. Schmutzler and C. Schiller. *Appl. Phys. Lett.* **99**, 102109 (2011).

References

- [257] D. Lagarde, L. Bouet, X. Marie, C. R. Zhu, B. L. Liu, T. Amand, P. H. Tan and B. Urbaszek. *Phys. Rev. Lett.* **112**, 047401 (2014).
- [258] H. C. Kamban, T. G. Pedersen and N. M. R. Peres. *Phys. Rev. B* **102**, 115305 (2020).
- [259] H. C. Kamban and T. G. Pedersen. *Phys. Rev. B* **104**, 235305 (2021).
- [260] Y. Cao, S. Gan, Z. Geng, J. Liu, Y. Yang, Q. Bao and H. Chen. *Sci. Rep.* **6**, 22899 (2016).
- [261] Z. Fan, Z. Geng, W. Fang, X. Lv, Y. Su, S. Wang, J. Liu and H. Chen. *AIP Adv.* **10**, 045304 (2020).

References

Publications

- Paper A:** *Field-induced dissociation of two-dimensional excitons in transition metal dichalcogenides*,
Høgni C. Kamban and Thomas G. Pedersen,
Phys. Rev. B **100**, 045307 (2019)
- Paper B:** *Finite-Difference Time-Domain Simulation of Strong-Field Ionization: A Perfectly Matched Layer Approach*,
Høgni C. Kamban, Sigurd S. Christensen, Thomas Søndergaard, and Thomas G. Pedersen,
Phys. Stat. Sol. B **257**, 1900467 (2020)
- Paper C:** *Interlayer excitons in van der Waals heterostructures: Binding energy, Stark shift, and field-induced dissociation*,
Høgni C. Kamban and Thomas G. Pedersen,
Sci. Rep. **10**, 5537 (2020)
- Paper D:** *Analytical quantitative semiclassical approach to the Lo Surdo–Stark effect and ionization in two-dimensional excitons*,
J. C. G. Henriques, **Høgni C. Kamban**, Thomas G. Pedersen, and N. M. R. Peres,
Phys. Rev. B **102**, 035402 (2020)
- Paper E:** *Anisotropic Stark shift, field-induced dissociation, and electroabsorption of excitons in phosphorene*,
Høgni C. Kamban, Thomas G. Pedersen, and N. M. R. Peres,
Phys. Rev. B **102**, 115305 (2020)
- Paper F:** *Calculation of the nonlinear response functions of intra-exciton transitions in two-dimensional transition metal dichalcogenides*,
J. C. G. Henriques, **Høgni C. Kamban**, Thomas G. Pedersen, and N. M. R. Peres,
Phys. Rev. B **103**, 235412 (2021)

Paper G: *Efficient ionization of two-dimensional excitons by intense single-cycle terahertz pulses,*
Høgne C. Kamban and Thomas G. Pedersen,
Phys. Rev. B **104**, 235305 (2021)

Paper A

Field-induced dissociation of two-dimensional excitons in
transition metal dichalcogenides

Høgni C. Kamban and Thomas G. Pedersen

This paper has been published in Physical Review B:
Phys. Rev. B **100**, 045307 (2019)
DOI: 10.1103/PhysRevB.100.045307

Field-induced dissociation of two-dimensional excitons in transition metal dichalcogenides

Høgne C. Kamban* and Thomas G. Pedersen

*Department of Materials and Production, Aalborg University, DK-9220 Aalborg Øst, Denmark
and Center for Nanostructured Graphene (CNG), DK-9220 Aalborg Øst, Denmark*



(Received 8 May 2019; published 17 July 2019)

Generation of photocurrents in semiconducting materials requires dissociation of excitons into free charge carriers. While thermal agitation is sufficient to induce dissociation in most bulk materials, an additional push is required to induce efficient dissociation of the strongly bound excitons in monolayer transition metal dichalcogenides (TMDs). Recently, static in-plane electric fields have proven to be a promising candidate. In the present paper, we introduce a numerical procedure, based on exterior complex scaling, capable of computing field-induced exciton dissociation rates for a wider range of field strengths than previously reported in the literature. We present both Stark shifts and dissociation rates for excitons in various TMDs calculated within the Mott-Wannier model. Here, we find that the field-induced dissociation rate is strongly dependent on the dielectric screening environment. Furthermore, applying weak-field asymptotic theory to the Keldysh potential, we are able to derive an analytical expression for exciton dissociation rates in the weak-field region.

DOI: [10.1103/PhysRevB.100.045307](https://doi.org/10.1103/PhysRevB.100.045307)

I. INTRODUCTION

Interest in two-dimensional transition-metal dichalcogenide (TMD) semiconductors has increased substantially in recent years due to their exceptional electronic and optical properties. They have a wide range of applications, including photodetectors [1–3], light-emitting diodes [4], solar cells [5,6], and energy storage devices [7–9], to name a few. One of the most important implications of the reduced screening in two-dimensional TMDs is the comparatively large exciton binding energy [10–13]. Such excitons may significantly reduce the efficiency of solar cells and photodetectors, as these devices require the dissociation of excitons into free charge carriers to generate an electrical current. Excitons in bulk semiconductors will usually dissociate by thermal agitation alone due to their low binding energies. This is not the case for their two-dimensional counterparts, however, and it is therefore of great interest to obtain efficient methods of inducing exciton dissociation in TMD monolayers. Dissociation induced by in-plane static electric fields has gained attention lately. For instance, dissociation rates for two-dimensional excitons in MoS₂ were theoretically investigated in Refs. [14] and [15], and for various bulk TMDs in [13].

Recently, the first systematic experimental study of field-induced dissociation of two-dimensional excitons in monolayer WSe₂ encapsulated by hBN was carried out [16]. It was found that the limiting factor in generating photocurrents when a weak in-plane field was present was the dissociation rate of electron-hole pairs. That work also showed that the photocurrent generated in fields weaker than 15 V/μm was accurately predicted by the Mott-Wannier model [17,18]. Nevertheless, these weak-field dissociation rates proved troublesome to obtain numerically [16], and they were therefore extrapolated by fitting to the rate of a two-dimensional

hydrogen atom [19]. In the present paper, we introduce a numerical method capable of computing exciton dissociation rates for significantly weaker fields with no compromise on the accuracy for stronger fields. It is based on the complex scaling approach [20,21] that was used in Refs. [14] and [16], but, rather than rotating the entire spatial region into the complex plane, we rotate the radial coordinate only in an exterior region $r > R$. For sufficiently weak fields, we show that the rates can be obtained analytically based on the recently developed weak-field asymptotic theory (WFAT) [22], which greatly simplifies their calculation. Furthermore, we show that the weak-field ionization rate of two-dimensional hydrogen is a special case of a more general formula for dissociation of a two-dimensional two-particle system.

II. TMD EXCITON IN ELECTROSTATIC FIELD

Throughout the present paper, excitons will be modeled as electron-hole pairs described by the two-dimensional Wannier equation [17,18], which reads (atomic units are used throughout)

$$\left[-\frac{1}{2\mu} \nabla^2 - w(\kappa r) \right] \psi(\mathbf{r}) = E \psi(\mathbf{r}), \quad (1)$$

where μ is the reduced exciton mass, $\mathbf{r} = \mathbf{r}_e - \mathbf{r}_h$ is the relative in-plane coordinate of the electron-hole pair, $\kappa = (\kappa_a + \kappa_b)/2$ is the average dielectric constant of the materials above and beneath the TMD sheet, and w is a screened Coulomb attraction. It is well known that screening in two-dimensional semiconductors, such as TMDs, is inherently nonlocal [23,24], i.e., momentum-dependent, and can be approximated by the linearized form $\epsilon(\mathbf{q}) = \kappa + r_0 q$, where \mathbf{q} is the wave vector, and the so-called screening length r_0 can be related to the polarizability of the sheet [23]. The interaction w may then be obtained as the inverse Fourier transform of $2\pi[\epsilon(\mathbf{q})q]^{-1}$, where $2\pi/q$ is the 2D Fourier transform of $1/r$.

*Corresponding author: hck@mp.aau.dk

The resulting interaction is given by the Keldysh [24,25] form

$$w(\mathbf{r}) = \frac{\pi}{2r_0} \left[H_0\left(\frac{r}{r_0}\right) - Y_0\left(\frac{r}{r_0}\right) \right], \quad (2)$$

where H_0 is the zeroth-order Struve function and Y_0 is the zeroth-order Bessel function of the second kind [26].

When an in-plane electrostatic field is applied to the exciton, Eq. (1) is modified to include a perturbation term

$$\left[-\frac{1}{2\mu} \nabla^2 - w(\kappa \mathbf{r}) + \boldsymbol{\varepsilon} \cdot \mathbf{r} \right] \psi(\mathbf{r}) = E \psi(\mathbf{r}). \quad (3)$$

In the present paper, we will restrict ourselves to electric fields pointing along the x -axis, i.e., $\boldsymbol{\varepsilon} = \varepsilon \mathbf{e}_x$. As is evident, the form of Eq. (3) is the same as that of the two-dimensional hydrogen atom in a static electric field [19], albeit with a different potential. It should therefore come as no surprise that excitons perturbed by an electrostatic field will eventually dissociate. An important distinction, however, is that the excitons will recombine if they are not dissociated [16,27]. This field-free recombination rate is in competition with the field-induced dissociation. For practical applications, recombination [28–30] and other forms of exciton decay (such as defect-assisted recombination [31] and exciton-exciton annihilation [32]), which do not yield free charge carriers, are often undesired.

The field-induced dissociation rate Γ is connected to the nonvanishing imaginary part of the energy eigenvalue in the presence of an electric field by the relation $\Gamma = -2 \text{Im} E$ [13,14,16,19]. The desired eigenvalues are therefore unobtainable through conventional Hermitian methods. Rather, one should solve Eq. (3) subject to regularity and outgoing boundary conditions [22,33]. This is a nontrivial task in all but the simplest cases, and in practice one usually computes the resonance energies by complex scaling of the Hamiltonian [20,21].

III. EXCITON DISSOCIATION

In its simplest form, complex scaling corresponds to rotating the radial coordinate into the complex plane uniformly [20,21], $r \rightarrow \exp(i\phi)r$, where ϕ is a fixed real-valued angle (note that if ϕ is chosen complex, the coordinate will simply be stretched as well as rotated). This transformation, referred to as uniform complex scaling (UCS), turns the outgoing waves mentioned above into exponentially decaying waves, provided that ϕ is chosen large enough [34]. Thus, the complex scaled resonance wave functions are square integrable, and the resonance energies can be obtained by solving Eq. (3) with the scaled operator and the boundary condition $\psi(r \rightarrow \infty) = 0$. This approach has been used to obtain the dissociation rates of two-dimensional TMD excitons in Refs. [14,16]. Nevertheless, as was discussed briefly in Ref. [16], numerical difficulties arise when the electric field becomes sufficiently weak. This is because the important region for weak fields is sufficiently far from the origin that the uniformly complex scaled resonance wave function has (numerically) vanished prior to reaching this region. By utilizing the so-called exterior complex scaling (ECS) approach

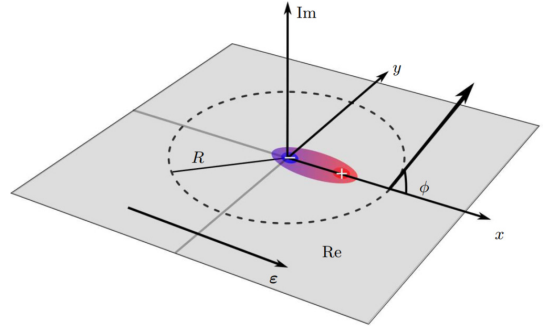


FIG. 1. Sketch of the two-dimensional exciton in the xy -plane with the radial coordinate rotated into the complex plane by an angle of ϕ for $r > R$.

[34–37], combined with a finite-element (FE) representation of the wave function, we are able to compute dissociation rates for significantly weaker fields, as we now demonstrate.

As the name suggests, ECS transforms the radial coordinate outside a scaling radius R ,

$$r \rightarrow \begin{cases} r & \text{for } r < R, \\ R + (r - R)e^{i\phi} & \text{for } r > R, \end{cases} \quad (4)$$

where ϕ is the angle of rotation, as illustrated in Fig. 1. The partitioning of the radial coordinate is efficiently dealt with by an FE basis representation, the details of which can be found in Appendix A. Fig. 2 shows the Stark shift and dissociation rate of the ground-state exciton as functions of in-plane field strength for four important materials in various dielectric environments. The screening lengths and reduced masses used in the calculations are obtained from Ref. [38]. As is evident, the dissociation rate increases rapidly with increasing field strength. The rates can also be seen to be strongly dependent on the screening environment, which is to be expected as increased screening leads to reduced binding energies. It is therefore possible to tune the dissociation rates of the TMDs as desired within a certain range. For example, encapsulating the TMDs in $h\text{BN}$ (with $\kappa = 4.9$ [11]) increases the dissociation rates by several orders of magnitude compared to their free-space counterparts. Rates for MoS_2 , $\text{MoS}_2/h\text{BN}$, and $h\text{BN}/\text{MoS}_2/h\text{BN}$ were presented in Ref. [14] for fields stronger than $50 \text{ V}/\mu\text{m}$. However, the experimental study of $h\text{BN}/\text{WSe}_2/h\text{BN}$ in Ref. [16] suggests that exciton dissociation rates are the limiting factor in generation of photocurrents for applied fields weaker than $15 \text{ V}/\mu\text{m}$ in this material. For stronger fields, the photocurrent measurements deviate from the field-induced rates predicted by the Wannier model, and other limitations dominate [16]. We expect to see the same effect for the other TMDs, and we furthermore expect this threshold field to increase as the screening is reduced.

In weak fields, the Stark shifts in Fig. 2 can be seen to vary approximately as ε^2 , in agreement with the lowest-order perturbation theory expansion of the energy $E \approx E_0 - \frac{1}{2}\alpha\varepsilon^2$, where E_0 is the unperturbed ground-state energy and α is the exciton polarizability. The shape of the shift is in agreement

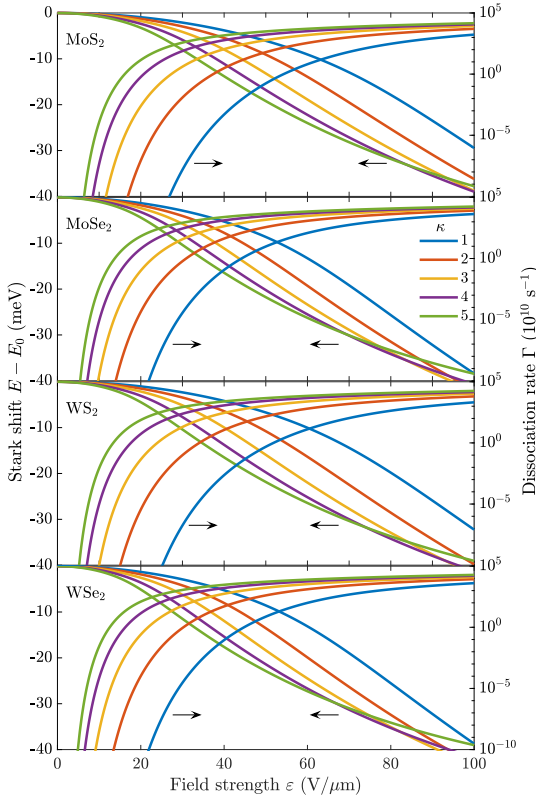


FIG. 2. Exciton Stark shift and dissociation rate of the ground-state exciton for four important materials in various dielectric environments.

with those observed for similar systems; the energy initially decreases rapidly with field strength and then levels off as the field strength increases [19]. A more detailed analysis of the shift in the weak-field region will be made in Sec. V.

The resonance discussed above corresponds to dissociation of an exciton in its ground state. Meanwhile, excitation by high-energy photons may produce higher excitons. It is therefore interesting to analyze the dissociation rates of excited states. The numerical procedure outlined in Appendix A is perfectly capable of handling excited states, and in Fig. 3 we show Stark shifts and dissociation rates for excitons occupying either the $1s$, $2s$, or $2p$ state in four different TMDs located in free space ($\kappa = 1$). As expected, the dissociation rates for the excited states are much larger than those of the ground state, and for weak electric fields in particular. This, along with the fast decay of excited states to the ground state, means that the limiting factor in generation of photocurrents in weak in-plane electric fields is dominated by the dissociation rate of ground-state excitons. This explains the excellent agreement between photocurrent measurements and calculated ground-state dissociation in Ref. [16] for weak electric fields. We also observe a substantially larger Stark shift in the $2s$ and $2p$ states, in agreement with expectations.

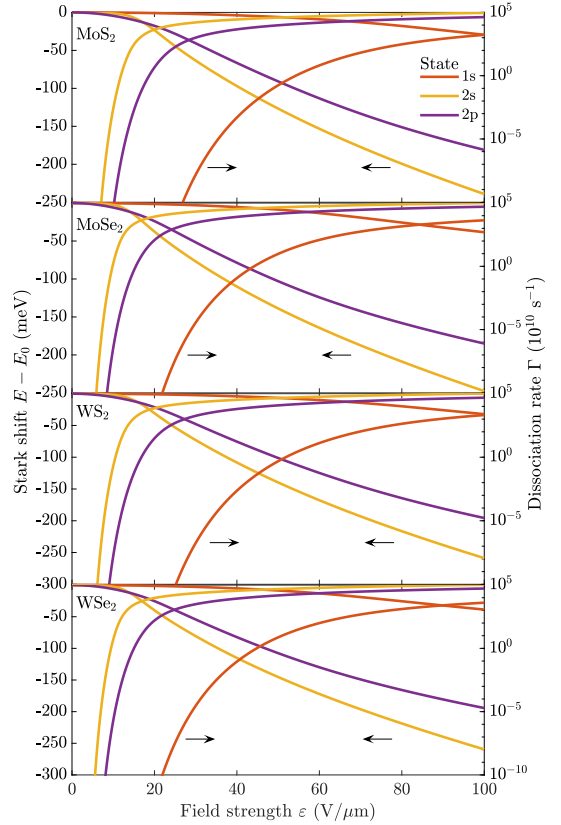


FIG. 3. Stark shift and dissociation rates for excitons occupying either the $1s$, $2s$, or $2p$ state in TMDs located in free space ($\kappa = 1$).

IV. WEAK-FIELD ASYMPTOTIC THEORY

Even with the improved numerical procedure, the dissociation rates for extremely weak fields are unobtainable. In fact, any numerical procedure with finite-precision arithmetic fails for sufficiently weak fields, when the ratio $\Gamma/|E_0|$ approaches the round-off error [39,40]. Fortunately, with the recent development of weak-field asymptotic theory (WFAT) [22], we are able to take advantage of the simple asymptotic form of the Keldysh potential and calculate the weak-field dissociation rates analytically. To this end, we first simplify Eq. (3) by introducing the scaling relations

$$\tilde{r}_0 = \frac{\mu}{\kappa^2} r_0, \quad \tilde{\mathbf{r}} = \frac{\mu}{\kappa} \mathbf{r}, \quad \text{and} \quad \tilde{\mathbf{e}} = \frac{\kappa^3}{\mu^2} \mathbf{e}, \quad (5)$$

which lead to

$$E(\mu, \kappa, r_0, \mathbf{e}) = \frac{\mu}{\kappa^2} E(1, 1, \tilde{r}_0, \tilde{\mathbf{e}}). \quad (6)$$

Thus, the only nontrivial parameters are \tilde{r}_0 and $\tilde{\mathbf{e}}$, and the analysis in the following will therefore be restricted to the simplified problem

$$\left[-\frac{1}{2} \nabla^2 - w(\mathbf{r}) + \mathbf{e} \cdot \mathbf{r} \right] \psi(\mathbf{r}) = E \psi(\mathbf{r}), \quad (7)$$

from which Stark shifts and dissociation rates can be obtained using Eq. (6). Note that in order to simplify the notation, the tilde has been omitted in Eq. (7) as well as in the following. Therefore, unless explicitly stated otherwise, r , r_0 , ε , and E in the following refer to the scaled parameters. As discussed in the previous section, the limiting factor in generating photocurrents is the dissociation rate of the ground-state exciton. For this reason, we restrict our analysis in the following to the ground state.

The potential in Eq. (7) has the large- r behavior [26]

$$w(r) = \frac{1}{r} + O\left(\frac{r_0^2}{r^3}\right), \quad (8)$$

which has the form required to use WFAT. A leading-order expression for the weak-field dissociation rate was derived for a three-dimensional system in Ref. [22] and extended to first order in ε in Ref. [39]. We shall only consider the leading-order approximation here. By modifying the approach in Ref. [22] to two dimensions, we find that the weak-field dissociation rate for the ground state of Eq. (7) is given by

$$\Gamma \approx |g_0|^2 W_0(\varepsilon), \quad (9)$$

with the asymptotic coefficient and field factor [41,42] given by

$$g_0 = \lim_{v \rightarrow \infty} v^{1/2-1/k} e^{kv/2} \int_0^\infty \varphi_0(u) \psi_0\left(\frac{u+v}{2}\right) \frac{1}{\sqrt{u}} du \quad (10)$$

and

$$W_0(\varepsilon) = k \left(\frac{4k^2}{\varepsilon}\right)^{2/k-1/2} \exp\left(-\frac{2k^3}{3\varepsilon}\right), \quad (11)$$

respectively. Here, $k = \sqrt{-2E_0}$, and u and v are the parabolic cylindrical coordinates defined by

$$u = r + x, \quad u \in [0, \infty), \quad (12)$$

$$v = r - x, \quad v \in [0, \infty). \quad (13)$$

The functions appearing in Eq. (10) are the unperturbed ground state ψ_0 and

$$\varphi_n(u) = \left[\frac{\sqrt{kn!}}{(n-1/2)!} \right]^{1/2} L_n^{(-1/2)}(ku) e^{-ku/2}, \quad (14)$$

with $L_n^{(\alpha)}(x)$ a generalized Laguerre polynomial [26]. To obtain the weak-field dissociation rate from Eq. (9), one therefore needs the unperturbed binding energy E_0 and the asymptotic coefficient g_0 of the simplified problem. Once they have been obtained, the physical weak-field dissociation rate for arbitrary monolayer TMDs can be obtained by scaling back to the original units, cf. Eq. (6),

$$\Gamma(\mu, \kappa, r_0, \varepsilon) = \frac{\mu}{\kappa^2} \Gamma(1, 1, \tilde{r}_0, \tilde{\varepsilon}). \quad (15)$$

We now turn to computing the asymptotic coefficient g_0 .

Computing the asymptotic coefficient

Finding g_0 given by Eq. (10) requires an accurate representation of the wave function for large v . Note that a traditional

basis expansion (e.g., a Gaussian basis) is generally not accurate enough, as only the most slowly decaying functions will contribute in this region. This problem was partially circumvented in Ref. [42] by using a Gaussian basis with optimized exponents. Here, we will implement Numerov's finite-difference scheme, which can accurately and efficiently construct the unperturbed wave function in the asymptotic region. The technical details can be found in Appendix B. As a preliminary, it is convenient to relate g_0 to the radial wave function. The ground state of a potential with cylindrical symmetry satisfies

$$\psi_0(r) \sim C_0 r^{1/k-1/2} e^{-kr} \quad \text{for } r \rightarrow \infty, \quad (16)$$

where C_0 is a constant. Using Eq. (16) in Eq. (10) leads to the relation

$$g_0 = \frac{2^{1/2-1/k} \pi^{1/4} C_0}{k^{1/4}}. \quad (17)$$

The problem of finding g_0 has therefore been reduced to obtaining the asymptotic coefficient of the radial wave function. It can be found by taking the limit

$$C_0 = \lim_{r \rightarrow \infty} \psi_0 r^{1/2-1/k} e^{kr}. \quad (18)$$

Note that in the unscreened limit ($r_0 \rightarrow 0$), $k = 2$ and $\psi_0 = 2^{3/2} \pi^{-1/2} \exp[-(u+v)]$ [43], which leads to $g_0 = 2^{5/4} \pi^{-1/4}$, and Eq. (9) is therefore in agreement with the expression found in Ref. [19] for the two-dimensional hydrogen atom. In practice, we find C_0 by fitting Eq. (18) to the asymptotic expansion

$$D(r) = \sum_{n=0}^4 \frac{d_n}{r^n}, \quad (19)$$

in a stable region (see Appendix B), as described in Ref. [42]. The asymptotic coefficient C_0 is then obtained by taking the limit $\lim_{r \rightarrow \infty} D = d_0$. The computational method above takes advantage of the fact that a high-order finite-difference scheme is able to accurately reproduce the wave function for large r . Recently, however, integral representations for the asymptotic coefficient that are insensitive to the wave function tail have been derived for a three-dimensional system [44,45]. This suggests that one may get away with using a sufficiently accurate representation of the wave function only in an interior region. We shall use the integral equations as a check to ensure the accuracy of the scheme presented above. To derive the corresponding equation for our two-dimensional system, we introduce the reference function Ω as a solution to

$$\left[-\frac{1}{2} \nabla^2 - \frac{1}{r} + \frac{k^2}{2} \right] \Omega_n(r) = 0. \quad (20)$$

The relevant function for the asymptotic coefficient of the ground state is

$$\Omega_0(r) = -2^{\frac{1}{k}+\frac{1}{2}} k^{\frac{1}{k}-\frac{1}{2}} \Gamma\left(\frac{1}{2} - \frac{1}{k}\right) e^{-kr} M\left(\frac{1}{2} - \frac{1}{k}; 1; 2kr\right), \quad (21)$$

where M is a confluent hypergeometric function [26]. If the exciton energy coincides with one of the energies of the

TABLE I. Binding energy $E_0(1, 1, \bar{r}_0)$ and asymptotic coefficient g_0 of the simplified problem for four important materials in different dielectric environments.

κ	MoS ₂		MoSe ₂		WS ₂		WSe ₂	
	E_0	g_0	E_0	g_0	E_0	g_0	E_0	g_0
1	0.0714	0.00098	0.0659	0.00057	0.0921	0.0044	0.0801	0.0020
2	0.1907	0.0889	0.1773	0.0707	0.2392	0.1671	0.2113	0.1200
3	0.3200	0.3210	0.2995	0.2805	0.3928	0.4650	0.3512	0.3829
4	0.4474	0.5695	0.4210	0.5195	0.5392	0.7323	0.4870	0.6420
5	0.5680	0.7796	0.5370	0.729	0.6740	0.9380	0.6142	0.8515

two-dimensional hydrogen atom

$$E_n^{(\text{hydr})} = \frac{1}{2(n-1/2)^2}, \quad (22)$$

where $n = 1, 2, \dots$ [43], the confluent hypergeometric function in Eq. (21) reduces to a polynomial of finite degree, and Ω_0 will vanish as r tends to infinity. In practical calculations, this is hardly ever the case and the reference function will therefore be exponentially increasing (see Ref. [46] for a discussion of the case in which $E_0 \approx E_n^{(\text{hydr})}$),

$$\Omega(r) \sim -k^{-1} r^{-1/2-1/k} e^{kr} \quad \text{for } r \rightarrow \infty. \quad (23)$$

Integrating by parts and using Eqs. (16) and (23) when r tends to infinity, we find

$$C_0 = \int_0^\infty \Omega_0(r) \left[\frac{1}{2} \nabla^2 + \frac{1}{r} - \frac{k^2}{2} \right] \psi_0(r) r dr, \quad (24)$$

which, using Eq. (7) with $\varepsilon = 0$, can be reduced to

$$C_0 = \int_0^\infty \Omega_0(r) \left[\frac{1}{r} - w(r) \right] \psi_0(r) r dr. \quad (25)$$

The integrand in Eq. (25) is a product of an exponentially increasing function Ω_0 and an exponentially decreasing function ψ_0 . Such an integral need not be convergent. Nevertheless, as is evident from the large- r behavior of these functions [see Eqs. (16) and (23)], the exponential terms cancel for r tending to infinity, resulting in the integrand tending to zero sufficiently quickly for the integral to converge. We have checked that Eqs. (18) and (25) agree when using the numerically exact wave function. The asymptotic coefficients and binding energies of the simplified Wannier problem for four important materials are presented in Table I. Note that these binding energies increase with κ . This is because the binding energies of the simplified problem increase when \bar{r}_0 decreases and \bar{r}_0 is proportional to κ^{-2} . In Fig. 4, we compare the dissociation rates for excitons in MoS₂ and WSe₂ given by the weak-field formula Eq. (9) to the numerically exact dissociation rates. As can be seen, the agreement between the weak field and the fully numerical results is reasonable for fields lower than 50 V/ μm and improves as the field strength decreases. For $\varepsilon \lesssim \kappa^{-1/2} 20 \text{ V}/\mu\text{m}$ the agreement in Fig. 4 becomes excellent.

V. STARK SHIFT

Applying perturbation theory to the ground state of a system with cylindrical symmetry leads to the well-known

result

$$E = E_0 - \frac{1}{2} \alpha \varepsilon^2 + O(\varepsilon^4), \quad (26)$$

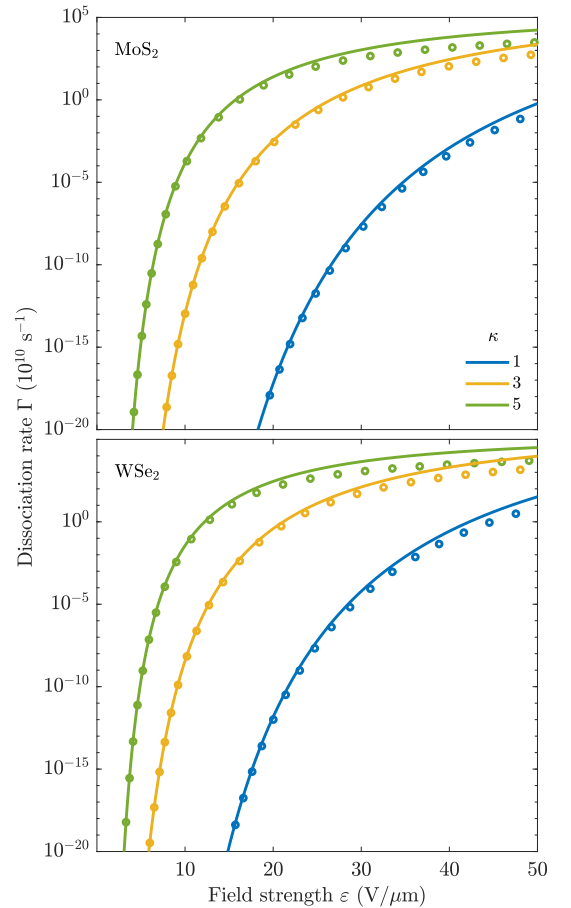


FIG. 4. Exciton dissociation rates for MoS₂ (upper) and WSe₂ (lower) encapsulated by various dielectric media. The circles are the numerically exact results obtained by the method in Appendix A (same as those in Fig. 2). The solid lines correspond to the weak-field formula Eq. (9) with the parameters found in Table I.

TABLE II. Exciton polarizability α for various TMDs in different dielectric environments in units of 10^{-18} eV(m/V)² calculated from Eq. (27) with ψ_0 and ψ_1 expanded in an FE basis with a spacing of 1 a.u.

κ	MoS ₂ α	MoSe ₂ α	WS ₂ α	WSe ₂ α
1	4.59	6.24	5.04	6.24
2	6.31	8.46	7.30	8.78
3	8.48	11.22	10.25	12.02
4	11.18	14.63	14.09	16.14
5	14.54	18.81	19.00	21.32

where α is the static polarizability. A shortcoming of perturbation theory is that it predicts the energy as a function of field strength to be purely real, which, as seen in the previous sections, is obviously not correct for a system in which dissociation is possible. Nevertheless, the nonperturbative behavior of the resonance energy can be reproduced by utilizing the first few perturbation coefficients together with the hypergeometric resummation technique [47]. This approach was used in Ref. [19] with great success for low-dimensional hydrogen. In the present section, we wish to analyze to what extent the change in the real part of the resonance energy, i.e., the exciton Stark shift, can be predicted by standard second-order perturbation theory (for previous work on exciton Stark shifts in TMDs, see Refs. [14,15,48,49]). To this end, we calculate the exciton polarizability given by

$$\alpha = -2\langle\psi_0|r\cos\theta|\psi_1\rangle, \quad (27)$$

where the first-order correction ψ_1 is a solution to the Dalgarno-Lewis [50] equation

$$\left[-\frac{1}{2\mu}\nabla^2 - w(\kappa r) - E_0\right]\psi_1 = -r\cos\theta\psi_0, \quad (28)$$

and will therefore be of the form $\psi_1 = \cos\theta f(r)$, where f is a purely radial function. Expanding ψ_0 and ψ_1 in a finite-element basis (without complex scaling), as described in Appendix A, Eq. (28) can be solved and the polarizability found (for alternative methods of finding the polarizability, see Ref. [48]). The exciton polarizability for various TMDs in different environments can be found in Table II, and Fig. 5 shows a comparison between the shift in the real part of the complex resonance energy and the perturbation series in Eq. (26). Evidently, a good agreement is found in the weak-field region. Furthermore, excitons in environments with large dielectric screening begin to deviate from their second-order expansion for weaker fields than their free-space counterparts. This is to be expected, as the binding energies of excitons with heavily screened interactions are lower and the characteristic fields of these excitons are therefore weaker.

VI. SUMMARY

In the present work, electric-field-induced dissociation of TMD excitons has been investigated using both numerical and analytical approaches. The dissociation rates as functions of the in-plane field strength for excitons in monolayer MoS₂,

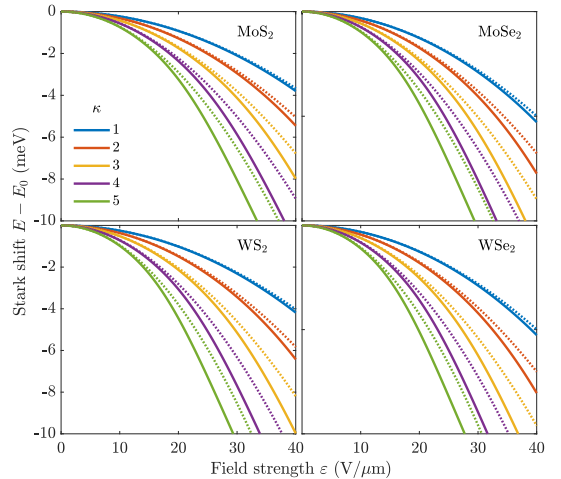


FIG. 5. Exciton Stark shift for four important TMDs in various dielectric environments. The solid lines correspond to the real part of the resonance energy, while the dotted lines show the shift predicted by perturbation theory, $E - E_0 \approx -\alpha\epsilon^2/2$.

MoSe₂, WS₂, and WSe₂ in various screening environments have been obtained. In particular, difficulties associated with dissociation rates in weak electric fields have been addressed and resolved. In this regard, an efficient numerical method capable of computing dissociation rates for a wide range of fields has been introduced. As the field becomes sufficiently weak, any numerical method with finite precision arithmetic breaks down, which calls for a different approach. We demonstrate that an analytical weak-field approximation is valid in this region, which makes the weak-field dissociation rates readily available for arbitrarily weak fields. Finally, the exciton Stark shift has been analyzed and compared to the results of second-order perturbation theory.

ACKNOWLEDGMENTS

The authors gratefully acknowledge financial support by the Center for Nanostructured Graphene (CNG), which is sponsored by the Danish National Research Foundation, Project No. DNRF103. Additionally, T.G.P. is supported by the QUSCOPE Center, sponsored by the Villum Foundation.

APPENDIX A: NUMERICAL PROCEDURE

To implement the finite-element (FE) approach, we first divide the radial grid into N segments $[r_{n-1}, r_n]$ for $n = 1, \dots, N$. Following the procedure in Ref. [51], we introduce a set of p_n linearly independent functions $h_i^{(n)}$, where $i = 1, \dots, p_n$ on each segment. These functions are then transformed into a different set of functions $f_i^{(n)}$, $i = 1, \dots, p_n$, that vanish at the segment boundaries, except for the first and last function, which are required to equal unity at the lower and upper element boundaries, respectively. To

summarize,

$$f_i^{(n)}(r_{n-1}) = f_i^{(n)}(r_n) = 0, \quad (\text{A1})$$

$$\text{except } f_1^{(n)}(r_{n-1}) = f_{p_n}^{(n)}(r_n) = 1. \quad (\text{A2})$$

We use Legendre polynomials $h_i^{(n)}(r) = P_{i-1}[y_n(r)]$, where y_n maps $[r_{n-1}, r_n]$ onto $[-1, 1]$, and $h_i^{(n)}$ is set equal to zero for $r \notin [r_{n-1}, r_n]$. Dirichlet boundary conditions are then implemented for some large $r_N \geq R$ by omitting the last function $f_{p_N}^{(N)}$. The scaling radius R is to be chosen to coincide with an element boundary. Note that if $r_N = R$, no complex scaling is implemented. The eigenstate can now be written as a sum of basis functions,

$$\psi(r) = \sum_{m=0}^M \sum_{n=1}^N \sum_{i=1}^{p_n} c_i^{(m,n)} f_i^{(n)}(r) \cos(m\theta), \quad (\text{A3})$$

where the radial part is resolved using the finite-element basis. Due to the cylindrical symmetry of the unperturbed problem, the angular dependence of the unperturbed eigenstates is the cylindrical harmonics $e^{im\theta}$. The angular part of the eigenstate is therefore resolved efficiently using a basis of cosine functions. To ensure continuity across the segment boundaries, we enforce

$$c_{p_{n-1}}^{(m,n-1)} = c_1^{(m,n)}, \quad n = 2, \dots, N. \quad (\text{A4})$$

To evaluate the radial part of the matrix elements, we use the Legendre quadrature rule [52].

We proceed by providing a recipe for constructing the overlap and Hamilton matrix, and we refer the interested reader to Refs. [34,51] and references therein for more details on the mathematical background. It is convenient to first construct segmentwise matrices containing only the radial part of the matrix elements. For segments with $r_n \leq R$ the procedure is familiar, and, as an example, the radial segmentwise overlap matrices are given by

$$S_{ij}^{(n)} = \int_0^\infty f_i^{(n)}(r) f_j^{(n)}(r) r dr \quad (\text{A5})$$

$$\approx \sum_{k=1}^K f_i^{(n)}(r_k^{(n)}) f_j^{(n)}(r_k^{(n)}) r_k^{(n)} w_k^{(n)}, \quad (\text{A6})$$

where $w_k^{(n)}$ and $r_k^{(n)}$ are the quadrature weights and sample points for the n th segment, respectively. For segments with $r_{n-1} \geq R$, the radial coordinate is transformed according to Eq. (4) and the matrix elements must be modified accordingly. The integral element dr must be multiplied by $e^{i\phi}$, and r must be replaced by the transformation in Eq. (4), all the while keeping the argument of the basis functions unchanged. As an example, the segmentwise overlap matrix becomes

$$S_{ij}^{(n)} \approx \sum_{k=1}^K \{f_i^{(n)}(r_k^{(n)}) f_j^{(n)}(r_k^{(n)}) [R + (r_k^{(n)} - R)e^{i\phi}] w_k^{(n)} e^{i\phi}\}.$$

The segmentwise matrices are then collected into the complete radial overlap matrix \mathbf{S}_r such that the last row and column of each segmentwise matrix overlaps with the first row and column of the next (see Ref. [51] for a visual demonstration). This conveniently enforces Eq. (A4). The complete overlap matrix \mathbf{S} is then a block-diagonal matrix with blocks consisting of $\pi(1 + \delta_{m0})\mathbf{S}_r$ for $m = 0, \dots, M$. The Hamilton matrix can be constructed in a similar manner, keeping in mind that $\frac{d}{dr}f_i$ should be replaced by $e^{-i\phi} \frac{d}{dr}f_i$ for segments outside the scaling radius, and that the (untransformed) segmentwise kinetic matrix elements are given by

$$T_{ij}^{(n)} = \frac{1}{2} \int_{r_{n-1}}^{r_n} \frac{df_i}{dr} \frac{df_j}{dr} r dr, \quad (\text{A8})$$

to comply with the correct definition of the kinetic energy in an FE basis [37,53]. The transformed Wannier equation is then readily solved as a matrix eigenvalue problem.

APPENDIX B: COMPUTATIONAL PROCEDURE FOR THE ASYMPTOTIC COEFFICIENT

Grid-based finite-difference methods (FDMs) are able to efficiently reproduce the correct behavior of the wave function for all values of r , as long as a dense enough grid is used. Numerov's method is a fourth-order FDM, on par with the fourth-order Runge-Kutta method. However, the advantage is that it is simpler to implement. The ground-state wave function can be presented in the form $\psi_0(r) = r^{-1/2}P(r)$, which transforms Eq. (7) (with $\varepsilon = 0$) to the differential equation

$$\frac{d^2 P(r)}{dr^2} + g(r)P(r) = 0, \quad (\text{B1})$$

where

$$g(r) = \frac{1}{4r^2} + 2[E_0 + w(r)]. \quad (\text{B2})$$

We now assume E_0 is known (it can easily be calculated by, e.g., diagonalizing a Gaussian basis or performing a variational calculation). Numerov's method then reduces this equation to the finite-difference equation

$$f_{n-1}P_{n-1} = (12 - 10f_n)P_n - f_{n+1}P_{n+1}, \quad (\text{B3})$$

where $P_n = P(r_n)$ and $f_n = 1 + (\Delta r)^2 g_n/12$ with $g_n = g(r_n)$. The $N + 1$ discrete points r_n are defined as $r_n = n\Delta r$, where $n = 0, \dots, N$ and $\Delta r = r_N/N$. The two initial points are then chosen as $P_N = 0$ for some large r_N and to comply with Eq. (16) for r_{N-1} . Integrating toward $r = 0$ then yields P at all r_n . The fitting procedure described in the main text is then implemented by fitting Eq. (18) to Eq. (19) in a region $r \in [(j-1)40, j40]$, where $j = 1, 2, \dots$, until convergence to four significant digits. The same P is then used in Eq. (25) and the agreeing significant digits (up to fourth order) are presented in Table I.

[1] H. Wang, C. Zhang, W. Chan, S. Tiwari, and F. Rana, *Nat. Commun.* **6**, 8831 (2015).

[2] O. Lopez-Sanchez, D. Lembke, M. Kayci, A. Radenovic, and A. Kis, *Nat. Nanotechnol.* **8**, 497 (2013).

- [3] Z. Yin, H. Li, H. Li, L. Jiang, Y. Shi, Y. Sun, G. Lu, Q. Zhang, X. Chen, and H. Zhang, *ACS Nano* **6**, 74 (2012).
- [4] F. Withers, O. D. Pozo-Zamudio, A. Mishchenko, A. P. Rooney, A. Gholinia, G. Watanabe, T. Taniguchi, S. J. Haigh, A. K. Geim, A. I. Tartakovskii, and K. S. Novoselov, *Nat. Mater.* **14**, 301 (2015).
- [5] O. Lopez-Sanchez, E. Alarcon Llado, V. Koman, A. Fontcuberta i Morral, A. Radenovic, and A. Kis, *ACS Nano* **8**, 3042 (2014).
- [6] M. Bernardi, M. Palummo, and J. C. Grossman, *Nano Lett.* **13**, 3664 (2013).
- [7] G. Du, Z. Guo, S. Wang, R. Zeng, Z. Chen, and H. Liu, *Chem. Commun.* **46**, 1106 (2010).
- [8] M. Chhowalla, H. S. Shin, G. Eda, L.-J. Li, K. P. Loh, and H. Zhang, *Nat. Chem.* **5**, 263 (2013).
- [9] J. M. Soon and K. P. Loh, *Electrochem. Solid State Lett.* **10**, A250 (2007).
- [10] A. Ramasubramaniam, *Phys. Rev. B* **86**, 115409 (2012).
- [11] S. Latini, T. Olsen, and K. S. Thygesen, *Phys. Rev. B* **92**, 245123 (2015).
- [12] T. C. Berkelbach, M. S. Hybertsen, and D. R. Reichman, *Phys. Rev. B* **88**, 045318 (2013).
- [13] T. G. Pedersen, S. Latini, K. S. Thygesen, H. Mera, and B. K. Nikolić, *New J. Phys.* **18**, 073043 (2016).
- [14] S. Hastrup, S. Latini, K. Bolotin, and K. S. Thygesen, *Phys. Rev. B* **94**, 041401(R) (2016).
- [15] B. Scharf, T. Frank, M. Gmitra, J. Fabian, I. Žutić, and V. Perebeinos, *Phys. Rev. B* **94**, 245434 (2016).
- [16] M. Massicotte, F. Vialla, P. Schmidt, M. B. Lundberg, S. Latini, S. Hastrup, M. Danovich, D. Davydovskaya, K. Watanabe, T. Taniguchi, V. I. Falko, K. Thygesen, T. G. Pedersen, and F. H. L. Koppens, *Nat. Commun.* **9**, 1633 (2018).
- [17] G. H. Wannier, *Phys. Rev.* **52**, 191 (1937).
- [18] F. L. Lederman and J. D. Dow, *Phys. Rev. B* **13**, 1633 (1976).
- [19] T. G. Pedersen, H. Mera, and B. K. Nikolić, *Phys. Rev. A* **93**, 013409 (2016).
- [20] E. Balslev and J. M. Combes, *Commun. Math. Phys.* **22**, 280 (1971).
- [21] J. Aguilar and J. M. Combes, *Commun. Math. Phys.* **22**, 269 (1971).
- [22] O. I. Tolstikhin, T. Morishita, and L. B. Madsen, *Phys. Rev. A* **84**, 053423 (2011).
- [23] P. Cudazzo, C. Attaccalite, I. V. Tokatly, and A. Rubio, *Phys. Rev. Lett.* **104**, 226804 (2010).
- [24] L. V. Keldysh, *JETP Lett.* **29**, 658 (1979).
- [25] M. L. Trolle, T. G. Pedersen, and V. Vénier, *Sci. Rep.* **7**, 39844 (2017).
- [26] M. Abramowitz, *Handbook of Mathematical Functions, With Formulas, Graphs, and Mathematical Tables* (Dover, New York, 1974).
- [27] S. Koch, M. Kira, G. Khitrova, and H. M. Gibbs, *Nat. Mater.* **5**, 523 (2006).
- [28] M. Palummo, M. Bernardi, and J. C. Grossman, *Nano Lett.* **15**, 2794 (2015).
- [29] H. Wang, C. Zhang, W. Chan, C. Manolatou, S. Tiwari, and F. Rana, *Phys. Rev. B* **93**, 045407 (2016).
- [30] C. Poellmann, P. Steinleitner, U. Leierseder, P. Nagler, G. Plechinger, M. Porer, R. Bratschitsch, C. Schüller, T. Korn, and R. Huber, *Nat. Mater.* **14**, 889 (2015).
- [31] H. Shi, R. Yan, S. Bertolazzi, J. Brivio, B. Gao, A. Kis, D. Jena, H. G. Xing, and L. Huang, *ACS Nano* **7**, 1072 (2013).
- [32] D. Sun, Y. Rao, G. A. Reider, G. Chen, Y. You, L. Brézin, A. R. Harutyunyan, and T. F. Heinz, *Nano Lett.* **14**, 5625 (2014).
- [33] A. J. F. Siegert, *Phys. Rev.* **56**, 750 (1939).
- [34] C. W. McCurdy, M. Baertschy, and T. N. Rescigno, *J. Phys. B* **37**, R137 (2004).
- [35] B. Simon, *Phys. Lett.* **71**, 211 (1979).
- [36] C. W. McCurdy, C. K. Stroud, and M. K. Wisinski, *Phys. Rev. A* **43**, 5980 (1991).
- [37] T. N. Rescigno and C. W. McCurdy, *Phys. Rev. A* **62**, 032706 (2000).
- [38] T. Olsen, S. Latini, F. Rasmussen, and K. S. Thygesen, *Phys. Rev. Lett.* **116**, 056401 (2016).
- [39] V. H. Trinh, O. I. Tolstikhin, L. B. Madsen, and T. Morishita, *Phys. Rev. A* **87**, 043426 (2013).
- [40] P. A. Batishchev, O. I. Tolstikhin, and T. Morishita, *Phys. Rev. A* **82**, 023416 (2010).
- [41] L. B. Madsen, O. I. Tolstikhin, and T. Morishita, *Phys. Rev. A* **85**, 053404 (2012).
- [42] L. B. Madsen, F. Jensen, O. I. Tolstikhin, and T. Morishita, *Phys. Rev. A* **87**, 013406 (2013).
- [43] X. L. Yang, S. H. Guo, F. T. Chan, K. W. Wong, and W. Y. Ching, *Phys. Rev. A* **43**, 1186 (1991).
- [44] A. I. Dnestryan and O. I. Tolstikhin, *Phys. Rev. A* **93**, 033412 (2016).
- [45] L. B. Madsen, F. Jensen, A. I. Dnestryan, and O. I. Tolstikhin, *Phys. Rev. A* **96**, 013423 (2017).
- [46] A. I. Dnestryan, O. I. Tolstikhin, L. B. Madsen, and F. Jensen, *J. Chem. Phys.* **149**, 164107 (2018).
- [47] H. Mera, T. G. Pedersen, and B. K. Nikolić, *Phys. Rev. Lett.* **115**, 143001 (2015).
- [48] T. G. Pedersen, *Phys. Rev. B* **94**, 125424 (2016).
- [49] L. S. R. Cavalcante, D. R. da Costa, G. A. Farias, D. R. Reichman, and A. Chaves, *Phys. Rev. B* **98**, 245309 (2018).
- [50] A. Dalgarno, J. T. Lewis, and D. R. Bates, *Proc. R. Soc. London, Ser. A* **233**, 70 (1955).
- [51] A. Scrinzi, *Phys. Rev. A* **81**, 053845 (2010); Eqs. (A1) and (A2) in that paper contain misprints. $(C^{-1})_{12}$ in Eq. (A1) should be replaced by $(C^{-1})_{21}$, and $(C^{-1})_{21}$ in Eq. (A2) should be replaced by $(C^{-1})_{12}$.
- [52] V. I. Krylov, *Approximate Calculation of Integrals* (Dover, New York, 2005).
- [53] A. Scrinzi and N. Elander, *J. Chem. Phys.* **98**, 3866 (1993).

Paper A.

Paper B

Finite-difference time-domain simulation of strong-field
ionization: a perfectly matched layer approach

Høgni C. Kamban, Sigurd S. Christensen, Thomas Søndergaard
and Thomas G. Pedersen

The paper has been published in *Physica Status Solidi B*:
Phys. Stat. Sol. B **257**, 1900467 (2020)
DOI: 10.1002/pssb.201900467

Finite-Difference Time-Domain Simulation of Strong-Field Ionization: A Perfectly Matched Layer Approach

Høgni C. Kamban,* Sigurd S. Christensen, Thomas Søndergaard, and Thomas G. Pedersen

A finite-difference time-domain (FDTD) scheme with perfectly matched layers (PMLs) is considered for solving the time-dependent Schrödinger equation and simulating the laser-induced ionization of two systems: 1) an electron initially bound to a 1D δ potential and 2) excitons in carbon nanotubes (CNTs). The performance of PMLs based on different absorption functions is compared, where slowly growing functions are found to be preferable. PMLs are shown to be able to reduce the computational domain, and thus the required numerical resources, by several orders of magnitude. This is demonstrated by testing the proposed method against an FDTD approach without PMLs and a very large computational domain. It is shown that PMLs outperform the well-known exterior complex scaling (ECS) technique for short-range potentials when implemented in FDTD. For long-range potentials such as in CNTs, however, ECS performs better than PMLs when propagating over many periods.

1. Introduction

It has long been established that excitons must be considered to accurately describe the optical properties of nonmetallic solids. In fact, with the increased interest in low-dimensional solids, understanding excitonic effects becomes even more important, as the reduced screening in low-dimensional semiconductors leads to excitons with extremely large binding energies. Of particular interest have been 2D transition metal dichalcogenides (TMDs) and 1D carbon nanotubes (CNTs). 2D TMDs are known to support exciton binding energies of up to several hundred millielectronvolts,^[1–3] and exciton binding energies in CNTs can be larger still for tubes with small radii.^[4,5] These strongly bound excitons dominate the absorption spectra of both TMDs^[6,7] and CNTs.^[8–11] Monolayer TMDs have been shown to absorb a large amount of sunlight relative to their thickness,^[12] which makes them interesting building blocks in solar cells


and other photocurrent devices.^[12,13] However, to produce a photocurrent in these devices, the excitons must be dissociated into free electrons and holes. Whereas, excitons in bulk semiconductors can usually be dissociated efficiently by thermal agitation, the strongly bound excitons in lower-dimensional structures cannot. Recently, applying a static in-plane electric field over the TMDs as a means of inducing dissociation has gained interest.^[7,14,15] Similarly, the large exciton binding energy in semiconducting CNTs makes it difficult to generate a photocurrent.^[16] Static field-induced exciton dissociation rates in CNTs have been studied both theoretically^[17] and experimentally^[18–20] and may contribute, e.g., to photoconductivity.^[18]

In this article, we are interested in computing exciton dissociation induced by time-dependent electric fields, i.e., laser fields. One of the most reliable techniques of obtaining accurate results in intense laser–matter interactions is to propagate the time-dependent Schrödinger equation (TDSE) and calculate the relevant observables. Strong electric fields lead to a large probability flux traveling out of the central region occupied by the initially localized wave function, which, of course, is exactly what we mean by ionization. If one simply uses Dirichlet boundary conditions at the edges of the simulation domain, a huge domain is required to avoid reflections of the wave function from the boundary. Several methods have been designed to circumvent this problem, with one of the most common ones being absorbing boundaries outside a specified interior domain. Popular methods include complex absorbing potentials (CAPs),^[21] absorbing masks,^[22] and exterior complex scaling (ECS).^[23,24] The goal of the absorbing layers is to leave the wave function unaltered in the interior region, while absorbing it as it moves out of this region. If it is absorbed sufficiently quickly, then one is able to use Dirichlet boundary conditions at a distance into the layer with minimal flux reaching this point and thus avoiding spurious reflections.

The ECS method has been given a lot of attention in recent years, and rightfully so, as it has been shown to be a very efficient absorber in time-dependent Schrödinger problems.^[25,26] A related method that has been given less attention in quantum mechanics is the use of perfectly matched layers (PMLs). The PML method was developed by Berenger for solving Maxwell's equations^[27] and has since been used extensively in classical electromagnetism, where PMLs are applied efficiently

H. C. Kamban, S. S. Christensen, T. Søndergaard, Prof. T. G. Pedersen
Department of Materials and Production
Aalborg University
DK-9220 Aalborg Øst, Denmark
E-mail: hck@mp.aau.dk

H. C. Kamban, Prof. T. G. Pedersen
Center for Nanostructured Graphene (CNG)
DK-9220 Aalborg Øst, Denmark

 The ORCID identification number(s) for the author(s) of this article can be found under <https://doi.org/10.1002/pssb.201900467>.

DOI: 10.1002/pssb.201900467

in FDTD,^[28,29] in frequency-domain finite-element,^[30] and in Fourier-series^[31] approaches. In addition, Lu and Zhu proposed a perturbative approach^[32] to deal with undesired effects of the PML when simulating optical wave guides, and PMLs have, furthermore, been utilized to study sound waves.^[33] Given the success of the PML method in solving problems in electromagnetism, interest in applying it to Schrödinger problems has slowly been increasing. Zheng used it to solve the non-linear Schrödinger equation,^[34] and Nissen and Kreiss have since tried to optimize the PML method for the Schrödinger equation with time-independent potentials^[35] and have, together with Karlsson, applied it to a reactive scattering problem.^[36] PMLs have also been applied to time-dependent density functional theory (TDDFT)^[37] and the Dirac equation.^[38] It is, however, surprising how comparatively little work has been done on applying PMLs in Schrödinger problems, in particular, for explicitly time-dependent problems, such as intense laser–matter interactions.

In this article, we develop a method based on a finite-difference time-domain (FDTD) scheme including a PML to describe the dissociation of excitons in CNTs. The focus of the article is therefore twofold: 1) to compute the laser-induced dissociation rates and 2) compare the accuracy of the PML method with the well-known ECS method. We therefore begin by describing the methodology behind absorbing layers and describe how they are imposed in the two methods. As a preliminary, we proceed by analyzing a zero-range potential. This potential has previously been used to, e.g., study the optical response in 1D semiconductors^[39] and model the ionization of the H^- ion.^[40] The motivation for analyzing the zero-range potential is that it is sufficiently simple that analytical results are available in limiting cases. It may therefore be used to ensure that the methods work as intended. We thereafter turn to analyze the interaction between CNT excitons and a laser field, and in so doing, we again compare the accuracy of the PML method to that of ECS.

2. Time-Dependent Schrödinger Problem with a Laser Field

As will be discussed later, the exciton problem may be reformulated as a Schrödinger-type problem. We therefore begin by setting up the Schrödinger problem quite generally. The time-dependent Schrödinger equation perturbed by a laser field reads (in atomic units)

$$i\frac{\partial}{\partial t}\psi(\mathbf{r},t) = \left[-\frac{1}{2}\nabla^2 + H_g(\mathbf{r},t) + V(\mathbf{r})\right]\psi(\mathbf{r},t), \quad (1)$$

where H_g describes the interaction induced by the laser field. Here, the subscript g refers to the gauge, in which the interaction is considered. We shall work only in the dipole approximation, such that neither electric fields, nor vector potentials have any spatial dependence. This leads to the interaction in the velocity gauge (VG) being

$$H_V = \mathbf{p} \cdot \mathbf{A}(t), \quad (2)$$

where \mathbf{p} is the momentum operator and \mathbf{A} is the vector potential. Note that the usual $A(t)^2/2$ term has been removed by a unitary

transformation. We will consider the monochromatic field defined by

$$\mathbf{A}(t) = A_0 \cos(\omega t) \hat{\mathbf{x}}. \quad (3)$$

In the length gauge (LG), the interaction is given, in terms of the electric field

$$\mathcal{E}(t) = -\frac{\partial \mathbf{A}(t)}{\partial t} = \mathcal{E}_0 \sin(\omega t) \hat{\mathbf{x}}, \quad (4)$$

by

$$H_L = \mathbf{r} \cdot \mathcal{E}(t). \quad (5)$$

When introducing absorbing layers into the Schrödinger equation, the goal is to be able to reproduce the exact wave function in an interior box $|\mathbf{r}| \leq R_0$ for relevant time periods. One therefore seeks to modify the TDSE so that the solution to the modified equation ψ satisfies

$$\psi(\mathbf{r},t) = \psi_{\text{ex}}(\mathbf{r},t) \quad \text{for } |\mathbf{r}| \leq R_0, \quad (6)$$

where ψ_{ex} is the exact wave function. To be able to quantify the error between the exact and approximate wave functions by a single number, the error measurement introduced by Scrinzi^[26] will be used

$$\sigma(R_0) = 1 - \frac{|\langle \psi_{\text{ex}} | \psi \rangle_{R_0}|^2}{\langle \psi_{\text{ex}} | \psi_{\text{ex}} \rangle_{R_0} \langle \psi | \psi \rangle_{R_0}}, \quad (7)$$

where the scalar product is to be taken in the region $|\mathbf{r}| \leq R_0$, i.e.

$$\langle f | g \rangle_{R_0} = \int_{|\mathbf{r}| \leq R_0} f^*(\mathbf{r}) g(\mathbf{r}) d\mathbf{r}. \quad (8)$$

3. Exterior Complex Scaling

The literature covering complex scaling is vast (see Balslev and Combes,^[41] Aguilar and Combes,^[42] Doolen et al.,^[43] Ho,^[44] Reed and Simon,^[45] and Bengtsson et al.,^[46] and references therein), and for this reason, we shall only describe briefly the most relevant aspects to this article before describing how PMLs are implemented. For simplicity, we will restrict the discussion to 1D x . The simplest form of complex scaling is implemented by scaling the coordinates uniformly according to $x \rightarrow xe^{i\theta}$, where θ will be taken as a purely real number. The motivation is that the outgoing waves $\exp(ikx)$ become exponentially decaying waves if the rotational angle θ is chosen large enough. This transformation, referred to as uniform complex scaling (UCS), has been used with great success in finding ionization rates for static electric fields^[7,47,48] and in solving the TDSE.^[46] In certain situations, however, one may wish to leave the domain untransformed in an interior region and introduce complex scaling only in an outer region. The original motivation was that UCS cannot be used with the Born–Oppenheimer approximation.^[49] Furthermore, when dealing with sufficiently weak electric fields, ionization rates typically become so low that UCS results in a wave function that (numerically) vanishes before it reaches the important region far from the core.^[15]

The ECS^[25,49–51] procedure circumvents these problems and is implemented in 1D by transformation

$$x \rightarrow \tilde{x} = \begin{cases} x & \text{for } |x| < R_0 \\ e^{i\theta}(x \pm R_0) \mp R_0 & \text{for } \mp x > R_0, \end{cases} \quad (9)$$

where R_0 is referred to as the scaling radius. This transformation turns outgoing waves into decaying waves in the absorbing layer while leaving them unaffected in the interior region.

The resulting behavior of the wave function in the absorbing layer is slightly different in the two gauges. The exponential propagator can be constructed as usual,^[23] and the perturbing part can be written as

$$\exp(-iH_L\Delta t) = \exp\{-i\mathcal{E}(t)[\cos\theta(x \pm R_0) \mp R_0]\Delta t\} \times \exp\{\mathcal{E}(t)\sin\theta(x \pm R_0)\Delta t\} \quad (10)$$

in LG, and as

$$\exp(-iH_V\Delta t) = \exp(-i\cos\theta A(t)p_x\Delta t) \times \exp(-\sin\theta A(t)p_x\Delta t) \quad (11)$$

in VG. The first terms on the right-hand sides of Equation (10) and (11) are oscillatory, whereas the second terms are either exponentially increasing or exponentially decreasing. In LG, this depends on the sign of the oscillatory field $\mathcal{E}(t)$ and in VG on the sign of $A(t)$. Thus, in both cases, one may obtain an undesired exponentially increasing behavior in the absorbing layer. Given that the behavior depends on the sign of the field or vector potential, the propagators will oscillate between amplifying and damping the wave function exponentially. In practice, we have found that the exponential behavior outside of the scaling radius is much more apparent in LG than in VG. Furthermore, in LG, the exponential behavior is more volatile for a larger x , which may lead to numerical instabilities if a wide absorbing layer is desired. In practice, we have not found these growing terms to cause numerical instabilities for moderate frequencies, whereas for low frequencies, they lead to a numerically diverging wave function. This is in agreement with the observations in the study by He et al.^[23]

4. Perfectly Matched Layers

The PML scheme for the TDSE is usually derived by assuming that the potential is both spatially and temporally invariant, and then modal analysis is performed on the Laplace-transformed equation to ensure that the solution decays outside the interior domain, i.e., $|x| > R_0$.^[34–36] The transformation can be formulated as

$$x \rightarrow \tilde{x} = \begin{cases} x & \text{for } |x| < R_0 \\ x + i\sigma_0 \int^x f(x')dx' & \text{for } |x| > R_0, \end{cases} \quad (12)$$

where σ_0 is a constant referred to as the absorption strength, and f is the absorption function. The absorption function is zero inside the interior $|x| \leq R_0$ and positive otherwise. Specific forms will be discussed later. Unlike in ECS, the transformation in Equation (12) is not applied to the potential. Thus, the PML

method can be understood as a transformation of the differential operator

$$\frac{\partial}{\partial x} \rightarrow c(x) \frac{\partial}{\partial \tilde{x}}, \quad (13)$$

where $c(x) = 1/[1 + i\sigma_0 f(x)]$. The PML equation in 1D therefore becomes

$$i \frac{\partial}{\partial t} \psi = \left[-\frac{1}{2} c(x) \frac{\partial}{\partial \tilde{x}} c(x) \frac{\partial}{\partial \tilde{x}} + H_g(x, t) + V(x) \right] \psi, \quad (14)$$

which coincides with the usual TDSE inside a box of radius R_0 as $c(|x| \leq R_0) = 1$. Note that the momentum operator in H_V (Equation (2)) is also transformed according to Equation (13). As the transformation is only applied to the spatial derivatives, it is only reasonable to expect Equation (14) to yield a good approximation if R_0 is chosen sufficiently large so that the variations in the potential $V(x)$ in the exterior are negligible. This is the case for any nonzero R_0 for the zero-range potential $V(x) = -\delta(x)$. However, the interaction in LG effectively modifies the potential so that it includes a linear term which does not vanish outside the interior. One may therefore speculate to which degree Equation (14) in LG is able to approximate the exact wave function in the interior. Indeed, as we show numerically later, implementing the PML in LG introduces significantly larger errors than in VG. The ECS and PML methods have been implemented using a Crank–Nicolson (CN) finite difference scheme. The technical details can be found in Appendix A.

Although the following analysis is made effectively for 1D systems, generalization of PMLs to cases of higher dimensions is straightforward. One simply transforms the spatial derivatives in the x -, y -, and z -directions independently as in Equation (13). The absorption functions need not be identical, and it is therefore possible to control the rate of absorption in different directions. When implemented in more than one dimension, it is advantageous to use the alternating direction implicit (ADI) method combined with Strang's splitting technique.^[34]

4.1. Absorption Function

It is important that the absorption function f be chosen positive to ensure decay of the wave function as it travels out of the interior domain. Previous choices include low-degree power functions^[27,34] and singular functions.^[52] It is interesting to examine whether or not there is a substantial difference between the numerical accuracy obtainable with the different functions. To this end, we will compare four different absorption functions, namely

$$f(y) = \Theta(y) \begin{cases} d(d - \gamma + \epsilon)^{-1} - 1 \\ \gamma^2 \\ \gamma^3 \\ \tanh(2\gamma d^{-1} - 1) - \tanh(-1), \end{cases} \quad (15)$$

where $\gamma = |x| - R_0$, ϵ is some small positive number, Θ is a step function equal to unity for $\gamma \geq 0$ and zero otherwise, and d is the width of the absorbing layer. For ϵ , we have used 10^{-4} , as we have not found the results to be highly dependent on ϵ .

5. Zero-Range Potential

The zero-range potential $-\delta(x)$ serves as a good check that the methods introduced behave as expected. The reason is that it is sufficiently simple that analytical results may be obtained in limiting cases, and we are, therefore, able to compare the numerical results with already known results. As expressing the exact $-\delta$ potential is not feasible in a finite-difference scheme, we approximate it by

$$V(x) = \begin{cases} -\frac{1}{2b} & \text{for } |x| < b, \\ 0 & \text{otherwise.} \end{cases} \quad (16)$$

We have used $b = 5 \times 10^{-3}$ for the calculations in this article, which leads to a ground-state energy of $E_0 = -0.4967$ a.u. (as opposed to $-1/2$ a.u. for the zero-range potential).

5.1. Error Analysis

To illustrate the effect of absorbing layers on the wave function, as well as the temporal oscillations outside R_0 when implementing ECS in LG that were discussed briefly in the ECS section earlier, we show the absolute square of the wave function in **Figure 1** at three different times. The oscillations are immediately clear. The absolute square of the wave function is, however, graphically indistinguishable in the interior for ECS implemented in LG and VG. For the PML calculations, the results are not as equal footed. The LG calculation introduces non-negligible reflections, leading to a large error inside the interior. This is, of course, what we seek to avoid, and thus one must be careful in implementing PML in LG. For VG, the PML and ECS wave functions are indistinguishable for $|x| \leq R_0$.

To perform error analysis, we need a reference function. It was obtained by calculating the error in Equation (7) inside $R_0 = 20$ a.u. at $t = 200$ a.u. between two wave functions without any transformation and with Dirichlet boundary conditions set at $x = \pm n \times 500$ for ψ and $x = \pm(n+1) \times 500$ a.u. for ψ_{ex} , where n is a positive integer, which was increased by one until the error vanished within numerical precision. This occurred at $n = 8$, and thus without any absorbing layer a domain width of at least 8000 a.u. is needed. To ensure a numerically exact reference function, we have used a domain width of 10 000 a.u. for ψ_{ex} in the error calculations. In **Figure 2**, we show the error calculated by Equation (7) at $t = 200$ a.u. as a function of the PML width d for the different absorption functions with various absorption strengths σ_0 . It is clear that PML should be implemented in VG to obtain an accurate wave function in the interior. We also notice that an absorption function that grows slowly leads to a lower error at the cost of slower convergence. The reason is that less of the wave function will be (numerically) reflected upon entering the absorbing layer when the transition is more gradual. The error introduced by the power functions converge to a constant value for a sufficiently large d . This indicates that the entire outgoing flux has either been absorbed or reflected from the layer, and further increasing d does not make any difference. It is worth noting that the PML method with a quadratic absorption function (Figure 2b) leads to errors of order

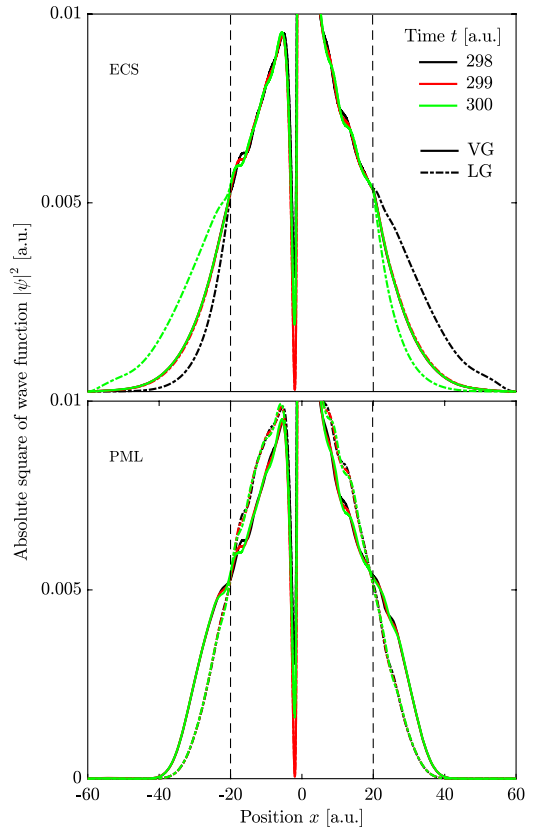


Figure 1. Absolute square of wave functions calculated with ECS (upper) and PML (lower) for three different times with $R_0 = 20$ a.u. (indicated by vertical dashed lines). The solid and dashed dotted lines are calculated in VG and LG, respectively. The field parameters are $E_0 = 0.1$ a.u. and $\omega = 0.52$ a.u., and the field has been turned on smoothly over three optical cycles.

10^{-15} for an absorbing layer of around $d = 40$ a.u. Thus, the domain width required to obtain an excellent approximation to the exact wave function is $2(d + R_0) = 120$ a.u., significantly lower than the domain width of 8000 a.u. needed without any absorbing layer. As the calculation scales directly with the number of points used to describe the entire domain (physical + absorbing), this results in a significant computational speed-up. To obtain a short computational time, it is therefore desirable to choose the box size, PML width, and σ_0 such that the entire domain becomes as small as possible, while ensuring that the errors introduced are not too large. For the nearly singular function and the tanh function, increasing d leads to an absorption function that grows more slowly. For this reason, the errors they induce do not converge in the same manner as those induced by the power functions. Rather, they continue to decrease as the absorbing layers become wider. The PML errors should be

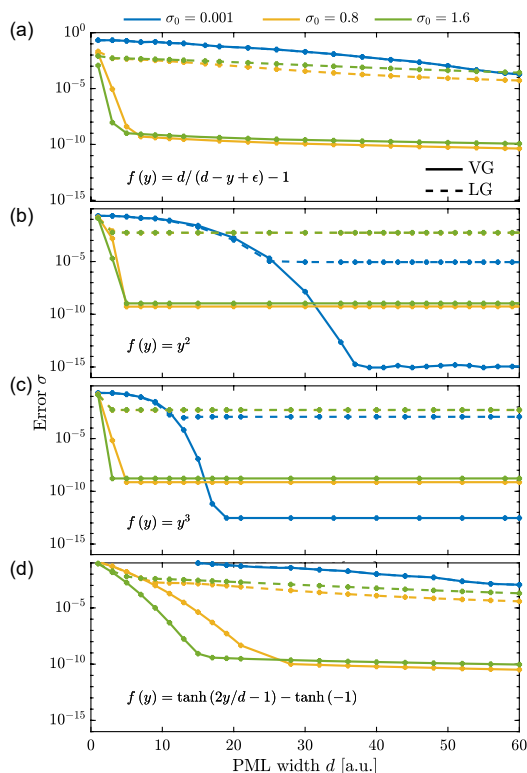


Figure 2. Error at $t = 200$ a.u. as a function of PML width for four different absorption functions and various absorption coefficients. The solid and dashed lines correspond to PML VG and LG, respectively. The scaling radius is set to $R_0 = 20$ a.u. The field parameters are the same as in Figure 1.

compared to those introduced by the ECS method, shown in Figure 3, for which both LG and VG calculations converge to the same error and are nearly indistinguishable. A low rotational angle θ can be seen to introduce lower errors, as less of the wave function will be reflected upon entering the absorbing layer, exactly as with the PML method. By comparing the errors introduced by ECS to those for PMLs with a quadratic absorption function in Figure 2b, we see that the ECS errors for comparable absorption widths converge to values that are around six orders of magnitude larger. For PMLs with a cubic absorption function (Figure 2c), the ECS errors are around four orders of magnitude larger. This might be due to the poor performance of ECS when implemented in finite-difference schemes.^[50] The same behavior is shown in Figure 4, where the error is shown as a function of time. The PML LG calculation introduces much larger errors than the other two methods, and the ECS LG and VG errors are graphically indistinguishable. Again, the PML VG calculation leads to the lowest error by several orders of magnitude. The dashed lines show a scaling radius of $R_0 = 10$ a.u. as opposed

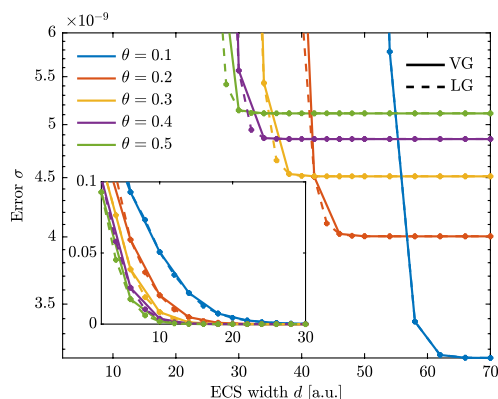


Figure 3. Error at $t = 200$ a.u. as a function of ECS width for various angles of rotation. The field parameters are the same as in Figure 1. The inset shows the behavior for smaller widths.

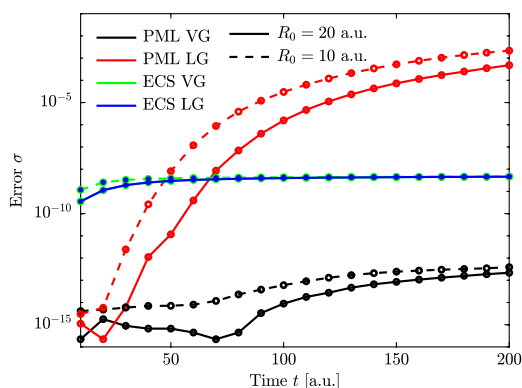


Figure 4. Error as a function of time. The absorbing boundary is located at $R_0 = 20$ and at $R_0 = 10$ a.u. for the solid and dashed lines, respectively. The PML calculations have been made with $\sigma_0 = 0.001$ and the cubic absorption function, whereas the ECS calculations have been made with $\theta = 0.35$. In both cases the absorption width is $d = 40$ a.u. The field parameters are the same as in Figure 1.

to $R_0 = 20$ a.u. As shown, reducing the size of the box does not have a large impact on the errors in the interior domain and particularly not for ECS.

5.2. Polarizability and Ionization

In the previous section, the error of the wave function inside the box $|x| < R_0$ was analyzed. If the wave function can be reproduced, then the desirable observables can be calculated, as long as the box size is chosen adequately. Although the error measurement defined by Equation (7) is a meaningful parameter, we are

unable to directly relate it to physical observables. As an additional check, we therefore demonstrate that we are able to reproduce the frequency dependent polarizability in the weak-field limit. Numerically, the polarizability α can be found by calculating $\langle x \rangle / \mathcal{E}_0$ in the weak-field limit and relating it to the real and imaginary part of α . Here, $\langle x \rangle$ is the expectation value of x . As the field amplitude is extremely low, and $\langle x \rangle$ is only needed over a single period, the integral in $\langle x \rangle$ can, to an excellent approximation, be restricted to the interior region. An analytical expression can be found for α of the δ -potential ground state using linear perturbation theory.^[53] It is given by

$$\alpha(\omega) = \frac{2 - \omega^2 - \sqrt{1 + 2\omega} - \sqrt{1 - 2\omega}}{\omega^4}. \quad (17)$$

As shown in **Figure 5**, the PML simulations using a low-field strength of $\mathcal{E}_0 = 10^{-6}$ a.u. are in excellent agreement with the analytical results.

A special interest in this article is to obtain the strong-field ionization rate. The probability of occupying a bound state (i.e., not being ionized) can be found by

$$P_{\text{bound}}(t; \mathcal{E}_0) = \sum_b |\langle \varphi_b | \psi_{\text{ex}} \rangle|^2, \quad (18)$$

where the sum is to be taken over all bound states. For numerical calculations, however, one may cut the sum after convergence to a desired number of digits. Let us denote the most delocalized state included in the sum by φ_B , such that from some number L

$$|\varphi_B(x)| \geq |\varphi_b(x)| \quad \text{for } |x| \geq L, \quad (19)$$

where b refers to all states included. If L is chosen such that φ_B is negligible for $|x| > L$, then all integrals in Equation (18) may be restricted to $|x| < L$. By choosing the scaling radius R_0 to coincide with L , we can therefore describe all bound states, as well as obtain an excellent approximation to the wave function, in the interior domain, allowing us to implement Equation (18) in

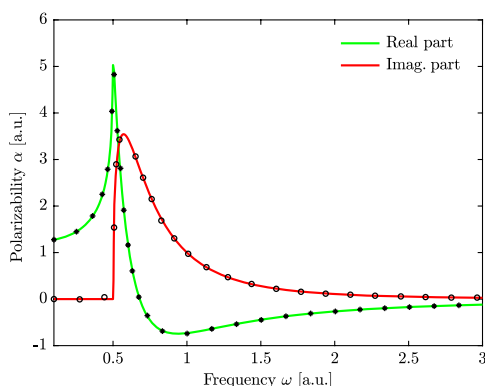


Figure 5. Polarizability calculated from first-order perturbation theory (solid lines) and the PML method (markers). A field strength of $\mathcal{E}_0 = 10^{-6}$ a.u. was used.

the present approach. For the short-range potential defined by Equation (16), there is only one bound state, and it decays exponentially for $|x| > b$. Therefore, a scaling radius of $R_0 = 20$ a.u. is expected to be adequate. The probability of not being ionized is shown as a function of time in **Figure 6**, where the ECS and PML calculations are compared with a converged CN calculation in an untransformed domain. As is evident, the result obtained by the PML method in LG is the only one that can be distinguished from the other ones. This is yet another indication that care must be taken when implementing PMLs in LG.

To obtain the time-dependent ionization rate Γ , we use

$$\Gamma(t; \mathcal{E}_0) = -\frac{d}{dt} \ln P_{\text{bound}}(t; \mathcal{E}_0). \quad (20)$$

The ionization rate defined by Equation (20) will oscillate in time. It is therefore convenient to average the time-dependent ionization rate over a number of periods to remove these oscillations and thereby obtain a time-independent ionization rate, i.e.

$$\langle \Gamma(\mathcal{E}_0) \rangle = \frac{\omega}{2n\pi} \int_{t_0}^{t_0 + 2n\pi/\omega} \Gamma(t; \mathcal{E}_0) dt, \quad (21)$$

where n is the number of periods, and t_0 is an initial time taken after the field has been turned on. The ionization rate averaged over two periods is shown in the upper panel of **Figure 7** for $\omega = 0.2$ a.u. As is evident, the four methods yield identical results. Furthermore, the shape of the ionization rate is consistent with the results for three-photon ionization in the study by Scharf et al.^[40]

In the adiabatic limit, one can obtain analytical results for the ionization rate of the zero-range potential. By setting up the Schrödinger equation for a static electric field $\mathcal{E}_{\text{DC}} > 0$ and requiring that the wave function becomes an outgoing wave as^[54] $x \rightarrow -\infty$, one can obtain the following condition

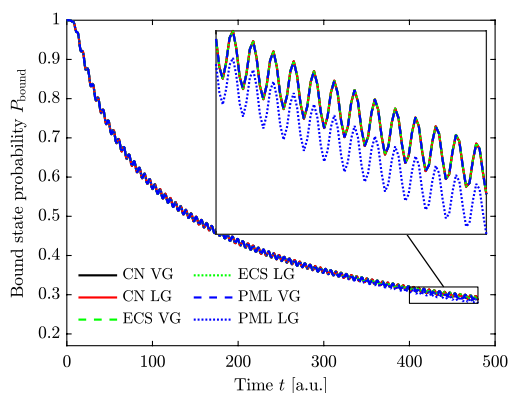


Figure 6. Probability of occupying a bound state as a function of time. The results obtained with absorbing layers (ECS and PML) are compared with those obtained with the CN scheme without any absorbing layers. The field parameters are the same as in Figure 1, and the field has been turned on smoothly over one optical cycle.

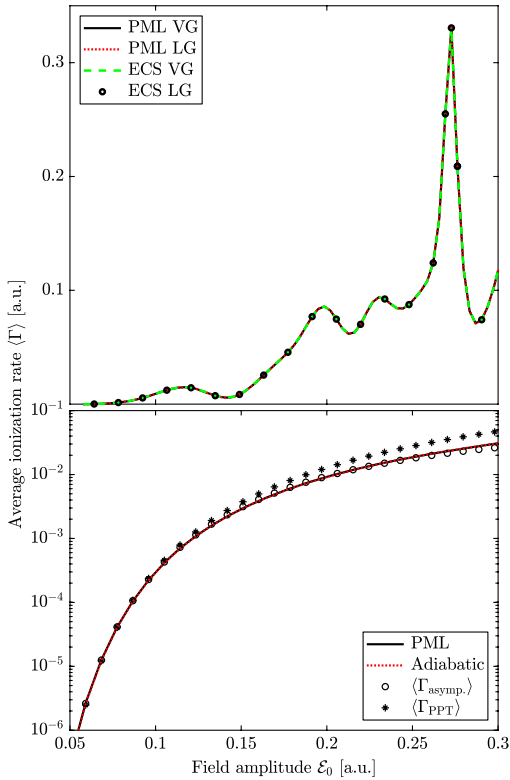


Figure 7. Ionization rate for $\omega = 0.2$ a.u. (upper) and $\omega = 0.01$ a.u. (lower). For the larger frequency, the vector potential has been turned on smoothly over $t = 35$ a.u., while for the lower frequency the electric field has been turned on linearly over the same amount of time. The ionization rate in Equation (20) has been averaged over $[4\pi/\omega; 8\pi/\omega]$ for the larger frequency, and over $[\pi/2\omega; 5\pi/2\omega]$ for the lower frequency.

$$\frac{\mathcal{E}_{\text{DC}}^{1/3}}{2^{2/3}\pi} - \text{Ai}(\lambda)\text{Bi}(\lambda) = i\text{Ai}^2(\lambda), \quad (22)$$

where $\lambda = -2^{1/3}E\mathcal{E}_{\text{DC}}^{-2/3}$, and Ai and Bi are Airy functions of the first and second kind,^[55] respectively. Solving Equation (22) numerically one obtains complex energies, and the DC ionization rate is then given by^[47,54] $\Gamma_{\text{DC}}(\mathcal{E}_{\text{DC}}) = -2\text{Im}[E(\mathcal{E}_{\text{DC}})]$. In the adiabatic regime, the ionization rate by an oscillating monochromatic field is the cycle average of the DC ionization rate corresponding to the instantaneous static electric field at a specific time^[56] $\mathcal{E}(t)$, that is

$$\langle \Gamma_{\text{Adiabatic}}(\mathcal{E}_0) \rangle = \frac{\omega}{2\pi} \int_0^{2\pi/\omega} \Gamma_{\text{DC}}[\mathcal{E}(t)] dt. \quad (23)$$

As shown in the lower panel of Figure 7, this adiabatic ionization rate corresponds exceptionally well with the average ionization rate obtained from Equation (21) with $t_0 = \pi/2\omega$ and $n = 1$,

i.e., $t \in [\pi/2\omega; 5\pi/2\omega]$. It should be noted here that, in this low-frequency limit, ECS in both LG and VG, as well as PML in VG, diverge numerically. This phenomenon was briefly discussed earlier and in more detail in the study by He et al.^[23] Thus, the low-frequency ionization rate has been calculated, implementing PML in LG. In general, one should choose the box size to be larger than the electron quiver amplitude \mathcal{E}_0/ω^2 . For the low frequency in Figure 7, the largest field considered results in a quiver amplitude of 3000 a.u., which is significantly larger than the $R_0 = 20$ a.u. used in the calculation. Nevertheless, the errors introduced by the PML LG method for low frequencies are fairly low for $t \lesssim 5\pi/2\omega$ even with $R_0 = 20$ a.u. In addition, the ionization rate is not as sensitive to errors in the wave function as the error measurement in Equation (7). We are therefore able to obtain accurate ionization rates using a very small box size.

Two further comparisons are made in the lower panel of Figure 7. The first is an analytical approximation to the low-frequency ionization rate. This can be obtained by analyzing the asymptotic behavior of the Airy functions. For low-field strengths, $|\lambda|$ tends to infinity. In fact, both the real and imaginary part of λ tend to $+\infty$ for $\mathcal{E}_0 \rightarrow 0$. Substituting the asymptotic expressions of the Airy functions^[55] into Equation (22), one obtains a polynomial in the electric field multiplied by an exponential function. Solving for the imaginary part of the energy, while retaining only first-order terms in the polynomial, then leads to

$$\Gamma_{\text{asympt.}}(\mathcal{E}_{\text{DC}}) = \left(1 - \frac{5}{3}\mathcal{E}_{\text{DC}}\right) \exp\left(-\frac{2}{3\mathcal{E}_{\text{DC}}}\right). \quad (24)$$

The ionization rate of the monochromatic field can then again be obtained by Equation (23) using Equation (24) for Γ_{DC} . It is shown to agree with the first two methods for weak fields. The final comparison is made with the expression obtained by Perelomov, Popov, and Terent'ev (PPT)^[57] for the adiabatic ionization rate for the zero-range potential in a monochromatic field with amplitude \mathcal{E}_0

$$\langle \Gamma_{\text{PPT}}(\mathcal{E}_0) \rangle = \left(\frac{3\mathcal{E}_0}{\pi}\right)^{1/2} \exp\left(-\frac{2}{3\mathcal{E}_0}\right). \quad (25)$$

It again agrees for weaker fields but as opposed to the approximation obtained by the asymptotic analysis it overestimates the ionization rate for strong fields.

6. Excitons in CNTs

While the zero-range potential discussed earlier is very useful for probing the accuracy of PMLs in laser-matter interactions, it does not represent any physical system. In this section, we are interested in computing dissociation rates for excitons in CNTs and in so doing analyze the errors introduced by PMLs and ECS for a more realistic potential. To describe excitons from first principles, one must solve the many-body Bethe-Salpeter equation, which is a computationally tedious task even for simple structures. Following previous work on excitons in CNTs,^[5,58] we model the excitons as electron-hole pairs confined to the surface of an infinitely long cylinder of radius r . By expressing the

problem in terms of the relative coordinate $\mathbf{r}_{eh} = \mathbf{r}_e - \mathbf{r}_h$ of the electron–hole pair, an equation that is mathematically similar to the single electron Schrödinger equation may be obtained. The separation between the electron and hole may then be written as

$$d = \sqrt{x^2 + 4r^2 \sin^2\left(\frac{\phi}{2}\right)}, \quad (26)$$

where r is the CNT radius, x is the electron–hole separation along the long axis, and ϕ the angular separation around circumference of the cylinder. If the radius of the nanotube is sufficiently small, then it is a reasonable approximation to average the interaction between the electron and hole around the circumference of the cylinder. For a screened Coulomb interaction, this leads to^[58,59]

$$V(x) = -\frac{1}{2\pi r} \int_0^{2\pi} \frac{1}{\epsilon \sqrt{x^2 + 4r^2 \sin^2\left(\frac{\phi}{2}\right)}} r d\phi = -\frac{2}{\pi|x|\epsilon} K\left(-\frac{4r^2}{x^2}\right), \quad (27)$$

where ϵ is the dielectric constant, and K is the complete elliptical integral of the first kind.^[55] This potential diverges logarithmically for $x \rightarrow 0$ and approaches a screened Coulomb potential $V(x) = -|ex|^{-1}$ in the limit $x \rightarrow \infty$. It does therefore not have the cut-off spatial behavior found for the zero-range potential in the previous section. The CNT excitons may then be described by the 1D equation

$$i \frac{\partial}{\partial t} \psi(x, t) = \left[-\frac{1}{2\mu} \frac{\partial^2}{\partial x^2} + H_g(x, t) + V(x) \right] \psi(x, t), \quad (28)$$

where μ is the reduced mass and H_g again describes the interaction with the laser field. It is convenient to define a different set of units^[5] which will be referred to as exciton units (e.u.). Whereas in atomic units one measures length and energy in Bohr radii $a_0 \approx 0.529 \text{ \AA}$ and Hartrees $E_h \approx 27.2 \text{ eV}$, they are measured as $a_0^* = \epsilon a_0 / \mu$ and $E_h^* = \mu E_h / \epsilon^2$ in exciton units. The units of time and electric field strength therefore become \hbar / E_h^* and E_h^* / ea_0^* , respectively, where e is the elementary charge. The advantage of using exciton units is that μ and ϵ are eliminated from Equation (28), which allows computation of quite general results using only a single nontrivial parameter r . Furthermore, it turns out that the radius r measured in exciton units is $\approx 0.1 \text{ e.u.}$, regardless of the chiral index of the CNT.^[5] A CNT radius of $r = 0.1 \text{ e.u.}$ will therefore be used throughout. Such a CNT supports an exciton ground state with energy $E_0 \approx -3.9 \text{ e.u.}$

6.1. Error Analysis

We will begin by analyzing the error σ as a function of absorption width d after propagating the ground state for $t = 50 \text{ e.u.}$ in a field with amplitude $\mathcal{E}_0 = 2.23 \text{ e.u.}$ and frequency $\omega = 1 \text{ e.u.}$ These errors are shown in **Figure 8** for the PML method and in **Figure 9** for ECS. It is clear from the previous section that a low absorption coefficient σ_0 is preferable, and therefore $\sigma_0 \in [0.001, 0.01, 0.1]$ will be used for the CNT potential. Similar trends are observed as for the zero-range potential: the quadratic absorption function with the lowest σ_0 again introduces the

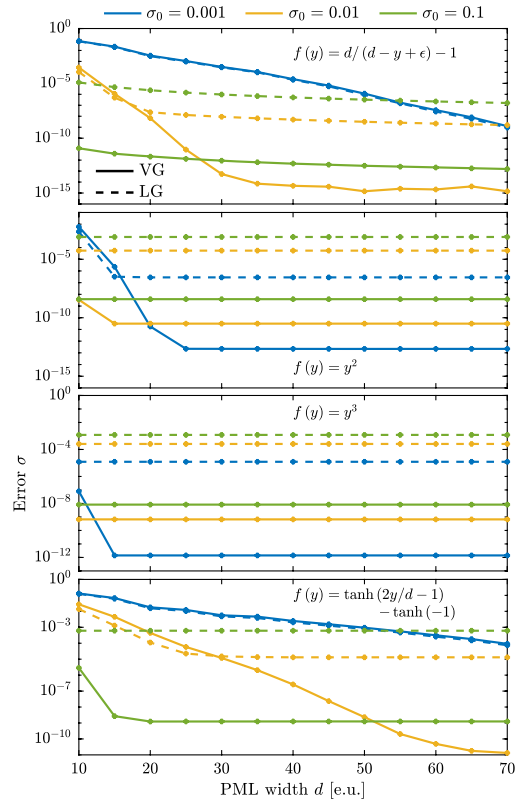


Figure 8. Error at time $t = 50 \text{ e.u.}$ as a function of PML width for four different absorption functions and various absorption coefficients. The solid and dashed lines correspond to PML VG and LG, respectively. The field parameters are $\mathcal{E}_0 = 2.23 \text{ e.u.}$ and $\omega = 1 \text{ e.u.}$, and the field has been turned on smoothly over three optical cycles.

lowest error, but the error converges slower than for, e.g., the cubic absorption function. The two power functions with a low absorption coefficient clearly outperform the other functions. Upon comparing the errors introduced by PMLs to those introduced by ECS in **Figure 9**, it is evident that the PML method again introduces lower errors for comparable absorption widths and properly chosen absorption functions. One may be tempted to reduce the ECS errors by simply choosing a lower θ . However, already at $\theta = 0.1$, an absorption width of $d \approx 25 \text{ e.u.}$ is required for convergence to an error of around 2.3×10^{-10} , whereas PMLs with $d = 25 \text{ e.u.}$, $\sigma_0 = 0.001$, and a quadratic absorption function yield an error of around 2.2×10^{-13} . If a cubic absorption function is used instead, an error of around 1.4×10^{-12} is obtained already at $d = 15 \text{ e.u.}$

By simply analyzing the error at $t = 50 \text{ e.u.}$, it seems the PML method far outperforms the ECS method. Nevertheless, the results are not as clear when analyzing the errors as a function of time. **Figure 10** shows the errors introduced by propagating

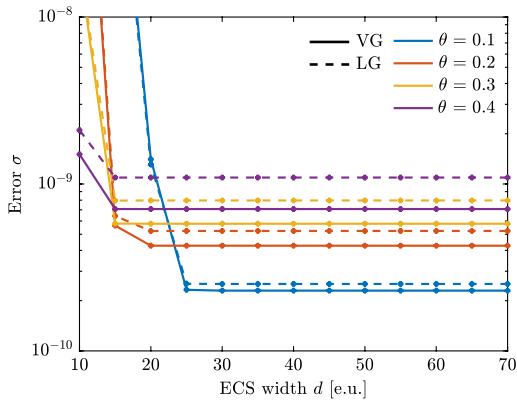


Figure 9. Error at time $t = 50$ e.u. as a function of ECS width for various angles of rotation. The field parameters are the same as in Figure 8.

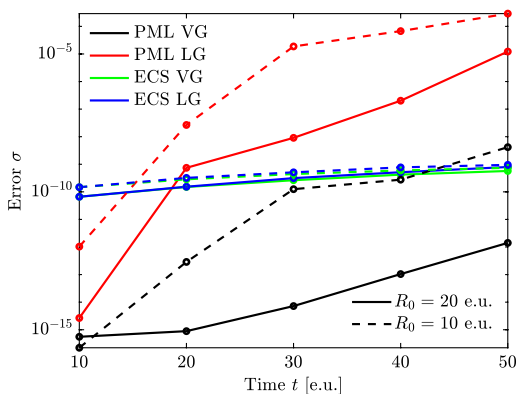


Figure 10. Error as a function of time. The absorbing boundary is located at $R_0 = 20$ e.u. and $R_0 = 10$ e.u. for the solid and dashed lines, respectively. The PML calculations have been made with $\sigma_0 = 0.001$ and the cubic absorption function, while the ECS calculations have been made with $\theta = 0.3$. In both cases the absorption width is $d = 20$ e.u. The field parameters are the same as in Figure 8.

the ground state in the same field but sampled at every $t = 10$ e.u. In addition, two differently sized physical domains are considered. One with the absorbing layers placed at $R_0 = 10$ e.u. (dashed) and another with $R_0 = 20$ e.u. (solid). For the larger physical domain, PML VG introduces the lowest errors for $t \leq 50$ e.u. It does, however, grow quite rapidly as the propagation time increases. This growth is even more pronounced for the smaller physical domain ($R_0 = 10$ e.u.), where it becomes larger than the errors for both ECS LG and ECS VG at $t = 50$ e.u. As the ideal absorbing layer is not this sensitive to the position of the layers nor propagation time, PMLs implemented in the FDTD scheme do not seem promising for potentials that reach into the absorbing layers.

6.2. Exciton Dissociation in CNTs

We now turn to discussing exciton dissociation in CNTs induced by a laser field. Unlike the zero-range potential used in the previous section, the CNT potential supports many bound states, some of which have large exciton radii. In principle, all of these states must be included in Equation (18) to obtain (numerically) exact dissociation probabilities. Nevertheless, the dissociation rate may be approximated by including only the first few states in the sum, as the higher excited states dissociate much faster than these states. The first three states have energies -3.9 , -0.46 , and -0.26 e.u., respectively, and are sufficiently localized such that a small physical domain with $R_0 = 20$ e.u. may be used. The approximate dissociation rate is shown in Figure 11, and it has been checked that all four methods yield identical results. It should be mentioned that the reason that the PML results are graphically indistinguishable from the ECS results, even though the error in the PML wave function is quite large (Section 6.1), is that the overlap integrals in Equation (18) are not sensitive to small variations in the wave function. The largest errors in the wave function are found near the edge of the physical domain. In this region, the three states considered are very close to zero, and the product $\phi_b^* \psi$ will therefore remain small in this region, leading to almost identical integrals. If, however, an observable that is sensitive to the details of the wave function is desired, a much larger box size will be required. The vector potential used in the calculation has been turned on smoothly over three optical cycles with $\omega = 1$ e.u., and the depletion rate has then been computed using Equation (21) with $n = 4$, i.e., averaging the time-dependent dissociation rate over four optical cycles. The reason for averaging over such a large number of periods is that one obtains a much more detailed spectrum. For example, the local minimum around $\mathcal{E}_0 = 1.9$ e.u. is not present when averaging over two periods. It is clear that certain field strengths lead to much larger dissociation rates than others,

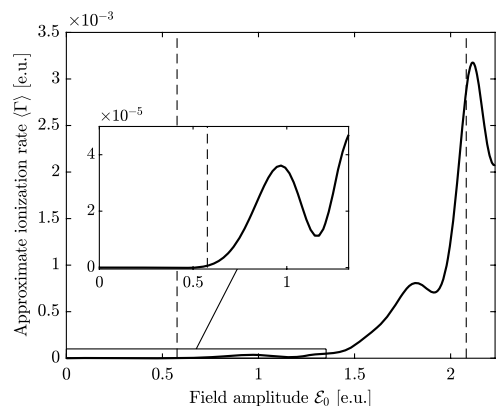


Figure 11. Exciton dissociation rate for $\omega = 1$ e.u. The vector potential has been turned on smoothly over three optical cycles, and the depletion rate has been averaged over four optical cycles (after the field has been turned on).

which suggests the possibility of tuning the laser amplitude to optimize dissociation. It is common to attribute the local extrema to the ponderomotive energy E_p , which is the cycle-averaged quiver energy of a free electron in a monochromatic laser field $E_p = \mathcal{E}_0^2/4\omega^2$. By assuming that the energy required to dissociate the exciton is $|E_0| + E_p$, dissociation is only possible with N photons if $N\omega$ is larger than this energy. The first and second vertical dashed lines in Figure 11 correspond to solutions of

$$|E_0| + \frac{\mathcal{E}_0^2}{4\omega^2} = N\omega, \quad (29)$$

where $N = 4$ and $N = 5$, respectively. Thus, dissociation by four photons is only possible for $\mathcal{E}_0 \lesssim 0.58$ e.u. and five-photon dissociation for $\mathcal{E}_0 \lesssim 2.1$ e.u. However, as shown in Figure 11, the ponderomotive energy does not correspond very well with the local extrema in the dissociation rate. Of course, one cannot expect a full agreement from a classical quantity. Furthermore, during the turn-on period, the electric field is not a monochromatic field. To obtain a detailed prediction of the shape of the dissociation rate, one must therefore turn to the full numerical calculation.

7. Conclusions

We have presented a simple FDTD scheme implementing PMLs to solve the time-dependent Schrödinger equation. The method introduces absorbing layers designed to absorb outgoing probability flux while retaining the exact solution inside a box of some desired size. The performance of the method is compared with the well-known ECS method. It is observed that the PMLs implemented in VG introduce errors that are much lower than those introduced by ECS when they are implemented for short-range potentials. In contrast, when the potential reaches into the absorbing domain, the PMLs do not function as proper absorbing layers, as the errors are very sensitive to the location of the layers, as well as the propagation time. This effect is not observed in ECS, and it is therefore safer to use ECS for long-range potentials. The methods have subsequently been used to compute the laser-induced ionization rate of an electron initially bound to a zero-range potential, as well as exciton dissociation rates in CNTs. In both cases, a pronounced dependence on the field amplitude was observed, which is to be expected. The ionization and dissociation rates, furthermore, show many local minima and maxima as a function of field amplitude, suggesting that one may induce faster exciton dissociation by optimizing the amplitude of the laser field.

Appendix A

Finite Difference Formulas

The finite difference (FD) approach used in this article is based on the Crank–Nicolson scheme.^[60] It consists of a combination of the forward (explicit) and backward (implicit) Euler method and reads

$$i \frac{\psi(x, t_{j+1}) - \psi(x, t_j)}{\Delta t} = \frac{1}{2} [H(t_{j+1})\psi(x, t_{j+1}) + H(t_j)\psi(x, t_j)], \quad (A1)$$

where $t_j = j\Delta t$ and $H(t_j)$ is the Hamilton operator at time t_j . What remains is to discretize the spatial derivatives. For the PML method, the kinetic term is given by

$$\begin{aligned} T_{\text{PML}} &= -\frac{1}{2} c(x) \frac{\partial}{\partial x} c(x) \frac{\partial}{\partial x} \psi \\ &= -\frac{1}{2} \left[c^2(x) \frac{\partial^2 \psi}{\partial x^2} + c(x) \frac{\partial c(x)}{\partial x} \frac{\partial \psi}{\partial x} \right]. \end{aligned} \quad (A2)$$

Both c and its derivative are known analytically. The derivatives of the wave function are approximated using the second-order approximations

$$\frac{\partial \psi}{\partial x} \approx \frac{\psi_{n+1} - \psi_{n-1}}{2\Delta x}, \quad (A3)$$

$$\frac{\partial^2 \psi}{\partial x^2} \approx \frac{\psi_{n+1} - 2\psi_n + \psi_{n-1}}{(\Delta x)^2}, \quad (A4)$$

with $\psi_n = \psi(x_n)$ and $x_n = n\Delta x$, where n is an integer running from $-N$ to N for a grid with a total of $2N + 1$ equidistant points. These simple FD formulas are one of the advantages of the PML method.

For the ECS method, in contrast, the transformation leads to modified FD formulas. They can be derived by writing the wave function as a standard approximation using Lagrange interpolating polynomials

$$\psi(\tilde{x}) \approx \sum_{n=-p}^p l_n(\tilde{x}) \psi(\tilde{x}_n), \quad (A5)$$

with

$$l_n(\tilde{x}) = \prod_{\substack{m=-p \\ m \neq n}}^p \frac{\tilde{x} - \tilde{x}_m}{\tilde{x}_n - \tilde{x}_m}. \quad (A6)$$

The FD formulas at any particular point are then derived by differentiating Equation (A5) and evaluating the result at said point, all the while keeping in mind Equation (9). That is,

$$\tilde{x}_n = \begin{cases} x_n & \text{for } x_n \leq R_0 \\ e^{i\theta}(x_n \pm R_0) \mp R_0 & \text{for } \mp x_n > R_0, \end{cases} \quad (A7)$$

where x_n is the equidistant grid described earlier. Here, we use $p = 1$, which leads to the standard FD formulas for $|x| < R_0$. Outside the scaling radius, we simply pick up a complex phase factor

$$\frac{\partial \psi}{\partial x} \approx \frac{e^{-i\theta}}{2\Delta x} (\psi_{n+1} - \psi_{n-1}), \quad (A8)$$

$$\frac{\partial^2 \psi}{\partial x^2} \approx \frac{e^{-i2\theta}}{(\Delta x)^2} (\psi_{n-1} - 2\psi_n + \psi_{n+1}), \quad (A9)$$

while at the scaling radius, we have the nonsymmetric formulas

$$\frac{\partial \psi}{\partial x} \approx \frac{1}{\Delta x} \left[-\frac{e^{\pm i\theta}}{e^{i\theta} + 1} \psi_{n-1} \pm (1 - e^{-i\theta}) \psi_n + \frac{e^{\mp i\theta}}{e^{i\theta} + 1} \psi_{n+1} \right] \quad \text{for } x = \pm R_0, \quad (\text{A10})$$

$$\frac{\partial^2 \psi}{\partial x^2} \approx \frac{1}{(\Delta x)^2} \left[\frac{2}{e^{i\theta} + 1} \psi_{n+1} - 2e^{-i\theta} \psi_n + \frac{2e^{-i\theta}}{e^{i\theta} + 1} \psi_{n-1} \right] \quad \text{for } x = \pm R_0. \quad (\text{A11})$$

As was discussed in the study by McCurdy et al.,^[50] the ECS FD formulas are $O[(\Delta x)^2]$ for $x \neq \pm R_0$ but only $O(\Delta x)$ for $x = \pm R_0$. For all calculations in this article, we have used $\Delta x = 10^{-2}$ and $\Delta t = 10^{-3}$.

Acknowledgements

Useful comments from Lars Bojer Madsen are gratefully acknowledged. This work was supported by the Villum Kann Rasmussen (VKR) Center of Excellence QUSCOPE. Additionally, H.C.K. and T.G.P. are supported by the Center for Nanostructured Graphene (CNG), which is sponsored by the Danish National Research Foundation, Project No. DNRF103.

Conflict of Interest

The authors declare no conflict of interest.

Keywords

carbon nanotubes, excitons, exterior complex scaling, ionization, perfectly matched layers

Received: August 7, 2019

Revised: February 3, 2020

Published online:

- [1] Q. H. Wang, K. Kalantar-Zadeh, A. Kis, J. N. Coleman, M. S. Strano, *Nat. Nanotechnol.* **2012**, 7, 699.
- [2] A. K. Geim, I. V. Grigorieva, *Nature* **2013**, 499, 419.
- [3] T. Olesen, S. Latini, F. Rasmussen, K. S. Thygesen, *Phys. Rev. Lett.* **2016**, 116, 056401.
- [4] T. Ando, *J. Phys. Soc. Jpn.* **1997**, 66, 1066.
- [5] T. G. Pedersen, *Phys. Rev. B* **2003**, 67, 073401.
- [6] T. G. Pedersen, *Phys. Rev. B* **2016**, 94, 125424.
- [7] M. Massicotte, F. Violla, P. Schmidt, M. B. Lundberg, S. Latini, S. Hastrup, M. Danovich, D. Davydovskaya, K. Watanabe, T. Taniguchi, V. I. Falko, K. Thygesen, T. G. Pedersen, F. H. L. Koppens, *Nat. Commun.* **2018**, 9, 1633.
- [8] C. D. Spataru, S. Ismail-Beigi, L. X. Benedict, S. G. Louie, *Phys. Rev. Lett.* **2004**, 92, 077402.
- [9] V. Perebeinos, J. Tersoff, P. Avouris, *Phys. Rev. Lett.* **2004**, 92, 257402.
- [10] F. Wang, G. Dukovic, L. E. Brus, T. F. Heinz, *Science* **2005**, 308, 838.
- [11] J. Maultzsch, R. Pomraenke, S. Reich, E. Chang, D. Prezzi, A. Ruini, E. Molinari, M. S. Strano, C. Thomsen, C. Lienau, *Phys. Rev. B* **2005**, 72, 241402.
- [12] M. Bernardi, M. Palummo, J. C. Grossman, *Nano Lett.* **2013**, 13, 3664.
- [13] O. Lopez-Sanchez, E. Alarcon Llado, V. Koman, A. Fontcuberta i Morral, A. Radenovic, A. Kis, *ACS Nano*, **2014**, 8, 3042.
- [14] S. Hastrup, S. Latini, K. Bolotin, K. S. Thygesen, *Phys. Rev. B* **2016**, 94, 041401.
- [15] H. C. Kamban, T. G. Pedersen, *Phys. Rev. B* **2019**, 100, 045307.
- [16] S.-W. Chang, J. Hazra, M. Amer, R. Kapadia, S. B. Cronin, *ACS Nano* **2015**, 9, 11551.
- [17] V. Perebeinos, P. Avouris, *Nano Lett.* **2007**, 7, 609.
- [18] A. Mohite, J.-T. Lin, G. Sumanasekera, B. W. Alphenaar, *Nano Lett.* **2006**, 6, 1369.
- [19] A. D. Mohite, P. Gopinath, H. M. Shah, B. W. Alphenaar, *Nano Lett.* **2008**, 8, 142.
- [20] T. Uda, M. Yoshida, A. Ishii, Y. K. Kato, *Nano Lett.* **2016**, 16, 2278.
- [21] U. V. Riss, H. Meyer, *J. Chem. Phys.* **1996**, 105, 1409.
- [22] J. L. Krause, K. J. Schafer, K. C. Kulander, *Phys. Rev. A* **1992**, 45, 4998.
- [23] F. He, C. Ruiz, A. Becker, *Phys. Rev. A* **2007**, 75, 053407.
- [24] L. Tao, W. Vanroose, B. Reps, T. N. Rescigno, C. W. McCurdy, *Phys. Rev. A* **2009**, 80, 063419.
- [25] C. W. McCurdy, C. K. Stroud, M. K. Wisniski, *Phys. Rev. A* **1991**, 43, 5980.
- [26] A. Scrinzi, *Phys. Rev. A* **2010**, 81, 053845.
- [27] J.-P. Berenger, *J. Comput. Phys.* **1994**, 114, 185.
- [28] U. S. Inan, R. A. Marshall, *Numerical Electromagnetics – The FDTD Method*, Cambridge University Press, New York, NY **2011**.
- [29] S. C. Hagness, A. Taflov, *Computational Electrodynamics: The Finite Difference Time Domain Method*, Artech House, Norwood, MA **2005**.
- [30] J. Jin, *The Finite Element Method in Electromagnetics*, 2nd edition, Wiley-Interscience, Hoboken, NJ **2002**.
- [31] D. Zhang, H. Jia, K. Yasumoto, *Int. J. Infrared. Milli.* **2008**, 29, 823.
- [32] Y. Y. Lu, J. Zhu, *IEEE Photonics Technol. Lett.* **2005**, 17, 2601.
- [33] P. Zuo, Z. Fan, J. Sound Vib. **2017**, 406, 181.
- [34] C. Zheng, *J. Comput. Phys.* **2007**, 227, 537.
- [35] A. Nissen, G. Kreiss, *Commun. Comput. Phys.* **2011**, 9, 147179.
- [36] A. Nissen, H. O. Karlsson, G. Kreiss, *J. Chem. Phys.* **2010**, 133, 054306.
- [37] L. Lehtovaara, V. Havu, M. Puska, *J. Chem. Phys.* **2011**, 135, 154104.
- [38] O. Pinaud, *J. Comput. Phys.* **2015**, 289, 169.
- [39] T. G. Pedersen, *Phys. Lett. A* **2015**, 379, 1785.
- [40] G. Scharf, K. Sonnenmoser, W. F. Wreszinski, *Phys. Rev. A* **1991**, 44, 3250.
- [41] E. Balslev, J. M. Combes, *Commun. Math. Phys.* **1971**, 22, 280.
- [42] J. Aguilar, J. M. Combes, *Commun. Math. Phys.* **1971**, 22, 269.
- [43] G. D. Doolen, J. Nuttall, R. W. Stagat, *Phys. Rev. A* **1974**, 10, 1612.
- [44] Y. K. Ho, *Phys. Rev. A* **1981**, 23, 2137.
- [45] M. Reed, B. Simon, *Methods of Modern Mathematical Physics*, Academic, New York, NY **1982**.
- [46] J. Bengtsson, E. Lindroth, S. Selstø, *Phys. Rev. A* **2008**, 78, 032502.
- [47] I. W. Herbst, B. Simon, *Phys. Rev. Lett.* **1978**, 41, 67.
- [48] T. G. Pedersen, H. Mera, B. K. Nikolic, *Phys. Rev. A* **2016**, 93, 013409.
- [49] B. Simon, *Phys. Lett. A* **1979**, 71, 211.
- [50] C. W. McCurdy, M. Baertschy, T. N. Rescigno, *J. Phys. B* **2004**, 37, R137.
- [51] T. N. Rescigno, C. W. McCurdy, *Phys. Rev. A* **2000**, 62, 032706.
- [52] A. Bermúdez, L. Hervella-Nieto, A. Prieto, R. Rodríguez, C. R. Math. Acad. Sci. Ser. A **2004**, 339, 803.
- [53] B. J. Postma, *Am. J. Phys.* **1984**, 52, 725.
- [54] F. M. Fernández, E. A. Castro, *Am. J. Phys.* **1985**, 53, 757.
- [55] *Handbook of Mathematical Functions, with Formulas, Graphs, and Mathematical Tables*, (Eds: M. Abramowitz, I. Stegun), Dover, New York, NY, **1972**.
- [56] C. J. Joachain, N. J. Kylstra, R. M. Potvliege, *Atoms in Intense Laser Fields*, Cambridge University Press, Cambridge **2011**.
- [57] A. Perelomov, V. Popov, M. Terent'ev, *Sov. Phys. JETP* **1966**, 23, 924.
- [58] T. F. Rønnow, T. G. Pedersen, H. D. Cornean, *Phys. Lett. A* **2009**, 373, 1478.
- [59] T. G. Pedersen, K. Pedersen, H. D. Cornean, P. Duclos, *Nano Lett.* **5**, 291 (2005)
- [60] J. Crank, P. Nicolson, *Adv. Comput. Math.* **1996**, 6, 207.

Paper C

Interlayer excitons in van der Waals heterostructures:
Binding energy, Stark shift, and field-induced
dissociation

Høgne C. Kamban and Thomas G. Pedersen

This paper has been published in Scientific Reports:
Sci. Rep. **10**, 5537 (2020)
DOI: 10.1038/s41598-020-62431-y

OPEN

Interlayer excitons in van der Waals heterostructures: Binding energy, Stark shift, and field-induced dissociation

Høgni C. Kamban^{1,2*} & Thomas G. Pedersen^{1,2}

Photoexcited intralayer excitons in van der Waals heterostructures (vdWHs) with type-II band alignment have been observed to tunnel into interlayer excitons on ultrafast timescales. Such interlayer excitons have sufficiently long lifetimes that inducing dissociation with external in-plane electric fields becomes an attractive option of improving efficiency of photocurrent devices. In the present paper, we calculate interlayer exciton binding energies, Stark shifts, and dissociation rates for six different transition metal dichalcogenide (TMD) vdWHs using a numerical procedure based on exterior complex scaling (ECS). We utilize an analytical bilayer Keldysh potential describing the interaction between the electron-hole pair, and validate its accuracy by comparing to the full multilayer Poisson equation. Based on this model, we obtain an analytical weak-field expression for the exciton dissociation rate. The heterostructures analysed are $\text{MoS}_2/\text{MoSe}_2$, MoS_2/WS_2 , $\text{MoS}_2/\text{WSe}_2$, $\text{MoSe}_2/\text{WSe}_2$, $\text{WS}_2/\text{MoSe}_2$, and WS_2/WSe_2 in various dielectric environments. For weak electric fields, we find that WS_2/WSe_2 supports the fastest dissociation rates among the six structures. We, furthermore, observe that exciton dissociation rates in vdWHs are significantly larger than in their monolayer counterparts.

Naturally occurring layered materials held together by van-der-Waals-like forces have been intensely studied in recent years. Peeling graphite layer-by-layer and forming graphene¹, a task thought impossible, turned researchers on to two-dimensional materials. Realizing that these layers may be used as building blocks of artificially layered materials, so-called van der Waals heterostructures, provides an endless array of possible combinations^{2,3}. The extraordinary electronic and optical properties of TMDs^{4–11} have made them one of the most interesting classes of building blocks for vdWHs. Potential electro-optical applications of TMDs include photodetectors^{12–14}, light-emitting diodes^{15–17}, and solar cells^{16,18,19}. It is well known that the optical properties of TMD monolayers are dominated by excitons^{2,3,6,8,20}, as such two-dimensional excitons can have giant binding energies^{6,8,21–23}. Strongly bound excitons, in turn, make generation of photocurrents difficult, as excitons must first be dissociated into free electrons and holes. This is one of the challenges facing the use of monolayer TMDs in efficient photocurrent devices. A further complication is the fast recombination rates of excitons in these monolayers^{24–26}. Without inducing dissociation in some way, excitons will typically recombine before they are dissociated. Applying an in-plane electric field to the excitons, however, enhances generation of photocurrents for two reasons: (i) the electric field counteracts recombination by pulling electrons and holes in opposite directions, and (ii) the electric field assists dissociation of excitons^{27–30}.

When two TMD monolayers are brought together with a type-II band alignment, the conduction band minimum and the valence band maximum reside in two different layers. Electrons and holes in the structure will therefore prefer to reside in separate layers, provided that the loss in exciton binding energy is smaller than the energy gained by band offsets. These spatially indirect electron-hole pairs can still form bound states with large binding energies and they are referred to as interlayer excitons^{31–35}. Experiments have shown that photoexcited intralayer excitons created in one of the sheets undergo ultrafast tunneling into interlayer excitons^{31,35}. For instance, in MoS_2/WS_2 heterostructures, it was found that the hole transferred from the MoS_2 layer to the WS_2 layer within 50 fs after optical excitation³¹, and similar time scales were reported for WSe_2/WS_2 ³⁵. After tunneling, the interlayer excitons have a long lifetime due to the small overlap of electron and hole wave functions^{33,36–40}.

¹Department of Materials and Production, Aalborg University, DK-9220, Aalborg Øst, Denmark. ²Center for Nanostructured Graphene (CNG), DK-9220, Aalborg Øst, Denmark. *email: hck@mp.aau.dk

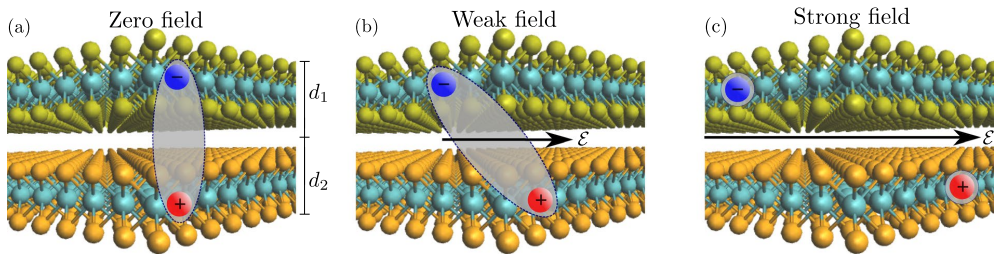


Figure 1. Interlayer exciton in a bilayer van der Waals heterostructure with zero external field (a), a weak in-plane field polarizing the exciton (b), and a strong in-plane field dissociating the exciton (c).

Thus, when a weak in-plane electric field is present, the photoexcited intralayer excitons will tunnel into interlayer excitons with sufficiently long lifetimes for them to be dissociated by the electric field. We therefore expect to see significantly larger photocurrents from this type of structure compared to TMD monolayers. This is corroborated by the much larger dissociation rates found for interlayer excitons. As an example, we find that interlayer excitons in freely suspended MoS_2/WS_2 have a dissociation rate of $\Gamma \approx 1.7 \times 10^4 \text{ s}^{-1}$ for a field strength of $10 \text{ V}/\mu\text{m}$, whereas for excitons in monolayer MoS_2 it is only $\Gamma \approx 5.3 \times 10^{-38} \text{ s}^{-1}$.

The paper is organized as follows. In Sec. 1, we set up the Wannier equation and analyse the interaction between electron-hole pairs in bilayer vdWHs. This is done by solving the multilayer Poisson equation, and subsequently showing that the full solution is excellently approximated by an analytical bilayer Keldysh potential. In Sec. 2, we then turn to computing binding energies as well as Stark shifts and dissociation rates for interlayer excitons. Here, we also compare the numerically exact results to an analytical weak-field approximation, derived by weak-field asymptotic theory. Finally, Sec. 3 concludes upon the results. The solution to the multilayer Poisson equation is presented in App. A.

Interlayer excitons

A bilayer vdWH supports two distinct types of excitons. The electron and hole may either be localized within the same layer, or they may reside in different layers. These two cases are referred to as intra- and interlayer excitons, respectively. The vdWHs considered in the present paper are bilayers with type-II band alignment. We name the structures TMD1/TMD2 so that the conduction band minimum and valence band maximum reside in the first and second layer, respectively. For the structures considered, the energy won from band offsets by the electron and hole residing in the first and second layer, respectively, is larger than the loss in exciton binding energy. The many-body excitonic ground state is therefore an interlayer exciton. Intralayer excitons in either layer are thus excited states, and will therefore tunnel into the ground state. Direct photoexcitation of interlayer excitons by resonance photons is not as likely as for intralayer excitons due to the weak overlap of the electron and hole wave functions. However, resonantly excited intralayer excitons in either layer quickly transition into interlayer excitons³⁵ that, therefore, become very important for many properties of vdWHs. To describe excitonic effects from first principles, one must turn to the many-body Bethe-Salpeter equation^{41,42}. Solving it is a computationally demanding task even for simple structures. Fortunately, under well-defined approximations, the many-body problem can be simplified to the Wannier equation^{43,44}, essentially reducing it to a Schrödinger-type problem with a hydrogenic Hamiltonian. The Wannier model has indeed been shown to yield a sufficiently accurate description of many excitonic properties^{29,45–48}. In terms of the relative coordinate $\mathbf{r} = \mathbf{r}_e - \mathbf{r}_h$ of the electron-hole pair, it reads (atomic units are used throughout)

$$\left[-\frac{1}{2\mu} \nabla^2 + V(\mathbf{r}) + \mathcal{E} \cdot \mathbf{r} \right] \psi(\mathbf{r}) = E \psi(\mathbf{r}), \quad (1)$$

where $\mu = m_e m_h / (m_e + m_h)$ is the reduced exciton mass, V is the screened Coulomb interaction between the electron and hole, and \mathcal{E} is the electric field. The electric field is taken to point along the x -axis throughout the paper, i.e. $\mathcal{E} = \mathcal{E} \mathbf{e}_x$. As the valence band maximum and conduction band minimum at the K point are primarily composed of the d orbitals of the metal atoms^{49,50}, electrons and holes will, to a good approximation, reside in the middle of their respective layers. We are therefore able to freeze their out-of-plane motion, which effectively makes solving Eq. (1) a two dimensional problem. Figure 1 shows an illustration of an interlayer exciton in a bilayer vdWH subjected to three different field strengths: zero (a), weak (b), and strong (c). When an electric field is present, the electron and hole will be pulled in opposite directions. For weak electric fields, the probability of dissociating the exciton is low. It will therefore become polarized, but most likely recombine rather than dissociate. In strong electric fields, however, field induced dissociation becomes likely, and dissociation rates may become extremely large as the field strength increases.

To describe the interaction V between the electron-hole pair, we fix the electron and hole to the middle of their respective sheets. The vertical separation between the electron and hole $d = |z_e - z_h|$ is therefore $d_{\text{intra}} = 0$ and $d_{\text{inter}} = (d_1 + d_2)/2$ for intra- and interlayer excitons, respectively, where d_1 and d_2 are the thicknesses of the two TMD sheets (see Fig. 1). The van der Waals heterostructure is then modeled as the four layer system in Fig. 2.

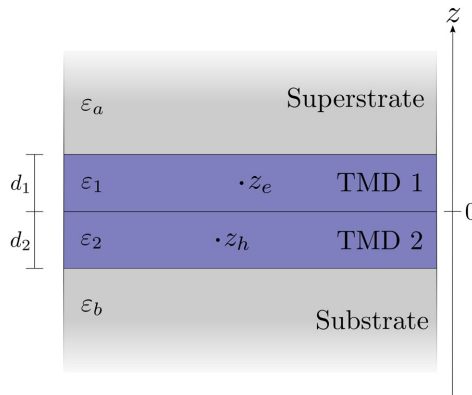


Figure 2. Sketch of the layered geometry used to describe the interaction between an electron at position z_e and a hole at z_h .

Here, the dielectric function $\varepsilon(z)$ is taken to be piecewise constant given by ε_a , ε_1 , ε_2 , and ε_b in the superstrate, upper TMD sheet, lower TMD sheet, and substrate, respectively. By Fourier decomposing V and solving the multilayer Poisson equation for the Fourier components (see App. A), one may obtain V expressed as an integral in momentum space

$$V(r) = - \int_0^\infty \frac{e^{-dq} J_0(qr)}{\varepsilon_{\text{eff}}(q)} dq, \quad (2)$$

where J_0 is a Bessel function. The effective dielectric function ε_{eff} is, of course, different for intra- and interlayer excitons. For $q \rightarrow 0$, both cases tend to the average dielectric constant of the surrounding media $(\varepsilon_a + \varepsilon_b)/2$, as expected. For $q \rightarrow \infty$, however, the dielectric function describing intralayer excitons tends to the dielectric constant of the layer to which they are confined, i.e. to ε_1 and ε_2 for intralayer excitons in the first and second layer, respectively. On the other hand, the function for interlayer excitons tends to the average dielectric constant of the two layers $(\varepsilon_1 + \varepsilon_2)/2$. The complete interlayer dielectric function is obtained in App. A and is given by Eq. (14). Appendix A also explains how to obtain the intralayer function. The full potential may readily be obtained for real r by using standard numerical integration techniques in Eq. (2). However, in the present paper, we seek to calculate dissociation rates by using exterior complex scaling (ECS)^{51–54}. This implies rotating the radial coordinate into the complex plane outside a radius R by an angle ϕ , i.e.

$$r \rightarrow \begin{cases} r & \text{for } r < R \\ R + (r - R)e^{i\phi} & \text{for } r > R. \end{cases} \quad (3)$$

It is a simple task to show that the integrand in Eq. (2) will become an exponentially increasing oscillating function when $r > d/\sin\phi + R$ by using the integral representation for the Bessel function⁵⁵. This makes Eq. (2) extremely difficult to handle while using ECS. Fortunately, the numerical solution is very accurately approximated by a bilayer Keldysh (BLK) potential. The Keldysh potential has been used extensively to describe excitons in monolayer TMDs. The monolayer Keldysh (MLK) interaction is given by^{56,57}

$$V_{\text{MLK}}(r) = -\frac{\pi}{2r_0} \left[H_0 \left(\frac{\kappa r}{r_0} \right) - Y_0 \left(\frac{\kappa r}{r_0} \right) \right], \quad (4)$$

where H_0 is the zeroth order Struve function⁵⁵, Y_0 is the zeroth order Bessel function of the second kind⁵⁵, $\kappa = (\varepsilon_a + \varepsilon_b)/2$ is the average dielectric constant of the surrounding media, and r_0 is the screening length proportional to the polarizability of the sheet⁴⁷. This potential diverges logarithmically at the origin. On the other hand, the potential describing interlayer excitons is finite at the origin due to the vertical separation between the electron-hole pair.

To obtain the bilayer Keldysh potential, we substitute $r \rightarrow \sqrt{r^2 + d^2}$ and $r_0 \rightarrow r_0^{(1)} + r_0^{(2)}$ into Eq. (4) which yields

$$V_{\text{BLK}}(r) = -\frac{\pi}{2(r_0^{(1)} + r_0^{(2)})} \left[H_0 \left(\frac{\kappa \sqrt{r^2 + d^2}}{r_0^{(1)} + r_0^{(2)}} \right) - Y_0 \left(\frac{\kappa \sqrt{r^2 + d^2}}{r_0^{(1)} + r_0^{(2)}} \right) \right]. \quad (5)$$

Here, $r_0^{(1)}$ and $r_0^{(2)}$ are the screening lengths of the first and second monolayer, respectively. The first substitution accounts for the possible vertical separation between electrons and holes in bilayer structures. The second

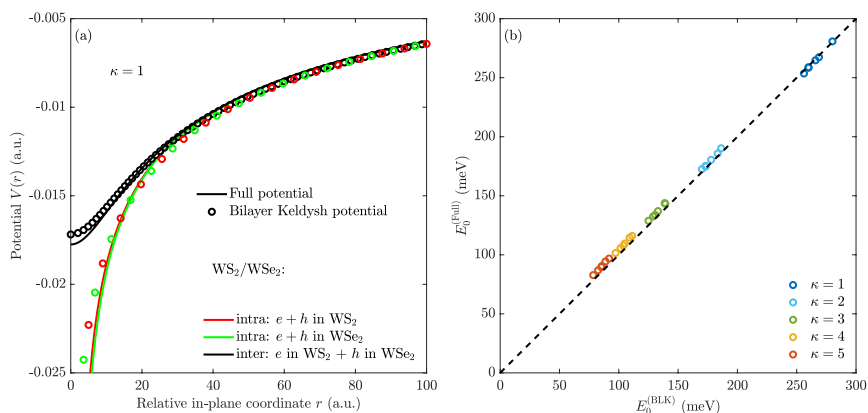


Figure 3. (a) Exciton Coulomb potential for freely suspended WS₂/WSe₂. The full and approximate potentials are shown as the solid lines and circles, respectively. The black line and symbols show the interlayer exciton potential while the red and green lines correspond to the potential of intralayer excitons in the WS₂ and WSe₂ halves of the bilayer, respectively. (b) Binding energies for interlayer excitons in the six structures obtained with the full potential vs. those obtained by the BLK potential.

substitution accounts for the increased thickness of the structure, as the total screening length is proportional to it^{56,57}. It should be noted that making the first substitution without the second leads to a potential that is far too strongly binding⁵⁸. Note, further, that to obtain the interaction for intralayer excitons in a bilayer structure, we use the BLK potential with $d = 0$. The screening lengths used in the present paper are *ab initio* values from ref. 21. In Fig. 3, we compare the bilayer Keldysh potential to the full potential obtained by solving the multilayer Poisson equation. Panel (a) shows the potential for the representative WS₂/WSe₂ case. Evidently, a good agreement is found. Both the intra- and interlayer potentials (exact and approximate) behave as $-1/\kappa r$ for $r \gg d$, as the vertical separation becomes negligible in this region. For small r , on the other hand, the intralayer potential diverges logarithmically, while the interlayer potential behaves as $a + br^2$, where a and b are constants. The quadratic form is readily understood by expanding the Bessel function in Eq. (2) to second order, i.e.

$$J_0(qr) = 1 - \left(\frac{qr}{2}\right)^2 + O(r^4). \quad (6)$$

Integrating using the second order expansion shows that the integral diverges for $d = 0$. For $d > 0$, on the other hand, the exponential function leads to converging integrals even for $r = 0$. The quadratic behaviour has inspired the use of a harmonic oscillator model, obtained by expanding a potential similar to Eq. (5) to second order, to analyse interlayer excitons⁵⁹. It should be noted, however, that the binding energies predicted by a second order expansion of Eq. (5) are in poor agreement with those obtained using the full potential. In contrast, the binding energies obtained with the BLK potential are in good agreement with the full potential results, as seen in panel (b) of Fig. 3. In fact, they never deviate more than 6% for the cases considered. The binding energies are, furthermore, in excellent agreement with those found in literature. As an example, the binding energy of 1s interlayer excitons in WS₂/WSe₂ on a diamond substrate ($\epsilon_a = 1$ and $\epsilon_b = 5$) was measured recently to be 126 ± 7 meV³⁵, and our model yields 125 meV. Furthermore, Ovesen *et al.*⁶⁰ found the binding energy of interlayer excitons in MoSe₂/WSe₂ in free space to be 246 meV using a model similar to our full potential, where we find 260 meV with the BLK model. It should be mentioned that the model used in the present paper predicts slightly lower free-space binding energies than some of the *ab initio* methods^{61–64}. Interlayer exciton binding energies for the six TMD bilayer combinations with type-II band alignment^{65,66} are summarized in Table 1 for various dielectric environments. The effective masses used are obtained from ref. 50, and the TMD widths have been taken as half the vertical lattice constants found in ref. 67.

Field induced dissociation

When the exciton is subjected to an electrostatic field, it may be dissociated. This is realized in the Wannier model by the energy eigenvalue obtaining a non-vanishing imaginary part^{27–29,68}. The field induced dissociation rate is then given by $\Gamma = -2 \text{Im}E$, where the imaginary part can be obtained efficiently by utilizing the ECS technique^{31–34}. As mentioned briefly in the previous section, this technique consists of rotating the radial coordinate into the complex plane outside a radius R (see Eq. (3)). The partitioning of the radial domain is efficiently dealt with by resolving the radial part of the eigenstate in a finite element basis consisting of Legendre polynomials, and the angular part in a cosine basis. We have previously used the same numerical procedure to calculate dissociation rates for excitons in various monolayer TMDs³⁰, and we refer the interested reader to that paper for the technical details of the method. The field induced dissociation rates and Stark shifts for interlayer excitons in the six van der Waals heterostructures are shown in Fig. 4. As is evident, the structures support excitons that behave very

	MoS ₂ /MoSe ₂		MoS ₂ /WS ₂		MoS ₂ /WSe ₂		MoSe ₂ /WSe ₂		WS ₂ /MoSe ₂		WS ₂ /WSe ₂	
	$\mu = 0.2636$		$\mu = 0.2039$		$\mu = 0.2039$		$\mu = 0.2221$		$\mu = 0.1862$		$\mu = 0.1543$	
κ	$ E_0 $	Γ_0	$ E_0 $	Γ_0	$ E_0 $	Γ_0	$ E_0 $	Γ_0	$ E_0 $	Γ_0	$ E_0 $	Γ_0
1	269	1.328×10^{-23}	280	3.781×10^{-20}	266	5.616×10^{-21}	256	1.653×10^{-22}	260	2.056×10^{-20}	260	1.265×10^{-18}
2	183	1.089×10^{-14}	186	7.200×10^{-13}	178	2.570×10^{-13}	173	3.925×10^{-14}	173	5.068×10^{-13}	170	4.371×10^{-12}
3	139	1.027×10^{-11}	139	1.864×10^{-10}	133	9.040×10^{-11}	131	2.445×10^{-11}	129	1.444×10^{-10}	125	6.316×10^{-10}
4	111	3.037×10^{-10}	109	2.830×10^{-9}	105	1.609×10^{-9}	104	5.849×10^{-10}	101	2.305×10^{-9}	97	7.091×10^{-9}
5	92	2.226×10^{-9}	89	1.372×10^{-8}	86	8.611×10^{-9}	85	3.759×10^{-9}	83	1.153×10^{-8}	78	2.847×10^{-8}

Table 1. Interlayer exciton binding energy $|E_0|$ in meV and the field-independent material front factor Γ_0 of the dissociation rate in atomic units for the six vdWHs in various dielectric environments $\kappa = (\epsilon_a + \epsilon_b)/2$. The reduced interlayer exciton mass μ is indicated for each heterostructure.

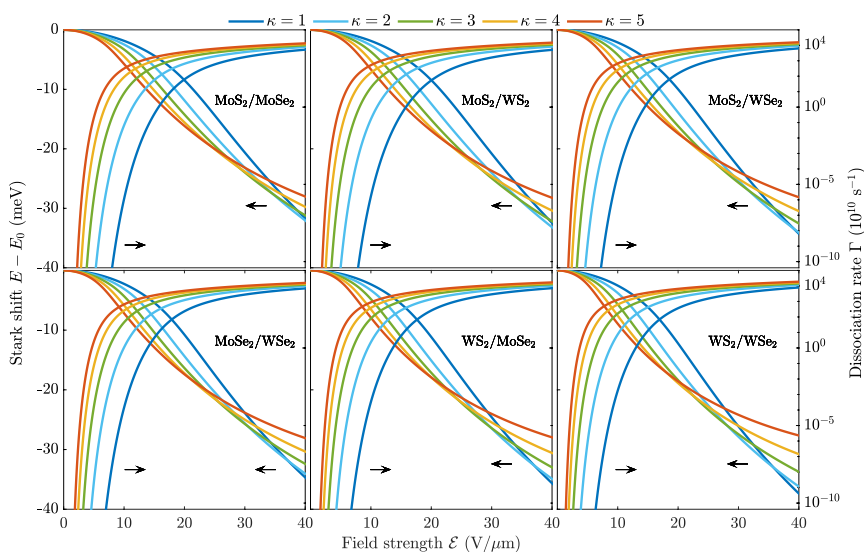


Figure 4. Stark shift (left axis) and dissociation rate (right axis) of interlayer excitons in six different bilayer van der Waals heterostructures in various dielectric environments κ .

similarly in electrostatic fields. The exciton Stark shifts can be seen to vary approximately as \mathcal{E}^2 for weak electric fields, in accordance with perturbation theory $E \approx E_0 - \frac{1}{2}\alpha\mathcal{E}^2$, where E_0 is the unperturbed energy and α the in-plane polarizability. Calculating the polarizability using the Dalgarno-Lewis equation⁶⁹ and a finite element basis³⁰ reveals that the interlayer exciton polarizabilities are significantly larger than their monolayer counterparts. For example, freely suspended MoS₂/WSe₂ supports interlayer excitons with $\alpha_{\text{MoS}_2/\text{WSe}_2}^{(\kappa=1)} = 41 \times 10^{-18} \text{ eV (m/V)}^2$, whereas monolayer MoS₂ and WSe₂ support exciton polarizabilities of around $\alpha_{\text{MoS}_2}^{(\kappa=1)} = 4.6 \times 10^{-18} \text{ eV (m/V)}^2$ and $\alpha_{\text{WSe}_2}^{(\kappa=1)} = 6.3 \times 10^{-18} \text{ eV (m/V)}^2$, respectively⁴⁸. Encapsulating the materials in hBN ($\kappa = 4.9$)⁴⁵ increases the polarizabilities to $\alpha_{\text{MoS}_2/\text{WSe}_2}^{(\kappa=4.9)} = 116 \times 10^{-18} \text{ eV (m/V)}^2$ whereas $\alpha_{\text{MoS}_2}^{(\kappa=4.9)} = 14.2 \times 10^{-18} \text{ eV (m/V)}^2$ and $\alpha_{\text{WSe}_2}^{(\kappa=4.9)} = 20.8 \times 10^{-18} \text{ eV (m/V)}^2$ ⁴⁸. The reason that these large polarizabilities are observed for interlayer excitons in bilayer vdWHs is the increased screening and the vertical separation of the electron and hole. Both reduce the binding energy and they are therefore much easier to polarize.

Turning to the dissociation rates, it is clear that the encapsulating media significantly alter how quickly interlayer excitons are dissociated. The same behaviour was observed for their monolayer counterparts³⁰, and one therefore has a large degree of freedom in device design. For extremely weak fields, the dissociation rates are very low, but they grow rapidly with an increasing field strength. As an example, the dissociation rate of interlayer excitons in freely suspended MoS₂/WS₂ is around $\Gamma \approx 1.7 \times 10^4 \text{ s}^{-1}$ already at $\mathcal{E} = 10 \text{ V/}\mu\text{m}$, and only $\Gamma \approx 5.3 \times 10^{-38} \text{ s}^{-1}$ and $\Gamma \approx 2.7 \times 10^{-33} \text{ s}^{-1}$ for monolayer MoS₂ and WS₂, respectively³⁰. It should be noted that dissociation rates of intralayer excitons are only important if they are comparable to the rate at which intralayer excitons tunnel over to interlayer excitons. In a recent experiment on MoS₂/WS₂ structures, the holes of photoexcited excitons in the MoS₂ layer of this structure were observed to tunnel into the WS₂ layer within 50 fs³¹.

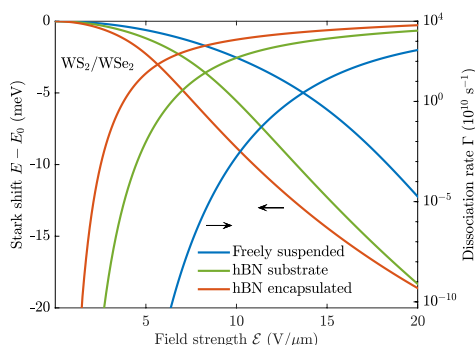


Figure 5. Stark shift (left axis) and dissociation rate (right axis) for interlayer excitons in a WS₂/WS₂ bilayer that is either (i) freely suspended, (ii) placed on an hBN substrate, or (iii) encapsulated by hBN.

Comparing to the dissociation rates of intralayer excitons in the top and bottom layer of MoS₂/WS₂ for $\mathcal{E} = 10 \text{ V}/\mu\text{m}$, we find $\Gamma \approx 2.1 \times 10^{-3} \text{ s}^{-1}$ and $\Gamma \approx 2.9 \times 10^4 \text{ s}^{-1}$, respectively. The large difference between these two rates can be traced back to the reduced masses, which are $\mu = 0.2513$ and $\mu = 0.1543$, respectively. The time it takes to dissociate these excitons with the given field may be approximated as $\tau = 1/\Gamma \approx 476 \text{ s}$ and $\tau \approx 3.5 \times 10^{-5} \text{ s}$, respectively. The intralayer excitons have therefore clearly transitioned to interlayer excitons before they are dissociated by the field. Interlayer tunneling rates are likely affected by material parameters as well as the surrounding media. Assuming, however, similar time scales as observed for MoS₂/WS₂ $\Gamma_{\text{Tunnel}} \approx 10^{13} \text{ s}^{-1}$, interlayer dissociation rates are the limiting factor in field induced exciton dissociation for weak to moderate fields. For the largest fields in Fig. 4, the competition between tunneling and dissociation will be important for an accurate description. Due to the risk of dielectric break-down, such large fields are best avoided in devices, however. The high interlayer dissociation rates suggest that using carefully chosen bilayer TMDs in photocurrent devices is much more attractive than their monolayer counterparts. Moreover, proper encapsulation will further improve device performance. As hBN is a very common material used to encapsulate samples, we show the interlayer dissociation rates for WS₂/WS₂ that is either (i) freely suspended, (ii) placed on an hBN substrate, or (iii) encapsulated by hBN in Fig. 5. Evidently, hBN surroundings increase the dissociation rates by several orders of magnitude, and for weak fields in particular.

Recently an analytical weak-field approximation was obtained for exciton dissociation rates in monolayer TMDs³⁰. The derivation was made using weak-field asymptotic theory⁷⁰, and the fact that the MLK potential has a simple asymptotic form. As mentioned in the previous section, the BLK potential has exactly the same asymptotic behaviour. The weak-field approximation for interlayer excitons therefore has exactly the same form, albeit with a different field-independent front factor. We arrive at

$$\Gamma \approx \Gamma_0 e^{1/2 - 2\sqrt{\mu}/(\kappa k)} \exp\left(-\frac{2\sqrt{\mu}k^3}{3\mathcal{E}}\right), \quad (7)$$

where $k = \sqrt{2|E_0|}$ and $\Gamma_0 = \Gamma_0(E_0, \mu, r_0^{(1)} + r_0^{(2)}, d, \kappa)$ is a field-independent material constant. The parameters needed to use Eq. (7) are presented in Table 1, where Γ_0 has been computed by the integral procedure in³⁰. Panel (a) of Fig. 6 shows the interlayer dissociation rates as functions of environment screening κ for a field of $5 \text{ V}/\mu\text{m}$ computed with the numerical procedure (dots) and the weak-field approximation (solid lines). Evidently a good agreement is found for such a low field. Nevertheless, as the inset shows, the weak-field approximation quickly begins to overestimate the dissociation rate for larger fields. This was also found for monolayer TMDs³⁰. It is clear that WS₂/WS₂ supports excitons with the largest dissociation rates at $\mathcal{E} = 5 \text{ V}/\mu\text{m}$, making it an interesting choice in device design. Note that the fully numerical procedure breaks down if the dissociation rate becomes extremely small, and, hence, we are unable to use it to obtain dissociation rates for MoS₂/MoSe₂ and MoS₂/WS₂ in surroundings with (very) low screening for this field strength. It is therefore advantageous to have a formula such as Eq. (7) when the fields become sufficiently weak.

In panel (b) of Fig. 6, we show the binding energies for the same excitons as functions of κ . They clearly follow similar trends as the dissociation rates do, suggesting that binding energy has a significant impact on dissociation rates. This is to be expected, as strongly bound excitons are harder to pull apart. It should, however, be noted that the binding energy does not uniquely determine the dissociation rate. As an example, the interlayer excitons in MoS₂/MoSe₂ and MoS₂/WS₂ have identical binding energies for surrounding media with $\kappa \approx 2.8$. Nevertheless, the dissociation rates are clearly different. In fact, several crossings are observed in the binding energies as a function of κ whereas only one is found in the dissociation rates at $5 \text{ V}/\mu\text{m}$. The origin is the different reduced exciton masses. For no structure does Γ_0 nor $\sqrt{\mu}/k$ contain any crossing for $\kappa \in [1; 5]$. However, $\sqrt{\mu}k^3$ crosses for MoS₂/WS₂ and MoSe₂/WS₂. This complicated behaviour suggests that, to obtain accurate estimates of interlayer exciton dissociation rates, one must turn to either the weak-field approximation or make a full numerical calculation.

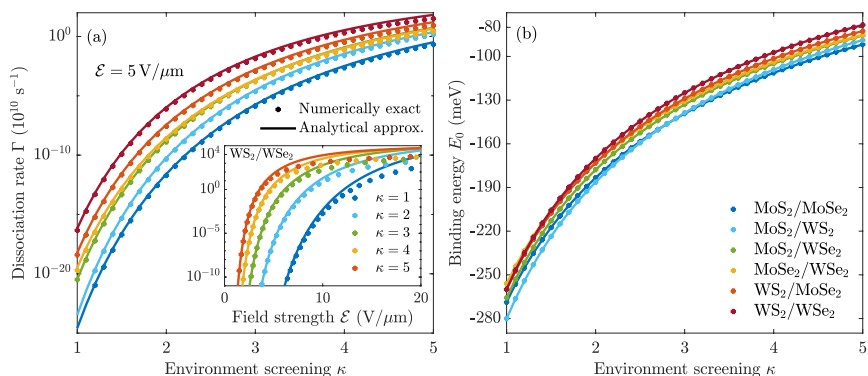


Figure 6. Dissociation rates (a) and binding energies (b) for interlayer excitons in six vdWHs as functions of environment screening κ . In panel (a), the dots and solid lines represent the numerically exact and analytical approximation Eq. (7), respectively. The inset shows the approximate and exact dissociation rates for interlayer excitons in WS_2/WSe_2 as a function of field strength.

Conclusion

In the present paper, we have studied binding energies, Stark shifts, and dissociation rates of interlayer excitons in van der Waals heterostructures (vdWHs). The structures analysed are the six bilayer vdWHs with type-II band alignment arising from combinations of MoS_2 , MoSe_2 , WS_2 , and WSe_2 . The bilayer excitons are described using an analytical bilayer Keldysh potential, which we have verified for accuracy by comparing to the full solution of the multilayer Poisson equation. Exciton binding energies, Stark shifts, and dissociation rates can therefore readily be calculated using the analytical potential. We find interlayer exciton binding energies ranging from 256 to 280 meV for freely suspended structures and from 78 to 92 meV for heavily screened structures, making them stable at room temperature. Furthermore, both the polarizabilities and dissociation rates found for these excitons are much larger than their monolayer counterparts. For example, interlayer excitons in freely suspended MoS_2/WS_2 are found to dissociate at a rate of $\Gamma \approx 1.7 \times 10^4 \text{ s}^{-1}$ in a field strength of $10 \text{ V}/\mu\text{m}$ whereas monolayer MoS_2 and WS_2 have $\Gamma \approx 5.3 \times 10^{-38} \text{ s}^{-1}$ and $\Gamma \approx 2.7 \times 10^{-33} \text{ s}^{-1}$, respectively.

For moderate field strengths, intralayer exciton dissociation rates are significantly lower than the rate at which such excitons tunnel into interlayer excitons. For this reason, interlayer exciton dissociation rates are the limiting factor in generation of photocurrents at weak to moderate fields. Since optically excited excitons in one of the layers tunnel to long-lived interlayer excitons on ultrafast timescales, bilayer vdWHs with favourable band offsets may potentially serve as building blocks in efficient photocurrent devices. Finally, the numerically exact dissociation rates are compared to an analytical weak-field dissociation formula obtained from weak-field asymptotic theory. A good agreement is found in the weak-field limit, and Eq. (7) therefore serves as a useful formula to quickly estimate field induced dissociation rates of excitons in bilayer vdWHs for weak electric fields.

A Multilayer Poisson equation

We want to find the interaction between the two particles in the system represented by Fig. 2. For charges at z and z' with in-plane separation r , the interaction can be Fourier decomposed as

$$-V(r, z, z') = \frac{1}{4\pi^2} \int \varphi(z, z'; q) e^{iq \cdot r} d^2q, \quad (8)$$

where the Fourier components satisfy the Poisson equation

$$4\pi\delta(z - z') = \left[q^2 \varepsilon(z; q) - \frac{\partial}{\partial z} \varepsilon(z; q) \frac{\partial}{\partial z} \right] \varphi(z, z'; q). \quad (9)$$

We take the dielectric function ε to be piecewise constant

$$\varepsilon(z; q) = \begin{cases} \varepsilon_a, & z > d_1 \\ \varepsilon_1, & 0 < z < d_1 \\ \varepsilon_2, & -d_2 < z < 0 \\ \varepsilon_b, & z < -d_2, \end{cases} \quad (10)$$

where d_1 and d_2 are the widths of the first and second layer, respectively. For z' confined to the second layer, the solution can be sought on the form

$$\varphi(z, z'; q) = \frac{2\pi}{q} \begin{cases} A_1 e^{-qz} \\ A_2 e^{-qz} + B_2 e^{qz} \\ A_3 e^{-qz} + B_3 e^{qz} + \varepsilon_2^{-1} e^{-q|z-z'|} \\ B_4 e^{qz}, \end{cases} \quad (11)$$

in the respective regions. The Fourier components can then be found analytically by solving the system of equations that arises from the boundary conditions. To describe charges confined to distinct layers, we fix the electron and hole to $z = d_1/2$ and $z' = -d_2/2$, respectively. This leads to the interlayer exciton potential

$$\varphi(d_1/2, -d_2/2; q) = \frac{\varphi_0(d_1/2, -d_2/2; q)}{\varepsilon_{\text{eff}}(q)}, \quad (12)$$

where

$$\varphi_0(z, z'; q) = \frac{2\pi}{q} e^{-|z-z'|q} \quad (13)$$

is the bare interaction. The effective dielectric function is given by

$$\varepsilon_{\text{eff}}(q) = \frac{A(q)}{B(q)}. \quad (14)$$

with

$$A(q) = (1 - e^{-2d_1 q})(\varepsilon_1^2 \gamma^+ + \varepsilon_a \varepsilon_2 \gamma^-) + (1 + e^{-2d_1 q})(\varepsilon_a \varepsilon_1 \gamma^+ + \varepsilon_1 \varepsilon_2 \gamma^-), \quad (15)$$

$$B(q) = 2[(1 - e^{-d_1 q})\varepsilon_a + (1 + e^{-d_1 q})\varepsilon_1] \times [(1 + e^{-d_2 q})\varepsilon_2 + (1 - e^{-d_2 q})\varepsilon_b], \quad (16)$$

where

$$\gamma^\pm = (1 \pm e^{-2d_2 q})\varepsilon_2 + (1 \mp e^{-2d_2 q})\varepsilon_b. \quad (17)$$

This effective dielectric function tends to $(\varepsilon_a + \varepsilon_b)/2$ for $q \rightarrow 0$ and to $(\varepsilon_1 + \varepsilon_2)/2$ for $q \rightarrow \infty$, as expected. The dielectric function describing charges confined to the same layer may be obtained in a similar manner by placing both charges at $z = -d_2/2$. The interaction in real space can then be obtained as the inverse Fourier transform

$$-V(r) = \int_0^\infty \frac{e^{-|z-z'|q} \varphi_0(qr)}{\varepsilon_{\text{eff}}(q)} dq. \quad (18)$$

For the dielectric constants, we have used the static in-plane dielectric constants calculated from first principles in ref. ⁷¹.

Received: 1 February 2020; Accepted: 12 March 2020;

Published online: 26 March 2020

References

- Novoselov, K. S. *et al.* Electric field effect in atomically thin carbon films. *Science* **306**, 666–669 (2004).
- Wang, Q. H., Kalantar-Zadeh, K., Kis, A., Coleman, J. N. & Strano, M. S. Electronics and optoelectronics of two-dimensional transition metal dichalcogenides. *Nat. Nanotechnol* **7**, 699 (2012).
- Geim, A. K. & Grigorieva, I. V. Van der Waals heterostructures. *Nature* **499**, 419 (2013).
- Mak, K. F., Lee, C., Hone, J., Shan, J. & Heinz, T. F. Atomically thin mos_2 : A new direct-gap semiconductor. *Phys. Rev. Lett.* **105**, 136805 (2010).
- Splendiani, A. *et al.* Emerging photoluminescence in monolayer mos_2 . *Nano Lett.* **10**, 1271–1275 (2010).
- Ramasubramaniam, A. Large excitonic effects in monolayers of molybdenum and tungsten dichalcogenides. *Phys. Rev. B* **86**, 115409 (2012).
- Tongay, S. *et al.* Defects activated photoluminescence in two-dimensional semiconductors: interplay between bound, charged, and free excitons. *Sci. Rep.* **3**, 2657 (2013).
- Qiu, D. Y., da Jornada, F. H. & Louie, S. G. Optical spectrum of mos_2 : Many-body effects and diversity of exciton states. *Phys. Rev. Lett.* **111**, 216805 (2013).
- Gutiérrez, H. R. *et al.* Extraordinary room-temperature photoluminescence in triangular ws_2 monolayers. *Nano Lett.* **13**, 3447–3454 (2013).
- Mouri, S., Miyauchi, Y. & Matsuda, K. Tunable photoluminescence of monolayer mos_2 via chemical doping. *Nano Lett.* **13**, 5944–5948 (2013).
- Scheuschner, N. *et al.* Photoluminescence of freestanding single- and few-layer mos_2 . *Phys. Rev. B* **89**, 125406 (2014).
- Wang, H., Zhang, C., Chan, W., Tiwari, S. & Rana, F. Ultrafast response of monolayer molybdenum disulfide photodetectors. *Nat. Commun.* **6**, 8831 (2015).
- Lopez-Sanchez, O., Lembke, D., Kayci, M., Radenovic, A. & Kis, A. Ultrasensitive photodetectors based on monolayer mos_2 . *Nat. Nanotechnol* **8**, 497 (2013).
- Yin, Z. *et al.* Single-layer mos_2 phototransistors. *ACS Nano* **6**, 74 (2012).

15. Ross, J. S. *et al.* Electrically tunable excitonic light-emitting diodes based on monolayer wse₂ p-n junctions. *Nat. Nanotechnol* **9**, 268 (2014).
16. Pospischil, A., Furchi, M. M. & Mueller, T. Solar-energy conversion and light emission in an atomic monolayer p-n diode. *Nat. Nanotechnol* **9**, 257 (2014).
17. Withers, F. *et al.* Light-emitting diodes by band-structure engineering in van der waals heterostructures. *Nat. Mater.* **14**, 301 (2015).
18. Lopez-Sanchez, O. *et al.* Light generation and harvesting in a van der waals heterostructure. *ACS Nano* **8**, 3042 (2014).
19. Bernardi, M., Palummo, M. & Grossman, J. C. Extraordinary sunlight absorption and one nanometer thick photovoltaics using two-dimensional monolayer materials. *Nano Lett.* **13**, 3664 (2013).
20. Trolle, M. L., Tsao, Y.-C., Pedersen, K. & Pedersen, T. G. Observation of excitonic resonances in the second harmonic spectrum of mos₂. *Phys. Rev. B* **92**, 161409 (2015).
21. Olsen, T., Latini, S., Rasmussen, F. & Thygesen, K. S. Simple screened hydrogen model of excitons in two-dimensional materials. *Phys. Rev. Lett.* **116**, 056401 (2016).
22. Chernikov, A. *et al.* Exciton binding energy and nonhydrogenic rydberg series in monolayer ws₂. *Phys. Rev. Lett.* **113**, 076802 (2014).
23. Hanbicki, A., Currie, M., Kioseoglou, G., Friedman, A. & Jonker, B. Measurement of high exciton binding energy in the monolayer transition-metal dichalcogenides ws₂ and wse₂. *Solid State Commun* **203**, 16–20 (2015).
24. Palummo, M., Bernardi, M. & Grossman, J. C. Exciton radiative lifetimes in two-dimensional transition metal dichalcogenides. *Nano Lett.* **15**, 2794 (2015).
25. Poellmann, C. *et al.* Resonant internal quantum transitions and femtosecond radiative decay of excitons in monolayer wse₂. *Nat. Mater.* **14**, 889 (2015).
26. Wang, H. *et al.* Radiative lifetimes of excitons and trions in monolayers of the metal dichalcogenide mos₂. *Phys. Rev. B* **93**, 045407 (2016).
27. Pedersen, T. G., Latini, S., Thygesen, K. S., Mera, H. & Nikolić, B. K. Exciton ionization in multilayer transition-metal dichalcogenides. *New J. Phys.* **18**, 073043 (2016).
28. Hastrup, S., Latini, S., Bolotin, K. & Thygesen, K. S. Stark shift and electric-field-induced dissociation of excitons in monolayer mos₂ and hBN/mos₂ heterostructures. *Phys. Rev. B* **94**, 041401 (2016).
29. Massicotte, M. *et al.* Dissociation of two-dimensional excitons in monolayer wse₂. *Nat. Commun.* **9**, 1633 (2018).
30. Kamban, H. C. & Pedersen, T. G. Field-induced dissociation of two-dimensional excitons in transition metal dichalcogenides. *Phys. Rev. B* **100**, 045307 (2019).
31. Hong, X. *et al.* Ultrafast charge transfer in atomically thin mos₂/ws₂ heterostructures. *Nat. Nanotechnol* **9**, 682 (2014).
32. Chen, H. *et al.* Ultrafast formation of interlayer hot excitons in atomically thin mos₂/ws₂ heterostructures. *Nat. Commun.* **7**, 12512 (2016).
33. Miller, B. *et al.* Long-lived direct and indirect interlayer excitons in van der waals heterostructures. *Nano Lett.* **17**, 5229–5237 (2017).
34. Kunstmann, J. *et al.* Momentum-space indirect interlayer excitons in transition-metal dichalcogenide van der waals heterostructures. *Nat. Phys.* **14**, 801 (2018).
35. Merkl, P. *et al.* Ultrafast transition between exciton phases in van der waals heterostructures. *Nat. Mater.* **18**, 691 (2019).
36. Fogler, M. M., Butov, L. V. & Novoselov, K. S. High-temperature superfluidity with indirect excitons in van der waals heterostructures. *Nat. Commun.* **5**, 4555 (2014).
37. Rivera, P. *et al.* Observation of long-lived interlayer excitons in monolayer mose₂-wse₂ heterostructures. *Nat. Commun.* **6**, 6242 (2015).
38. Rivera, P. *et al.* Valley-polarized exciton dynamics in a 2d semiconductor heterostructure. *Science* **351**, 688–691 (2016).
39. Nagler, P. *et al.* Interlayer exciton dynamics in a dichalcogenide monolayer heterostructure. *2D Mater* **4**, 025112 (2017).
40. Jin, C. *et al.* Imaging of pure spin-valley diffusion current in ws₂-wse₂ heterostructures. *Science* **360**, 893–896 (2018).
41. Salpeter, E. E. & Bethe, H. A. A relativistic equation for bound-state problems. *Phys. Rev.* **84**, 1232–1242 (1951).
42. Onida, G., Reining, L. & Rubio, A. Electronic excitations: density-functional versus many-body green's-function approaches. *Rev. Mod. Phys.* **74**, 601–659 (2002).
43. Wannier, G. H. The structure of electronic excitation levels in insulating crystals. *Phys. Rev.* **52**, 191–197 (1937).
44. Lederman, F. L. & Dow, J. D. Theory of electroabsorption by anisotropic and layered semiconductors. i. two-dimensional excitons in a uniform electric field. *Phys. Rev. B* **13**, 1633–1642 (1976).
45. Latini, S., Olsen, T. & Thygesen, K. S. Excitons in van der waals heterostructures: The important role of dielectric screening. *Phys. Rev. B* **92**, 245123 (2015).
46. Cudazzo, P., Attaccalite, C., Tokatly, I. V. & Rubio, A. Strong charge-transfer excitonic effects and the bose-einstein exciton condensate in graphane. *Phys. Rev. Lett.* **104**, 226804 (2010).
47. Cudazzo, P., Tokatly, I. V. & Rubio, A. Dielectric screening in two-dimensional insulators: Implications for excitonic and impurity states in graphane. *Phys. Rev. B* **84**, 085406 (2011).
48. Pedersen, T. G. Exciton stark shift and electroabsorption in monolayer transition-metal dichalcogenides. *Phys. Rev. B* **94**, 125424 (2016).
49. Wang, F. *et al.* Tuning coupling behavior of stacked heterostructures based on mos₂, ws₂, and wse₂. *Sci. Rep.* **7**, 44712 (2017).
50. Kormányos, A. *et al.* k-p theory for two-dimensional transition metal dichalcogenide semiconductors. *2D Mater* **2**, 022001 (2015).
51. Simon, B. The definition of molecular resonance curves by the method of exterior complex scaling. *Phys. Lett.* **71**, 211–214 (1979).
52. McCurdy, C. W., Stroud, C. K. & Wisinski, M. K. Solving the time-dependent schrödinger equation using complex-coordinate contours. *Phys. Rev. A* **43**, 5980–5990 (1991).
53. Rescigno, T. N. & McCurdy, C. W. Numerical grid methods for quantum-mechanical scattering problems. *Phys. Rev. A* **62**, 032706 (2000).
54. McCurdy, C. W., Baertschy, M. & Rescigno, T. N. Solving the three-body coulomb breakup problem using exterior complex scaling. *J. Phys. B* **37**, R137 (2004).
55. Abramowitz, M. & Stegun, I. (eds.) *Handbook of Mathematical Functions, With Formulas, Graphs, and Mathematical Tables* (Dover, New York, 1972).
56. Keldysh, L. Coulomb interaction in thin semiconductor and semimetal films. *JETP Lett* **29**, 658 (1979).
57. Trolle, M. L., Pedersen, T. G. & Vénier, V. Model dielectric function for 2d semiconductors including substrate screening. *Sci. Rep.* **7**, 39844 (2017).
58. Van der Donck, M. & Peeters, F. M. Interlayer excitons in transition metal dichalcogenide heterostructures. *Phys. Rev. B* **98**, 115104 (2018).
59. Berman, O. L. & Kezerashvili, R. Y. Superfluidity of dipolar excitons in a transition metal dichalcogenide double layer. *Phys. Rev. B* **96**, 094502 (2017).
60. Ovesen, S. *et al.* Interlayer exciton dynamics in van der waals heterostructures. *Commun. Phys.* **2**, 23 (2019).
61. Meckbach, L., Huttner, U., Bannow, L. C., Stroucken, T. & Koch, S. W. Interlayer excitons in transition-metal dichalcogenide heterostructures with type-II band alignment. *J. Phys. Condens. Matter* **30**, 374002 (2018).
62. Gillen, R. & Maultzsch, J. Interlayer excitons in mose₂/wse₂ heterostructures from first principles. *Phys. Rev. B* **97**, 165306 (2018).
63. Torun, E., Miranda, H. P. C., Molina-Sánchez, A. & Wirtz, L. Interlayer and intralayer excitons in mos₂/ws₂ and mose₂/wse₂ heterobilayers. *Phys. Rev. B* **97**, 245427 (2018).
64. Deilmann, T. & Thygesen, K. S. Interlayer trions in the mos₂/ws₂ van der waals heterostructure. *Nano Lett.* **18**, 1460–1465 (2018).

65. Gong, C. *et al.* Band alignment of two-dimensional transition metal dichalcogenides: Application in tunnel field effect transistors. *Appl. Phys. Lett.* **103**, 053513 (2013).
66. Komsa, H.-P. & Krasheninnikov, A. V. Electronic structures and optical properties of realistic transition metal dichalcogenide heterostructures from first principles. *Phys. Rev. B* **88**, 085318 (2013).
67. He, J., Hummer, K. & Franchini, C. Stacking effects on the electronic and optical properties of bilayer transition metal dichalcogenides MoS_2 , MoSe_2 , WS_2 , and WSe_2 . *Phys. Rev. B* **89**, 075409 (2014).
68. Pedersen, T. G., Mera, H. & Nikolić, B. K. Stark effect in low-dimensional hydrogen. *Phys. Rev. A* **93**, 013409 (2016).
69. Dalgarno, A., Lewis, J. T. & Bates, D. R. The exact calculation of long-range forces between atoms by perturbation theory. *Proc. R. Soc. London, Ser. A* **233**, 70–74 (1955).
70. Tolstikhin, O. I., Morishita, T. & Madsen, L. B. Theory of tunneling ionization of molecules: Weak-field asymptotics including dipole effects. *Phys. Rev. A* **84**, 053423 (2011).
71. Laturia, A., Van de Put, M. L. & Vandenbergh, W. G. Dielectric properties of hexagonal boron nitride and transition metal dichalcogenides: from monolayer to bulk. *NPJ 2D Mater. Appl.* **2**, 6 (2018).

Acknowledgements

The authors gratefully acknowledge financial support from the Center for Nanostructured Graphene (CNG), which is sponsored by the Danish National Research Foundation, Project No. DNRF103. Additionally, T.G.P. is supported by the QUSCOPE Center, sponsored by the Villum Foundation.

Author contributions

H.C.K. initiated the work, performed all calculations, and prepared the initial manuscript. T.G.P. assisted in solving the Poisson equation. H.C.K. and T.G.P. analysed the results and prepared the final manuscript.

Competing interests

The authors declare no competing financial interest.

Additional information

Correspondence and requests for materials should be addressed to H.C.K.

Reprints and permissions information is available at www.nature.com/reprints.

Publisher's note Springer Nature remains neutral with regard to jurisdictional claims in published maps and institutional affiliations.



Open Access This article is licensed under a Creative Commons Attribution 4.0 International License, which permits use, sharing, adaptation, distribution and reproduction in any medium or format, as long as you give appropriate credit to the original author(s) and the source, provide a link to the Creative Commons license, and indicate if changes were made. The images or other third party material in this article are included in the article's Creative Commons license, unless indicated otherwise in a credit line to the material. If material is not included in the article's Creative Commons license and your intended use is not permitted by statutory regulation or exceeds the permitted use, you will need to obtain permission directly from the copyright holder. To view a copy of this license, visit <http://creativecommons.org/licenses/by/4.0/>.

© The Author(s) 2020

Paper D

Analytical quantitative semiclassical approach to the Lo
Surdo-Stark effect and ionization in two-dimensional
excitons

João C. G. Henriques, Høgni C. Kamban, Thomas G. Pedersen,
and Nuno M. R. Peres

This paper has been published in Physical Review B:
Phys. Rev. B **102**, 035402 (2020)
DOI: 10.1103/PhysRevB.102.035402

Analytical quantitative semiclassical approach to the Lo Surdo–Stark effect and ionization in two-dimensional excitons

J. C. G. Henriques¹,² Høgni C. Kamban^{2,3}, Thomas G. Pedersen^{2,3} and N. M. R. Peres^{1,4}

¹*Department and Centre of Physics, and QuantaLab, University of Minho, Campus of Gualtar, 4710-057, Braga, Portugal*

²*Department of Materials and Production, Aalborg University, DK-9220 Aalborg Øst, Denmark*

³*Center for Nanostructured Graphene (CNG), DK-9220 Aalborg Øst, Denmark*

⁴*International Iberian Nanotechnology Laboratory (INL), Av. Mestre José Veiga, 4715-330, Braga, Portugal*



(Received 30 April 2020; revised 18 June 2020; accepted 22 June 2020; published 1 July 2020)

Using a semiclassical approach, we derive a fully analytical expression for the ionization rate of excitons in two-dimensional materials due to an external static electric field, which eliminates the need for complicated numerical calculations. Our formula shows quantitative agreement with more sophisticated numerical methods based on the exterior complex scaling approach, which solves a non-Hermitian eigenvalue problem yielding complex energy eigenvalues, where the imaginary part describes the ionization rate. Results for excitons in hexagonal boron nitride and the *A* exciton in transition metal dichalcogenides are given as simple examples. The extension of the theory to include spin-orbit-split excitons in transition metal dichalcogenides is trivial.

DOI: [10.1103/PhysRevB.102.035402](https://doi.org/10.1103/PhysRevB.102.035402)

I. INTRODUCTION

The Lo Surdo–Stark effect has a venerable history in both atomic, molecular, and condensed matter physics [1]. This effect refers to the modification of the position of the energy levels of a quantum system due to the application of an external electric field and, in addition, to the possible ionization of atoms, molecules, and excitons due to the very same field. The latter effect is a nice example of quantum tunneling through an electrostatic barrier. The difference between values of the energy levels with and without the field is dubbed the Stark shift. The ionization process is characterized by an ionization rate, which depends on the magnitude of the external electric field, as well as material parameters. Although the calculation of the Stark shift can be easily accomplished using perturbation theory [2], the calculation of the ionization rate is nonperturbative [3] since it is proportional to $\exp(-\beta/F)$, where β is a material-dependent parameter and F is the magnitude of the external electric field. For the case of the hydrogen atom in three dimensions the literature on the Lo Surdo–Stark effect, spanning a period of about 100 years, is vast. On the contrary, for low-dimensional systems, such as the two-dimensional hydrogen atom, the calculation of both the Stark shift and the ionization rate for very strong electric fields was only recently considered [4,5]; the weak field limit had been studied by Tanaka *et al* prior [6]. In the previous work, the authors used a low order perturbation expansion of the energy, combined with the hypergeometric resummation technique [4,5] to extract the full nonperturbative behavior of the energy and thus address the Lo Surdo–Stark effect in a system they dubbed low-dimensional hydrogen. Other numerical methods for tackling the calculation of Stark shifts and the ionization rates include the popular complex scaling method [7], as well as the Riccati-Padé method [8], which is based on

the transformation of the Schrödinger equation to a nonlinear Riccati equation. Also, using the same mapping, Dolgov and Turbiner devised a numerical perturbative method [9], starting from an interpolated solution of the Riccati equation, for computing the ionization rate at strong fields. The Lo Surdo–Stark problem has also been addressed using JWKB schemes [10–13] and variational methods [14]. Fully analytical results have been found for the three-dimensional hydrogen atom [15]. Another interesting approach uses Gordon-Volkov wave functions [16,17], which are semiclassical-type wave functions for an electron in the electric field of an incoming electromagnetic wave.

In the field of two-dimensional (2D) excitons [18], there are already experimental reports of both valley selective Stark shift [19–21] and exciton dissociation via external electric fields [22]. In the same context, Stark shifts and ionization rates of excitons in these condensed matter systems have been calculated theoretically for arbitrary field intensities [23–25]. In [25] a semianalytical method was used, where the field dependence of these two quantities (shift and ionization rate) are determined analytically, and a material-dependent constant is determined numerically. The method only requires the electrostatic potential to have a Coulomb $1/r$ tail, but involves the introduction of an extra basis of functions to deal with the nonseparability of the electrostatic potential. Their results are asymptotically exact and capture commendably the low-field regime. The same authors have recently extended the method to excitons in van der Waals heterostructures [26] with success [27]. Recently, Cavalcante *et al.* have extended the interest in the Stark effect to trions in 2D semiconductors [28].

At the time of this writing, there is not a fully analytical description of the Lo Surdo–Stark effect for excitons in 2D materials. Although the previous methods can be used to describe this effect, the lack of a fully analytical expression

prevents their use by a wider community and lacks the insight provided by an analytical description. This is especially true for the material-dependent coefficient which is both hard to obtain numerically and varies by orders of magnitude even for modest changes of the dielectric function of the materials encapsulating the 2D material. An additional difficulty is the nonseparability of the electrostatic, non-Coulombic, potential between the hole and the electron in 2D excitons. This nonseparability has hindered the use of well known methods based on parabolic coordinates [9,29–31]. As we will see, however, this difficulty may be circumvented if one introduces the concept of an effective potential [32], with the only requirement being the existence of a Coulomb tail at large distances in the electrostatic potential [33,34]. This concept, in essence, renders the original potential approximately separable if one focuses on the relevant coordinate. Indeed, in parabolic coordinates ξ and η , and for the hydrogen atom in 2D in a static electric field, the eigenvalue problem is separable. The two resulting equations describe two different types of quantum problems. Whereas in the ξ coordinate the eigenvalue problem is that of a bound state, in the η coordinate the resulting eigenvalue problem describes a scattering state, where the exciton dissociates via tunneling through the Coulomb barrier, the latter rendered finite by the presence of the static electric field. Since tunneling is the relevant mechanism for dissociation and occurs (for weak fields) at large values of η , the problem, which is initially nonseparable, effectively becomes a function of one of the coordinates alone, depending on which of the two eigenvalue problems we are considering.

In this paper we take advantage of a number of techniques and obtain a fully analytical formula for the nonperturbative ionization rate of 2D excitons. Our approach highlights the role of both the excitons' effective mass and the dielectric environment, providing a simple formula for the ionization rate, in full agreement with more demanding numerical methods for weak fields. Such a formula is very useful for quick estimates of the ionization rate of excitons in 2D materials, and provides physical intuition that is helpful in, e.g., device design.

This paper is organized as follows: In Sec. II we present the Wannier equation describing the relative motion of an electron-hole pair and discuss the approximate separability of the Rytova-Keldysh potential. In Sec. III we obtain the expression for the ionization rate and discuss the semiclassical solution of the tunneling problem. In Sec. IV we apply our formula to the calculation of the ionization rate of excitons in 2D materials, taking the examples of hexagonal boron nitride and transition metal dichalcogenides. Finally, in Sec. V we give some final notes about our work and possible extension of the results.

II. WANNIER EQUATION

In this section we introduce the Wannier equation, originating from a Fourier transform of the Bethe-Salpeter equation [35–37], that defines the exciton problem in real space. We have found in previous publications [35–38] a good agreement between the solution of the Bethe-Salpeter equation and the binding energies arising from the solution of the Wannier

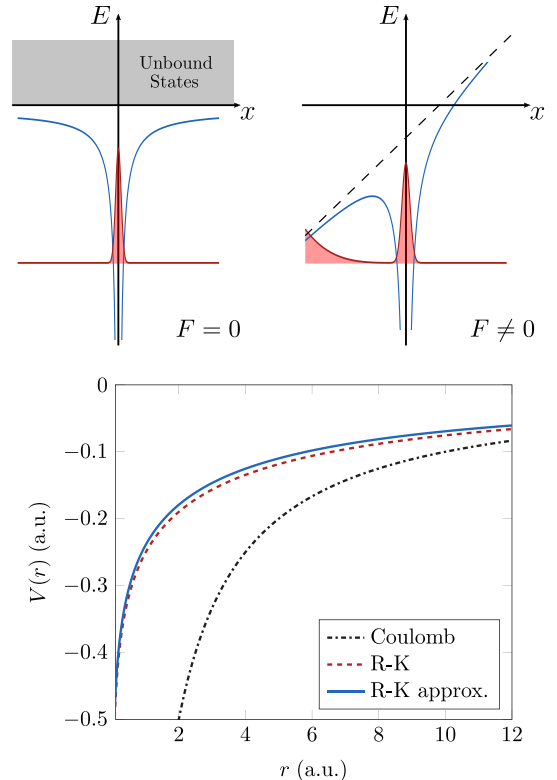


FIG. 1. (Top) Electrostatic potential and wave functions of the Lo Surdo-Stark effect. In the left panel the system is represented in the absence of the electric field and a bound state is formed. In the right panel an external electric field is superimposed on the attractive electrostatic field distorting the latter. Along one of the directions the total potential becomes more confining, whereas in the opposite direction the external field creates a barrier through which the exciton can tunnel and thereby ionize. (Bottom) Comparison between the Coulomb potential and the two expressions defined in the text for the Rytova-Keldysh potential. While for large values of r the potentials present an identical behavior, for small r a significant difference between the Coulomb and Rytova-Keldysh potentials is visible. Moreover, it is clear that the approximate expression for the Rytova-Keldysh potential gives an excellent approximation of Eq. (2). The parameters $\kappa = 1$ and $r_0 = 10 \text{ \AA}$ were used.

equation. The physics of the Lo Surdo-Stark effect is qualitatively represented in Fig. 1.

Following the steps of [29–31] we will pass from polar to parabolic coordinates with the goal of decoupling the original two-variable differential equation into two one-dimensional differential equations. Unlike the pure Coulomb problem, this problem is not exactly separable. However, as will become apparent, this problem is separable under justifiable approximations.

In this work we are interested in studying the ionization rate of excitons in 2D materials due to an external static electric field. The Wannier equation in atomic units (a.u.) and

in terms of the relative coordinate reads

$$\nabla^2 \psi(\mathbf{r}) - 2\mu[-E + \mathbf{F} \cdot \mathbf{r} + V(\mathbf{r})]\psi(\mathbf{r}) = 0, \quad (1)$$

where μ is the reduced mass of the electron-hole system, E is the energy, and $\mathbf{F} = F\hat{x}$, with $F > 0$, the external electric field, that we consider aligned along the x direction. The electron-hole interaction $V(\mathbf{r})$ is given by the Rytova-Keldysh potential [39,40]

$$V(\mathbf{r}) = -\frac{\pi}{2r_0} \left[\mathbf{H}_0\left(\frac{\kappa r}{r_0}\right) - Y_0\left(\frac{\kappa r}{r_0}\right) \right], \quad (2)$$

where the so-called screening length r_0 is proportional to the polarizability of the 2D sheet [41]. Macroscopically, it may be related to the thickness d and dielectric function ϵ of the sheet as $r_0 \sim d\epsilon/2$. Furthermore, κ is the mean dielectric constant of the media above and below the 2D material, \mathbf{H}_0 is the Struve function, and Y_0 is the Bessel function of the second kind. The fact that the electrostatic interaction between electron-hole pairs in 2D materials is given by the Rytova-Keldysh potential is what gives rise to the nonhydrogenic Rydberg series [42]. Inspired by the work of [41], where an approximate expression for the Rytova-Keldysh potential is presented, we use the following expression as an approximation to Eq. (2):

$$V(\mathbf{r}) \approx \frac{1}{r_0} \log \frac{\kappa r}{\kappa r + r_0}. \quad (3)$$

In Fig. 1 we plot Eq. (2) and the previous expression in the same graph and observe that the latter formula is an excellent approximation of the former.

Next we note that several authors [29–31] used parabolic coordinates in order to separate the Schrödinger equation into two differential equations of a single variable. In those works, however, the Coulomb potential was considered in the three-dimensional (3D) case. In our case, the Rytova-Keldysh potential does not allow a simple solution by separation of variables. To be able to do so, an effective potential has to be introduced. Let us consider the following set of parabolic coordinates [43,44] in 2D:

$$x = \frac{\xi - \eta}{2}, \quad (4)$$

$$y = \pm\sqrt{\xi\eta}, \quad (5)$$

$$r = \frac{\xi + \eta}{2}, \quad (6)$$

with both ξ and η belonging to the interval $[0, \infty[$. In these new coordinates the Laplacian reads

$$\nabla^2 = \frac{4}{\eta + \xi} \left[\sqrt{\eta} \frac{\partial}{\partial \eta} \left(\sqrt{\eta} \frac{\partial}{\partial \eta} \right) + \sqrt{\xi} \frac{\partial}{\partial \xi} \left(\sqrt{\xi} \frac{\partial}{\partial \xi} \right) \right]. \quad (7)$$

Applying this variable change to Eq. (1), and considering that $\psi(\eta, \xi) = v(\eta)u(\xi)$, we obtain an equation that can be separated, except for the potential term where ξ and η are still coupled by

$$\frac{(\eta + \xi)}{2} V\left(\frac{\eta + \xi}{2}\right). \quad (8)$$

To fully separate the ξ and η dependencies we propose the following effective potential:

$$\frac{(\eta + \xi)}{2} V\left(\frac{\eta + \xi}{2}\right) \approx \frac{\eta}{2} V\left(\frac{\eta}{2}\right) + \frac{\xi}{2} V\left(\frac{\xi}{2}\right). \quad (9)$$

The reasoning behind this choice is as follows: We know that in the usual polar coordinates the Rytova-Keldysh potential obeys the following two limits:

$$\lim_{r \rightarrow 0} rV(r) = 0, \quad (10)$$

$$\lim_{r \rightarrow \infty} rV(r) = -\frac{1}{\kappa}. \quad (11)$$

It is therefore clear that the decoupling we have introduced respects the two previous limits. We have chosen the above separation for having asymptotically the Coulomb potential in both η and ξ coordinates. Moreover, as we will see in the next section, we will be concerned with the limit $\eta \gg \xi$; in this case one can easily show that the difference between the effective potential and the initially inseparable one approximately scales as ξ/η . The only criterion the potential $V(x)$ must verify in order to make this a suitable separation is the existence of a Coulomb $1/x$ tail. The quality of the approximation has to be judged by the accuracy of the formula for the ionization rate (anticipating the results, we find an excellent qualitative and quantitative agreement between the analytical results and the numerical ones). In view of the approximation made, the decoupled equations read

$$\left[\sqrt{\eta} \frac{\partial}{\partial \eta} \left(\sqrt{\eta} \frac{\partial}{\partial \eta} \right) + \frac{\mu E}{2} \eta - \frac{\mu}{2} \eta V\left(\frac{\eta}{2}\right) + \mu \frac{F}{4} \eta^2 - Z \right] u(\eta) = 0, \quad (12)$$

$$\left[\sqrt{\xi} \frac{\partial}{\partial \xi} \left(\sqrt{\xi} \frac{\partial}{\partial \xi} \right) + \frac{\mu E}{2} \xi - \frac{\mu}{2} \xi V\left(\frac{\xi}{2}\right) - \mu \frac{F}{4} \xi^2 + Z \right] v(\xi) = 0, \quad (13)$$

where Z was introduced as a separation constant. Its value is determined below, demanding the correct large distance asymptotic behavior of the wave function. Using the proposed effective potential, the equations become mathematically identical, as they should, except for the external field term. Moreover, both equations reproduce the Coulomb problem in the asymptotic limit. We note that the two quantum problems defined in terms of the ξ and η coordinates have a completely different nature. While the ξ equation defines a bound state problem, and is therefore tractable by simple methods, the η equation defines a tunneling problem and obtaining its exact solution is challenging. These differential equations can be further simplified with the introduction of

$$u(\eta) = \frac{u_1(\eta)}{\eta^{1/4}}, \quad (14)$$

$$v(\xi) = \frac{v_1(\xi)}{\xi^{1/4}}, \quad (15)$$

which leads to

$$\left[\frac{d^2}{d\eta^2} + \frac{3}{16\eta^2} + \frac{\mu E}{2} - \frac{\mu}{2} V\left(\frac{\eta}{2}\right) + \frac{\mu F}{4} \eta - \frac{Z}{\eta} \right] u_1(\eta) = 0 \quad (16)$$

$$\left[\frac{d^2}{d\xi^2} + \frac{3}{16\xi^2} + \frac{\mu E}{2} - \frac{\mu}{2} V\left(\frac{\xi}{2}\right) - \frac{\mu F}{4} \xi + \frac{Z}{\xi} \right] v_1(\xi) = 0. \quad (17)$$

As noted, solutions of these two equations at large distances from the origin have two different behaviors: The first one has an oscillatory behavior, whereas the second one decays exponentially. Furthermore, while the second equation has a discrete spectrum, the first has a continuous one. This is due to the different sign of the field term in the two equations.

Finally, to end this section, we introduce another change of variable that has already proven to be of great value in this type of problems, known as the Langer transformation [45–48], which is defined by

$$\eta = e^t \Rightarrow d\eta = e^t dt, \quad (18)$$

$$u_1(\eta) = e^{t/2} T(t). \quad (19)$$

Making use of this transformation, Eq. (16) acquires the form

$$T''(t) + P^2(t)T(t) = 0, \quad (20)$$

with

$$P^2(t) = \frac{\mu E}{2} e^{2t} + \frac{\mu F}{4} e^{3t} - Ze^t - \frac{\mu}{2} V\left(\frac{e^t}{2}\right) e^{2t} - \frac{1}{16}. \quad (21)$$

A similar transformation could be applied to Eq. (17). This, however, is not necessary. We note that the advantages of the above transformation are twofold: On one side, the initial problem, valid only for $\eta \in [0, \infty[$, is transformed into a one-dimensional problem in the interval $t \in]-\infty, \infty[$, and on the other it removed the singular behavior at the origin due to the terms associated with $3/16\xi^2$. As shown by Berry and Ozorio de Almeida [47], the Langer transformation is a key step in solving the 2D hydrogen problem for zero angular momentum, which is similar to the problem at hand.

III. IONIZATION RATE

In this section we will present a derivation for the ionization rate of excitons in 2D materials due to the external electric field. We will start by associating the ionization rate with an integral of the probability current density. This integral will contain the function $T(t)$, presented in the end of the previous section. Then, this function will be explicitly computed. Afterwards, combining the previous two steps, a fully analytical expression for the ionization rate will be presented.

A. The ionization rate formula

In the beginning of the text we considered the electric field to be applied along the x direction, implying that the electrons will escape via the negative x direction, which in the parabolic coordinates introduced in Eqs. (4)–(6) corresponds to large values of η . Since the electrons will escape along the negative

x direction, we can define the ionization rate W as [33]

$$W = - \int_{-\infty}^{\infty} j_x dy. \quad (22)$$

That is, the number of particles per unit time transversing a line perpendicular to the probability current density j_x , which reads

$$j_x = \frac{i}{2\mu} \left(\psi \frac{\partial \psi^*}{\partial x} - \psi^* \frac{\partial \psi}{\partial x} \right), \quad (23)$$

where, once again, μ is the reduced mass. In terms of parabolic coordinates, the position vector is

$$\mathbf{r} = \frac{\xi - \eta}{2} \hat{\mathbf{x}} + \sqrt{\xi\eta} \hat{\mathbf{y}}. \quad (24)$$

The differentials in Cartesian coordinates are related to the parabolic ones through the following relations:

$$dx = \frac{1}{2} d\xi - \frac{1}{2} d\eta, \quad (25)$$

$$dy = \frac{1}{2} \sqrt{\frac{\eta}{\xi}} d\xi + \frac{1}{2} \sqrt{\frac{\xi}{\eta}} d\eta. \quad (26)$$

From here we find

$$\frac{\partial}{\partial x} = \frac{\partial \xi}{\partial x} \frac{\partial}{\partial \xi} + \frac{\partial \eta}{\partial x} \frac{\partial}{\partial \eta} \approx -2 \frac{\partial}{\partial \eta}, \quad (27)$$

where the final approximation comes from considering the limit $x \rightarrow -\infty$. Recalling what was done in the previous section we write

$$\psi(\eta, \xi) = u(\eta)v(\xi) \quad (28)$$

$$= \frac{u_1(\eta)}{\eta^{1/4}} \frac{v_1(\xi)}{\xi^{1/4}}. \quad (29)$$

Employing Eq. (19) this may also be written as

$$\psi(\eta, \xi) = \eta^{1/4} T[t(\eta)] \frac{v_1(\xi)}{\xi^{1/4}}. \quad (30)$$

The probability current density introduced in Eq. (23) can now be computed in parabolic coordinates as

$$j_x \approx \frac{i}{\mu} \sqrt{\eta} \frac{|v_1(\xi)|^2}{\xi^{1/2}} \left(T^* \frac{dT}{d\eta} - T \frac{dT^*}{d\eta} \right), \quad (31)$$

where, following the same reasoning as before, the derivatives in ξ were ignored. Inserting this expression into Eq. (22) and approximating the differential in the y coordinate by $dy \approx \sqrt{\eta/\xi} d\xi/2$ a generic expression for the ionization rate W in 2D is obtained:

$$W = -\frac{i}{\mu} \eta \left(T^* \frac{dT}{d\eta} - T \frac{dT^*}{d\eta} \right) \int_0^\infty \frac{|v_1(\xi)|^2}{\xi^{1/2}} d\xi. \quad (32)$$

Note the extra factor of 2 picked up by the symmetric integral in Eq. (22). Having obtained this expression, we turn our attention to the computation of T .

B. Solution of the tunneling problem using a semiclassical method

To determine $T(t)$ we need to solve Eq. (20), which is so far fully equivalent to Eq. (16). In order to do so, we will

use a uniform JWKB-type solution (where JWKB stands for Jeffrey-Wentzel-Kramers-Brillouin), known as the Miller and Good approach [47,49]. This method consists of introducing an auxiliary problem, whose solution is already established, to solve the main equation. The desired wave function will be given by the product of the solution to the auxiliary problem and a coordinate dependent amplitude. This amplitude consists of the quotient of two functions: In the denominator we have all the elements of the main equation associated with the nondifferentiated term; in the numerator we have the analogous elements but for the auxiliary equation. This last term is the key difference between the Miller and Good approach and the usual JWKB method. While the latter leads to wave functions with divergences at the classical turning points, the former produces smooth wave functions across the whole domain. As the auxiliary problem that will help us solve Eq. (20), we introduce the Airy equation

$$\frac{d^2}{d\zeta^2}\phi(\zeta) + \zeta\phi(\zeta) = 0, \quad (33)$$

whose solution reads

$$\phi(\zeta) = b_2 \text{Ai}(-\zeta) + b_1 \text{Bi}(-\zeta), \quad (34)$$

with $\text{Ai}(x)$ and $\text{Bi}(x)$ the Airy functions. This equation has a single turning point at $\zeta = 0$; the allowed and forbidden regions are located at $\zeta > 0$ and $\zeta < 0$, respectively. In order to have an outgoing wave in the propagating region we need to choose the coefficients b_1 and b_2 in a way that allows us to recover the correct asymptotic behavior. The asymptotic form of Eq. (34) reads

$$\phi(\zeta) \xrightarrow{\zeta \rightarrow \infty} b_2 \frac{\sin\left[\frac{\pi}{4} + \frac{2}{3}\zeta^{3/2}\right]}{\sqrt{\pi}\zeta^{1/4}} + b_1 \frac{\cos\left[\frac{\pi}{4} + \frac{2}{3}\zeta^{3/2}\right]}{\sqrt{\pi}\zeta^{1/4}}. \quad (35)$$

In order to obtain a traveling wave we choose $b_2 = ib_1$; with this choice we obtain

$$\phi_{\text{out}}(\zeta) \sim b_1 \frac{e^{i\frac{\pi}{4} + i\frac{2}{3}\zeta^{3/2}}}{\sqrt{\pi}\zeta^{1/4}}, \quad (36)$$

as we desired. When $\zeta \rightarrow -\infty$ the solution $\text{Bi}(-\zeta)$ grows while $\text{Ai}(-\zeta)$ vanishes; thus, deep inside the forbidden region we choose to approximate Eq. (34) by

$$\phi_{\text{forbidden}}(\zeta) \sim b_1 \frac{e^{\frac{2}{3}(-\zeta)^{3/2}}}{\sqrt{\pi}(-\zeta)^{1/4}}. \quad (37)$$

Using these results we write the solution of (20) in the allowed region as

$$T[t(\eta)] = b_1 \left(\frac{\zeta}{P^2(t)} \right)^{1/4} \frac{e^{i\frac{\pi}{4} + i\frac{2}{3}\zeta^{3/2}}}{\sqrt{\pi}\zeta^{1/4}}, \quad (38)$$

with $P^2(t)$ given by Eq. (21) and $\zeta(t)$ is defined via the relation

$$\int_0^\zeta \sqrt{\zeta'} d\zeta' = \frac{2}{3}\zeta^{3/2} = \int_{t_0}^t \sqrt{P^2(t')} dt', \quad (39)$$

where t_0 corresponds to the classical turning point of $P^2(t)$, that is $P^2(t_0) = 0$. Combining Eq. (39) with Eq. (38) it is

easily shown that

$$T^* \frac{dT}{d\eta} - T \frac{dT^*}{d\eta} = \frac{2i}{\pi} \frac{|b_1|^2}{\eta}, \quad (40)$$

which produces an ionization rate given by

$$W = \frac{|b_1|^2}{\pi\mu} \int_0^\infty \frac{|v_1(\xi)|^2}{\xi^{1/2}} d\xi. \quad (41)$$

Thus, to obtain W two tasks remain: Find b_1 and compute the integral in ξ . Let us now focus on the first one and only turn our attention to the second one later in the text.

C. Matching the wave function to an asymptotic one due to a Coulomb tail

In order to obtain b_1 we follow a conceptually simple procedure: We will determine the wave function $T[t(\eta)]$ deep inside the forbidden region $-\infty \ll t \ll t_0$, in the limit of a small field F , and using the Miller and Good approach we will extract b_1 from the comparison of this equation with the asymptotic solution of the radial Wannier equation.

Once more, using the Miller and Good approach, but this time for the forbidden region, we write $T[t(\eta)]$ as

$$T(t) \sim \frac{b_1}{\sqrt{\pi}} \left[\frac{1}{-P^2(t)} \right]^{1/4} e^{\frac{2}{3}(-\zeta)^{3/2}}. \quad (42)$$

Note the sign differences between this equation and Eq. (38); these appear due to the different validity regions of the respective functions. In the limit of a weak field $F \rightarrow 0$, we can approximate the $P^2(t)$ present in the denominator of the prefactor with

$$-P^2(t) \approx -\frac{\mu E}{2} e^{2t}. \quad (43)$$

The function ζ is defined by the relation

$$\frac{2}{3}(-\zeta)^{3/2} = \int_t^{t_0} \sqrt{-P^2(t')} dt', \quad (44)$$

where once again t_0 denotes the zero of $P^2(t)$, and is approximately

$$t_0 \sim \log \left(-\frac{2E}{F} \right). \quad (45)$$

To compute the integral in Eq. (44) we recall the form of $P^2(t)$ presented in Eq. (21) and discard the term $1/16$, since its contribution to the overall integral is insignificant. Then, we expand the integrand for small λ , a bookkeeping multiplicative parameter associated with the potential and the separation constant. Afterwards, we compute the integral, return to the original η coordinate using the Langer transformation, and expand the result for small F and large η , in this order. We note that the approximation presented in Eq. (43), although suitable for the prefactor, is too crude to produce a reasonable result inside the integral. Now, the key step in this procedure is the judicious choice of the separation constant Z ; this is a degree of freedom we can take advantage of by choosing it as we desire. Accordingly, we choose Z as

$$Z = \frac{\sqrt{-E\mu}}{2\sqrt{2}}. \quad (46)$$

This choice is made in order to allow us to recover a function with an η dependence that matches the solution of the asymptotic differential equation for the Coulomb tail of the interaction potential. The wave function $u(\eta)$ is obtained from

$$u(\eta) = \eta^{1/4} T(t), \quad (47)$$

which can be written as

$$u(\eta) = b_1 \frac{2^{1+\frac{3\sqrt{-E\mu}}{2E\kappa}} e^{-\frac{2\sqrt{2E}\sqrt{-E\mu}}{3F}}}{\sqrt{\pi}\mu^{1/4}} (-E)^{\frac{\sqrt{-E\mu}}{2E\kappa}} F^{-\frac{1}{4}-\frac{\sqrt{-E\mu}}{2E\kappa}} \times e^{-\frac{\eta\sqrt{-E\mu}}{2}} \eta^{-\frac{1}{2}-\frac{\sqrt{-E\mu}}{2E\kappa}}. \quad (48)$$

As briefly explained above, we now compare this wave function with the asymptotic solution for a particle (the exciton) of energy E bound by a potential with a Coulomb tail. The asymptotic wave function in radial coordinates reads

$$\psi_{\text{asympt}}(r) \sim A e^{-r\sqrt{-2E\mu}} r^{\frac{\sqrt{2}\sqrt{\mu}-\sqrt{-E\kappa}}{2\sqrt{-E\kappa}}}, \quad (49)$$

where A is a constant determined from the normalization of the full wave function due to a Coulomb potential. Note that the wave function in parabolic coordinates reads $\psi(\eta, \xi) = u(\eta)v(\xi)$. In the ground state, and due to the symmetry of the equations defining both $u(\eta)$ and $v(\xi)$ in the absence of the field, we must have $u(\eta) = v(\eta)$. In the large η limit $\eta \gg \xi$, we find from Eq. (49) that $u(\eta)$ must be of the form

$$u(\eta) \sim \sqrt{A} e^{-\frac{\eta}{2}\sqrt{-2E\mu}} (\eta/2)^{\frac{\sqrt{2}\sqrt{\mu}-\sqrt{-E\kappa}}{2\sqrt{-E\kappa}}}. \quad (50)$$

Comparing Eqs. (48) and (50) it follows that b_1 reads

$$b_1 = \sqrt{A} \sqrt{\pi} \mu^{1/4} \frac{e^{\frac{2\sqrt{2E}\sqrt{-E\mu}}{3F}}}{F^{-\frac{1}{4}-\frac{\sqrt{-E\mu}}{2E\kappa}}} 2^{-\frac{1}{2}-2\frac{\sqrt{-2E\mu}}{2E\kappa}} (-E)^{-\frac{\sqrt{-2E\mu}}{2E\kappa}}. \quad (51)$$

Once b_1 has been determined, the remaining task is the calculation of the integral in the rate equation. Again, we take advantage of the Coulomb tail present in the potential binding the exciton. In this case, the radial wave function in a Coulomb potential, for a particle with energy E , reads

$$R(r) = A e^{-\sqrt{-2E\mu}r} U\left(-\frac{\sqrt{2\mu}-\sqrt{-E\kappa}}{2\sqrt{-E\kappa}}, 1, 2\sqrt{-2E\mu}r\right), \quad (52)$$

where $U(a, b, z)$ is the hypergeometric U function. We now take $v(\xi) = A^{-1/2} R(\xi/2)$ and perform the integral. The result can be written as

$$\int_0^\infty |R(\xi/2)|^2 \frac{d\xi}{\sqrt{\xi}} \equiv A A_\xi. \quad (53)$$

In general, it follows that the ionization rate W reads

$$W = \frac{2}{\mu} A_\xi A^2 \sqrt{\mu} \frac{e^{\frac{4\sqrt{2E}\sqrt{-E\mu}}{3F}}}{F^{-\frac{1}{2}-\frac{2\sqrt{-E\mu}}{2E\kappa}}} 2^{-1-4\frac{\sqrt{-2E\mu}}{2E\kappa}} (-E)^{-\frac{\sqrt{-2E\mu}}{E\kappa}}, \quad (54)$$

and for the particular case of a 2D exciton bound by the Coulomb interaction we obtain

$$W = 32 \sqrt{\frac{2}{\pi}} \frac{\mu^2 e^{-\frac{16\mu^2}{3F\kappa^3}}}{\sqrt{F\kappa^{7/2}}}, \quad (55)$$

a result identical to that found by Tanaka *et al.* [6]. In general, for any potential with a Coulomb tail we find

$$W = g_0^2 W_0(F), \quad (56)$$

where

$$W_0(F) = \frac{e^{\frac{4\sqrt{2E}\sqrt{-E\mu}}{3F}}}{F^{-\frac{1}{2}-\frac{2\sqrt{-E\mu}}{2E\kappa}}} \quad (57)$$

and

$$g_0^2 \approx \frac{\kappa 2^{\frac{2\sqrt{2\mu}}{\kappa\sqrt{-E\mu}}+\frac{5}{4}} (-E)^{\frac{\sqrt{2\mu}}{\kappa\sqrt{-E\mu}}+\frac{5}{4}} \Gamma\left(\frac{\sqrt{2\mu}}{\kappa\sqrt{-E\mu}} - \frac{1}{2}\right)}{\pi^{\frac{1}{4}} \sqrt{\mu} \Gamma\left(\frac{\sqrt{2\mu}}{\kappa\sqrt{-E\mu}}\right)}, \quad (58)$$

where $\Gamma(z)$ is the gamma function. Equation (56) together with Eq. (58) are the central results of this paper. Special limits of this last result can be obtained for carefully chosen values of E , κ , and μ . In particular, for E given by $E = -2\mu/\kappa^2$, corresponding to the ground state energy of a 2D exciton bound by the Coulomb potential, we recover the result given by Eq. (55) for the rate W . In the next section we explore the consequences of Eqs. (56) and (54).

IV. RESULTS

Having determined the form of the ionization rate, we can compare our results with numerical ones obtained via the solution of an eigenvalue problem for the exciton's motion using the complex scaling method, which allow us to access complex eigenvalues, with the imaginary part interpreted as the rate W computed above. Below we give a brief account of how the numerical calculations are performed.

A. Complex scaling method

When a system that may be ionized is subjected to an external electric field, the energy eigenvalue turns complex. The ionization rate of the system is then described by the imaginary part of the energy as $\Gamma = -2\text{Im} E$. A formally exact method of computing the complex energy is to transform the original eigenvalue problem into a non-Hermitian eigenvalue problem via the complex scaling technique [7,50–52]. Here one rotates the radial coordinate into the complex plane by an angle ϕ to circumvent the diverging behavior of the resonance states [53]. The method is incredibly flexible, and one may choose to either rotate the entire radial domain as $r \rightarrow r e^{i\phi}$ or choose to only rotate the coordinate outside a desired radius R as

$$r \rightarrow \begin{cases} r & \text{for } r < R, \\ R + (r - R)e^{i\phi} & \text{for } r > R. \end{cases} \quad (59)$$

Early motivations for introducing the latter, so-called exterior complex scaling (ECS) [54,55], technique were to extend the applicability of the complex scaling method. For instance, the uniform complex scaling (UCS) technique was not applicable within the Born-Oppenheimer approximation [56]. We point out that when both methods may be applied to the same potential, which is the case for all potentials considered here, they yield identical eigenvalues. Nevertheless, there are numerical advantages to consider for each technique. UCS is easier to implement, and has previously been used to obtain ionization

rates of excitons in monolayer MoS₂ [57] and WSe₂ [22] for relatively large fields. However, the ECS technique [56,58] is much more efficient for the weak fields that are relevant for excitons in 2D semiconductors [25]. Using the contour defined by Eq. (59) in the eigenvalue problem, we obtain states that behave differently in the interior $r < R$ and exterior $r > R$ domains. Furthermore, there are discontinuities at R that we have to deal with [58,59]. An efficient method of solving these types of problems is to use a finite element basis to resolve the radial behavior of the states. To this end, we divide the radial domain into N segments $[r_{n-1}, r_n]$. A set of p functions satisfying

$$\begin{aligned} f_i^{(n)}(r_{n-1}) &= f_i^{(n)}(r_n) = 0, \\ \text{except } f_1^{(n)}(r_{n-1}) &= f_p^{(n)}(r_n) = 1 \end{aligned} \quad (60)$$

is then introduced on each segment n in order to make enforcing continuity across the segment boundaries simple. In practice, we transform the Legendre polynomials such that they satisfy Eq. (60) [59]. The wave function may then be written as

$$\psi(\mathbf{r}) = \sum_{m=0}^M \sum_{n=1}^N \sum_{i=1}^p c_i^{(m,n)} f_i^{(n)}(r) \cos(m\theta), \quad (61)$$

where continuity across the segment boundaries is ensured by enforcing

$$c_p^{(m,n-1)} = c_1^{(m,n)}, \quad n = 2, \dots, N, \quad (62)$$

in the expansion coefficients. As the unperturbed problems considered here are radially symmetric, an efficient angular basis of cosine functions may be used to resolve the angular behavior of the states. Using this expansion, the Wannier equation may be transformed into a matrix eigenvalue problem and solved efficiently using techniques for sparse matrices. Note that we keep the radial coordinate in the basis functions real and leave it to the expansion coefficients to describe the behavior along the complex contour. This technique has previously been used to compute ionization rates of excitons in monolayer semiconductors [25] as well as bilayer heterostructures [27], and we shall use it here to validate the analytical results.

B. An application

To illustrate the validity of our analytical formula over a significant range of values of the external field F , we compute the ionization rate for excitons in the 2D hydrogen atom, hBN, WSe₂, and MoS₂. In previous publications we have shown that excitons in hBN and TMDs are well described by the Wannier equation with the Rytova-Keldysh potential [35,60]. In Fig. 2 we present a comparison of our analytical results with the finite element method (FEM) approach described above. There is a remarkable agreement between both approaches across the four cases of study. The analytical results excel at moderate and small field values, but start to deviate from the exact numerical methods at extremely large fields. This is to be expected, since our analytical result was obtained in the limit of small fields. At very small fields the FEM struggles to give accurate results, a region where the analytical approach is highly accurate. Moreover, the FEM

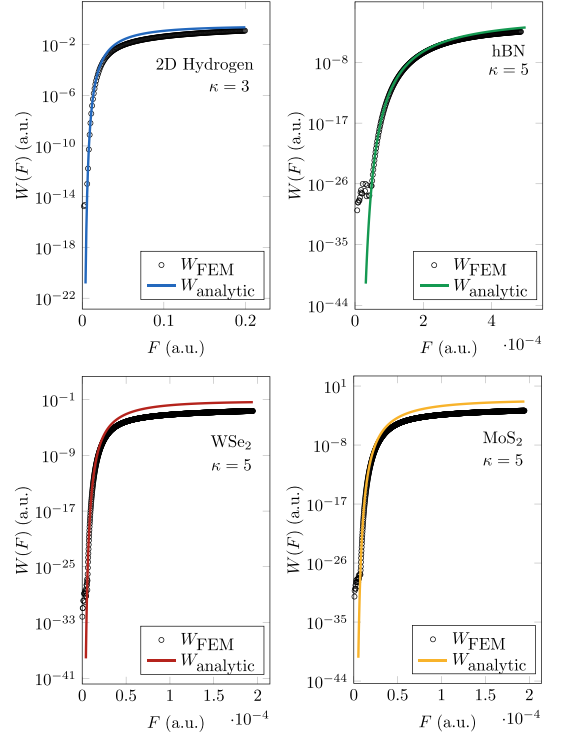


FIG. 2. Comparison of the numerical and analytical calculation of the rate for hBN excitons. The reduced mass of the exciton in H, hBN, MoS₂, and WSe₂ is $\mu = 1, 0.5, 0.28, 0.23$, respectively, the parameters describing the polarizability of hBN, MoS₂, and WSe₂ is $r_0 = 10, 43.4, 46.2$ Å, respectively, and the dielectric constants is $\kappa = 5$ for all but hydrogen, for which $\kappa = 3$. All quantities depicted are given in atomic units (a.u.) and the parameters were taken from Ref. [25].

requires time-expensive calculations and convergence needs to be confirmed for every case. Needless to say, the analytical approach suffers not from these two shortcomings. Also, the analytical approach makes studying the dependence on the dielectric environment surrounding the 2D material [61] easy.

V. FINAL REMARKS

In this paper we have derived an expression for the ionization rate of excitons in a 2D material due to the application of an external static electric field. Our result is quantitatively accurate, as was shown in the bulk of the text. Our approach took a semiclassical path, based on an approximate separation of the Rytova-Keldysh potential in parabolic coordinates. This step is key in the derivation, and is justifiable on the basis of the behavior of the potential near the origin and at large distances. The next key step is the solution of a tunneling problem, described by one of the equations arising from the separability procedure, the η equation. The solution of the tunneling problem was achieved via a uniform semiclassical method, developed by Miller and Good and used by Berry

and Ozorio de Almeida for the 2D Coulomb problem, for the zero angular momentum channel. Once the semiclassical solution is found, we match it with the asymptotic solution of a particle of reduced mass μ (the exciton reduced mass) and energy E , in a dielectric environment characterized by a dielectric function κ , in a Coulomb potential. This matching requires that the original potential binding the electron and hole has a Coulomb tail, which is fortunately true in our case. Therefore, for every potential with a Coulomb tail our method is applicable. An interesting system that satisfies these conditions is interlayer excitons in bilayer structures [62–64]. They may be described by the RK potential with the radial coordinate substituted by the 3D distance between the electron and hole, and adding the screening lengths of both layers [27]. For large distances, the vertical separation is negligible, and the interaction potential thus assumes its Coulomb tail in this region. It is therefore simple to extend the method to this case. An additional advantage of the method, besides giving an analytical solution for the ionization rate, is that it is easily extendable to other classes of potentials such as those discussed by Pfeiffer [32]. Finally, we note that our result can be extended to the calculation of the photoionization rate of the exciton due to an external electric field of frequency

ω . To achieve this, we replace the electric field strength by $F(t) = F_0 \cos(\omega t)$ in the rate equation and average over one cycle. Although this procedure is not exact, it should give good results in the low frequency regime.

ACKNOWLEDGMENTS

N.M.R.P. acknowledges support from the European Commission through the project “Graphene-Driven Revolutions in ICT and Beyond” (Ref. No. 881603 – core 3), and the Portuguese Foundation for Science and Technology (FCT) in the framework of the Strategic Financing UID/FIS/04650/2019. In addition, N.M.R.P. acknowledges COMPETE2020, PORTUGAL2020, FEDER and the Portuguese Foundation for Science and Technology (FCT) through projects POCI- 01-0145-FEDER-028114, POCI-01-0145-FEDER-029265, PTDC/NAN-OPT/29265/2017, and POCI-01-0145-FEDER-02888. H.C.K. and T.G.P. gratefully acknowledge financial support from the Center for Nanostructured Graphene (CNG), which is sponsored by the Danish National Research Foundation, Project No. DNR103. Additionally, T.G.P. is supported by the QUSCOPE Center, sponsored by the Villum Foundation.

-
- [1] J. P. Connerade, in *Atoms in Strong Fields*, NATO ASI Series, edited by Cleanthes A. Nicolaides, Charles W. Clark, and Munir H. Nayfeh (Springer, New York, 1990), Vol. 212.
 - [2] V. Franceschini, V. Grecchi, and H. J. Silverstone, *Phys. Rev. A* **32**, 1338 (1985).
 - [3] C. A. Nicolaides and S. I. Themelis, *Phys. Rev. A* **45**, 349 (1992).
 - [4] T. G. Pedersen, H. Mera, and B. K. Nikolic, *Phys. Rev. A* **93**, 013409 (2016).
 - [5] H. Mera, T. G. Pedersen, and B. K. Nikolić, *Phys. Rev. Lett.* **115**, 143001 (2015).
 - [6] K. Tanaka, M. Kobashi, T. Shichiri, T. Yamabe, D. M. Silver, and H. J. Silverstone, *Phys. Rev. B* **35**, 2513 (1987).
 - [7] I. W. Herbst and B. Simon, *Phys. Rev. Lett.* **41**, 67 (1978).
 - [8] F. M. Fernandez and J. Garcia, *Appl. Math. and Comp.* **317**, 101 (2018).
 - [9] A. Dolgov and A. Turbner, *Phys. Lett. A* **77**, 15 (1980).
 - [10] M. H. Rice and R. H. Good, *J. Opt. Soc. Am.* **52**, 239 (1962).
 - [11] J. D. Bekenstein and J. B. Krieger, *Phys. Rev.* **188**, 130 (1969).
 - [12] J. A. C. Gallas, H. Walther, and E. Werner, *Phys. Rev. A* **26**, 1775 (1982).
 - [13] D. A. Harmin, *Phys. Rev. A* **26**, 2656 (1982).
 - [14] P. Froelich and E. Brändas, *Phys. Rev. A* **12**, 1 (1975).
 - [15] T. Yamabe, A. Tachibana, and H. J. Silverstone, *Phys. Rev. A* **16**, 877 (1977).
 - [16] C. Joachain, N. Kylstra, and R. Potvliege, *Atoms in Intense Fields*, 1st ed. (Cambridge University Press, Cambridge, 2012).
 - [17] T. Schultz and M. Vrakking, *Attosecond and XUV Physics*, 1st ed. (Wiley, Singapore, 2014).
 - [18] G. Wang, A. Chernikov, M. M. Glazov, T. F. Heinz, X. Marie, T. Amand, and B. Urbaszek, *Rev. Mod. Phys.* **90**, 021001 (2018).
 - [19] E. J. Sie, J. W. McIver, Y.-H. Lee, L. Fu, J. Kong, and N. Gedik, *Nat. Mater.* **14**, 290 (2015).
 - [20] E. J. Sie, J. W. McIver, Y.-H. Lee, L. Fu, J. Kong, and N. Gedik, in *Ultrafast Bandgap Photonics*, edited by M. K. Rafailov and E. Mazur, International Society for Optics and Photonics (SPIE, Bellingham, WA, 2016), Vol. 9835, pp. 129–137.
 - [21] P. D. Cunningham, A. T. Hanbicki, T. L. Reinecke, K. M. McCreary, and B. T. Jonker, *Nat. Commun.* **10**, 5539 (2019).
 - [22] M. Massicotte, F. Vialla, P. Schmidt *et al.*, *Nat. Commun.* **9**, 1633 (2018).
 - [23] T. G. Pedersen, *Phys. Rev. B* **94**, 125424 (2016).
 - [24] B. Scharf, T. Frank, M. Gmitra, J. Fabian, I. Žutić, and V. Perebeinos, *Phys. Rev. B* **94**, 245434 (2016).
 - [25] H. C. Kamban and T. G. Pedersen, *Phys. Rev. B* **100**, 045307 (2019).
 - [26] S. Das, J. A. Robinson, M. Dubey, H. Terrones, and M. Terrones, *Annu. Rev. Mater. Res.* **45**, 1 (2015).
 - [27] H. C. Kamban and T. G. Pedersen, *Sci. Rep.* **10**, 5537 (2020).
 - [28] L. S. R. Cavalcante, D. R. da Costa, G. A. Farias, D. R. Reichman, and A. Chaves, *Phys. Rev. B* **98**, 245309 (2018).
 - [29] M. H. Alexander, *Phys. Rev.* **178**, 34 (1969).
 - [30] G. Torres del Castillo and E. N. Morales, *Rev. Mex. Fis.* **54**, 454 (2008).
 - [31] R. J. Damburg and V. V. Kolosov, *J. Phys. B: At. Mol. Phys.* **11**, 1921 (1978).
 - [32] A. N. Pfeiffer, C. Cirelli, M. Smolarski, D. Dimitrovski, M. Abu-samha, L. B. Madsen, and U. Keller, *Nat. Phys.* **8**, 76 (2012).
 - [33] C. Z. Bisgaard and L. B. Madsen, *Am. J. Phys.* **72**, 249 (2004).
 - [34] O. I. Tolstikhin, T. Morishita, and L. B. Madsen, *Phys. Rev. A* **84**, 053423 (2011).
 - [35] J. Henriques, G. Ventura, C. Fernandes, and N. Peres, *J. Phys.: Condens. Matter* **32**, 025304 (2020).
 - [36] J. C. G. Henriques and N. M. R. Peres, *Phys. Rev. B* **101**, 035406 (2020).

- [37] J. C. G. Henriques, G. Catarina, A. T. Costa, J. Fernández-Rossier, and N. M. R. Peres, *Phys. Rev. B* **101**, 045408 (2020).
- [38] J. Have, G. Catarina, T. G. Pedersen, and N. M. R. Peres, *Phys. Rev. B* **99**, 035416 (2019).
- [39] S. Rytova, Moscow Univ. Phys. Bull. **22**, 30 (1967).
- [40] L. V. Keldysh, Sov. J. Exp. Theor. Phys. Lett. **29**, 658 (1979).
- [41] P. Cudazzo, I. V. Tokatly, and A. Rubio, *Phys. Rev. B* **84**, 085406 (2011).
- [42] A. Chernikov, T. C. Berkelbach, H. M. Hill, A. Rigosi, Y. Li, O. B. Aslan, D. R. Reichman, M. S. Hybertsen, and T. F. Heinz, *Phys. Rev. Lett.* **113**, 076802 (2014).
- [43] J. A. R. Sohnesen, Master's thesis, Aalborg University, Denmark, 2016.
- [44] H. C. Kamban and S. S. Christensen, Master's thesis, Aalborg University, Denmark, 2018.
- [45] R. E. Langer, *Phys. Rev.* **51**, 669 (1937).
- [46] R. H. Good, *Phys. Rev.* **90**, 131 (1953).
- [47] M. Berry and A. O. de Almeida, *J. Phys. A* **6**, 1451 (1973).
- [48] D. Farrelly and W. P. Reinhardt, *J. Phys. B: At. Mol. Phys.* **16**, 2103 (1983).
- [49] S. C. Miller, Jr. and R. Good, Jr., *Phys. Rev.* **91**, 174 (1953).
- [50] E. Balslev and J. M. Combes, *Commun. Math. Phys.* **22**, 280 (1971).
- [51] J. Aguilar and J. M. Combes, *Commun. Math. Phys.* **22**, 269 (1971).
- [52] M. Reed and B. Simon, *Methods of Modern Mathematical Physics* (Academic, New York, 1982).
- [53] Y. Ho, *Phys. Rep.* **99**, 1 (1983).
- [54] C. A. Nicolaides and D. R. Beck, *Phys. Lett. A* **65**, 11 (1978).
- [55] C. A. Nicolaides, H. J. Gotsis, M. Chrysos, and Y. Komninos, *Chem. Phys. Lett.* **168**, 570 (1990).
- [56] B. Simon, *Phys. Lett.* **71**, 211 (1979).
- [57] S. Haastrup, S. Latini, K. Bolotin, and K. S. Thygesen, *Phys. Rev. B* **94**, 041401(R) (2016).
- [58] A. Scrinzi and N. Elander, *J. Chem. Phys.* **98**, 3866 (1993).
- [59] A. Scrinzi, *Phys. Rev. A* **81**, 053845 (2010).
- [60] F. Ferreira, A. J. Chaves, N. M. R. Peres, and R. M. Ribeiro, *J. Opt. Soc. Am. B* **36**, 674 (2019).
- [61] A. J. Chaves, R. M. Ribeiro, T. Frederico, and N. M. R. Peres, *2D Mater.* **4**, 025086 (2017).
- [62] O. L. Berman and R. Y. Kezerashvili, *Phys. Rev. B* **93**, 245410 (2016).
- [63] M. Fogler, L. Butov, and K. Novoselov, *Nat. Commun.* **5**, 4555 (2014).
- [64] F.-C. Wu, F. Xue, and A. H. MacDonald, *Phys. Rev. B* **92**, 165121 (2015).

Paper E

Anisotropic Stark shift, field-induced dissociation, and
electroabsorption of excitons in phosphorene

Høgni C. Kamban, Thomas G. Pedersen, and Nuno M. R. Peres

This paper has been published in Physical Review B:
Phys. Rev. B **102**, 115305 (2020)
DOI: 10.1103/physrevb.102.115305

Anisotropic Stark shift, field-induced dissociation, and electroabsorption of excitons in phosphoreneHøgne C. Kamban^{*} and Thomas G. Pedersen*Department of Materials and Production, Aalborg University, DK-9220 Aalborg Øst, Denmark
and Center for Nanostructured Graphene (CNG), DK-9220 Aalborg Øst, Denmark*

Nuno M. R. Peres

*Department and Centre of Physics, QuantaLab, University of Minho, Campus of Gualtar, 4710-057 Braga, Portugal
and International Iberian Nanotechnology Laboratory (INL), Avenida Mestre Jos Veiga, 4715-330 Braga, Portugal*

(Received 3 July 2020; revised 24 August 2020; accepted 27 August 2020; published 17 September 2020)

We compute binding energies, Stark shifts, electric-field-induced dissociation rates, and the Franz-Keldysh effect for excitons in phosphorene in various dielectric surroundings. All three effects show a pronounced dependence on the direction of the in-plane electric field with the dissociation rates, in particular, decreasing by several orders of magnitude upon rotating the electric field from the armchair to the zigzag axis. To better understand the numerical dissociation rates, we derive an analytical approximation to the anisotropic rates induced by weak electric fields thereby generalizing the previously obtained result for isotropic two-dimensional semiconductors. This approximation is shown to be valid in the weak-field limit by comparing it to the exact rates. The anisotropy is also apparent in the large difference between armchair and zigzag components of the exciton polarizability tensor, which we compute for the five lowest-lying states. As expected, we also find much more pronounced Stark shifts in either the armchair or the zigzag direction, depending on the symmetry of the state in question. Finally, an isotropic interaction potential is shown to be an excellent approximation to a more accurate anisotropic interaction derived from the Poisson equation, confirming that the anisotropy of phosphorene is largely due to the direction dependence of the effective masses.

DOI: [10.1103/PhysRevB.102.115305](https://doi.org/10.1103/PhysRevB.102.115305)**I. INTRODUCTION**

With the experimental discovery of graphene in 2004 [1], interest in two-dimensional (2D) materials increased enormously. Just a few years later, the successful exfoliation of monolayer MoS₂ [2] produced the first atomically thin direct band-gap semiconductor. One of the newest members of the 2D semiconductor family is monolayer black phosphorus (BP), referred to, here, as phosphorene [3–7]. It has seen a remarkable rate of growth in research interest, even more so than graphene [8]. Unlike transition-metal dichalcogenides (TMDs) where the band gap is direct only in their monolayer form [9], BP is a direct band-gap semiconductor regardless of the number of layers [10–13]. The magnitude of the gap evolves from around 0.3 eV in its bulk form to around 2 eV in monolayers [5,6,14–16]. The extreme tunability of the band gap as well as its highly anisotropic nature, make phosphorene an exceptionally interesting material for both practical applications and theoretical investigation. For instance, the tunable gap makes phosphorene a promising material for converting solar energy to chemical energy [17]. The anisotropy of phosphorene shows up in almost all of its physical properties, such as its electrical [18,19], magneto-optical [20–22], thermal [23,24], and mechanical [25] properties. Particular examples of highly anisotropic

quantities in phosphorene are the conductivity [26], optical absorption [7], and photoluminescence [16].

Very strong absorption peaks have been observed in monolayer and bilayer phosphorene [5,27] due to strongly bound excitons [15,28–30]. How such strongly bound excitons interact with external electric fields is an interesting area of study, particularly, in phosphorene as the direction of the in-plane field will matter. An applied electric field pulls electrons and holes in opposite directions, which causes a shift in the exciton energy and may even lead to dissociation of the exciton. Collectively, these effects have been studied intensely in carbon nanotubes [31–33] as well as monolayer [34–39], bilayer [40], and multilayer TMDs [41]. They have been studied to a lesser degree in phosphorene [38,42] where focus has been on the energy shift rather than field-induced exciton dissociation, which is one of the main novel results of the present paper. One of the motivations for applying external electric fields to low-dimensional semiconductors from a device perspective is to induce exciton dissociation and thereby improve photocurrent generation in, e.g., solar cells and photodetectors. The exciton Stark effect is also promising as a means of manipulating the properties of semiconductors. For instance, the shift in exciton energy and possibility of dissociation caused by an applied field shifts and broadens the optical absorption peaks. This is known as the Franz-Keldysh effect [43,44] and was studied for monolayer TMDs in Ref. [34]. In TMDs, both Stark and Franz-Keldysh effects are independent of the direction of an in-plane electric field. In contrast, the highly

^{*}hck@mp.aau.dk

anisotropic nature of phosphorene leads to a Stark effect that is strongly dependent on the direction of the field [38,42], and this effect should also be visible in the Franz-Keldysh effect.

In the present paper, we study the exciton Stark and Franz-Keldysh effects in phosphorene. The paper is structured as follows. In Sec. II, we introduce the model used and show that using an isotropic interaction potential between the electron and the hole is an excellent approximation to a more accurate anisotropic interaction. For phosphorene, the majority of the anisotropy, therefore, comes from the direction dependent effective masses. In this section, we also compute the energies of the five lowest-lying exciton states in phosphorene in three different dielectric surroundings and discuss their symmetries. In Sec. III, the focus is on the exciton Stark effect. Here, we observe Stark shifts and exciton dissociation rates that are strongly dependent on the direction of the field. We compare the Stark shifts to previously published results [38,42] and find a good agreement. The exciton dissociation rates, however, have not been computed before. To better understand these effects, we compare the Stark shifts and dissociation rates to analytical approximations derived from perturbation theory and weak-field asymptotic theory (WFAT), respectively. In Sec. IV, we turn to the Franz-Keldysh effect, which also exhibits pronounced direction dependence. Finally, the results are concluded upon in Sec. V. The text is supplemented by three appendices. In Appendix A, the exciton interaction potential in an anisotropic semiconductor is discussed; in Appendix B, we consider how strain induced by a lattice mismatch between phosphorene and the encapsulating material affects the effective masses, and, in turn, the exciton Stark effect; and in Appendix C, an anisotropic weak-field approximation for the exciton dissociation rate is derived.

II. EXCITONS IN PHOSPHORENE

By now, it is well known that many excitonic effects are accurately described by modeling the excitons as electron-hole pairs satisfying the Wannier equation [45,46]. It has been shown repeatedly that the Wannier model reproduces the exciton binding energies obtained from first-principles calculations to a satisfactory degree [47–50]. This is fortunate, as first-principles calculations require solving the computationally demanding Bethe-Salpeter equation [51,52]. Importantly, the Wannier model has also been shown to agree with experimental results for the exciton Stark effect, field-induced dissociation, and the Franz-Keldysh effect [37]. For anisotropic 2D semiconductors, the Wannier equation in the absence of an electric field reads (in atomic units)

$$\left[-\frac{1}{2\mu_x} \frac{\partial^2}{\partial x^2} - \frac{1}{2\mu_y} \frac{\partial^2}{\partial y^2} + V(\mathbf{r}) - E \right] \psi(\mathbf{r}) = 0, \quad (1)$$

where V is the electron-hole interaction, E is the energy, and

$$\mu_{x/y} = \frac{m_e^{(x/y)} m_h^{(x/y)}}{m_e^{(x/y)} + m_h^{(x/y)}} \quad (2)$$

is the direction-specific reduced mass with $m_e^{(x/y)}$ and $m_h^{(x/y)}$ being the electron and hole effective masses along the x/y direction, respectively. The exciton interaction V in anisotropic semiconductors is, of course, anisotropic. It may be found

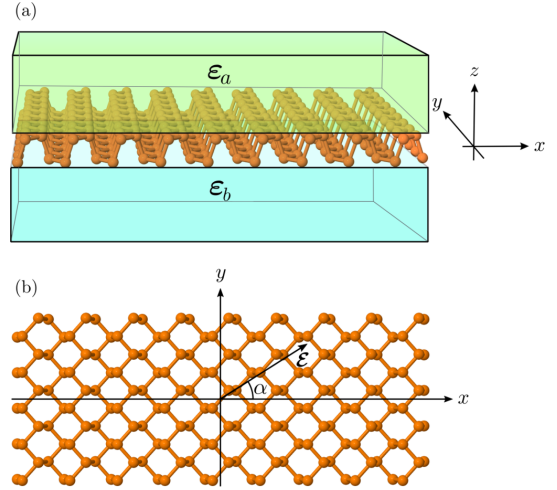


FIG. 1. Sketch of the geometry. (a) Side view of a phosphorene sheet encapsulated by media with dielectric tensors ϵ_a and ϵ_b . (b) Top view indicating the electric-field orientation.

by modeling the encapsulated 2D semiconductor [depicted in Fig. 1(a)] as a three-layer structure with a piecewise constant dielectric function and, then, solving the Poisson equation for two charges in this structure. This is performed in Appendix A. For a superstrate, a 2D semiconductor, and a substrate with dielectric tensors $\epsilon_a = \text{diag}(\epsilon_{xx}^{(a)}, \epsilon_{yy}^{(a)}, \epsilon_{zz}^{(a)})$, $\epsilon = \text{diag}(\epsilon_{xx}, \epsilon_{yy}, \epsilon_{zz})$, and $\epsilon_b = \text{diag}(\epsilon_{xx}^{(b)}, \epsilon_{yy}^{(b)}, \epsilon_{zz}^{(b)})$, respectively, we find with a linearized dielectric function,

$$V(r, \theta) \approx - \int_0^\infty \frac{J_0(qr)}{\sqrt{\epsilon_x \epsilon_y}} dq - 2 \sum_{k=1}^\infty \cos(2k\theta) \int_0^\infty \left(\frac{\sqrt{\epsilon_x} - \sqrt{\epsilon_y}}{\sqrt{\epsilon_x} + \sqrt{\epsilon_y}} \right)^k J_{2k}(qr) dq, \quad (3)$$

where $\epsilon_x = \kappa + r_{0x}q$, $\epsilon_y = \kappa + r_{0y}q$, and $\kappa = \frac{\sqrt{\epsilon_{xx}^{(a)} \epsilon_{zz}^{(a)}} + \sqrt{\epsilon_{xx}^{(b)} \epsilon_{zz}^{(b)}}}{2}$. The screening lengths are defined as $r_{0x} = 2\pi\alpha_{xx}^{(2D)}$ and $r_{0y} = 2\pi\alpha_{yy}^{(2D)}$, where $\alpha_{xx}^{(2D)}$ and $\alpha_{yy}^{(2D)}$ are the 2D sheet polarizabilities in the x and y directions, respectively. These are the microscopic definitions of the screening lengths [53]. The macroscopic definitions may be seen in Appendix A. Note that Eq. (3) reduces to the usual Rytova-Keldysh potential [54–56] in the isotropic case.

The polarizabilities for phosphorene were computed in Ref. [28] where the authors found $\alpha_{xx}^{(2D)} = 4.20$ and $\alpha_{yy}^{(2D)} = 3.97$ Å. These values are quite close, which, in turn, leads to a very weak angular contribution to the interaction. As a first approximation, we may, therefore, consider only the leading term. Further expanding $\sqrt{\epsilon_x \epsilon_y}$ to first order in q , we find the Rytova-Keldysh (RK) form [54,55]

$$V(r, \theta) \approx V_{RK}(r) = -\frac{\pi}{2r_0} \left[H_0\left(\frac{\kappa r}{r_0}\right) - Y_0\left(\frac{\kappa r}{r_0}\right) \right], \quad (4)$$

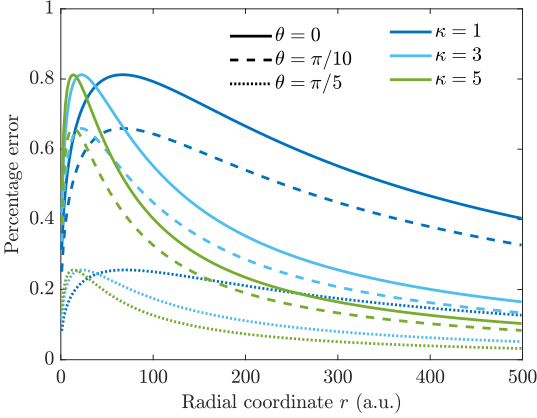


FIG. 2. Error introduced by using the isotropic approximation in Eq. (4) instead of the full interaction in Eq. (3) to describe excitons in phosphorene.

with $r_0 = (r_{0x} + r_{0y})/2$. This form agrees with the interaction used by many authors to study excitons in phosphorene [28,30,57]. Using the isotropic approximation to describe the excitons is justified by noting that it agrees with the full potential in Eq. (3) to within 1% for all r and θ . Errors for three different dielectric surroundings and directions are shown in Fig. 2. As is evident, these errors are low, and they decrease as θ tends to $\pi/4$ as the dominating angular contribution from the $k = 1$ term tends to zero in this region. The parameters used to describe excitons in phosphorene in the present paper are summarized in Table I.

To perform numerical calculations, it is convenient to switch to the coordinates introduced in Ref. [28] defined by

$$X = \sqrt{\frac{\mu_x}{2\mu}}x, \quad Y = \sqrt{\frac{\mu_y}{2\mu}}y, \quad \mu = \frac{\mu_x\mu_y}{\mu_x + \mu_y}. \quad (5)$$

This transforms Eq. (1) into

$$\left\{ -\frac{1}{4\mu} \nabla^2 + V_{\text{RK}}[R\sqrt{1 + \beta \cos 2\Theta}] - E \right\} \psi(\mathbf{R}) = 0, \quad (6)$$

with $\beta = (\mu_y - \mu_x)/(\mu_y + \mu_x)$, R and Θ the polar representation of the XY plane and where the Laplacian is to be taken with respect to these coordinates. The transformation makes the kinetic energy isotropic at the cost of making the potential energy anisotropic. The reasons that this transformation is useful are threefold: First, it is more intuitive to work with an anisotropic potential than an anisotropic kinetic energy; second, the numerical procedure we will use consists of resolving

TABLE I. Parameters used to describe excitons in phosphorene. The effective masses are from Ref. [58], the polarizabilities are from Ref. [28], and the rest of the parameters are computed from these values.

$\alpha_{xx}^{(2D)}$	$\alpha_{yy}^{(2D)}$	$m_e^{(x)}$	$m_e^{(y)}$	$m_h^{(x)}$	$m_h^{(y)}$	r_0	μ_x	μ_y
4.20 Å	3.97 Å	0.46	1.12	0.23	1.61	25.67 Å	0.1533	0.6605

TABLE II. Symmetry of the four types of unperturbed states. The first column indicates the axis or point considered, and the remaining columns indicate the symmetries or properties of the states about said axis or point. The final two rows indicate whether or not the states have angular nodes along the X or Y axes. A zero indicates an angular node, whereas a dash indicates that nothing general may be inferred about the states along the axes from their symmetry.

	State ce	State co	State se	State so
About X axis	Even	Even	Odd	Odd
About Y axis	Even	Odd	Odd	Even
About origin	Even	Odd	Even	Odd
Along X axis	—	—	0	0
Along Y axis	—	0	0	—

the wave function in a basis, and the number of basis functions needed to represent the polar wave function is significantly less than those needed to represent the Cartesian wave function; and, finally, the polar representation of the kinetic energy is simple and, thus, leads to simple matrix elements. The states may be expressed generally as

$$\psi(\mathbf{R}) = \sum_{m=-\infty}^{\infty} \varphi_m(R) \times \begin{cases} \cos(m\Theta), & m \leq 0, \\ \sin(m\Theta), & m > 0, \end{cases} \quad (7)$$

where φ_m may be understood as the Fourier coefficients. Note that the coefficients depend continuously on R and will later be expanded in a radial basis. As pointed out in Ref. [28], the unperturbed eigenstates of Eq. (6) fall into four distinct groups. This is most easily seen by recognizing that the potential is even in Θ and is invariant under the shift $\Theta \rightarrow \Theta + \pi$. It, therefore, has a Fourier series consisting of cosines of even order, and it becomes easy to see that for coupling to occur, the angular functions must be of the same type (i.e., sine/cosine) and have the same angular momentum parity. This results in the following four types of states:

$$\psi_{ce} = \sum_{m=0}^{\infty} \varphi_m^{(ce)}(R) \cos(2m\Theta), \quad (8)$$

$$\psi_{co} = \sum_{m=0}^{\infty} \varphi_m^{(co)}(R) \cos[(2m+1)\Theta], \quad (9)$$

$$\psi_{se} = \sum_{m=1}^{\infty} \varphi_m^{(se)}(R) \sin(2m\Theta), \quad (10)$$

$$\psi_{so} = \sum_{m=0}^{\infty} \varphi_m^{(so)}(R) \sin[(2m+1)\Theta], \quad (11)$$

where the subscripts c/s and e/o denote whether the trigonometric function is a cosine/sine and whether the angular momentum parity is even/odd, respectively. A couple of symmetry observations follow immediately and are summarized in Table II. Importantly, states with even and odd angular momenta are symmetric and antisymmetric about the origin, respectively. This means that the co and so states are necessarily zero at the origin and are, therefore, not optically active when no external electric field is present as we will see later on when we compute the optical absorption. The shape of the states may be inferred from the fact that some of them have

TABLE III. Five lowest exciton energies in phosphorene in three different dielectric surroundings. The first column numerates the states with increasing energy, the second column indicates which of the four types [Eqs. (8)–(11)] the state belongs to, and the remaining columns show the exciton energies in the three dielectric surroundings.

n	Type	Freely suspended E_n (meV)	SiO ₂ substrate E_n (meV)	hBN encapsulation E_n (meV)
0	<i>ce</i>	−822	−459	−260
1	<i>so</i>	−519	−227	−99
2	<i>ce</i>	−410	−163	−67
3	<i>co</i>	−385	−145	−55
4	<i>so</i>	−320	−113	−42

angular nodes along a specific axis. In particular, the *co* and *so* states have nodes along the Y and X axes, respectively, and the *se* state has nodes along both. They will, therefore, be slightly deformed versions of the familiar p_x , p_y , and d_{xy} orbitals.

The numerical procedure we will use throughout the paper is to solve the Wannier equation using a finite element representation of the exciton wave functions. The wave functions are expanded as in Eq. (7), including angular momenta up to some number M . The radial φ_m functions are then expanded in a finite element basis $f_i^{(n)}$ that are nonzero only on a single radial segment n defining a particular range of the radial coordinate. Their exact form as well as further details of the numerical procedure can be found in Ref. [39]. To summarize

$$\varphi_m(\mathbf{R}) = \sum_{n=1}^N \sum_{i=1}^p c_i^{(m,n)} f_i^{(n)}(\mathbf{R}), \quad (12)$$

where $c_i^{(m,n)}$ are the expansion coefficients obtained by solving the resulting matrix eigenvalue problem.

In the present paper, we will study phosphorene in three different dielectric environments. Namely, freely suspended ($\kappa = 1$), on an SiO₂ substrate ($\kappa = 2.4$), and encapsulated by hBN ($\kappa = 4.5$). The energy and symmetry of the five lowest-lying states for the three dielectric surroundings are shown in Table III. As can be seen, we find exciton binding energies of 822, 459, and 260 meV, respectively, which corresponds well with those presented in Refs. [28–30,42,57,59] (see Ref. [30] for a table summarizing the binding energies from more references). Additionally, the energies of the excited states are in good agreement with those found in Ref. [42]. Note that the $n = 1$ state is a *so* state that has an angular node along the X axis. The fact that this state has a lower energy than the *co* state can be understood by considering the potential in Eq. (6). It is weaker along the X axis than it is along the Y axis, thus, favoring a state along Y . As a final note, the *se* state is not among the first five states. That it has such a large energy is no surprise given its d_{xy} -like shape.

III. ANISOTROPIC EXCITON STARK EFFECT

We are interested in seeing how the anisotropic nature of phosphorene affects both the exciton Stark shifts and dissociation rates when an in-plane electrostatic field is applied to the sheet. In the presence of an electric field, the Wannier equation

reads

$$\left\{ -\frac{1}{4\mu} \nabla^2 + V[R\sqrt{1 + \beta \cos 2\Theta}] + \mathcal{E} \cos \alpha \sqrt{\frac{2\mu}{\mu_x}} X + \mathcal{E} \sin \alpha \sqrt{\frac{2\mu}{\mu_y}} Y - E \right\} \psi(\mathbf{R}) = 0, \quad (13)$$

where \mathcal{E} is the electric-field strength and $\alpha \in [0, \pi/2]$ its angle to the original x axis. The setup is pictured in Fig. 1, where the field direction is indicated in panel (b). If the density of excitons becomes very large, e.g., if they are induced by an intense AC field, then exciton-exciton interactions become important. However, we will limit ourselves to the low-density regime so that these interactions can be ignored. Applying an electric field to the exciton causes the bound states to become resonance states with a finite lifetime. Such states may be described as eigenstates of the Hamiltonian subjected to outgoing wave boundary conditions, simulating that the electron and hole are accelerating in opposite directions. The Hamiltonian is not Hermitian when operating on these states, and the eigenvalue is, therefore, generally complex [35,41]. The Stark shift, then, corresponds to the change in the real part of the energy as a function of field strength, whereas the imaginary part describes the dissociation rate by the relation $\Gamma = -2 \text{Im } E$. This complex eigenvalue is most easily obtained by using the complex scaling procedure [60,61]. Here, the radial coordinate is rotated into the complex plane, which transforms the diverging behavior of the resonance states for real r into bound states along a complex contour $re^{i\psi}$.

The procedure we will use, here, has been laid out in Ref. [39] where we compute the exciton Stark effect in TMDs. It consists of expanding the resonance state in a finite element basis as described above and only complex scaling the coordinate outside a desired radius. This technique is referred to as exterior complex scaling [62], and it makes it much easier to obtain the dissociation rates for weak fields numerically. The results for phosphorene in free space on an SiO₂ substrate and encapsulated by hBN can be seen in the top, middle, and bottom panels of Fig. 3, respectively. It is immediately clear that the field direction, indicated by the line color, is very important. This is in contrast to the effect in TMDs, which is fully isotropic [35,37,39]. The largest Stark shifts (left axis) and dissociation rates (right axis) are seen for fields pointing along the x axis, which coincides with the direction of lowest effective mass. Rotating the field from the x axis to the y axis reduces the dissociation rate by several orders of magnitude due to the increased effective mass. The direction-dependent Stark shifts and dissociation rates add an additional degree of freedom when using phosphorene in device design as not only can they be controlled by the dielectric environment, but also by the field direction as well. Taking a closer look at the effect of the dielectric surroundings, both the Stark shifts and the dissociation rates increase significantly by placing the phosphorene sheet on an SiO₂ substrate, and even more so by encapsulating it in hBN. This is to be expected as the exciton binding energy is reduced considerably with increased screening. It should also be noted that the shifts and rates are much lower than those in popular TMDs [39], which is a direct consequence of the larger binding energies of excitons in phosphorene.

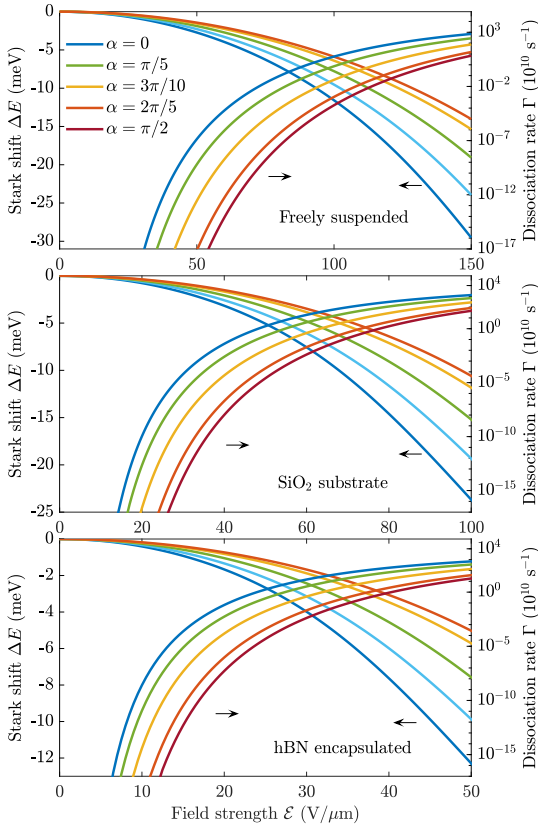


FIG. 3. Stark shifts $\Delta E = \text{Re}(E - E_0)$ (left axis) and dissociation rates $\Gamma = -2 \text{Im} E$ (right axis) of excitons in phosphorene that is freely suspended (top), on an SiO_2 substrate (middle), or encapsulated by hBN (bottom). For each of the three cases, electric fields with an angle to the x -axis α ranging from 0 to $\pi/2$ are considered. Evidently, the Stark shifts and dissociation rates decrease with an increasing angle as expected since the y component of the reduced mass is much larger than the x component.

In the Wannier model, effective masses are taken as those of free-standing phosphorene. However, if the phosphorene lattice is strained due to mismatch with the surrounding media, both the effective masses as well as the screening length r_0 will be altered. The relative change in the former is much greater than the latter [63]. Hence, strain effects on the effective masses dominate, and we discuss the impact on Stark shifts and dissociation rates in Appendix B. We find that taking into account the modified effective masses does not change the results qualitatively. The Stark shifts remain almost identical, whereas the dissociation rates are reduced due to the change in binding energy.

A. Exciton Stark shift and polarizability

In this section, we will look at the exciton Stark shift in more detail and compare to the shift predicted by perturbation theory. The anisotropic exciton Stark shift in few layer BP in

free space and in hBN surroundings was studied in Ref. [38] and on an SiO_2 substrate in Ref. [42], and we will, thus, perform a detailed comparison to the results in these papers for a single layer of BP, i.e., phosphorene. One of the most important quantities describing how anisotropic excitons interact with the electric field is their polarizabilities. The perturbation series for the Stark shift of state n may be written as [64]

$$\Delta E_n = \text{Re}[E_n(\mathcal{E}) - E_n^{(0)}] = E_n^{(1)} + E_n^{(2)} + O(\mathcal{E}^3), \quad (14)$$

with

$$E_n^{(1)} = \langle \psi_n^{(0)} | H' | \psi_n^{(0)} \rangle, \quad (15)$$

and

$$E_n^{(2)} = \sum_{k \neq n} \frac{|\langle \psi_k^{(0)} | H' | \psi_n^{(0)} \rangle|^2}{E_n^{(0)} - E_k^{(0)}}, \quad (16)$$

where

$$H' = \mathcal{E} \cos \alpha \sqrt{\frac{2\mu}{\mu_x}} X + \mathcal{E} \sin \alpha \sqrt{\frac{2\mu}{\mu_y}} Y, \quad (17)$$

and the sum is to be taken over all the unperturbed states. The perturbation H' only couples states with different parity angular momenta [see Eqs. (8)–(11)]. The first-order correction, therefore, immediately reduces to zero. The second-order correction, on the other hand, may be written as

$$E_n^{(2)} = -\frac{1}{2} \chi_n^{XX} \cos^2 \alpha \mathcal{E}^2 - \frac{1}{2} \chi_n^{YY} \sin^2 \alpha \mathcal{E}^2, \quad (18)$$

where the X and Y components of the exciton polarizability tensor for the four types of states are given by

$$\chi_{ce}^{XX} = \frac{4\mu}{\mu_x} \sum_{co} \frac{|X_{co,ce}|^2}{E_{co,ce}}, \quad \chi_{ce}^{YY} = \frac{4\mu}{\mu_y} \sum_{so} \frac{|Y_{so,ce}|^2}{E_{so,ce}}, \quad (19)$$

$$\chi_{co}^{XX} = \frac{4\mu}{\mu_x} \sum_{ce} \frac{|X_{ce,co}|^2}{E_{ce,co}}, \quad \chi_{co}^{YY} = \frac{4\mu}{\mu_y} \sum_{se} \frac{|Y_{se,co}|^2}{E_{se,co}}, \quad (20)$$

$$\chi_{se}^{XX} = \frac{4\mu}{\mu_x} \sum_{so} \frac{|X_{so,se}|^2}{E_{so,se}}, \quad \chi_{se}^{YY} = \frac{4\mu}{\mu_y} \sum_{co} \frac{|Y_{co,se}|^2}{E_{co,se}}, \quad (21)$$

$$\chi_{so}^{XX} = \frac{4\mu}{\mu_x} \sum_{se} \frac{|X_{se,so}|^2}{E_{se,so}}, \quad \chi_{so}^{YY} = \frac{4\mu}{\mu_y} \sum_{ce} \frac{|Y_{ce,so}|^2}{E_{ce,so}}, \quad (22)$$

with the shorthand notation,

$$X_{ij} = \langle \psi_i^{(0)} | X | \psi_j^{(0)} \rangle, \quad Y_{ij} = \langle \psi_i^{(0)} | Y | \psi_j^{(0)} \rangle, \quad (23)$$

$$E_{ij} = E_i^{(0)} - E_j^{(0)}. \quad (24)$$

The finite element expansion described above is very flexible and perfectly capable of resolving both the bound and the continuous spectrum of unperturbed states. In this manner, we compute the exciton polarizabilities for the five lowest-lying exciton states. They are summarized in Table IV, and a comparison between Eq. (18) and the numerically exact Stark shifts is shown in Fig. 4 for very weak fields. It is clear that all of the states have a highly anisotropic response to an applied field. We observe, as expected, that the X component of the polarizability is larger than the Y component for the fundamental exciton. The opposite is the case for the so states, which is of no surprise given their p_y -like shape. Perhaps more

TABLE IV. Exciton polarizabilities in units of $10^{-18} \text{ eV m}^{-1} \text{ V}^{-2}$ of the five lowest-lying excitons in phosphorene in three different dielectric surroundings. The first column numerates the states with increasing energy (shown in Table III), the second column indicates which of the four types [Eqs. (8)–(11)] the states belong to, and the remaining columns show the exciton polarizabilities in the three dielectric surroundings.

n	Type	Freely suspended		SiO ₂ substrate		hBN encapsulation	
		χ_n^{XX}	χ_n^{YY}	χ_n^{XX}	χ_n^{YY}	χ_n^{XX}	χ_n^{YY}
0	<i>ce</i>	2.149	1.137	3.830	1.870	8.058	3.614
1	<i>so</i>	7.603	15.65	20.01	43.69	71.08	168.7
2	<i>ce</i>	55.57	20.02	184.9	59.49	749.1	195.8
3	<i>co</i>	3.303	10.77	18.46	34.70	184.9	158.5
4	<i>so</i>	67.42	120.3	290.0	583.5	1559	3673

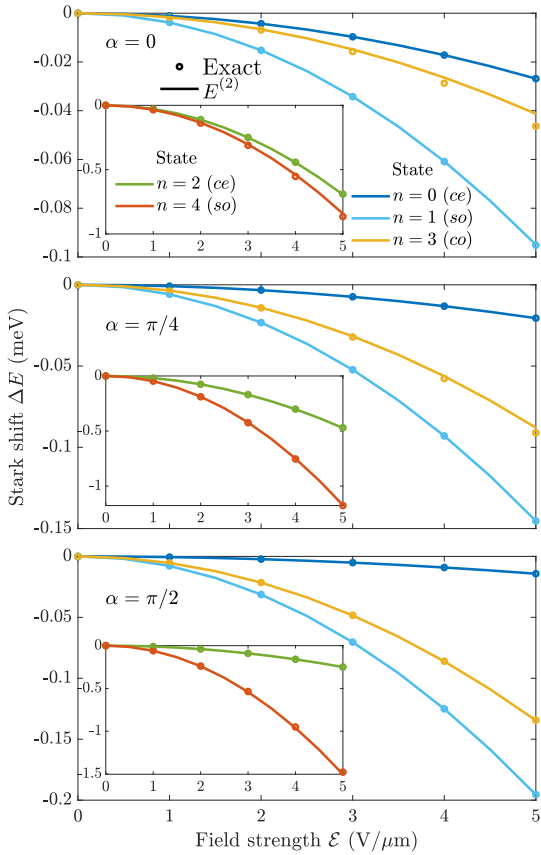


FIG. 4. Comparison between the numerically exact Stark shifts (circles) and second-order perturbation theory Eq. (18) (solid lines) for the five lowest-lying exciton states in freely suspended phosphorene. States $n \in \{0, 1, 3\}$ are shown in the large panels, whereas the insets show $n \in \{2, 4\}$. The top, middle, and bottom panels represent fields with an angle to the x axis of 0 , $\pi/4$, and $\pi/2$, respectively. Good agreement is found across all field angles for very weak electric fields.

surprisingly we find that the Y component of the co state is larger than the X component.

In Ref. [42], the authors use the RK potential with parameters that are almost identical to ours to study excitons in phosphorene on an SiO₂ substrate. However, our reduced masses are slightly different from theirs. Specifically, the authors use $\mu_x = 0.089$ and $\mu_y = 0.650$ from Ref. [6], instead, of our $\mu_x = 0.153$ and $\mu_y = 0.661$ from Ref. [58]. We, therefore, expect our exciton energies to be slightly lower as well as a lower degree of anisotropy. Indeed, they find $E_0 = -396$ and $E_2 = -143$ meV where we find $E_0 = -459$ and $E_2 = -163$ meV, showing a good qualitative agreement. Turning to the polarizabilities, the authors of Ref. [42] determine the polarizabilities of the $n = 0$ and $n = 2$ states by fitting to the numerical Stark shifts. Using this procedure, the authors find the polarizabilities in the X (Y) directions to be 7.4 (2.7) and 200 (96) for the $n = 0$ and $n = 2$ excitons, respectively, all in units of $10^{-18} \text{ eV m}^{-1} \text{ V}^{-2}$. Comparing to our results in Table IV, we find 3.8 (1.9) and 185 (59.5) for the same cases. We, thus, obtain slightly lower polarizabilities as expected from the larger binding energies. The same authors also compute the Stark shifts of the fundamental exciton for field strengths up to $20 \text{ V}/\mu\text{m}$ and find shifts of around 1.6 and 0.6 meV for fields in the X and Y directions, respectively. For the same fields, we find shifts of 0.8 and 0.4 meV. In Ref. [38], the authors study the Stark shifts for freely suspended phosphorene as well as phosphorene in hBN surroundings. These authors use the same reduced mass as the authors of Ref. [42] and find polarizabilities of 1.186 (0.871) and 6.162 (2.598) $\times 10^{-18} \text{ eV m}^{-1} \text{ V}^{-2}$ in the X (Y) directions for freely suspended and hBN encapsulated phosphorene, respectively. These values are in good agreement with our results.

B. Analytical weak-field approximation for exciton dissociation

Analytical weak-field expressions for the dissociation rates of excitons in monolayer [39,65] and bilayer TMDs [40] have been derived previously using WFAT [66]. These expressions are useful for obtaining a better understanding of field-induced exciton dissociation as well as obtaining quick

TABLE V. Asymptotic coefficient $g_0(\alpha)$ for phosphorene in three different dielectric surroundings for various field directions. The coefficient is used in the analytical approximation to the exciton dissociation rate Eq. (31) and has been obtained by extrapolating $\Gamma_{\text{exact}}/W_0$ to $\mathcal{E} = 0$.

α	Freely suspended g_0	SiO ₂ substrate g_0	hBN encapsulation g_0
0	1.835×10^{-2}	1.344×10^{-1}	2.122×10^{-1}
$\frac{\pi}{5}$	1.714×10^{-2}	1.271×10^{-1}	2.051×10^{-1}
$\frac{3\pi}{10}$	1.239×10^{-2}	1.090×10^{-1}	1.812×10^{-1}
$\frac{2\pi}{5}$	2.614×10^{-3}	4.879×10^{-2}	9.985×10^{-2}
$\frac{\pi}{2}$	1.495×10^{-5}	2.892×10^{-3}	1.322×10^{-2}

estimates of the rates at weak electric fields without performing heavy numerical computations. This latter point is of great importance as the numerical procedures break down for sufficiently weak fields [67]. To implement WFAT, the binding potential must have a sufficiently simple asymptotic behavior (specified later), and the electric field must point along the x axis (or z axis for three-dimensional problems). The reason that the field must point along this axis is that it is very simple to deal with in parabolic coordinates, and leads to differential equations that decouple in the asymptotic region. For TMDs, advantage was taken of the isotropic nature of the problem by letting the electric field point in the x direction, and the resulting problem, therefore, had the form

$$\left[-\frac{1}{2}\nabla^2 + V(r) + \mathcal{E}x - E \right] \psi(\mathbf{r}) = 0, \quad (25)$$

$$V(r) \sim -\frac{1}{\kappa r} \quad \text{for } r \rightarrow \infty,$$

where V is a radial potential. Parabolic coordinates, thus, allow separation of this problem in the asymptotic region. A similar procedure may be used in the present case, but a coordinate transformation is needed in order to get the desired axis to coincide with the field direction.

Generalizing the coordinate transformations in the previous section slightly, we write

$$\zeta_x = \sqrt{\mu_x} \cos \tilde{\alpha}x + \sqrt{\mu_y} \sin \tilde{\alpha}y, \quad (26)$$

$$\zeta_y = -\sqrt{\mu_x} \sin \tilde{\alpha}x + \sqrt{\mu_y} \cos \tilde{\alpha}y. \quad (27)$$

Choosing $\tilde{\alpha} = \arctan(\sqrt{\frac{\mu_x}{\mu_y}} \tan \alpha)$ the Wannier equation for phosphorene becomes

$$\left\{ -\frac{1}{2}\nabla^2 + V \left[\frac{\zeta}{\sqrt{2\mu}} \sqrt{1 + \beta \cos[2(\Phi + \tilde{\alpha})]} \right] + \tilde{\mathcal{E}}\zeta_x - E \right\} \times \psi(\zeta) = 0, \quad (28)$$

with the effective field strength,

$$\tilde{\mathcal{E}} = \mathcal{E} \sqrt{\frac{\cos^2 \alpha}{\mu_x} + \frac{\sin^2 \alpha}{\mu_y}}. \quad (29)$$

Here, ζ and Φ are the polar representations of the ζ_x and ζ_y coordinates. This brings the equation on the desired form. As

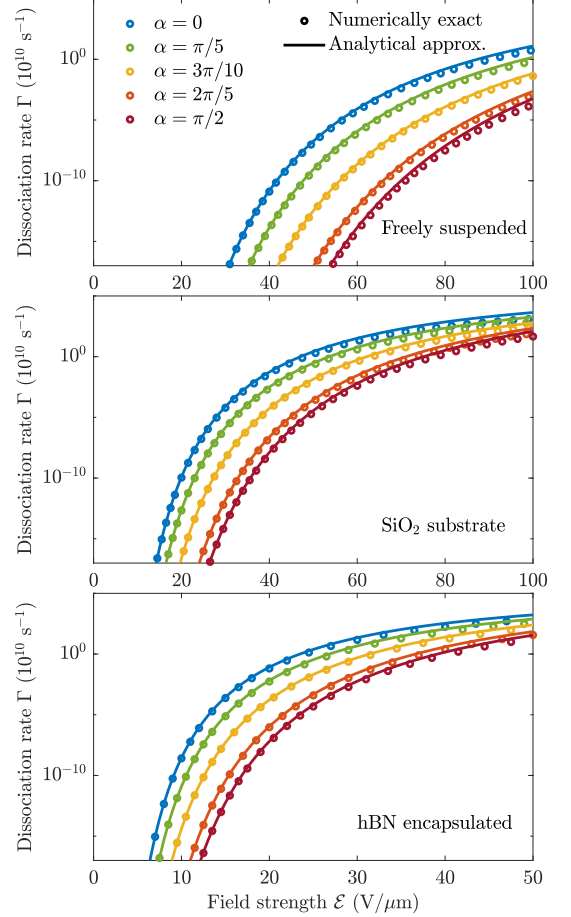


FIG. 5. Comparison between the numerically exact dissociation rates (circles) and the anisotropic analytical weak-field approximation in Eq. (31) (solid lines). Good agreement is found across all field angles for weak electric fields.

shown in Appendix C, applying a weak external field along the ζ_x axis to a system with an isotropic kinetic energy and an anisotropic potential satisfying

$$\lim_{\zeta_x \rightarrow -\infty} -\zeta V(\zeta) = Z_{\text{asympt}}. \quad (30)$$

where Z_{asympt} is a positive constant, induces the dissociation rate,

$$\Gamma_{\text{approx}}(\mathcal{E}, \alpha) = |g_0(\alpha)|^2 W_0(\mathcal{E}, \alpha). \quad (31)$$

Here,

$$W_0(\mathcal{E}, \alpha) = k \left(\frac{4k^2}{\tilde{\mathcal{E}}} \right)^{2Z_{\text{asympt}}/k-1/2} \exp\left(-\frac{2k^3}{3\tilde{\mathcal{E}}}\right), \quad (32)$$

and $k = \sqrt{2|E_0|}$ where $|E_0|$ is the exciton binding energy. For the present case, we find

$$Z_{\text{asympt}}(\alpha) = \frac{1}{\kappa} \sqrt{\frac{2\mu(\mu_y \cos^2 \alpha + \mu_x \sin^2 \alpha)}{(1 + \beta)\mu_y \cos^2 \alpha + (1 - \beta)\mu_x \sin^2 \alpha}}. \quad (33)$$

Equation (31) generalizes the result in Ref. [39] to take into account anisotropic effective masses. In the limit of zero screening length $r_0 \rightarrow 0$, the RK potential simplifies to the Coulomb potential, and the expression, therefore, also generalizes the ionization rate of a 2D hydrogen atom [68] to one with an anisotropic reduced mass. Note that it reduces to that of the isotropic case when $\mu_x = \mu_y$. The three direction-dependent quantities in Eq. (31) are the field-independent asymptotic coefficient g_0 , the effective field strength $\tilde{\mathcal{E}}$, and Z_{asympt} . The asymptotic coefficient g_0 may be computed from the wave function far from the origin [see Eq. (C37)]. To do so, however, one needs a very accurate numerical wave function. This is reasonably easy to do for the isotropic case as one may relate the coefficient to the solution of the radial Schrödinger equation, obtaining effectively a one-dimensional problem [39]. This procedure cannot be applied in the present case, and we, therefore, determine g_0 by extrapolating $\Gamma_{\text{exact}}/W_0$ to $\mathcal{E} = 0$. The obtained coefficients are shown in Table V, and the results are compared in Fig. 5 where the agreement between the numerically exact results and the analytical approximation is good for weak fields.

Evidently, the error grows very rapidly with increasing field strength. However, for moderate field strengths, the errors are acceptable, and Eq. (31), therefore, serves as a decent first approximation to the weak-field exciton dissociation rates in phosphorene.

IV. FRANZ-KELDYSH EFFECT

The Franz-Keldysh effect [43,44] constitutes a change in optical absorption of a semiconductor due to an applied external electric field. The effect was computed for monolayer TMDs in Ref. [34], and the same methodology used in that paper will be used here. Assuming that the momentum matrix elements are k independent, the exciton oscillator strength may be determined by evaluating the wave function at the origin [69]. The exciton susceptibility may then be evaluated as

$$\chi(\omega) = \chi_0 \sum_{\text{exc}} \frac{|\psi_{\text{exc}}(0)|^2}{E_{\text{exc}}[E_{\text{exc}}^2 - (\hbar\omega + i\hbar\Gamma)^2]}, \quad (34)$$

where the sum is taken over all exciton states. Here, χ_0 is a material-dependent constant, $\hbar\omega$ is the photon energy, and $\hbar\Gamma$ is a phenomenological line-shape broadening. The exciton energy is $E_{\text{exc}} = E_g + E_n$, where E_g is the band gap and E_n 's are the (real) eigenvalues of Eq. (13). This corresponds to measuring the exciton energies from the top of the valence band. For the calculations in the present paper, we use a band gap of $E_g = 2$ eV which is obtained from calculations within the

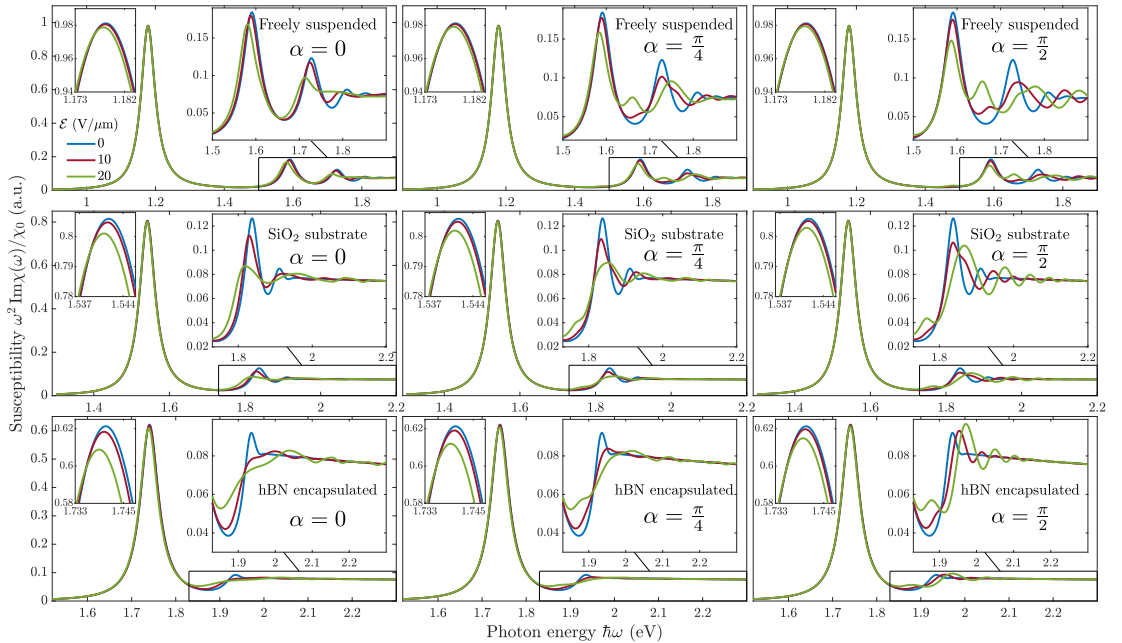


FIG. 6. Imaginary part of the susceptibility of phosphorene. The top, middle, and bottom rows correspond to phosphorene in free space, on an SiO_2 substrate, and encapsulated by hBN, respectively. The first, second, and third columns correspond to field angles of $\alpha \in \{0, \frac{\pi}{4}, \frac{\pi}{2}\}$, respectively. Field strengths are indicated by line color where blue, red, and green represent $\mathcal{E} \in \{0, 10, 20\}$ V/ μm , respectively. Two zooms are shown in each panel: the left is a zoom of the fundamental peak, while the right enhances the spectra at higher photon energies.

GW approximation in Ref. [15] and confirmed experimentally by scanning tunneling microscopy/spectroscopy in Ref. [70]. Additionally, a line broadening of $\hbar\Gamma = 25$ meV is used. The energy eigenvalues are efficiently obtained by expressing the wave function in a finite element basis as described above, and solving the resulting eigenvalue problem.

The imaginary part of the susceptibility for phosphorene in free space, on an SiO₂ substrate, and encapsulated by hBN are shown in the top, middle, and bottom rows of Fig. 6, respectively. The structures are subjected to external in-plane electric fields with angles $\alpha \in \{0, \frac{\pi}{4}, \frac{\pi}{2}\}$ to the x axis, indicated in the first, second, and third columns, respectively. For each case, field strengths of 0, 10, and 20 V/ μm are considered and represented by the blue, red, and green lines, respectively. As the field strength is increased, the peak absorption corresponding to the fundamental exciton is redshifted. This is indicated in the zoom plot on the left-hand side in each panel. Evidently, the redshift decreases as the field is rotated from the x axis to the y axis. This is to be expected as the effective mass in the y direction is larger than in the x direction, and it is, therefore, more difficult to polarize the fundamental exciton along y than it is along x . This is also apparent from the large differences between the x and the y components of the polarizabilities shown in Table IV. In addition to the redshift, the height of the fundamental peaks decreases with increasing field strength. This is natural as a field pulls electrons and holes in opposite directions thereby reducing the magnitude of the wave function at the origin. The second peak in the field free spectra corresponds to the third exciton $n = 2$. That is, the exciton of type ce (see Table III). The reason that the $n = 1$ state does not contribute to any peak in the field-free spectra is that the state is antisymmetric about the origin [see Eq. 11] and is, therefore, zero at the origin. When the field is turned on, these wave functions become polarized and are, thus, no longer zero at the origin, explaining their contribution to the field-induced absorption spectra. Interestingly, the peak close to the $n = 1$ transition energy is more pronounced for an electric field along y than it is for a field along x . This is easy to explain considering that the y component of the polarizability is more than twice as large as the x component for this state. It is, therefore, much easier to polarize along y than it is along x . As a final note, we note that the characteristic field-induced oscillations above the band gap [71] are clearly visible. Additionally, the field-free fundamental peak on an SiO₂ substrate at around 1.54 eV corresponds well with the experimentally observed peak at 1.45 eV [5].

V. CONCLUSION

In the present paper, excitons in phosphorene subjected to an external in-plane electric field have been studied. In particular, we have calculated the unperturbed energies and exciton polarizabilities of the five lowest excitonic states in phosphorene in three different dielectric surroundings. Furthermore, exciton Stark shifts, dissociation rates, and electroabsorption have been computed for various field strengths and directions. A pronounced dependence on the field direction is found for all three quantities. For the fundamental exciton, a field along the armchair axis leads to much more pronounced effects than one along the zigzag direction. For example, the field-induced

exciton dissociation rates in phosphorene encapsulated by hBN decrease by several orders of magnitude upon rotating the electric field from the armchair to the zigzag axis. This is due to the much larger effective masses found for the zigzag direction than for the armchair direction. An analytical weak-field approximation for the dissociation rate has been derived and shown to agree with the numerically exact rates for weak fields. The larger shift for fields pointing along the armchair direction is again seen by the shift of the fundamental absorption peak when we compute the electroabsorption. On the other hand, the different symmetries of the excited states often lead to larger effects for fields pointing along the zigzag axis as is apparent from the polarizability tensors.

ACKNOWLEDGMENTS

H.C.K. and T.G.P. gratefully acknowledge financial support by the Center for Nanostructured Graphene (CNG), which is sponsored by the Danish National Research Foundation, Project No. DNRF103. Additionally, T.G.P. is supported by the QUSCOPE Center, sponsored by the Villum Foundation. N.M.R.P. acknowledges support from the European Commission through the Project Graphene-Driven Revolutions in ICT and Beyond (Project No. 881603, CORE 3) and the Portuguese Foundation for Science and Technology (FCT) in the framework of the Strategic Financing Grant No. UID/FIS/04650/2019. In addition, N.M.R.P. acknowledges COMPETE2020, PORTUGAL2020, FEDER, and the FCT through Projects No. PTDC/FIS-NAN/3668/2013, No. POCI-01-0145-FEDER-028114, No. POCI-01-0145-FEDER-029265, No. PTDC/NAN-OPT/29265/2017, and No. POCI-01-0145-FEDER-02888.

APPENDIX A: ANISOTROPIC POISSON EQUATION

In this Appendix, we derive an expression for the interaction energy between two particles in an anisotropic 2D semiconductor. This problem was considered in Ref. [72] where the aim was to obtain closed form expressions for the case of weak anisotropy. In this Appendix, we will not assume weak anisotropy but rather try to obtain as simple an expression for the anisotropic interaction as possible. Note that parts of the derivation are very similar to those in Ref. [72] but are included for completeness. The Poisson equation for the potential-energy function V between charges Q and Q' located at (x, y, z) and $(0, 0, z')$, respectively, may be written as

$$\nabla \cdot [\epsilon \cdot \nabla V(x, y, z, z')] = -4\pi QQ' \delta(x) \delta(y) \delta(z - z'), \quad (\text{A1})$$

where ϵ is a dielectric tensor. Assuming the tensor is diagonal and Fourier decomposing the potential-energy function as

$$V(x, y, z, z') = \frac{1}{4\pi^2} \int_{-\infty}^{\infty} \int_{-\infty}^{\infty} \varphi(z, z'; q_x, q_y) e^{i(q_x x + q_y y)} dq_x dq_y \quad (\text{A2})$$

leads to

$$\left[\epsilon_{xx}(z) q_x^2 + \epsilon_{yy}(z) q_y^2 - \frac{\partial}{\partial z} \epsilon_{zz}(z) \frac{\partial}{\partial z} \right] \varphi(z, z'; q_x, q_y) = 4\pi QQ' \delta(z - z'). \quad (\text{A3})$$

We take the dielectric functions to be piecewise constant

$$\varepsilon_{ii}(z) = \begin{cases} \varepsilon_{ii}^{(a)}, & z > d/2, \\ \varepsilon_{ii}, & d/2 > z > -d/2, \\ \varepsilon_{ii}^{(b)}, & z < -d/2, \end{cases} \quad (\text{A4})$$

where $ii = \{xx, yy, zz\}$. Thus, we model the encapsulated 2D sheet as a slab of thickness d surrounded by dielectric media extending to infinity. The solution may then be sought on the form

$$\varphi(z, z'; q_x, q_y) = \frac{2\pi QQ'}{q} \begin{cases} A_1 e^{-q_a z}, \\ A_2 e^{-qz} + B_2 e^{qz} + \varepsilon_{zz}^{-1} e^{-q|z-z'|}, \\ B_3 e^{q_b z}, \end{cases} \quad (\text{A5})$$

where

$$q_a = \left(\frac{\varepsilon_{xx}^{(a)} q_x^2 + \varepsilon_{yy}^{(a)} q_y^2}{\varepsilon_{zz}^{(a)}} \right)^{1/2}, \quad (\text{A6})$$

$$q = \left(\frac{\varepsilon_{xx} q_x^2 + \varepsilon_{yy} q_y^2}{\varepsilon_{zz}} \right)^{1/2}, \quad (\text{A7})$$

$$q_b = \left(\frac{\varepsilon_{xx}^{(b)} q_x^2 + \varepsilon_{yy}^{(b)} q_y^2}{\varepsilon_{zz}^{(b)}} \right)^{1/2}. \quad (\text{A8})$$

The Fourier components satisfy the boundary conditions,

$$\varphi\left(\pm \frac{d}{2}, z'; q_x, q_y\right) = \varphi\left(\pm \frac{d}{2}, z'; q_x, q_y\right), \quad (\text{A9})$$

$$\varepsilon_{zz}^{(j)} \frac{\partial}{\partial z} \varphi(z, z'; q_x, q_y) \Big|_{z=\pm d/2} = \varepsilon_{zz} \frac{\partial}{\partial z} \varphi(z, z'; q_x, q_y) \Big|_{z=\pm d/2}, \quad (\text{A10})$$

with $j = a$ and $j = b$ for $z = d/2$ and $z = -d/2$, respectively. Enforcing these boundary conditions, placing both charges in the middle of the sheet, and switching to polar coordinates, we obtain

$$\varphi(0, 0; q, \phi) = \frac{\varphi_0(q)}{\varepsilon_{\text{eff}}(q, \phi)}, \quad (\text{A11})$$

where $\varphi_0 = 2\pi QQ'/q$ is the bare interaction and ε_{eff} is the effective dielectric function given by

$$\varepsilon_{\text{eff}}(q, \phi) = \frac{g^2(g_a + g_b) \cosh\left(\frac{dq}{\varepsilon_{zz}} g\right) + g(g^2 + g_a g_b) \sinh\left(\frac{dq}{\varepsilon_{zz}} g\right)}{g^2 - g_a g_b + (g^2 + g_a g_b) \cosh\left(\frac{dq}{\varepsilon_{zz}} g\right) + g(g_a + g_b) \sinh\left(\frac{dq}{\varepsilon_{zz}} g\right)}, \quad (\text{A12})$$

with

$$g_a(\phi) = \sqrt{\varepsilon_{zz}^{(a)} (\varepsilon_{xx}^{(a)} \cos^2 \phi + \varepsilon_{yy}^{(a)} \sin^2 \phi)}, \quad (\text{A13})$$

and g and g_b defined analogously. We now specialize to the case where the super- and substrate have isotropic in-plane dielectric constants, i.e., $\varepsilon_{xx}^{(a)} = \varepsilon_{yy}^{(a)}$ and $\varepsilon_{xx}^{(b)} = \varepsilon_{yy}^{(b)}$. This leads to

$$g_a = \sqrt{\varepsilon_{zz}^{(a)} \varepsilon_{xx}^{(a)}}, \quad g_b = \sqrt{\varepsilon_{zz}^{(b)} \varepsilon_{xx}^{(b)}}, \quad (\text{A14})$$

and

$$g(\phi) = \sqrt{\varepsilon_{zz} (\varepsilon_{xx} \cos^2 \phi + \varepsilon_{yy} \sin^2 \phi)}. \quad (\text{A15})$$

The resulting dielectric function agrees with the one in Ref. [72]. Note that the interaction only depends on the dielectric constants of the surrounding media via their geometrical mean. Expanding to first order in q , we obtain

$$\varepsilon_{\text{eff}}^{(1)}(q, \phi) = \kappa + r_0(\phi)q + O(q^2), \quad (\text{A16})$$

with

$$\kappa = \frac{\sqrt{\varepsilon_{xx}^{(a)} \varepsilon_{zz}^{(a)}} + \sqrt{\varepsilon_{xx}^{(b)} \varepsilon_{zz}^{(b)}}}{2}, \quad (\text{A17})$$

$$r_0(\phi) = \frac{d[2\varepsilon_{zz}(\varepsilon_{xx} \cos^2 \phi + \varepsilon_{yy} \sin^2 \phi) - \varepsilon_{xx}^{(a)} \varepsilon_{zz}^{(a)} - \varepsilon_{xx}^{(b)} \varepsilon_{zz}^{(b)}]}{4\varepsilon_{zz}}. \quad (\text{A18})$$

The first-order approximation to the interaction is, then,

$$V(q, \phi) = \frac{QQ'}{2\pi} \int_0^{2\pi} \int_0^\infty \frac{e^{iqr \cos(\theta-\phi)}}{\kappa + r_0(\phi)q} dq d\phi. \quad (\text{A19})$$

The first-order dielectric function may be rewritten as

$$\varepsilon_{\text{eff}}^{(1)}(q, \phi) = \alpha(q)[1 - \gamma^2(q) \cos^2 \phi], \quad (\text{A20})$$

where

$$\alpha(q) = \kappa + (a + r_{0y})q, \quad (\text{A21})$$

$$\gamma^2(q) = \frac{(r_{0y} - r_{0x})q}{\alpha(q)}, \quad (\text{A22})$$

with

$$a = -\frac{d(\varepsilon_a^2 + \varepsilon_b^2)}{4\varepsilon_{zz}}, \quad r_{0x} = \frac{d\varepsilon_{xx}}{2}, \quad \text{and} \quad r_{0y} = \frac{d\varepsilon_{yy}}{2}. \quad (\text{A23})$$

Here, we have defined screening lengths $r_{0x/y}$ equivalent to the macroscopic definitions in Ref. [53]. The Fourier series for $1/\varepsilon_{\text{eff}}^{(1)}$ may be found by the method in Ref. [73]. We get

$$\frac{1}{\varepsilon_{\text{eff}}^{(1)}} = \frac{1}{\alpha \sqrt{1 - \gamma^2}} \left[1 + 2 \sum_{k=1}^{\infty} \left(\frac{\gamma}{1 + \sqrt{1 - \gamma^2}} \right)^{2k} \cos(2k\phi) \right]. \quad (\text{A24})$$

The angular integral in the interaction may then be written as

$$I(q) = \int_0^{2\pi} \frac{e^{iqr \cos(\phi-\theta)}}{\varepsilon_{\text{eff}}^{(1)}(q, \phi)} d\phi = \int_0^{2\pi} \frac{e^{iqr \cos(\phi-\theta)}}{\alpha \sqrt{1-\gamma^2}} \times \left[1 + 2 \sum_{k=1}^{\infty} \left(\frac{\gamma}{1+\sqrt{1-\gamma^2}} \right)^{2k} \cos(2k\phi) \right], \quad (\text{A25})$$

which leads to

$$I(q) = \frac{2\pi}{\alpha \sqrt{1-\gamma^2}} \left[J_0(qr) + 2 \sum_{k=1}^{\infty} (-1)^k \times \left(\frac{\gamma}{1+\sqrt{1-\gamma^2}} \right)^{2k} J_{2k}(qr) \cos(2k\theta) \right]. \quad (\text{A26})$$

Now, a is typically very small compared to r_{0y} , i.e., $a \ll r_{0y}$, and we get $\alpha \approx \kappa + r_{0y}q$. Defining

$$\varepsilon_x = \kappa + r_{0x}q \quad \text{and} \quad \varepsilon_y = \kappa + r_{0y}q, \quad (\text{A27})$$

we may write

$$\frac{1}{\varepsilon_{\text{eff}}^{(1)}} \approx \frac{1}{\sqrt{\varepsilon_x \varepsilon_y}} \left[1 + 2 \sum_{k=1}^{\infty} \left(\frac{\sqrt{\varepsilon_y} - \sqrt{\varepsilon_x}}{\sqrt{\varepsilon_y} + \sqrt{\varepsilon_x}} \right)^k \cos(2k\phi) \right], \quad (\text{A28})$$

and the integral as

$$I(q) \approx \frac{2\pi}{\sqrt{\varepsilon_x \varepsilon_y}} \left\{ J_0(qr) + 2 \sum_{k=1}^{\infty} \left(\frac{\sqrt{\varepsilon_x} - \sqrt{\varepsilon_y}}{\sqrt{\varepsilon_x} + \sqrt{\varepsilon_y}} \right)^k \times J_{2k}(qr) \cos(2k\theta) \right\}. \quad (\text{A29})$$

The full interaction with a linearized dielectric function may, thus, be computed as

$$V(r, \theta) = \frac{QQ'}{2\pi} \int_0^\infty I(q) dq. \quad (\text{A30})$$

APPENDIX B: EFFECT OF STRAIN

If a mismatch exists between the lattices of phosphorene and the surrounding media, then, both the effective masses and the screening length r_0 will be altered due to lattice-mismatch-induced strain. That is, the effective masses and r_0 of a layer of phosphorene in a heterostructure will not be the same as for a free-standing layer. In the present paper, we have described phosphorene in different dielectric surroundings by changing the dielectric constant κ while using the effective masses and screening length of a free-standing layer regardless of the dielectric surroundings as is commonly performed in the Wannier model. The relative change in the effective masses due to strain is much greater than that of r_0 [63,74]. Hence, the effect on the effective masses dominates and will be considered here. As we will see, taking into account the change in effective masses does not change the results qualitatively. Table VI shows the direction-dependent effective masses of electrons and holes in a freely suspended phosphorene layer, as well as one that is encapsulated by two layers of hBN. Note that these masses are obtained from Ref. [74], whereas the masses used in the main part of the paper are from

TABLE VI. Effective masses of isolated phosphorene and a phosphorene layer encapsulated by two layers of hBN [74].

Structure	$m_e^{(x)}$	$m_e^{(y)}$	$m_h^{(x)}$	$m_h^{(y)}$	μ	β
Phosphorene	0.19	1.20	0.17	7.43	0.1651	0.8402
hBN/phosphorene/hBN	0.23	1.25	0.23	8.5	0.2080	0.8091

Ref. [58], and that the two references find slightly different unstrained masses. The changing effective masses lead to modified μ_x , μ_y , μ , and β . The following computations are all made for a phosphorene layer encapsulated by hBN ($\kappa = 4.5$), using either the effective masses of isolated phosphorene (referred to as unstrained), or the effective masses of phosphorene encapsulated by two layers of hBN (referred to as strained). Using the unstrained effective masses, we find an exciton binding energy of 238 meV, whereas the strained effective masses yield 261 meV. Figure 7 shows the Stark shifts (left axis) and dissociation rates (right axis) for the ground-state exciton in phosphorene encapsulated by hBN. The solid lines are computed with the unstrained effective masses, whereas the dashed lines incorporate strained masses. As is evident, the Stark shifts are almost identical whether or not the strain-induced change in effective masses is taken into account. This is the case for a field along both the armchair (blue) and the zigzag (red) direction. The dissociation rates for both masses are qualitatively similar with the only major difference being a significant reduction of the rates due to the higher binding energy. The large reduction is explained by the sensitive dependence on the binding energy. Although relatively significant changes are predicted, we expect the effect seen here to be an extreme case that is only encountered in the case of perfect alignment. If one or more among the layers are

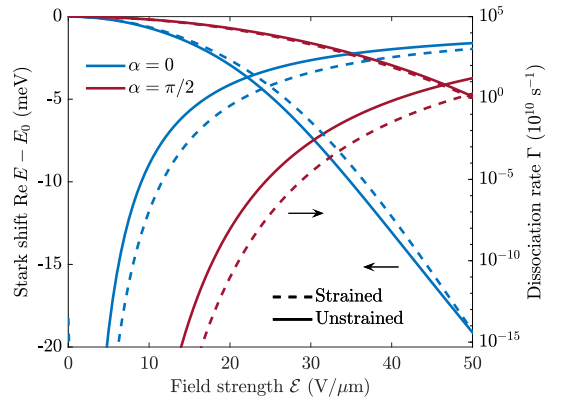


FIG. 7. Stark shifts (left axis) and dissociation rates (right axis) for the ground-state exciton in phosphorene encapsulated by hBN. The solid lines are computed using the effective masses of isolated phosphorene, whereas the dashed lines are computed using the effective masses of phosphorene encapsulated by two layers of hBN. A dielectric screening of $\kappa = 4.5$ is used in both cases. The red and blue curves correspond to an electric field along the x (armchair) or the y direction (zigzag), respectively.

rotated such that the lattices are no longer commensurate, the strain on the phosphorene layer is likely reduced. Hence, the effect on excitonic properties would not be as significant.

APPENDIX C: ANISOTROPIC WEAK-FIELD ASYMPTOTIC THEORY

In this Appendix, we show how the WFAT of tunneling ionization [66,75] may be extended to a two-dimensional system with an anisotropic potential. The aim of this Appendix is, thus, to derive an analytical weak-field approximation for the ionization rate of the auxiliary system defined by

$$\left[-\frac{1}{2}\nabla^2 + V(x, y) + \mathcal{E}x - E\right]\psi(x, y) = 0, \quad (\text{C1})$$

where we assume that

$$\lim_{x \rightarrow -\infty} -rV(x, y) = Z_{\text{asym}}, \quad (\text{C2})$$

with $Z_{\text{asym}} > 0$ as a real constant. Note that V need not be isotropic for this condition to be satisfied. In parabolic cylindrical coordinates,

$$u = r + x, \quad u \in [0, \infty), \quad (\text{C3})$$

$$v = r - x, \quad v \in [0, \infty), \quad (\text{C4})$$

Eq. (C1) reads

$$\left[\sqrt{v}\frac{\partial}{\partial v}\sqrt{v}\frac{\partial}{\partial v} + \frac{\mathcal{E}v^2}{4} + \frac{Ev}{2} + \beta(v)\right]\psi(u, v) = 0, \quad (\text{C5})$$

where

$$\beta(v) = \sqrt{u}\frac{\partial}{\partial u}\sqrt{u}\frac{\partial}{\partial u} - rV(x, y) + \frac{Eu}{2} - \frac{\mathcal{E}u^2}{4} \quad (\text{C6})$$

operates on functions of u and depends on v as a parameter through V . It has a purely discrete spectrum defined by

$$\beta(v)\varphi_n(u; v) = b_n\varphi_n(u; v). \quad (\text{C7})$$

It is symmetric (but not Hermitian due to generally complex E) with respect to the weighting function $w(u) = 1/\sqrt{u}$, and we may, therefore, choose the eigenfunctions orthonormal,

$$(\varphi_n|\varphi_m)_{u,w} = \int_0^\infty \varphi_n(u; v)\varphi_m(u; v)\frac{1}{\sqrt{u}}du = \delta_{nm}, \quad (\text{C8})$$

where we have used regular parentheses for the inner product to indicate that there is no complex conjugation, which is a general property of the theory of Siegert states [76–80]. The subscript u, w denotes that the integral is taken with respect to u , using the weighting function w .

We will proceed by writing the solution to Eq. (C5) as

$$\psi(\mathbf{r}) = \sum_n v^{-1/4} f_n(v) \varphi_n(u; v). \quad (\text{C9})$$

This approach is based on the adiabatic expansion applied to a three-dimensional system in Refs. [66,75]. In essence, it corresponds to treating v as a slow variable, much like the internuclear distance in the Born-Oppenheimer approximation. It should be noted, however, that the expansion does not constitute an approximation as long as all nonadiabatic coupling terms are taken into account. Substituting the expansion into

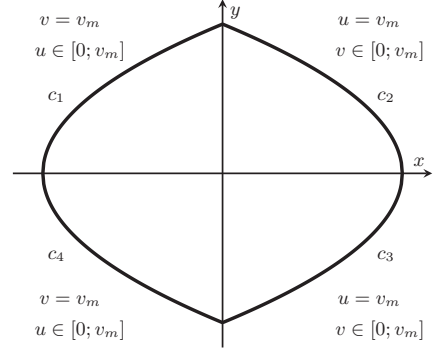


FIG. 8. The area enclosed by curves of constant u and v , respectively. Note that the curves on the lower half-plane correspond to the negative sign in y .

Eq. (C5), we obtain

$$\left[\frac{\partial^2}{\partial v^2} + \frac{\mathcal{E}v}{4} + \frac{E}{2} + \frac{b_n(v)}{v} + \frac{3}{16v^2}\right]f_n(v) + \sum_n \left[\left(\varphi_m \left| \frac{\partial \varphi_n}{\partial v} \right| \right)_{u,w} 2 \frac{\partial}{\partial v} + \left(\varphi_m \left| \frac{\partial^2 \varphi_n}{\partial v^2} \right| \right)_{u,w} \right] f_n(v) = 0. \quad (\text{C10})$$

Recalling the assumption in Eq. (C2) [and noting that $x = (u - v)/2$], the φ functions cease to depend on v for $v \rightarrow \infty$ and the coupling matrix elements, therefore, reduce to zero. Explicitly,

$$\left[\frac{\partial^2}{\partial v^2} + \frac{\mathcal{E}v}{4} + \frac{E}{2} + \frac{b_n}{v} + \frac{3}{16v^2}\right]f_n(v) = 0. \quad (\text{C11})$$

This equation is identical to the one in Refs. [66,67]. For $\mathcal{E} = 0$, the solutions behave as

$$f_n^{(0)}(v) = v^{b_n/k} e^{-kv/2} \left[1 + \frac{c_1}{v} + \frac{c_2}{v^2} + O(v^{-3}) \right]. \quad (\text{C12})$$

For $\mathcal{E} > 0$, the outgoing solution satisfies [75]

$$f_n(v)_{v \rightarrow \infty} = c_n f(v), \quad (\text{C13})$$

$$f(v) = \frac{\sqrt{2}}{(\mathcal{E}v)^{1/4}} \exp \left[\frac{i\sqrt{\mathcal{E}}v^{3/2}}{3} + \frac{iE\sqrt{v}}{\sqrt{\mathcal{E}}} \right]. \quad (\text{C14})$$

Thus, the asymptotics only depend on b_n through the coefficients c_n . The dissociation rate may be related to the probability current \mathbf{j} as follows:

$$\Gamma|\psi|^2 = \nabla \cdot \left[-\frac{i}{2}(\psi^* \nabla \psi - \psi \nabla \psi^*) \right] = \nabla \cdot \mathbf{j}. \quad (\text{C15})$$

In the weak-field region, the resonance state ψ will coincide with the unperturbed bound state in a region $v < v_m$, where v_m is defined by $v_t \ll v_m \ll \mathcal{E}/\Gamma^2$. Here, $v_t \approx -2E_0/\mathcal{E}$ [see Eq. (C11)] is the turning point, and the fact that this holds can be seen from the fact that the exponential growth of f_n starts at around $v \gtrsim \mathcal{E}/\Gamma^2$. Let A be the area enclosed by curves of constants $u = v_m$ and $v = v_m$, respectively (see Fig. 8). Then,

inside this area, the SS will be approximately equal to the unperturbed state and, therefore,

$$\int_A |\psi|^2 dA \approx 1, \quad (\text{C16})$$

and integrating both sides of Eq. (C15) over the area A , therefore, yields

$$\Gamma = \int_A \nabla \cdot \mathbf{j} dA = \int_c \hat{n} \cdot \mathbf{j} dl, \quad (\text{C17})$$

where the final equality follows from the divergence theorem. Now, if v_m is large enough, integrating along c_2 and c_3 will yield zero because $\varphi_n \rightarrow 0$ for $u \rightarrow \infty$. The integration, therefore, immediately reduces to integrating along c_1 and c_4 (see Fig. 8). By symmetry, the integration along c_4 must equal the integration along c_1 , and, thus, we get

$$\Gamma = 2 \int_{c_1} \hat{n} \cdot \mathbf{j} dc_1. \quad (\text{C18})$$

The parametrization of the curve c_1 is given by

$$\mathbf{r} = \frac{u - v_m}{2} \hat{x} + \sqrt{uv_m} \hat{y}, \quad (\text{C19})$$

and

$$\left| \frac{\partial}{\partial u} \mathbf{r} \right| = \sqrt{\frac{r}{2u}}. \quad (\text{C20})$$

The normal vector \hat{v} picks out the v component of the gradient in \mathbf{j} so that

$$\hat{v} \cdot \nabla = \sqrt{\frac{2v}{r}} \frac{\partial}{\partial v}, \quad (\text{C21})$$

and we have

$$\begin{aligned} \Gamma = -i \int_0^{v_m} \sqrt{\frac{v_m}{u}} \left[\psi^*(u, v_m) \frac{\partial}{\partial v} \psi(u, v_m) \right. \\ \left. - \psi(u, v_m) \frac{\partial}{\partial v} \psi^*(u, v_m) \right] du, \end{aligned} \quad (\text{C22})$$

where $\partial \psi(u, v_m)/\partial v$ denotes the derivative of ψ evaluated at the point v_m . For sufficiently weak fields, v_m will become so large that we might take the limit $v_m \rightarrow \infty$. This allows us to use the asymptotic basis functions that are independent of v in the expression. We obtain

$$\Gamma = -i \sum_n \left[f_n^*(v_m) \frac{\partial}{\partial v} f_n(v_m) - f_n(v_m) \frac{\partial}{\partial v} f_n^*(v_m) \right]. \quad (\text{C23})$$

Recalling the asymptotic expression for f_n in Eq. (C13), one obtains

$$\Gamma = 2 \sum_n |c_n| \left(1 + \frac{E_R}{\mathcal{E} v_m} \right) \exp \left(\Gamma \sqrt{\frac{v_m}{\mathcal{E}}} \right). \quad (\text{C24})$$

In the weak-field region, Γ will be exponentially small, and we can approximate the exponential function by unity. Furthermore, for v_m large enough, the second term in the parentheses can be neglected (recall one of the assumptions

we made was $v_m \gg v_l \approx -2E_0/\mathcal{E}$). Ultimately, this leads to

$$\Gamma = 2 \sum_n |c_n|. \quad (\text{C25})$$

Thus, to find the weak-field ionization rate, all we require is the coefficients c_n . We will find those by matching the state with a field present to the unperturbed state in a matching region that is far enough from the origin that the asymptotics apply, yet close enough that the unperturbed and the perturbed states coincide. We may write the unperturbed state as

$$\psi_0(\mathbf{r}) = \sum_n g_n v^{-1/4} f_n^{(0)}(v) \varphi_n^{(0)}(u) \quad \text{for } v \rightarrow \infty, \quad (\text{C26})$$

where g_n is a field-independent coefficient. Recalling the solution for $\mathcal{E} = 0$ is given by Eq. (C12), we have

$$\psi_0(\mathbf{r}) = \sum_n g_n v^{b_n/k-1/4} e^{-kv/2} \varphi_n^{(0)}(u) \quad \text{for } v \rightarrow \infty. \quad (\text{C27})$$

In the matching region, a Wentzel–Kramers–Brillouin-type expression for the perturbed f_n functions can be found to be [66]

$$\begin{aligned} f_n(v) = c_n \sqrt{\frac{2}{k}} \left(\frac{\mathcal{E}}{4k^2} \right)^{b_n^{(0)}/k} \exp \left[-\frac{i\pi}{4} - \frac{i\pi b_n^{(0)}}{k} + \frac{k^3}{3\mathcal{E}} \right] \\ \times v^{b_n/k} e^{-kv/2}. \end{aligned} \quad (\text{C28})$$

Comparing Eq. (C28) to Eq. (C27) leads to the conclusion that

$$c_n = g_n \sqrt{\frac{k}{2}} \left(\frac{4k^2}{\mathcal{E}} \right)^{b_n^{(0)}/k} \exp \left[\frac{i\pi}{4} + \frac{i\pi b_n^{(0)}}{k} - \frac{k^3}{3\mathcal{E}} \right], \quad (\text{C29})$$

and, therefore,

$$\Gamma = \sum_n |g_n|^2 k \left(\frac{4k^2}{\mathcal{E}} \right)^{2b_n^{(0)}/k} \exp \left(-\frac{2k^3}{3\mathcal{E}} \right). \quad (\text{C30})$$

What remains is to find the field-free eigenvalues $b_n^{(0)}$. For $\mathcal{E} = 0$, we have

$$\left(\sqrt{u} \frac{\partial}{\partial u} \sqrt{u} \frac{\partial}{\partial u} + Z_{\text{asympt}} - \frac{k^2 u}{4} - b_n^{(0)} \right) \varphi_n^{(0)}(u) = 0. \quad (\text{C31})$$

We find

$$\varphi_n^{(0)}(u) = N_n L_n^{(-1/2)}(ku) e^{-ku/2}, \quad (\text{C32})$$

where $n = 0, 1, 2, \dots$, and the normalization coefficient,

$$N_n = \left[\frac{k^{1/2} n!}{(n-1/2)!} \right]^{1/2}. \quad (\text{C33})$$

The eigenvalues are

$$b_n^{(0)} = Z_{\text{asympt}} - k \left(n + \frac{1}{4} \right), \quad \text{where } n = 0, 1, 2, \dots, \quad (\text{C34})$$

and the dissociation rate becomes

$$\Gamma = \sum_n |g_n|^2 k \left(\frac{4k^2}{\mathcal{E}} \right)^{2Z_{\text{asympt}}/k-2n-1/2} \exp \left(-\frac{2k^3}{3\mathcal{E}} \right). \quad (\text{C35})$$

As discussed in Ref. [66], only the dominant contribution may be included in Eq. (C25) within the present approximation. It corresponds to $n = 0$, thus, the weak-field approximation to

the dissociation rate is

$$\Gamma = |g_0|^2 k \left(\frac{4k^2}{\mathcal{E}} \right)^{2Z_{\text{asympt}}/k-1/2} \exp\left(-\frac{2k^3}{3\mathcal{E}}\right). \quad (\text{C36})$$

The coefficient g_0 is defined by the asymptotics of the unperturbed state. It can be obtained by taking the inner product between Eq. (C27) and $\varphi_0^{(0)}$, i.e.,

$$g_0 = \lim_{v \rightarrow \infty} v^{1/2-Z/k} e^{kv/2} \int_0^\infty \varphi_0^{(0)}(u) \psi_0\left(\frac{u+v}{2}\right) \frac{1}{\sqrt{u}} du. \quad (\text{C37})$$

-
- [1] K. S. Novoselov, A. K. Geim, S. V. Morozov, D. Jiang, Y. Zhang, S. V. Dubonos, I. V. Grigorieva, and A. A. Firsov, *Science* **306**, 666 (2004).
- [2] K. F. Mak, C. Lee, J. Hone, J. Shan, and T. F. Heinz, *Phys. Rev. Lett.* **105**, 136805 (2010).
- [3] L. Li, Y. Yu, G. J. Ye, Q. Ge, X. Ou, H. Wu, D. Feng, X. H. Chen, and Y. Zhang, *Nat. Nanotechnol.* **9**, 372 (2014).
- [4] S. P. Koenig, R. A. Doganov, H. Schmidt, A. H. Castro Neto, and B. Özyilmaz, *Appl. Phys. Lett.* **104**, 103106 (2014).
- [5] H. Liu, A. T. Neal, Z. Zhu, Z. Luo, X. Xu, D. Tomnek, and P. D. Ye, *ACS Nano* **8**, 4033 (2014).
- [6] A. Castellanos-Gomez, L. Vicarelli, E. Prada, J. O. Island, K. L. Narasimha-Acharya, S. I. Blanter, D. J. Groenendijk, M. Buscema, G. A. Steele, J. V. Alvarez, H. W. Zandbergen, J. J. Palacios, and H. S. J. van der Zant, *2D Mater.* **1**, 025001 (2014).
- [7] F. Xia, H. Wang, and Y. Jia, *Nat. Commun.* **5**, 4458 (2014).
- [8] A. Castellanos-Gomez, *J. Phys. Chem. Lett.* **6**, 4280 (2015).
- [9] M. Chhowalla, H. S. Shin, G. Eda, L.-J. Li, K. P. Loh, and H. Zhang, *Nat. Chem.* **5**, 263 (2013).
- [10] R. W. Keyes, *Phys. Rev.* **92**, 580 (1953).
- [11] H. Asahina and A. Morita, *J. Phys. C: Solid State Phys.* **17**, 1839 (1984).
- [12] A. Morita, *Appl. Phys. A* **39**, 227 (1986).
- [13] A. N. Rudenko and M. I. Katsnelson, *Phys. Rev. B* **89**, 201408(R) (2014).
- [14] J. Qiao, X. Kong, Z.-X. Hu, F. Yang, and W. Ji, *Nat. Commun.* **5**, 4475 (2014).
- [15] V. Tran, R. Soklaski, Y. Liang, and L. Yang, *Phys. Rev. B* **89**, 235319 (2014).
- [16] X. Wang, A. M. Jones, K. L. Seyler, V. Tran, Y. Jia, H. Zhao, H. Wang, L. Yang, X. Xu, and F. Xia, *Nat. Nanotechnol.* **10**, 517 (2015).
- [17] J. Hu, Z. Guo, P. E. McWilliams, J. E. Darges, D. L. Druffel, A. M. Moran, and S. C. Warren, *Nano Lett.* **16**, 74 (2016).
- [18] R. Fei and L. Yang, *Nano Lett.* **14**, 2884 (2014).
- [19] Y. Xu, J. Dai, and X. C. Zeng, *J. Phys. Chem. Lett.* **6**, 1996 (2015).
- [20] X. Y. Zhou, R. Zhang, J. P. Sun, Y. L. Zou, D. Zhang, W. K. Lou, F. Cheng, G. H. Zhou, F. Zhai, and K. Chang, *Sci. Rep.* **5**, 12295 (2015).
- [21] X. Zhou, W.-K. Lou, F. Zhai, and K. Chang, *Phys. Rev. B* **92**, 165405 (2015).
- [22] X. Zhou, W.-K. Lou, D. Zhang, F. Cheng, G. Zhou, and K. Chang, *Phys. Rev. B* **95**, 045408 (2017).
- [23] Z.-Y. Ong, Y. Cai, G. Zhang, and Y.-W. Zhang, *J. Phys. Chem. C* **118**, 25272 (2014).
- [24] A. Jain and A. J. H. McGaughey, *Sci. Rep.* **5**, 8501 (2015).
- [25] Q. Wei and X. Peng, *Appl. Phys. Lett.* **104**, 251915 (2014).
- [26] F. Xia, H. Wang, D. Xiao, M. Dubey, and A. Ramasubramaniam, *Nat. Photonics* **8**, 899 (2014).
- [27] S. Zhang, J. Yang, R. Xu, F. Wang, W. Li, M. Ghufuran, Y.-W. Zhang, Z. Yu, G. Zhang, Q. Qin, and Y. Lu, *ACS Nano* **8**, 9590 (2014).
- [28] A. S. Rodin, A. Carvalho, and A. H. Castro Neto, *Phys. Rev. B* **90**, 075429 (2014).
- [29] R. J. Hunt, M. Szyniszewski, G. I. Prayogo, R. Maezono, and N. D. Drummond, *Phys. Rev. B* **98**, 075122 (2018).
- [30] J. C. G. Henriques and N. M. R. Peres, *Phys. Rev. B* **101**, 035406 (2020).
- [31] V. Perebeinos and P. Avouris, *Nano Lett.* **7**, 609 (2007).
- [32] A. D. Mohite, P. Gopinath, H. M. Shah, and B. W. Alphenaar, *Nano Lett.* **8**, 142 (2008).
- [33] H. C. Kamban, S. S. Christensen, T. Søndergaard, and T. G. Pedersen, *Phys. Status Solidi B* **257**, 1900467 (2020).
- [34] T. G. Pedersen, *Phys. Rev. B* **94**, 125424 (2016).
- [35] S. Haastrup, S. Latini, K. Bolotin, and K. S. Thygesen, *Phys. Rev. B* **94**, 041401(R) (2016).
- [36] B. Scharf, T. Frank, M. Gmitra, J. Fabian, I. Žutić, and V. Perebeinos, *Phys. Rev. B* **94**, 245434 (2016).
- [37] M. Massicotte, F. Vialla, P. Schmidt, M. B. Lundeberg, S. Latini, S. Haastrup, M. Danovich, D. Davydovskaya, K. Watanabe, T. Taniguchi, V. I. Falko, K. Thygesen, T. G. Pedersen, and F. H. L. Koppens, *Nat. Commun.* **9**, 1633 (2018).
- [38] L. S. R. Cavalcante, D. R. da Costa, G. A. Farias, D. R. Reichman, and A. Chaves, *Phys. Rev. B* **98**, 245309 (2018).
- [39] H. C. Kamban and T. G. Pedersen, *Phys. Rev. B* **100**, 045307 (2019).
- [40] H. C. Kamban and T. G. Pedersen, *Sci. Rep.* **10**, 5537 (2020).
- [41] T. G. Pedersen, S. Latini, K. S. Thygesen, H. Mera, and B. K. Nikolić, *New J. Phys.* **18**, 073043 (2016).
- [42] A. Chaves, T. Low, P. Avouris, D. Çakır, and F. M. Peeters, *Phys. Rev. B* **91**, 155311 (2015).
- [43] W. Franz, *Z. Naturforsch. A* **13**, 484 (1958).
- [44] L. V. Keldysh, *Zh. Eksp. Teor. Fiz.* **34**, 1138 (1958) [*Sov. Phys. JETP* **7**, 788 (1958)].
- [45] G. H. Wannier, *Phys. Rev.* **52**, 191 (1937).
- [46] F. L. Lederman and J. D. Dow, *Phys. Rev. B* **13**, 1633 (1976).
- [47] P. Cudazzo, C. Attaccalite, I. V. Tokatly, and A. Rubifo, *Phys. Rev. Lett.* **104**, 226804 (2010).
- [48] O. Pulci, P. Gori, M. Marsili, V. Garbuio, R. D. Sole, and F. Bechstedt, *Europhys. Lett.* **98**, 37004 (2012).
- [49] S. Latini, T. Olsen, and K. S. Thygesen, *Phys. Rev. B* **92**, 245123 (2015).
- [50] J. C. G. Henriques, G. B. Ventura, C. D. M. Fernandes, and N. M. R. Peres, *J. Phys.: Condens. Matter* **32**, 025304 (2019).
- [51] E. E. Salpeter and H. A. Bethe, *Phys. Rev.* **84**, 1232 (1951).
- [52] G. Onida, L. Reining, and A. Rubio, *Rev. Mod. Phys.* **74**, 601 (2002).

- [53] T. C. Berkelbach, M. S. Hybertsen, and D. R. Reichman, *Phys. Rev. B* **88**, 045318 (2013).
- [54] N. S. Rytova, *MOSC U PHYS B+* **3**, 18 (1967).
- [55] L. V. Keldysh, *JETP Lett.* **29**, 658 (1979).
- [56] M. L. Trolle, T. G. Pedersen, and V. Vénier, *Sci. Rep.* **7**, 39844 (2017).
- [57] P. E. Faria Junior, M. Kurpas, M. Gmitra, and J. Fabian, *Phys. Rev. B* **100**, 115203 (2019).
- [58] J.-H. Choi, P. Cui, H. Lan, and Z. Zhang, *Phys. Rev. Lett.* **115**, 066403 (2015).
- [59] J. Yang, R. Xu, J. Pei, Y. W. Myint, F. Wang, Z. Wang, S. Zhang, Z. Yu, and Y. Lu, *Light: Sci. Appl.* **4**, e312 (2015).
- [60] E. Balslev and J. M. Combes, *Commun. Math. Phys.* **22**, 280 (1971).
- [61] J. Aguilar and J. M. Combes, *Commun. Math. Phys.* **22**, 269 (1971).
- [62] A. Scrinzi and N. Elander, *J. Chem. Phys.* **98**, 3866 (1993).
- [63] S. Arra, R. Babar, and M. Kabir, *Phys. Rev. B* **99**, 045432 (2019).
- [64] L. D. Landau and L. M. Lifshitz, *Quantum Mechanics: Non-Relativistic Theory*, 3rd ed. (Pergamon, Oxford, UK, 1989).
- [65] J. C. G. Henriques, H. C. Kamban, T. G. Pedersen, and N. M. R. Peres, *Phys. Rev. B* **102**, 035402 (2020).
- [66] O. I. Tolstikhin, T. Morishita, and L. B. Madsen, *Phys. Rev. A* **84**, 053423 (2011).
- [67] V. H. Trinh, O. I. Tolstikhin, L. B. Madsen, and T. Morishita, *Phys. Rev. A* **87**, 043426 (2013).
- [68] T. G. Pedersen, H. Mera, and B. K. Nikolić, *Phys. Rev. A* **93**, 013409 (2016).
- [69] R. J. Elliott, *Phys. Rev.* **108**, 1384 (1957).
- [70] L. Liang, J. Wang, W. Lin, B. G. Sumpter, V. Meunier, and M. Pan, *Nano Lett.* **14**, 6400 (2014).
- [71] T. G. Pedersen and T. B. Lyngé, *Phys. Rev. B* **65**, 085201 (2002).
- [72] A. Galiutdinov, *Phys. Lett. A* **383**, 3167 (2019).
- [73] S. Mikhlin, *Integral Equations and Their Applications to Certain Problems in Mechanics, Mathematical Physics and Technology*, 2nd ed. (Pergamon, Oxford, UK, 1964).
- [74] T. Hu and J. Hong, *ACS Appl. Mater. Interfaces* **7**, 23489 (2015).
- [75] P. A. Batishchev, O. I. Tolstikhin, and T. Morishita, *Phys. Rev. A* **82**, 023416 (2010).
- [76] A. J. F. Siegert, *Phys. Rev.* **56**, 750 (1939).
- [77] O. I. Tolstikhin, V. N. Ostrovsky, and H. Nakamura, *Phys. Rev. A* **58**, 2077 (1998).
- [78] G. V. Sitnikov and O. I. Tolstikhin, *Phys. Rev. A* **67**, 032714 (2003).
- [79] K. Toyota, T. Morishita, and S. Watanabe, *Phys. Rev. A* **72**, 062718 (2005).
- [80] P. A. Batishchev and O. I. Tolstikhin, *Phys. Rev. A* **75**, 062704 (2007).

Paper F

Calculation of the nonlinear response functions of
intra-exciton transitions in two-dimensional transition
metal dichalcogenides

João C. G. Henriques, Høgni C. Kamban, Thomas G. Pedersen,
and Nuno M. R. Peres

This paper has been published in Physical Review B:
Phys. Rev. B **103**, 235412 (2021)
DOI: 10.1103/PhysRevB.103.235412

Calculation of the nonlinear response functions of intraexciton transitions in two-dimensional transition metal dichalcogenides

J. C. G. Henriques^{1,2}, Høgni C. Kamban^{3,4}, Thomas G. Pedersen^{3,4} and N. M. R. Peres^{1,2}

¹*Department and Centre of Physics, and QuantaLab, University of Minho, Campus of Gualtar, 4710-057 Braga, Portugal*

²*International Iberian Nanotechnology Laboratory (INL), Av. Mestre José Veiga, 4715-330 Braga, Portugal*

³*Department of Materials and Production, Aalborg University, DK-9220 Aalborg Øst, Denmark*

⁴*Center for Nanostructured Graphene (CNG), DK-9220 Aalborg Øst, Denmark*



(Received 28 February 2021; revised 28 May 2021; accepted 28 May 2021; published 8 June 2021)

In this paper we study the third-order nonlinear optical response due to transitions between excitonic levels in two-dimensional transition metal dichalcogenides. To accomplish this we use methods not applied to the description of excitons in two-dimensional materials so far and combined with a variational approach to describe the $1s$ excitonic state. The aforementioned transitions allow us to probe dark states which are not revealed in absorption experiments. We present general formulas capable of describing any third-order process. The specific case of two-photon absorption in WSe_2 is studied. The case of the circular well is also studied as a benchmark of the theory.

DOI: [10.1103/PhysRevB.103.235412](https://doi.org/10.1103/PhysRevB.103.235412)

I. INTRODUCTION

Since graphene [1] was first studied, the family of two-dimensional (2D) materials has been expanding, and other materials such as hexagonal-boron nitride (hBN) [2], phosphorene [3], and transition metal dichalcogenides (TMDs) [4], such as MoS_2 , MoSe_2 , WS_2 , and WSe_2 , have gained considerable attraction over the years. These last ones correspond to semiconducting materials with a direct band gap of about 1.5 eV [5], and are currently extensively studied due to their remarkable electronic and optical properties.

Like other 2D materials, the optical properties of TMDs are strongly dependent on their excitonic response [6]. When a material is optically excited, if the photon energy is large enough, electrons may be removed from the valence band to the conduction band. The electron promoted to the conduction band and the hole left in the valence band form a quasiparticle due to the Coulomb-like interaction between them. This particle is similar to a hydrogen atom, and it is termed an exciton. Contrary to their three-dimensional (3D) counterparts, where the energy spectrum is well described by a Rydberg series, excitons in 2D materials present a more complex energy landscape as a consequence of the nonlocal dielectric screening of the interaction potential between the electron and the hole [7]. Also, their reduced dimensionality leads to more tightly bound excitonic states, which are stable even at room temperature [8].

When studying the optical properties of TMDs two distinct regimes can be identified. The first one corresponds to the case where optical excitation induces transitions from the excitonic vacuum to a given state of the exciton, and is termed the excitonic interband regime. This regime is the origin of the well-known peaks in an absorption spectrum, corresponding to transitions from the excitonic vacuum to different s states

of the exciton [9]. In recent years, nonlinear optical effects originated from interband transitions have been the topic of many works, both experimental and theoretical. The study of nonlinearities in MoS_2 was explored in Refs. [10–13], while Refs. [14,15] studied similar effects in WS_2 and Refs. [16,17] in WSe_2 . A thorough comparison between the nonlinear response of different TMDs is presented in Ref. [18]. Studies on the effect of strain and the coupling to exciton-plasmons have also been performed [19,20]. In Ref. [21] an analytical study of the nonlinear optical response of monolayer TMDs was presented. Due to their broken inversion symmetry TMDs are not centrosymmetric (at least when stacked in an odd number of layers), and as a consequence both even and odd orders of nonlinear optical processes are always permitted [22]. Moreover, these materials shown large nonlinear optical coefficients [21], increasing their potential for applications, such as optical modulators [23,24]. The possibility of characterizing different properties of the 2D material from their nonlinear optical response has also been considered [25,26]. The second regime one should consider when studying the optical properties of these systems is associated with transition between the excitonic energy levels themselves, and we label it as the intraexciton regime. This type of excitation can be experimentally realized in a pump-probe setup, where first the pump laser populates the $1s$ exciton state and then the probe induces transitions from the $1s$ to the remaining bound states of the exciton (see Fig. 1). Recently, in Ref. [27], this type of procedure was implemented to characterize the linear optical response of WSe_2 in the intraexciton regime, and probe the excitonic dark states which are not accessible from luminescence methods. Contrary to the interband regime, the nonlinear response associated with optical transitions when the ground state is already populated remains vastly unstudied. Its comprehension could unlock

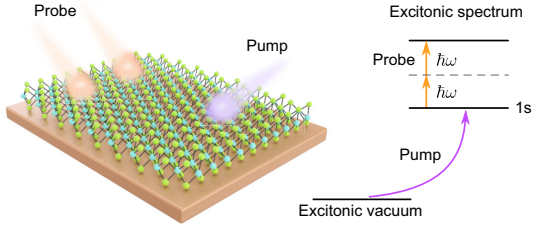


FIG. 1. Schematic representation of the two photon absorption process in WSe₂ excitons when the 1s excitonic state is already populated.

new degrees of freedom exploitable in nonlinear optical applications.

Our goal with this paper is to provide a theoretical framework based on the ideas presented in Refs. [28–32], which allows the description of third-order nonlinear optical processes in the intraexciton regime, namely the two photon absorption (TPA) for excitons in WSe₂. Contrarily to the approach of a sum over states usually found from time-dependent perturbation theory, where different excited wave functions are needed, our approach only requires the 1s wave function, which can be accurately described using variational techniques [33,34]. We then expand the perturbed wave function directly in a basis. It follows that, formally, our approach is equivalent to a sum of states computation approximating excited states by expanding in the same basis. However, the present approach is conceptually simpler. The text is organized as follows. In Sec. II we present the general method used to compute the nonlinear third-order optical susceptibility. This corresponds to a generalization of the approach presented in Ref. [35] where the linear response was studied. In Sec. III we focus on the more interesting problem of excitons in WSe₂, when the excitonic ground state is already populated and the optical excitation induces transitions between the excitonic levels. A section with our final remarks and Appendixes close the paper.

II. NONLINEAR THIRD-ORDER OPTICAL RESPONSE

In the first part of this section we will give a detailed description of a method to compute the third-order optical susceptibility of a given system. The only requirement is that the ground-state wave function of the system is known (at least approximately). This method contrasts with the usual sum over states where both the ground-state and the excited-state wave functions are needed. The presented approach is based on Refs. [28–32] and corresponds to an extension of what was recently used in Ref. [35] regarding the linear optical response. In the second part of the section the problem of a circular potential well will be studied as a first application of the formalism. This example will set the stage for the posterior study of two-dimensional excitons in WSe₂.

A. Outline of the method

1. Third-order susceptibility

Since we will be interested in computing the third-order nonlinear response, we start by introducing the expression

for the third-order optical susceptibility, as derived from perturbation theory. Throughout the work we will use atomic units unless stated otherwise. Following Ref. [36] we write the third-order susceptibility as

$$\chi_{\alpha\beta\gamma\delta}^{(3)}(\omega_\sigma; \omega_1, \omega_2, \omega_3) = \frac{1}{3!} \mathcal{P} \left\{ \sum_{n,m,l \neq 0} \frac{\langle 0 | \mathbf{d}_\alpha | n \rangle \langle n | \mathbf{d}_\beta | m \rangle \langle m | \mathbf{d}_\gamma | l \rangle \langle l | \mathbf{d}_\delta | 0 \rangle}{(E_{n0} - \omega_\sigma)(E_{m0} - \omega_2 - \omega_3)(E_{l0} - \omega_3)} - \sum_{n,m \neq 0} \frac{\langle 0 | \mathbf{d}_\alpha | n \rangle \langle n | \mathbf{d}_\beta | 0 \rangle \langle 0 | \mathbf{d}_\gamma | m \rangle \langle m | \mathbf{d}_\delta | 0 \rangle}{(E_{n0} - \omega_\sigma)(E_{m0} - \omega_2)(E_{m0} + \omega_1)} \right\}, \quad (1)$$

where $E_{n0} = E_n - E_0$ is the energy difference between the levels $|n\rangle$ and $|0\rangle$, \mathbf{d} is the dipole moment, $\{\alpha, \beta, \gamma, \delta\}$ are indexes corresponding to different spatial orientations (x or y), $\omega_\sigma = \omega_1 + \omega_2 + \omega_3$, \mathcal{P} is the permutation operator of the pairs $(\alpha, -\omega_\sigma; \beta, \omega_1; \gamma, \omega_2; \delta, \omega_3)$, and $|n\rangle$ corresponds to the unperturbed states of the system, with $|0\rangle$ its ground state. The direct application of Eq. (1) corresponds to the sum over states approach. Since the different sums run over all the excited states of the system, this way of calculating the optical susceptibility presents the major drawback of requiring the knowledge of all the excited-state wave functions, at least in a naive approach. (Obviously one can expand the unknown eigenstates in a complete basis and obtain the expansion coefficients. This latter approach can be seen as an alternative to the method developed in Appendix A). Although in simple systems the exact wave functions may be trivially known, in more complex ones they may be elusive (this is precisely the case of excitons in 2D materials to be discussed ahead).

In order to avoid the usual sum over states method, we follow the ideas of Refs. [28–32]. Doing so, we write the time-dependent Schrödinger equation

$$[H_0 + \mathbf{d} \cdot \mathcal{E}(t)]|\psi(t)\rangle = i \frac{\partial}{\partial t} |\psi(t)\rangle, \quad (2)$$

where H_0 corresponds to the unperturbed Hamiltonian of a given system (this may contain a kinetic and a potential term), $\mathbf{d} \cdot \mathcal{E}(t)$ describes the interaction of the system with an external time-dependent harmonic electric field $\mathcal{E}(t)$ in the dipole approximation, and $|\psi(t)\rangle$ is the state vector of the system in the presence of the external electric field. Note that the electric field \mathcal{E} corresponds to the probe in a pump-probe type of experiment. Next, we expand $|\psi(t)\rangle$ in powers of \mathcal{E} as

$$|\psi\rangle = |0\rangle e^{-iE_0 t} + \mathcal{E}_\alpha |\psi_\alpha\rangle e^{-i(E_0 - \omega_\alpha)t} + \mathcal{E}_\alpha \mathcal{E}_\beta |\xi_{\alpha\beta}\rangle e^{-i(E_0 - \omega_\alpha - \omega_\beta)t} + \dots, \quad (3)$$

where $\mathcal{E}_\alpha e^{i\omega_\alpha t}$ refers to an harmonic electric field applied along the α direction (either x or y) with frequency ω_α , E_0 is the energy of the unperturbed ground state of the system, and $|\psi_\alpha\rangle$ and $|\xi_{\alpha\beta}\rangle$ are yet to be determined. Inserting this in the time-dependent Schrödinger equation and grouping equivalent terms in \mathcal{E} , up to second order in the electric field, we find the following three equations:

$$0 = (H_0 - E_0)|0\rangle, \quad (4)$$

$$0 = (H_0 - E_0 + \omega_\alpha)|\psi_\alpha\rangle + \mathbf{d}_\alpha |0\rangle, \quad (5)$$

$$0 = (H_0 - E_0 + \omega_\alpha + \omega_\beta)|\xi_{\alpha\beta}(\omega_\alpha, \omega_\beta)\rangle + \mathbf{d}_\beta |\psi_\alpha(\omega_\alpha)\rangle. \quad (6)$$

The first one simply states the eigenvalue relation for the ground state of the system in the absence of the external electric field. The second and third ones define the $|\psi_\alpha\rangle$ and $|\xi_{\alpha\beta}\rangle$, respectively. Expanding these two states in the basis of the eigenstates of H_0 one easily arrives at

$$|\psi_\alpha(\omega_a)\rangle = -\sum_{n \neq 0} \frac{\langle n|\mathbf{d}_\alpha|0\rangle}{E_n - E_0 + \omega_a} |n\rangle, \quad (7)$$

$$|\xi_{\alpha\beta}(\omega_a, \omega_b)\rangle = -\sum_{n \neq 0} \frac{\langle n|\mathbf{d}_\beta|\psi_\alpha(\omega_a)\rangle}{E_n - E_0 + \omega_a + \omega_b} |n\rangle, \quad (8)$$

where we assumed $\langle 0|\psi_\alpha\rangle = 0$ and $\langle 0|\xi_{\alpha\beta}\rangle = 0$. The first requirement corresponds to choosing a coordinate system placing $\langle 0|\mathbf{d}|0\rangle$ at the origin, which is always possible. The second assumption will be discussed further ahead. Now we note that with the introduction of $|\psi_\alpha\rangle$ and $|\xi_{\alpha\beta}\rangle$ we are able to rewrite Eq. (1) as

$$\chi_{\alpha\beta\gamma\delta}^{(3)} = \frac{1}{3!} \mathcal{P} \{ -\langle \psi_\alpha(-\omega_\sigma^*) | \mathbf{d}_\beta | \xi_{\delta\gamma}(-\omega_3, -\omega_2) \rangle + \langle 0 | \mathbf{d}_\alpha | \psi_\beta(-\omega_\sigma) \rangle \langle \psi_\gamma(-\omega_2^*) | \psi_\delta(\omega_1) \rangle \}. \quad (9)$$

Determining $|\psi_\alpha\rangle$ and $|\xi_{\alpha\beta}\rangle$ allows us to obtain the third-order susceptibility through the computation of only three matrix elements. Note that we are considering the possibility of the frequencies to be complex valued. We do so in order to obtain both the real and imaginary parts of $\chi^{(3)}$. This is achieved by shifting the energies by a small imaginary part, that is $\omega \rightarrow \omega + i\delta$.

2. Computing the new state vectors

Computing $|\psi_\alpha\rangle$ and $|\xi_{\alpha\beta}\rangle$ using Eqs. (7) and (8) would reverse our progress, and leave us again with a problem requiring the evaluation of a sum over states. To continue with the calculations, we follow Ref. [28] and introduce the functionals

$$\mathcal{J} = \langle \psi_\alpha(\omega) | H_0 - E_0 + \omega | \psi_\alpha(\omega) \rangle + [\langle \psi_\alpha(\omega) | \mathbf{d}_\alpha | 0 \rangle + \text{c.c.}] \quad (10)$$

and

$$\mathcal{K} = \langle \xi_{\alpha\beta}(\omega_a, \omega_b) | (H_0 - E_0 + \omega_a + \omega_b) | \xi_{\alpha\beta}(\omega_a, \omega_b) \rangle + [\langle \xi_{\alpha\beta}(\omega_a, \omega_b) | \mathbf{d}_\beta | \psi_\alpha(\omega_a) \rangle + \text{c.c.}]. \quad (11)$$

Finding the extrema \mathcal{J} with respect to $|\psi_\alpha\rangle$ and \mathcal{K} with respect to $|\xi_{\alpha\beta}\rangle$ allows us to explicitly compute these new state vectors. Moreover, we note that the extremization of these functionals is equivalent to directly solving Eqs. (5) and (6), where $|\psi_\alpha\rangle$ and $|\xi_{\alpha\beta}\rangle$ were first introduced.

Since we will be interested in 2D systems, the first step in our procedure is to confine our system within a disk of radius R . If the problem we are interested in is not naturally bounded, we can first force it to be defined inside a disk of finite radius, and later chose $R \gg 1$ and check the convergence of the results by varying R . This procedure is always possible as long as the wave functions vanish for a large enough distance away from the origin. After this is done we can expand $|\psi_\alpha\rangle$ and $|\xi_{\alpha\beta}\rangle$ in a Fourier-Bessel series with a normalized radial basis

$$j_{ln}(r) = \frac{\sqrt{2} J_l\left(\frac{z_{ln} r}{R}\right)}{J_{l+1}(z_{ln}) R}, \quad (12)$$

where $J_l(z)$ is the Bessel function of the first kind of l th order, z_{ln} corresponds to the n th zero of $J_l(z)$, and R is the radius of the disk where the problem is defined. In terms of this basis,

$$\begin{aligned} \psi_\alpha(\omega; \mathbf{r}) &= \frac{1}{\sqrt{2\pi}} \sum_{n=1}^N \sum_{l=\pm 1} c_{ln}^\alpha(\omega) j_{ln}(r) e^{il\theta} \\ &= \frac{1}{\sqrt{2\pi}} \sum_{n=1}^N [c_{+,n}^\alpha(\omega) e^{i\theta} - c_{-,n}^\alpha(\omega) e^{-i\theta}] j_{1n}(r) \end{aligned} \quad (13)$$

and

$$\xi_{\alpha\beta}(\omega_a, \omega_b; \mathbf{r}) = \frac{1}{\sqrt{2\pi}} \sum_{n=1}^N \sum_{l=-\infty}^{\infty} \zeta_{ln}^{\alpha\beta}(\omega_a, \omega_b) j_{ln}(r) e^{il\theta}, \quad (14)$$

where N is the number of functions in the radial basis, c_{ln}^α and $\zeta_{ln}^{\alpha\beta}$ are the expansion coefficients, and (r, θ) are polar coordinates. Although we choose to work with a Fourier-Bessel basis, other options could have been used, e.g., orthogonal polynomials or Sturmian functions. Now we insert these expressions in the definitions of \mathcal{J} and \mathcal{K} and minimize each functional with respect to the c_{ln}^α and $\zeta_{ln}^{\alpha\beta}$, respectively. Doing so we arrive at two linear system of equations whose solutions define the expansion coefficients. In Appendix A we give the detailed description of the necessary steps to obtain the linear system of equations, which is numerically well behaved and can be easily solved. Also discussed in Appendix A is the implication of the condition $\langle 0|\xi_{\alpha\beta}\rangle = 0$, which imposes a restriction on the coefficient $\zeta_{01}^{\alpha\beta}$, requiring special care when dealing with the term $l = 0$ in the functional \mathcal{K} .

B. The case of the circular well

Now, as a first application of the ideas presented so far, we will study the problem of a circular well. This study will allow for a concrete application of the general expressions previously derived, as well as gaining some intuition that will prove helpful when the excitonic problem is studied ahead.

Consider a particle with mass μ trapped inside a circular well of radius R . The Hamiltonian of such a system reads

$$H = -\frac{1}{2\mu} \nabla^2, \quad 0 \leq r/R < 1. \quad (15)$$

The eigenstates are given by

$$\psi_{nm}(r, \theta) = \frac{1}{\sqrt{2\pi}} j_{mn}(r) e^{im\theta}. \quad (16)$$

Following common practice, we label n as the principal quantum number and m as the angular quantum number. The energy spectrum reads

$$E_{nm} = \frac{1}{2\mu} \left(\frac{z_{mn}}{R} \right)^2. \quad (17)$$

The ground-state wave function is $\psi_{GS}(r) = j_{01}(r)/\sqrt{2\pi}$.

There are many nonlinear third-order optical processes [37]. To be definitive, let us now focus on a specific third-order nonlinear optical process. We will be interested in computing

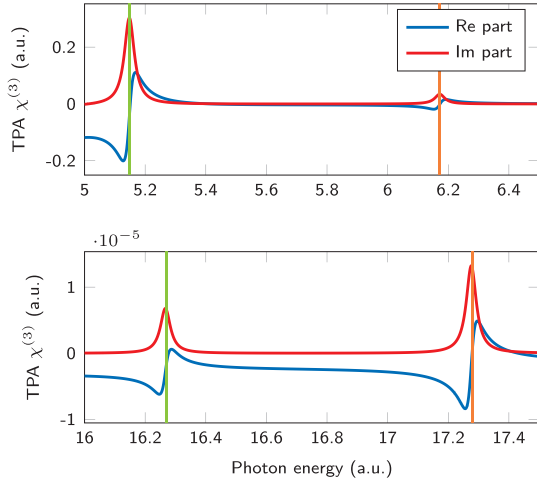


FIG. 2. Plot of the two-photon absorption (TPA) third-order susceptibility as a function of the photon energy for a particle with mass $\mu = 1$ in a circular well of radius $R = 1$. Both quantities are presented in atomic units (a.u.). The resonances marked with the orange lines correspond to transitions from the ground state ($1s$) to the states $2s$ and $3s$ with the absorption of two photons. The resonances marked with the green lines are associated with the transitions $1s \rightarrow 1d$ and $1s \rightarrow 2d$. A small imaginary shift was introduced in the photon frequency ω , that is, $\omega \rightarrow \omega + i\delta$ with $\delta = 0.02$ a.u. $N = 5$ basis functions were used.

the $xxxx$ component of the two photon absorption (TPA) third-order susceptibility $\chi_{xxxx}^{\text{TPA}}(\omega) = \chi_{xxxx}^{(3)}(-\omega; \omega, -\omega, \omega)$. Using Eq. (9) we write

$$\chi_{xxxx}^{\text{TPA}} = \frac{1}{3!} \mathcal{P} \{ -\langle \psi_x(-\omega^*) | \mathbf{d}_x | \xi_{xx}(-\omega, \omega) \rangle + \langle 0 | \mathbf{d}_x | \psi_x(-\omega) \rangle \langle \psi_x(-\omega^*) | \psi_x(\omega) \rangle \}. \quad (18)$$

To obtain the TPA spectrum we need only compute ψ_x and ξ_{xx} using the procedure discussed previously, and then evaluate three matrix elements. A detailed description of this is given in Appendix B. Considering $\mu = 1$ and $R = 1$, using $N = 5$ basis functions, and accounting for all the necessary permutations in Eq. (18), we obtain the results depicted in Fig. 2. This value of N already allows the results to converge; increasing it produces no change in the TPA spectrum. In order to obtain the real and imaginary parts of $\chi_{xxxx}^{\text{TPA}}(\omega)$ we introduced a small imaginary shift in the frequency ω , i.e., $\omega \rightarrow \omega + i\delta$. The resonances that appear in Fig. 2 have two distinct origins, the ones marked with the orange lines correspond to transitions from the ground state (which we call the $1s$ state) to other s states (where the angular quantum number is $m = 0$) with the absorption of two photons; the ones marked with the green lines are associated with transitions from the ground state to d states ($m = 2$), due to the absorption of two photons. As the principal quantum number of the final state increases, the oscillator strength of the transition decreases and the resonances become less pronounced. One of the main advantages of studying the circular well lies in its parabolic

energy spectrum [see Eq. (17)], since the energy levels are significantly separated, allowing for an effortless identification of the relevant optical transitions.

III. TWO-PHOTON ABSORPTION FOR EXCITONS IN WSe₂

In the current section we will discuss the interesting topic of 2D excitons in WSe₂. More accurately, we will study the third-order optical response associated with transitions from the ground state ($1s$) to excited states of the 2D exciton. This problem is the natural extension of the work done in [35] and the computed physical quantity can be measured experimentally in a pump-probe experiment.

The Hamiltonian that describes the excitonic problem reads

$$H_0 = -\frac{1}{2\mu} \nabla^2 + V_{\text{RK}}(r), \quad (19)$$

where μ is the reduced mass of the electron-hole pair, ∇^2 is the 2D Laplacian, and $V_{\text{RK}}(r)$ is the Rytova-Keldysh potential [38,39]

$$V_{\text{RK}} = -\frac{\pi}{2r_0} \left[\mathbf{H}_0 \left(\frac{\kappa r}{r_0} \right) - Y_0 \left(\frac{\kappa r}{r_0} \right) \right], \quad (20)$$

where κ is the mean dielectric constant of the media above and below the TMD, r_0 is an intrinsic parameter of the 2D material which can be interpreted as an in-plane screening length and is related to the effective thickness of the material, and \mathbf{H}_0 and Y_0 are the Struve function and the Bessel function of the second kind, both of order 0, respectively. This potential is the solution of the Poisson equation for a charge embedded in a thin film. For large distances the Rytova-Keldysh presents a Coulomb $-1/\kappa r$ tail, but diverges logarithmically near the origin.

Contrary to the circular well, or even the hydrogen atom, the 2D excitonic problem does not offer a simple analytical solution. In fact, computing the wave functions of the different excitonic states is an involved problem, where the wave functions are only known either numerically or semianalytically (where the wave functions can be computed analytically up to a set of numerical coefficients). In the present approach, perturbed wave functions are computed directly by expanding in a basis without the intermediate step of finding excited states. We have shown that in order to apply the formalism presented in Sec. II only the wave function of the exciton ground state is required. Finding this wave function is a considerably simpler task, and in order to work with an analytical expression we follow a variational approach. To obtain accurate results for the optical susceptibility, it is necessary to use an appropriate ground-state wave function. It is thus imperative that our variational ansatz produces an excellent description of the exact solution. A first proposal for the variational ansatz, inspired by the 2D hydrogen atom, could be a single exponential such as $\exp(-ar)$, where a is a variational parameter. Although this already produces a good description of the exact ground-state wave function, we turn to Ref. [33], where a more sophisticated double exponential ansatz was proposed:

$$\psi_{\text{GS}}(r) = \frac{1}{\sqrt{N}} (e^{-ar} + be^{-ayr}), \quad (21)$$

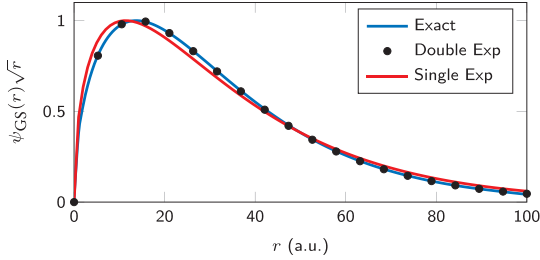


FIG. 3. Comparison between the excitonic ground-state wave function obtained exactly (using a shooting algorithm), and the ones obtained with the single and double variational ansatz. The values of the variational parameters were obtained from the minimization of the expected value of the Hamiltonian of Eq. (20). The values of Table I were used.

with a , b , and γ variational parameters and \mathcal{N} a normalization constant. As one can observe in Fig. 3, where the exact wave function is compared with the single and double exponential ansatz for excitons in WSe₂, Eq. (21) produces an outstanding description of the exact solution, the latter computed with a numerical shooting algorithm. As we have already noted in Sec. II, the domain of our problem should be enclosed within a disk of finite radius for numerical stability.

As in the case of the circular well, let us consider the $xxxx$ component of the TPA susceptibility associated with transitions from the $1s$ to the excited excitonic states. Its general expression was already given in Eq. (18). To evaluate the TPA spectrum we return once more to the problem of extremizing the \mathcal{J} and \mathcal{K} functionals (see Appendixes A and B). A difference relative to the circular well lies in the value of ζ_{01} . The orthogonality of Bessel functions on a disk implied that $\zeta_{01} = 0$ for the circular well. For the excitonic problem no simple rule applies, and the value of ζ_{01} must be determined from Eq. (A9).

Using the parameters given in Table I the TPA spectrum for WSe₂ on diamond was computed; its plot is depicted in Fig. 4. The value of R was chosen such that $\psi_{GS}(R) \approx 0$. A small value for the radius modifies the results due to the effect of the confinement, while a large value suppresses this effect with the cost of increased computational work. We found that $R = 2500$ allows an accurate description of the excitonic problem, while keeping the method efficient.

Analyzing Fig. 4 we observe a similar result to the one found for the circular well. In order to clearly identify the optical transitions behind each resonance we computed the energy of the different excitonic states using a shooting al-

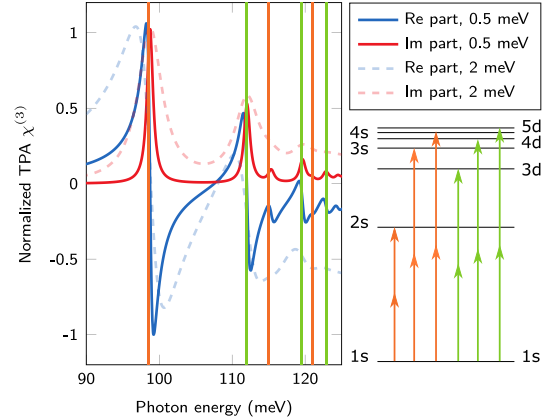


FIG. 4. Real and imaginary parts of the TPA susceptibility (normalized to its maximum value) for two different degrees of disorder (0.5 and 2 meV). The resonances correspond to transitions from the $1s$ to the $2s$, $3s$, and $4s$ states (marked in orange) and to the $3d$, $4d$, and $5d$ states (marked in green) with the absorption of two photons. A diagram of the optical transitions behind the resonances is also depicted.

gorithm, and from there the energies of the transitions from the $1s$ to other states were computed. This allowed us to assert that the resonances in Fig. 4 are due to transitions from the ground state ($1s$) to the $2s$, $3s$, and $4s$ states (marked in orange) and to the $3d$, $4d$, and $5d$ states (marked in green) with the absorption of two photons. Note, however, that computation of the binding energies is not necessary to identify the underlying transition behind each of the main resonances. This has been done here purely to demonstrate that the method provides physically accurate results. By recalling that the excitonic $1s$ state has no angular dependence, it is immediately clear from dipole induced transitions selection rules that the numerators in the definition of the susceptibility in Eq. (1) must be either of the form $\langle 1s | \dots | np \rangle \langle np | \dots | ms \rangle \langle ms | \dots | kp \rangle \langle kp | \dots | 1s \rangle$ or $\langle 1s | \dots | np \rangle \langle np | \dots | md \rangle \langle md | \dots | kp \rangle \langle kp | \dots | 1s \rangle$, with n , m , and k referring to the principal quantum numbers of the exciton state and s , p , and d labeling the angular dependence. Hence, from dipole selection rules, one already expects the appearance of the resonances associated with transitions from the $1s$ to other s and d states. Knowing this, the least energetic resonance in the relevant energy window could be assigned to the $1s \rightarrow 2s$ transition, as this lies clearly below the other ones; the next resonance could be ascribed to a $1s \rightarrow 3d$ transition, and so on. The identification of the optical transitions behind each resonance was also facilitated by the intuition gained by studying the circular well, where similar selection rules apply.

To obtain the real and imaginary parts of the TPA susceptibility a small imaginary part was included on the photon energy $\omega \rightarrow \omega + i\delta$, where the parameter δ phenomenologically parametrizes the broadening of the excitonic level. As expected, increasing the value of δ leads to broader and less intense resonances. For large values of δ a nonphysical shift of the resonance starts to appear, which is one of the main

TABLE I. Parameters used to compute the TPA spectrum due to intraexcitonic transition in WSe₂. All the quantities are given in atomic units. The values of μ , κ , and r_0 were taken from Ref. [27]. The value of R was chosen in order to have $\psi_{GS}(R) \approx 0$. The value of N allowed the results to converge.

μ	κ	r_0	R	N
0.167	3.32	51.9	2500	150

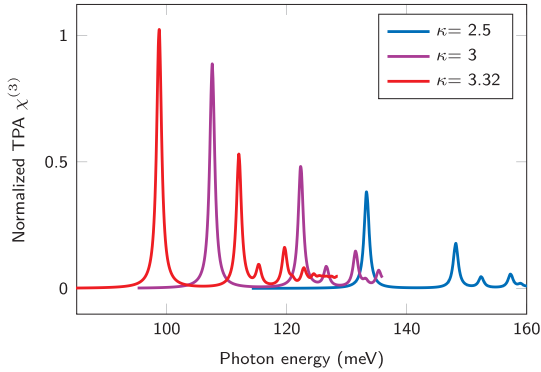


FIG. 5. Comparison of the TPA spectrum for three different dielectric environments, $\kappa = 3.32$ (TMD on diamond), $\kappa = 3$, and $\kappa = 2.5$ (TMD on quartz).

limitation of our approach. Currently it is possible to study this kind of system with a linewidth of about 20 meV for a sample on glass [40], and for encapsulated systems at low temperatures spectral broadening as low as 2 meV can be achieved [41]. From the results depicted in Fig. 4, where the maximum broadening is 2 meV, we expect that experimental measurements of the TPA performed on encapsulated systems should be able to clearly capture the resonances originated by the $1s \rightarrow 2s$, $1s \rightarrow 3d$, and $1s \rightarrow 3s$ transitions. In order to capture more resonances it is necessary to decrease the linewidth, or change the studied material to another where the excitonic resonances are further apart (such as hBN).

So far we have only discussed the case of WSe_2 on diamond. If other TMDs had been considered, such as MoS_2 , MoSe_2 , and WS_2 , the results would be qualitatively identical to the ones found for WSe_2 . This is so due to the similarities between the excitonic response of these systems. The main difference between the susceptibilities of these TMDs would be on the relevant energy window, since excitons have slightly different binding energies in each TMD as a result of the differences in the reduced mass μ and the screening parameter r_0 that enters in the Rytova-Keldysh potential. The linewidth of the resonances should also be expected to vary slightly from one TMD to another. Something which is also worth considering is the role of dielectric screening from the environment, characterized by the constant κ entering in the interaction potential. In Fig. 5 we study the role of the dielectric environment on the TPA spectrum of WSe_2 , by considering the experimentally relevant cases where WSe_2 is placed on diamond $\kappa = 3.32$ and on quartz $\kappa = 2.5$, as well as an intermediate case with $\kappa = 3$ (used just for reference). As the dielectric screening from the environment is reduced, that is, as κ decreases, the excitons become more tightly bound. As a consequence of the larger binding energy, the energy difference between the $1s$ and the excited excitonic states increases. This behavior is reflected in Fig. 5, where we observe a blueshift of the resonances as κ decreases. Moreover, one also sees from Fig. 5 that as the dielectric screening increases, the intensity of the resonances also increases. We identify this as a consequence of the larger spacial extension of the wave

functions when the dielectric screening increases resulting in larger dipole matrix elements.

Since the phenomena we are studying are experimentally accessed with pump-probe experiments, one crucial aspect to consider is the $1s$ exciton density. Initially, when the pump laser acts on the system, excitons quickly populate the $1s$ state. This population decreases with time as a result of different recombination processes, such as radiative or Auger recombination. Hence, in an experimental realization of such an experiment, the time delay between the application of the pump and probe lasers should play a significant role in the results, because of the decay of the $1s$ population. Furthermore, the exciton density is also of importance due to possible exciton-exciton interactions. When the exciton density is large, the overlap of the exciton wave functions may be significant, and as a consequence new phenomena, which we have not accounted for, should appear. Based on Ref. [27], where the $1s \rightarrow 2p$ transitions were studied, one should expect exciton-exciton interactions to lead to renormalization of the resonances as well as modifications in their linewidth. These effects should be increasingly more noticeable as the overlap of the exciton wave functions increases. Since the wave functions tend to be more extended in real space as the principal quantum number increases, one should expect resonances involving highly energetic excited states (for example, the $3d$ state and above) to suffer more from exciton-exciton interaction, than the resonances originated by transitions to the first excited states. This, however, should not be a too much of a problem, since the more energetic excited states lead to small oscillator strengths, and their resonances are hardly resolved in realistic experiments. A simple way of estimating the possible effect of the exciton-exciton interactions is to compare the exciton Bohr radius of the $1s$ state, easily obtained with the variational ansatz of Eq. (21), with the inverse square root of the exciton density (similarly to the Mott criterion). We stress that the Mott criterion should only be taken as a qualitative reference, since the picture of excitons as well-defined quasiparticles may already be compromised below the threshold it establishes. Nonetheless, this criterion should still be helpful to predict the relevance of exciton-exciton interactions.

IV. CONCLUSION

In this work, following the ideas of Refs. [28–32], we developed a method to study nonlinear third-order processes involving transitions from the $1s$ to excited excitonic states. The usual approach to this type of problem would require the knowledge of several excited states in order to compute the different matrix elements that appear in Eq. (1). The excited states wave functions are often computed by expanding them in a given basis, e.g., Bessel-Fourier, followed by the diagonalization of the Hamiltonian. This yields the sets of coefficients that define the wave functions of the different excited states, which can then be used to evaluate the many matrix elements in the sum over states. At odds with this procedure, our approach avoids the sum over states, and requires only three wave functions: the ground state wave function, which can be described using a variational ansatz with high accuracy (see Fig. 3); and two wave functions de-

fined by Eqs. (7) and (8) which we determined through an expansion in a Bessel-Fourier basis.

The main result of our work is the TPA spectrum which presents resonances associated with transitions from the $1s$ state to the remaining s states as well as from the $1s$ to the d states with the absorption of two photons. In high purity systems different resonances should be resolvable. However, in systems with a significant spectral broadening only the $1s \rightarrow 2s$ resonance should be identifiable. When the role of dielectric screening was studied, a blueshift of the resonances was observed with decreasing dielectric constant, in agreement with the increased exciton binding energy and higher energy separation between the ground state and the excited states. We focused on the case of excitons in WSe_2 , but other materials may easily be explored using the method.

Although we focused primarily on the $xxxx$ component of the TPA susceptibility, we presented general formulas capable of describing any third-order process. To do so one only needs to combine Eq. (9) with the discussion presented in Appendix A. However, most of the components are automatically zero since we are considering isotropic systems (all of those χ_{ijkl} with an odd number of x or y indexes vanish from symmetry). Also, since the x and y directions are equivalent, the $xxxx$ and $yyyy$ components are equivalent, as well as the $xyxy$ and $yyxx$, and so on. In the end we can reduce the number of components to the $xxxx$, $xyxy$, $xyyx$, and $xyxx$. When the last three components are summed, the first one should be recovered. Besides TMDs, other systems could also be studied with this method, such as quantum dots, quantum wells, and even bulk materials.

ACKNOWLEDGMENTS

N.M.R.P. acknowledges support by the Portuguese Foundation for Science and Technology (FCT) in the framework of the Strategic Funding UIDB/04650/2020. J.C.G.H. acknowledges the Center of Physics for a grant funded by the UIDB/04650/2020 strategic project and POCI-01-0145-FEDER-028887. N.M.R.P. acknowledges support from the European Commission through the project “Graphene-Driven Revolutions in ICT and Beyond” (Ref. No. 881603, CORE 3), COMPETE 2020, PORTUGAL 2020, FEDER, and the FCT through projects POCI-01-0145-FEDER-028114, PTDC/NAN-OPT/29265/2017. H.C.K. and T.G.P. gratefully acknowledge financial support by the Center for Nanostructured Graphene (CNG), which is sponsored by the Danish National Research Foundation, Project No. DNR103.

APPENDIX A: COMPUTING THE NEW STATE VECTORS

In this Appendix we will give a detailed description of how to obtain the linear systems whose solution defines the state vectors $|\psi_\alpha\rangle$ and $|\xi_{\alpha\beta}\rangle$. Let us consider the H_0 to be the unperturbed Hamiltonian of a given system which in general can be written as

$$H_0 = -\frac{1}{2\mu}\nabla^2 + V(r), \quad (\text{A1})$$

where the first term, with μ a mass term and ∇^2 the 2D Laplacian, corresponds to the kinetic energy, and $V(r)$ corresponds

to the potential energy. Here we consider a central potential for which the ground state may be expressed as $\psi_{\text{GS}}(\mathbf{r}) = R_{\text{GS}}(r)/\sqrt{2\pi}$. Inserting Eqs. (13) and (A1) into Eq. (10) one finds

$$\begin{aligned} \mathcal{J} = & \sum_{n=1}^N \sum_{l=\pm} c_{ln}^\alpha (c_{ln}^\alpha)^* \left[\frac{1}{2\mu} \left(\frac{z_{ln}}{R} \right)^2 - E_0 + \omega \right] \\ & + \sum_{n=1}^N \sum_{k=1}^N \sum_{l=\pm} c_{ln}^\alpha (c_{lk}^\alpha)^* \mathcal{V}_{kn}^{(l)} \\ & + \frac{1}{2} \sum_{n=1}^N \sum_{l=\pm} [(\delta_{\alpha,x} - i l \delta_{\alpha,y})(c_{ln}^\alpha)^* \mathcal{S}_n^{(l)} + \text{c.c.}], \quad (\text{A2}) \end{aligned}$$

where c.c. stands for complex conjugated and the following integrals were introduced:

$$\mathcal{V}_{kn}^{(l)} = \int_0^R j_{lk}(r) V(r) j_{ln}(r) r dr, \quad (\text{A3})$$

$$\mathcal{S}_n^{(l)} = \int_0^R j_{ln}(r) R_{\text{GS}}(r) r^2 dr. \quad (\text{A4})$$

The first one corresponds to the matrix elements of the potential between different basis functions, while the second one is proportional to dipole transitions between the ground state of the unperturbed system and the functions of the basis. Furthermore, we note that $\mathcal{V}_{kn}^{(l)}$ is symmetric, that is, $\mathcal{V}_{kn}^{(l)} = \mathcal{V}_{nk}^{(l)}$. We have omitted the argument of the coefficients c_{ln}^α to simplify the notation, however one should keep in mind that these are ω -dependent quantities.

Now, differentiating \mathcal{J} with respect to the coefficients $(c_{ln}^\alpha)^*$, we obtain a linear system of equations whose solution determines the coefficients themselves. In matrix notation the linear system reads

$$\mathbb{M}^{(l)}(\omega) \mathbf{c}_l^\alpha(\omega) = -\frac{1}{2}(\delta_{\alpha,x} - i l \delta_{\alpha,y}) \mathbf{S}^{(l)}, \quad l = \pm 1, \quad (\text{A5})$$

where

$$[\mathbb{M}^{(l)}(\omega)]_{ij} = \delta_{ij} g_j^{(l)}(\omega) + \mathcal{V}_{ij}^{(l)}, \quad (\text{A6})$$

with

$$g_j^{(l)}(\omega) = \frac{z_{lj}^2}{2\mu R^2} - E_0 + \omega, \quad (\text{A7})$$

and

$$[\mathbf{S}^{(l)}]^T = [\mathcal{S}_1^{(l)}, \mathcal{S}_2^{(l)}, \dots, \mathcal{S}_N^{(l)}],$$

$$[\mathbf{c}_l^\alpha(\omega)]^T = [c_{l1}^\alpha(\omega), c_{l2}^\alpha(\omega), \dots, c_{lN}^\alpha(\omega)].$$

Let us emphasize that to obtain the coefficients that define $|\psi_\alpha\rangle$ we need only compute the vector $\mathbf{S}^{(l)}$ and the matrix $\mathbb{M}^{(l)}$. The most expensive part of the numerical computation is the calculation of all the $\mathcal{V}_{ij}^{(l)}$. However, since $\mathcal{V}_{ij}^{(l)}$ is independent of ω this only needs to be computed once, regardless of the value of ω one wishes to use. The fact that $\mathcal{V}_{ij}^{(l)}$ is symmetric also greatly reduces the number of integrals that need to be evaluated. Finally, we point out that when $\alpha = x$ we have $c_{+,n}^x = -c_{-,n}^x$, since $\mathbb{M}^{(+)} = \mathbb{M}^{(-)}$ and $\mathbf{S}^{(+)} = -\mathbf{S}^{(-)}$. Following the same reasoning, when dealing with the y direction we have $c_{+,n}^y = c_{-,n}^y$, due to the term $i l \delta_{\alpha,y}$ which changes sign when l changes sign.

With the problem associated with the functional \mathcal{J} taken care of, let us move on to the functional \mathcal{K} . Once again we choose to work in a Fourier-Bessel basis. Now, let us recall that in the beginning, following Eq. (8), we assumed $\langle 0|\xi_{\alpha\beta}(\omega_a, \omega_b)\rangle = 0$. In order to satisfy this, we must have

$$\sum_{n=1}^N \zeta_{0n}^{\alpha\beta}(\omega_a, \omega_b) \int_0^R j_{0n}(r) R_{GS}(r) r dr = 0, \quad (\text{A8})$$

where all the remaining terms in the definition of $\xi_{\alpha\beta}$ are guaranteed to vanish from the angular integration, since for an isotropic system we have an isotropic ground-state wave function. This condition can be put in the equivalent form

$$\zeta_{01}^{\alpha\beta}(\omega_a, \omega_b) = - \sum_{n=2}^N \zeta_{0n}^{\alpha\beta}(\omega_a, \omega_b) f_n, \quad (\text{A9})$$

where

$$f_n = \frac{\int j_{0n}(r) R_{GS}(r) r dr}{\int j_{01}(r) R_{GS}(r) r dr}.$$

Thus, hereinafter, we no longer consider $\zeta_{01}^{\alpha\beta}$ as an independent variable, but rather as a parameter defined from the remaining $\zeta_{0n}^{\alpha\beta}$. Inserting Eq. (14) in Eq. (11), and once again using the definition for H_0 given in Eq. (A1), one finds after some algebra

$$\begin{aligned} \mathcal{K} = & \sum_{n=1}^N \sum_{l=-\infty}^{\infty} \zeta_{ln}^{\alpha\beta} [\zeta_{ln}^{\alpha\beta}]^* g_n^{(l)}(\omega_a + \omega_b) \\ & + \sum_{n,m=1}^N \sum_{l=-\infty}^{\infty} \zeta_{lm}^{\alpha\beta} [\zeta_{ln}^{\alpha\beta}]^* \mathcal{V}_{nm}^{(l)} \\ & + \frac{1}{2} \sum_{n,m=1}^N \sum_{s=\pm} \{ c_{sm}^{\alpha} [\zeta_{0n}^{\alpha\beta}]^* \mathcal{T}_{nm}^{(0,s)} (\delta_{\beta,x} + is\delta_{\beta,y}) \\ & + c_{sm}^{\alpha\beta} [\zeta_{s2,n}^{\alpha\beta}]^* \mathcal{T}_{nm}^{(s2,s)} (\delta_{\beta,x} - is\delta_{\beta,y}) + \text{c.c.} \}, \quad (\text{A10}) \end{aligned}$$

where c.c. stands for complex conjugated, $g_n^{(l)}$ and $\mathcal{V}_{nk}^{(l)}$ were defined in Eqs. (A7) and (A3), respectively, and we introduced

$$\mathcal{T}_{nm}^{(l,s)} = \int_0^R j_{ln}(r) j_{sm}(r) r^2 dr, \quad (\text{A11})$$

which is associated with the dipole transition amplitude between the functions of the basis. This integral has an analytical solution given by

$$\begin{aligned} \int_0^1 J_\nu(\alpha r) J_{\nu+1}(\beta r) r^2 dr = & \frac{\alpha J_{\nu+1}(\alpha)}{(\alpha^2 - \beta^2)^2} [-2\beta J_\nu(\beta) \\ & + (\alpha^2 - \beta^2) J_{\nu+1}(\beta)], \quad (\text{A12}) \end{aligned}$$

for any ν given that $J_\nu(\alpha) = 0$. When β is such that $J_{\nu+1}(\beta) = 0$ (which is our case) the last term vanishes. From Eq. (A11) we conclude that $\mathcal{T}_{nk}^{(l,s)}$ is not symmetric, since $\mathcal{T}_{nk}^{(l,s)} \neq \mathcal{T}_{kn}^{(l,s)}$. Since these integrals have analytical solutions, the lack of symmetry does not significantly impact the numerical efficiency of our approach. Once again, to simplify the notation, we have omitted the arguments of the coefficients c_{lm}^{α} and $\zeta_{ln}^{\alpha\beta}$.

With the functional \mathcal{K} in its current form we can differentiate it with respect to the $\zeta_{ln}^{\alpha\beta}$ and obtain a linear system in a

similar fashion to what was previously done for the functional \mathcal{J} . However, we should remember that in order to satisfy the relation $\langle 0|\xi_{\alpha\beta}(\omega_a, \omega_b)\rangle = 0$ the coefficient $\zeta_{01}^{\alpha\beta}$ must be treated with care, since according to Eq. (A9) it is a function of the remaining $\zeta_{0n}^{\alpha\beta}$. Thus, it is convenient to deal with the cases where $l = 0$ and $l \neq 0$ separately.

Starting with the $l = 0$ case, we substitute $\zeta_{0n}^{\alpha\beta}$ in Eq. (A10) by its definition, given in Eq. (A9), and differentiate the result with respect to the $(\zeta_{0n}^{\alpha\beta})^*$, with $n \geq 2$. Proceeding as described one finds the following linear system defining the coefficients $\zeta_{0n}^{\alpha\beta}$ with $n \geq 2$:

$$[\mathbb{F} + \mathbb{M}^{(0)}(\omega_a + \omega_b)] \cdot \zeta_0^{\alpha\beta}(\omega_a, \omega_b) = -\mathbf{W}_0^{\alpha\beta}(\omega_a) + \mathbf{f}_0^{\alpha\beta}(\omega_a), \quad (\text{A13})$$

where $\mathbb{M}^{(0)}(\omega_a + \omega_b)$ is defined as before, and

$$(\mathbb{F})_{ij} = [g_1^{(0)}(\omega_a + \omega_b) + \mathcal{V}_{11}^{(0)}] f_i f_j - \mathcal{V}_{i1}^{(0)} f_j - f_i \mathcal{V}_{1j}^{(0)}, \quad (\text{A14})$$

$$\mathbf{W}_0^{\alpha\beta} = \frac{1}{2} \sum_{s=\pm} (\delta_{\beta,x} + is\delta_{\beta,y}) \mathbb{T}^{(0,s)} \cdot \mathbf{c}_s^{\alpha}, \quad (\text{A15})$$

$$(\mathbf{f}_0^{\alpha\beta})_n = \frac{1}{2} f_n \sum_{m=1}^N \sum_{s=\pm} c_{sm}^{\alpha} \mathcal{T}_{lm}^{(0,s)} (\delta_{\beta,x} + is\delta_{\beta,y}), \quad (\text{A16})$$

with $(\mathbb{T}^{(0,s)})_{ij} = \mathcal{T}_{ij}^{(0,s)}$, and

$$[\zeta_0^{\alpha\beta}]^T = [\zeta_{02}^{\alpha\beta}, \zeta_{03}^{\alpha\beta}, \dots, \zeta_{0N}^{\alpha\beta}].$$

We note that the vectors $\zeta_0^{\alpha\beta}$, $\mathbf{W}_0^{\alpha\beta}$, and $\mathbf{f}_0^{\alpha\beta}$ are $(N-1) \times 1$; the vector \mathbf{c}_s^{α} is $N \times 1$; the matrices \mathbb{F} and $\mathbb{M}^{(0)}$ are $(N-1) \times (N-1)$, and the matrix $\mathbb{T}^{(0,s)}$ is $(N-1) \times N$. The solution of this system gives the $\zeta_{0n}^{\alpha\beta}$ with $n \geq 2$, from which the value of $\zeta_{01}^{\alpha\beta}$ can be computed.

Having dealt with the delicate case of $l = 0$ we can now study the contributions originating from the cases where $l \neq 0$. Since no restrictions are imposed on coefficients with $l \neq 0$ this is a simpler problem. Returning to Eq. (A10), and differentiating \mathcal{K} with respect to the $(\zeta_{ln}^{\alpha\beta})^*$, with $n \geq 1$ and $l \neq 0$, one finds

$$\mathbb{M}^{(l)}(\omega_a + \omega_b) \cdot \zeta_l^{\alpha\beta}(\omega_a, \omega_b) = -\mathbf{W}_l^{\alpha\beta}(\omega_a), \quad l \neq 0, \quad (\text{A17})$$

where $\mathbb{M}^{(l)}$ and $\zeta_l^{\alpha\beta}$ are defined as before, only this time they are $N \times N$ and $N \times 1$, respectively. The definition of $\mathbf{W}_l^{\alpha\beta}(\omega_a)$ reads

$$\begin{aligned} \mathbf{W}_l^{\alpha\beta}(\omega_a) = & \frac{1}{2} \delta_{l,2} (\delta_{\beta,x} - i\delta_{\beta,y}) \mathbb{T}^{(2,1)} \cdot \mathbf{c}_+^{\alpha}(\omega_a) \\ & - \frac{1}{2} \delta_{l,-2} (\delta_{\beta,x} + i\delta_{\beta,y}) \mathbb{T}^{(2,1)} \cdot \mathbf{c}_-^{\alpha}(\omega_a), \quad l \neq 0. \quad (\text{A18}) \end{aligned}$$

This linear system is numerically well behaved and, therefore, can be solved with any linear-algebra numerical package. Its

solution gives the coefficients $\zeta_l^{\alpha\beta}$, with $l \neq 0$, necessary to compute $|\xi_{\alpha\beta}\rangle$. Comparing Eq. (A17) with Eq. (A13), we observe that their structure is very much alike, the only difference being the appearance of $\mathbf{f}_0^{\alpha\beta}$ and \mathbb{F} in Eq. (A13). These two terms have their origin on the restriction imposed by the condition $\langle 0|\xi_{\alpha\beta}(\omega_a, \omega_b)\rangle = 0$, and thus do not appear in Eq. (A17). For both cases where $l = 0$ and $l \neq 0$, it is necessary to first solve the problem associated with the functional \mathcal{J} in order to obtain the coefficients $\mathbf{c}_l^{\alpha}(\omega_a)$. Moreover, it is clear that the terms with $l = \pm 2$ play a distinct role in the problem. In fact, the only relevant terms are the ones with $l = 0, \pm 2$, since only they yield finite matrix elements when the susceptibility is computed. Terms with different values of l vanish when the angular part of the matrix elements is calculated. Finally, we note that since $\mathbb{M}^{(2)} = \mathbb{M}^{(-2)}$ and $\mathbf{W}_2^{\alpha\beta} = \mathbf{W}_{-2}^{\alpha\beta}$ when $\alpha = \beta$, we have $\zeta_2^{\alpha\beta} = \zeta_{-2}^{\alpha\beta}$ when $\alpha = \beta$. If $\alpha \neq \beta$, then $\zeta_2^{\alpha\beta} = -\zeta_{-2}^{\alpha\beta}$.

APPENDIX B: DETAILS ON THE CIRCULAR WELL PROBLEM

In this Appendix we give a detailed description of the necessary calculations to compute the TPA of the circular well. We start by writing the wave function $\psi_x(\omega, \mathbf{r})$ as

$$\psi_x(\omega, \mathbf{r}) = \sqrt{\frac{2}{\pi}} \sum_{n=1}^N c_{+,n}^x(\omega) j_{1n}(r) \cos \theta, \quad (\text{B1})$$

where we used the fact that $c_{+,n}^x = -c_{-,n}^x$ (see Appendix A). Regarding the wave function $\xi_{xx}(\omega_1, \omega_2; \mathbf{r})$, and using Eq. (14), we obtain

$$\begin{aligned} \xi_{xx}(\omega_1, \omega_2; \mathbf{r}) = & \frac{1}{\sqrt{2\pi}} \sum_{n=1}^N \{ \zeta_{0n}^{xx}(\omega_1, \omega_2) j_{0n}(r) \\ & + 2\zeta_{2n}^{xx}(\omega_1, \omega_2) j_{2n}(r) \cos 2\theta \}, \end{aligned} \quad (\text{B2})$$

where the relation $\zeta_{2n}^{xx} = \zeta_{-2n}^{xx}$ was used (see Appendix A). To obtain $\chi_{xxxx}^{\text{TPA}}(\omega)$ we have to compute three different types of matrix elements, which can be written in a fairly compact form using Eqs. (B1) and (B2):

$$\langle \psi_x(\omega_2^*) | \psi_x(\omega_1) \rangle = \sum_{n=1}^N c_{+,n}^x(\omega_2^*)^* c_{+,n}^x(\omega_1), \quad (\text{B3})$$

$$\langle 0 | \mathbf{d}_x | \psi_x(\omega_1) \rangle = \mathbf{c}_+^x(\omega_1) \cdot \mathbf{S}^{(+)}, \quad (\text{B4})$$

$$\begin{aligned} & \langle \psi_x(\omega_1^*) | \mathbf{d}_x | \xi_{xx}(\omega_2, \omega_3) \rangle \\ &= ([\zeta_0^{xx}(\omega_2, \omega_3)]^T \cdot \mathbb{T}^{(0,1)} \\ &+ [\zeta_2^{xx}(\omega_2, \omega_3)]^T \cdot \mathbb{T}^{(2,1)}) \cdot \mathbf{c}_+^x(\omega_1^*)^*, \end{aligned} \quad (\text{B5})$$

where the vector $\mathbf{S}^{(+)}$ and the matrices \mathbb{T} were first introduced when the functionals \mathcal{J} and \mathcal{K} were studied. The fact that these only need to be computed once, but appear in different instances of the calculation contributes to the simplicity and efficiency of the approach.

The only thing left to do is to compute all the necessary coefficients \mathbf{c}_+^x , ζ_{0n}^{xx} , and ζ_{2n}^{xx} . Since inside the disk where the problem is defined the potential vanishes, all the terms containing $\mathcal{V}_{nk}^{(l)}$ disappear; this significantly simplifies the computation of the coefficients. The \mathbf{c}_+^x are given by

$$[\mathbf{c}_+^x(\omega)]_j = -\frac{1}{2g_j^{(+)}(\omega)} [\mathbf{S}^{(+)}]_j, \quad 1 \leq j \leq N. \quad (\text{B6})$$

It is easily verified that these coefficients quickly approach zero even for modest values of N . This is a direct consequence of the fast decay of $\mathcal{S}_j^{(+)}$ as j increases. To compute the ζ_{0n}^{xx} the first thing to note is that for the circular disk, where the ground-state wave function is proportional to the Bessel function $J_0(z_{01}r/R)$, all the f_j vanish, due to the orthogonality relation of Bessel functions on a disk. As a consequence, $\zeta_{01}^{xx} = 0$. The remaining ζ_{0n}^{xx} follow from

$$\zeta_0^{xx}(\omega_a, \omega_b) = -[\mathbb{M}^{(0)}(\omega_a + \omega_b)]^{-1} \cdot \mathbb{T}^{(0,1)} \cdot \mathbf{c}_+^x(\omega_a), \quad (\text{B7})$$

where ζ_0^{xx} is a $(N-1) \times 1$ vector. This becomes a $N \times 1$ vector once the value of $\zeta_{01}^{xx} = 0$ is introduced. The inverse of the matrix $\mathbb{M}^{(0)}$ is simply given by $[\mathbb{M}^{(0)}]_j^{-1} = 1/g_j^{(0)}$. Finally, to compute the ζ_{2n}^{xx} one uses

$$\zeta_2^{xx}(\omega_a, \omega_b) = -\frac{1}{2} [\mathbb{M}^{(2)}(\omega_a + \omega_b)]^{-1} \cdot \mathbb{T}^{(2,1)} \cdot \mathbf{c}_+^x(\omega_a), \quad (\text{B8})$$

where $[\mathbb{M}^{(2)}]_j^{-1} = 1/g_j^{(2)}$. The fast convergence of the \mathbf{c}_+^x aides the convergence of the various ζ^{xx} coefficients.

- [1] K. S. Novoselov, V. Fal, L. Colombo, P. Gellert, M. Schwab, and K. Kim, A roadmap for graphene, *Nature (London)* **490**, 192 (2012).
- [2] J. D. Caldwell, I. Aharonovich, G. Cassabois, J. H. Edgar, B. Gil, and D. N. Basov, Photonics with hexagonal boron nitride, *Nat. Rev. Mater.* **4**, 552 (2019).
- [3] A. Carvalho, M. Wang, X. Zhu, A. S. Rodin, H. Su, and A. H. C. Neto, Phosphorene: From theory to applications, *Nat. Rev. Mater.* **1**, 16061 (2016).
- [4] Q. H. Wang, K. Kalantar-Zadeh, A. Kis, J. N. Coleman, and M. S. Strano, Electronics and optoelectronics of

two-dimensional transition metal dichalcogenides, *Nat. Nanotechnol.* **7**, 699 (2012).

- [5] K. F. Mak, C. Lee, J. Hone, J. Shan, and T. F. Heinz, Atomically Thin MoS₂: A New Direct-Gap Semiconductor, *Phys. Rev. Lett.* **105**, 136805 (2010).
- [6] G. Wang, A. Chernikov, M. M. Glazov, T. F. Heinz, X. Marie, T. Amand, and B. Urbaszek, Colloquium: Excitons in atomically thin transition metal dichalcogenides, *Rev. Mod. Phys.* **90**, 021001 (2018).
- [7] W.-T. Hsu, J. Quan, C.-Y. Wang, L.-S. Lu, M. Campbell, W.-H. Chang, L.-J. Li, X. Li, and C.-K. Shih, Dielectric impact on

- exciton binding energy and quasiparticle bandgap in monolayer WS_2 and WSe_2 , *2D Mater.* **6**, 025028 (2019).
- [8] A. Chernikov, T. C. Berkelbach, H. M. Hill, A. Rigosi, Y. Li, O. B. Aslan, D. R. Reichman, M. S. Hybertsen, and T. F. Heinz, Exciton Binding Energy and Nonhydrogenic Rydberg Series in Monolayer WS_2 , *Phys. Rev. Lett.* **113**, 076802 (2014).
 - [9] M. Koperski, M. R. Molas, A. Arora, K. Nogajewski, A. O. Slobodeniuk, C. Faugeras, and M. Potemski, Optical properties of atomically thin transition metal dichalcogenides: Observations and puzzles, *Nanophotonics* **6**, 1289 (2017).
 - [10] R. Wang, H.-C. Chien, J. Kumar, N. Kumar, H.-Y. Chiu, and H. Zhao, Third-harmonic generation in ultrathin films of MoS_2 , *ACS Appl. Mater. Interfaces* **6**, 314 (2014).
 - [11] D. B. S. Soh, C. Rogers, D. J. Gray, E. Chatterjee, and H. Mabuchi, Optical nonlinearities of excitons in monolayer MoS_2 , *Phys. Rev. B* **97**, 165111 (2018).
 - [12] A. Syntjoki, L. Karvonen, H. Rostami, A. Autere, S. Mehravar, A. Lombardo, R. A. Norwood, T. Hasan, N. Peyghambarian, H. Lipsanen, and K. Kieu, Ultra-strong nonlinear optical processes and trigonal warping in MoS_2 layers, *Nat. Commun.* **8**, 893 (2017).
 - [13] Y. Li, Y. Rao, K. F. Mak, Y. You, S. Wang, C. R. Dean, and T. F. Heinz, Probing symmetry properties of few-layer MoS_2 and h-BN by optical second-harmonic generation, *Nano Lett.* **13**, 3329 (2013).
 - [14] C. Torres-Torres, N. Perea-Lpez, A. L. Elas, H. R. Gutirrez, D. A. Cullen, A. Berkdemir, F. Lpez-Uras, H. Terrones, and M. Terrones, Third order nonlinear optical response exhibited by mono-and few-layers of WS_2 , *2D Mater.* **3**, 021005 (2016).
 - [15] C. Janisch, Y. Wang, D. Ma, N. Mehta, A. L. Elas, N. Perea-Lpez, M. Terrones, V. Crespi, and Z. Liu, Extraordinary second harmonic generation in tungsten disulfide monolayers, *Sci. Rep.* **4**, 5530 (2014).
 - [16] H. G. Rosa, Y. W. Ho, I. Verzhbitskiy, M. J. F. L. Rodrigues, T. Taniguchi, K. Watanabe, G. Eda, V. M. Pereira, and J. C. V. Gomes, Characterization of the second- and third-harmonic optical susceptibilities of atomically thin tungsten diselenide, *Sci. Rep.* **8**, 10035 (2018).
 - [17] H. Zeng, G. B. Liu, J. Dai, Y. Yan, B. Zhu, R. He, L. Xie, S. Xu, X. Chen, W. Yao, and X. Cui, Optical signature of symmetry variations and spin-valley coupling in atomically thin tungsten dichalcogenides, *Sci. Rep.* **3**, 1608 (2013).
 - [18] A. Autere, H. Jussila, A. Marini, J. R. M. Saavedra, Y. Dai, A. Syntjoki, L. Karvonen, H. Yang, B. Amirsolaimani, R. A. Norwood *et al.*, Optical harmonic generation in monolayer group-VI transition metal dichalcogenides, *Phys. Rev. B* **98**, 115426 (2018).
 - [19] J. Liang, H. Ma, J. Wang, X. Zhou, W. Yu, C. Ma, M. Wu, P. Gao, K. Liu, and D. Yu, Giant pattern evolution in third-harmonic generation of strained monolayer WS_2 at two-photon excitonic resonance, *Nano Res.* **13**, 3235 (2020).
 - [20] M. Sukharev and R. Pachter, Effects of exciton-plasmon strong coupling on third harmonic generation by two-dimensional WS_2 at periodic plasmonic interfaces, *J. Chem. Phys.* **148**, 094701 (2018).
 - [21] A. Taghizadeh and T. G. Pedersen, Nonlinear optical selection rules of excitons in monolayer transition metal dichalcogenides, *Phys. Rev. B* **99**, 235433 (2019).
 - [22] A. Autere, H. Jussila, Y. Dai, Y. Wang, H. Lipsanen, and Z. Sun, Nonlinear optics with 2D layered materials, *Adv. Mater.* **30**, 1705963 (2018).
 - [23] Z. Sun, A. Martinez, and F. Wang, Optical modulators with 2D layered materials, *Nat. Photon.* **10**, 227 (2016).
 - [24] G. Wang, S. Zhang, X. Zhang, L. Zhang, Y. Cheng, D. Fox, H. Zhang, J. N. Coleman, W. J. Blau, and J. Wang, Tunable nonlinear refractive index of two-dimensional MoS_2 , WS_2 , and MoSe_2 nanosheet dispersions, *Photon. Res.* **3**, A51 (2015).
 - [25] L. Karvonen, A. Syntjoki, M. J. Huttunen, A. Autere, B. Amirsolaimani, S. Li, R. A. Norwood, N. Peyghambarian, H. Lipsanen, G. Eda, and K. Kieu, Rapid visualization of grain boundaries in monolayer MoS_2 by multiphoton microscopy, *Nat. Commun.* **8**, 15714 (2017).
 - [26] A. Autere, C. R. Ryder, A. Saynatjoki, L. Karvonen, B. Amirsolaimani, R. A. Norwood, N. Peyghambarian, K. Kieu, H. Lipsanen, M. C. Hersam *et al.*, Rapid and large-area characterization of exfoliated black phosphorus using third-harmonic generation microscopy, *J. Phys. Chem. Lett.* **8**, 1343 (2017).
 - [27] C. Pllmann, P. Steinleitner, U. Leierseder, P. Nagler, G. Plechinger, M. Porer, R. Bratschitsch, C. Schller, T. Korn, and R. Huber, Resonant internal quantum transitions and femtosecond radiative decay of excitons in monolayer WSe_2 , *Nat. Mater.* **14**, 889 (2015).
 - [28] M. Karplus and H. Kolker, A variation-perturbation approach to the interaction of radiation with atoms and molecules, *J. Chem. Phys.* **39**, 1493 (1963).
 - [29] H. F. Hamerka and E. N. Svendsen, A variational method for calculating dynamic polarizabilities, *Int. J. Quantum Chem.* **11**, 129 (1977).
 - [30] E. N. Svendsen and T. Stroyer-Hansen, Calculation of polarizabilities by the CNDO method, *Theor. Chim. Acta* **45**, 53 (1977).
 - [31] E. N. Svendsen, C. Willand, and A. Albrecht, Variational calculation of dynamic second-order susceptibilities, *J. Chem. Phys.* **83**, 5760 (1985).
 - [32] E. N. Svendsen, A variational method for calculation of dynamic third-order susceptibilities, *Int. J. Quantum Chem.* **34**, 477 (1988).
 - [33] T. G. Pedersen, Exciton stark shift and electroabsorption in monolayer transition-metal dichalcogenides, *Phys. Rev. B* **94**, 125424 (2016).
 - [34] M. F. C. M. Quintela and N. M. R. Peres, A colloquium on the variational method applied to excitons in 2D materials, *Eur. Phys. J. B* **93**, 222 (2020).
 - [35] J. C. G. Henriques, M. F. C. Quintela, and N. M. R. Peres, Microscopic theory of the polarizability of transition metal dichalcogenides excitons: Application to WSe_2 , *arXiv:2012.03335*.
 - [36] B. Orr and J. Ward, Perturbation theory of the non-linear optical polarization of an isolated system, *Mol. Phys.* **20**, 513 (1971).
 - [37] R. W. Boyd, *Nonlinear Optics* (Academic Press, New York, 2020).
 - [38] N. S. Rytova, The screened potential of a point charge in a thin film, *Moscow Univ. Phys. Bull.* **22**, 3 (1967).
 - [39] L. V. Keldysh, Coulomb interaction in thin semiconductor and semimetal films, *Sov. J. Exp. Theor. Phys. Lett.* **29**, 658 (1979).

- [40] S. Koirala, S. Mouri, Y. Miyauchi, and K. Matsuda, Homogeneous linewidth broadening and exciton dephasing mechanism in MoTe_2 , [Phys. Rev. B **93**, 075411 \(2016\)](#).
- [41] C. Robert, M. A. Semina, F. Cadiz, M. Manca, E. Courtade, T. Taniguchi, K. Watanabe, H. Cai, S. Tongay, B. Lassagne, P. Renucci, T. Amand, X. Marie, M. M. Glazov, and B. Urbaszek, Optical spectroscopy of excited exciton states in MoS_2 monolayers in van der Waals heterostructures, [Phys. Rev. Materials **2**, 011001\(R\) \(2018\)](#).




Paper G

Efficient ionization of two-dimensional excitons by
intense single-cycle terahertz pulses

Høgne C. Kamban and Thomas G. Pedersen

This paper has been published in Physical Review B:
Phys. Rev. B **104**, 235305 (2021)
DOI: 10.1103/physrevb.104.235305

Efficient ionization of two-dimensional excitons by intense single-cycle terahertz pulses

Høgner C. Kamban ^{*} and Thomas G. Pedersen *Department of Materials and Production, Aalborg University, DK-9220 Aalborg Øst, Denmark
and Center for Nanostructured Graphene (CNG), DK-9220 Aalborg Øst, Denmark* (Received 12 August 2021; revised 6 December 2021; accepted 7 December 2021; published 20 December 2021)

External electric fields are highly attractive for dynamical manipulation of excitons in two-dimensional materials. Here, we theoretically study the ionization of excitons in monolayer transition metal dichalcogenides (TMDs) by intense pulsed electric fields in the terahertz (THz) regime. We find that THz pulses with realistic field strengths are capable of ionizing a significant fraction of photogenerated excitons in TMDs into free charge carriers. Short THz pulses are therefore an efficient, noninvasive method of dynamically controlling the free carrier concentration in monolayer TMDs, which is useful for applications such as THz modulators. We further demonstrate that exciton ionization probabilities should be experimentally measurable by comparing free carrier absorption before and after the THz pulse. Detailed results are provided for different TMDs in various dielectric environments.

DOI: [10.1103/PhysRevB.104.235305](https://doi.org/10.1103/PhysRevB.104.235305)

I. INTRODUCTION

Monolayer transition metal dichalcogenides (TMDs) are exciting materials for optoelectronic applications [1,2]. They are promising components in applications such as photodetectors [3–5], THz modulators [6,7], and solar cells [8,9], where they can absorb up to 5–10% of incident sunlight in a thickness less than 1 nm [8]. One of the most important characteristics of monolayer TMDs is the strongly bound excitons that form due to confinement and reduced screening in two-dimensional (2D) materials [10–12]. The optical properties of 2D materials are completely dominated by these excitons [10,13–15], and methods of manipulating them are therefore highly sought after. These methods may be as simple as altering the structural design of the device components by controlling, e.g., substrate screening. However, a major disadvantage with these approaches is that the properties are fixed once the components have been constructed. A more attractive option is therefore to control the properties using external fields that may be switched on or off at will and thereby obtain dynamic control of the material properties.

In recent years, interest in applying static in-plane electric fields to excitons in TMD monolayers, multilayers, and van der Waals heterostructures has been increasing [16–22]. This process induces excitons to ionize into free electrons and holes. Recently, this was observed in photocurrent measurements on WSe₂ [18]. The authors of Ref. [18] found an increase in the photoresponse rate as a function of field strength that was well explained by exciton ionization. However, to apply the electric field, the authors of Ref. [18] incorporated buried electrical contacts with a tiny gap into their TMD sample. This is by no means a trivial task, as it involves making complicated modifications to the sample.

Consequently, static electric fields become less attractive as a means of manipulating excitons.

With the rapid progression of THz technology, it is natural to ask how efficient pulsed THz electric fields are at inducing exciton ionization. A significant advantage of using THz pulses rather than static fields for this purpose is that no modifications need to be made to the sample. Whereas THz induced ionization of atoms in gaseous samples is typically measured by counting the number of ions produced during the pulse [23,24], the solid-state equivalent is typically discussed in electroabsorption experiments [25–27]. In these experiments, the absorption spectrum of a sample is measured in the presence of an electric field. In this case, one finds a shift and broadening of the exciton absorption peaks that depend on the strength of the electric field. The shift is well explained by the exciton Stark effect [17,28–30], while the broadening is commonly attributed to the reduced exciton lifetime due to field-induced exciton ionization [26,31,32]. However, detailed interpretations of recent electroabsorption experiments on both monolayer MoS₂ [33] and carbon nanotubes [34] reveal that exciton ionization is not the dominating contribution to this broadening. The authors of Refs. [33,34] base their arguments on the fact that the measured broadening is proportional to the square of the electric field strength, which is not predicted by exciton ionization [18,20]. The apparent contradiction is resolved by noting that the contribution to the broadening by exciton ionization alone [16,18,20] is much lower than the field-induced phonon contribution [33]. As a result, it is very difficult to measure exciton ionization rates in electroabsorption experiments.

In the present paper, we theoretically study exciton ionization in two-dimensional TMDs induced by intense single-cycle THz pulses. We find that nearly all ionization occurs within a very short time interval near the peak field strength of the THz pulse. For the longest pulse duration considered here, this ionization interval is about 0.5 ps, which

^{*}hck@mp.aau.dk

is much shorter than the typical field-free exciton lifetimes of a few to hundreds of picoseconds in the popular TMDs WS₂ [35], WSe₂ [18,36,37], and MoS₂ [38,39]. We further show that a THz pulse with realistic field strength is capable of transforming a considerable portion of photogenerated excitons into free charge carriers in monolayer TMDs. This process happens over just a few picoseconds and therefore suggests that THz pulses are remarkably efficient for obtaining dynamic control over the number of free charge carriers, which is highly relevant for applications such as THz modulators [6,7]. Additionally, such a substantial change in the number of free charge carriers should be measurable in the free carrier absorption of a sample, or by collection via biased contacts, providing a direct method of estimating the exciton ionization probabilities in experiments. Our analysis clearly demonstrates that THz ionization of excitons in two-dimensional materials is feasible, and we provide quantitative estimates of the yield. To the best of our knowledge, previous works do not consider these phenomena and we hope our results will inspire attempts at experimental verification.

II. SIMULATION DETAILS

Within the two-band, effective mass approximation, excitons in a 2D TMD may be described by the two-dimensional Wannier equation [40,41], which has been shown to accurately reproduce exciton binding energies computed by more numerically demanding methods in various 2D materials [42–44]. In terms of the relative exciton coordinate $\mathbf{r} = \mathbf{r}_e - \mathbf{r}_h$, it reads (atomic units are used throughout)

$$\left[-\frac{1}{2\mu} \nabla^2 + V(\mathbf{r}) \right] \varphi_{mn}(\mathbf{r}) = E_{mn} \varphi_{mn}(\mathbf{r}), \quad (1)$$

where μ is the reduced exciton mass, V the interaction potential, and m and n denote the angular and principle quantum number, respectively. Due to cylindrical symmetry, angular momentum is a good quantum number in the Wannier model in the unperturbed case. In the present paper, we are interested in TMDs surrounded by in-plane isotropic media with dielectric tensor $\epsilon_{a/b} = \text{diag}(\epsilon_x^{(a/b)}, \epsilon_x^{(a/b)}, \epsilon_z^{(a/b)})$ above (a) and below (b) the sheet, respectively. The dielectric function of the encapsulated TMD may be approximated by a linearized form $\epsilon(\mathbf{q}) = \kappa + r_0 q$, where \mathbf{q} is the momentum space coordinate, $\kappa = (\sqrt{\epsilon_x^{(a)} \epsilon_z^{(a)}} + \sqrt{\epsilon_x^{(b)} \epsilon_z^{(b)}})/2$ is the average dielectric constant between the sub- and superstrate [45,46], and the screening length r_0 is related to the polarizability of the TMD monolayer by $r_0 = 2\pi\alpha_{2D}$ [45,47]. In this case, V is given by the Rytova-Keldysh form [45,46,48,49]

$$V(\mathbf{r}) = -\frac{\pi}{2r_0} \left[H_0\left(\frac{\kappa r}{r_0}\right) - Y_0\left(\frac{\kappa r}{r_0}\right) \right], \quad (2)$$

where H_0 is the zeroth order Struve function and Y_0 the zeroth order Bessel function of the second kind [50]. We use the experimentally verified values for μ and r_0 from Ref. [51]. Additionally, when hBN surroundings are considered, we use the values for κ found in Ref. [51].

To study exciton ionization induced by THz pulses, a time-dependent dipole field term is included in the Wannier equation. We have obtained a trace of the experimental THz pulse used in Ref. [33], and the shape of the pulse used

throughout the present paper is based on this experimental pulse to ensure realistic simulations. It should be noted that this is only one of many possible pulse shapes. For instance, one could imagine using chirped pulses with a frequency content designed to ionize excitons through a sequence of transiently occupied excited states as an alternative. For performing computations, we assume that only the excitonic ground state is occupied initially and then let the wave function $\psi(t)$ evolve in time. The ionization probability P_{ion} is computed by subtracting the total occupation probability of all bound states P_{BS} from unity, i.e., $P_{\text{ion}}(t) = 1 - P_{\text{BS}}(t)$ where $P_{\text{BS}}(t) = \sum_b P_b(t)$. The bound states φ_b are the states with energy less than zero, and their occupation probabilities are given by $P_b = |\langle \varphi_b | \psi(t) \rangle|^2$. In order to get accurate ionization probabilities, we begin by studying excitons with an infinite field-free lifetime. That is, the only exciton removal mechanism is field-induced ionization. Note that the figures show the accumulated probability in contrast to the time resolved ionization rate, which roughly follows the pulse shape and, therefore, dies out after the pulse subsides. In Sec. IV, other mechanisms required for a realistic dynamical model will be included. In particular, excitons may reform from free carriers leading to re-establishment of equilibrium exciton concentrations after the THz pulse. Numerical computations are made feasible by forcing the wave functions to zero outside a large radius and external complex scaling is used to avoid spurious reflections from the boundary [20,52,53]. Further computational details may be found in Appendix A.

Figure 1(a) shows a schematic illustration of the exciton dynamics during the THz pulse. It may be divided into three temporal regions: (i) The exciton is initially in its unperturbed ground state. (ii) When the pulse is close to its peak field strength, the electron and hole are pulled in opposite directions. It is in this region that the vast majority of ionization occurs [54]. (iii) As the pulse subsides, the exciton has probabilities P_{ion} and $1 - P_{\text{ion}}$ of being in an ionized and bound state, respectively. Traces of the experimental and fitted THz pulses used in the simulations are shown in Fig. 1(b). Here, the black circles represent the experimental THz pulse obtained from the authors of Ref. [33]. To ensure easy reproducibility of the results, we introduce a fitted pulse with a simple functional form. This pulse is represented by the red line in Fig. 1(b), and it is justified by noting that the results obtained using both pulses are in excellent agreement. A simple functional form also has the advantage of making simulation of time propagation easier. The functional form is motivated by Ref. [55] and is given by $\mathcal{E}(t) = -\frac{\partial A(t)}{\partial t}$, where the vector potential reads

$$A(t) = -\frac{\mathcal{E}_0 \tau}{c} \exp \left\{ \left[\frac{1}{a} \tanh\left(\frac{bt}{\tau}\right) - 5^2 \right] \frac{t^2}{\tau^2} \right\}. \quad (3)$$

Here, \mathcal{E}_0 is the peak field strength, and a and b dictate the shape of the pulse. In the present paper, we choose $a = 0.12$ and $b = 3$ to accurately reproduce the main features of the experimental pulse. The coefficient c is chosen such that the peak field strength becomes \mathcal{E}_0 . We define the pulse duration to be from the moment it reaches 1% of its peak field strength to the moment it again reduces to 1% as it subsides. This duration is approximately τ . To approximate the experimental

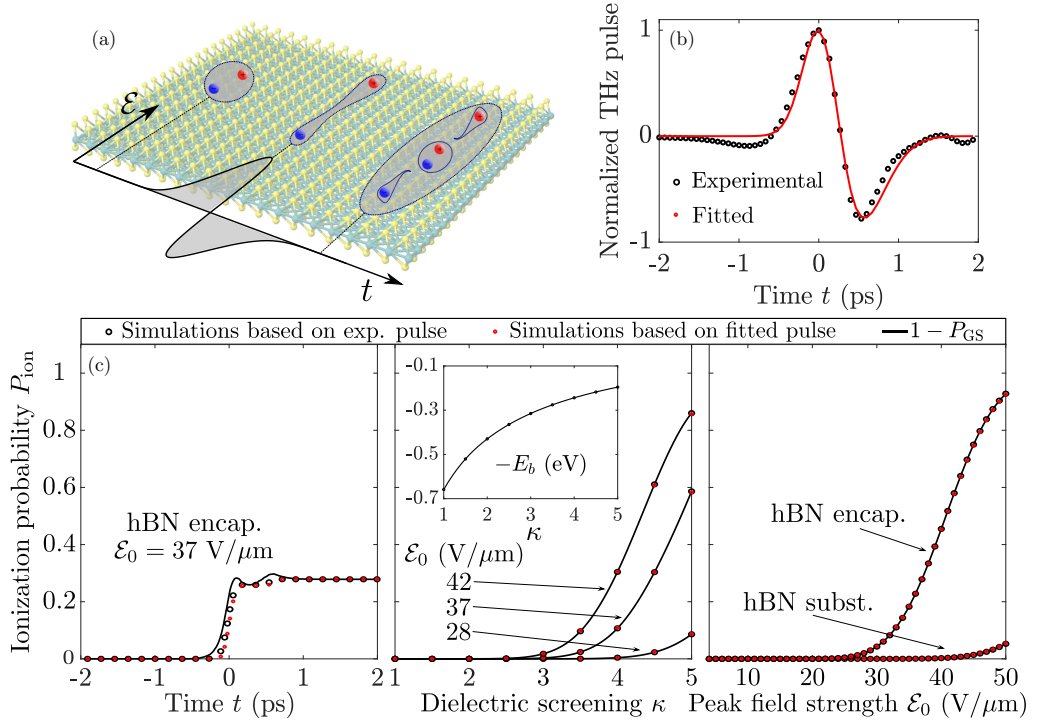


FIG. 1. (a) Schematic illustration of an exciton in a THz pulse. The initially bound exciton is polarized as a result of the pulse and is in a superposition of bound and ionized states as the pulse subsides. (b) Traces of the experimental pulse in Ref. [33] and the fitted pulse in Eq. (3) are shown as the black circles and red curve, respectively. Figure (c) summarizes the results for a single noninteracting exciton with an infinite field-free lifetime in MoS_2 subjected to the THz pulses in (b) with the black and red circles representing experimental and fitted pulses, respectively. The solid lines show the probability of depleting the ground state. (Left) Time-resolved exciton ionization probability during the THz pulse with a peak field strength of $37 \text{ V}/\mu\text{m}$ in hBN-encapsulated MoS_2 . (Middle) Exciton ionization probabilities after the pulse for three different field strengths as functions of the dielectric surroundings. The inset shows the corresponding binding energies. (Right) Ionization probabilities after the pulse as functions of peak field strength for MoS_2 encapsulated by hBN as well as for MoS_2 on an hBN substrate.

pulse, we initially set $\tau = 2.1 \text{ ps}$ and later investigate changes in P_{ion} as τ is varied. Also, in all time-resolved results below, we shift the t axis such that the pulse reaches its peak value at $t = 0$.

III. RESULTS

Figure 1(c) summarizes the results for a single noninteracting exciton with an infinite field-free lifetime in MoS_2 exposed to a THz pulse. The three panels show the time-resolved ionization probability during the pulse (left), as well as the ionization probability after the pulse as a function of dielectric screening (middle) and peak field strength (right). In these panels, the black and red circles represent ionization probabilities P_{ion} obtained by using the experimental and fitted THz pulses, respectively, while the solid black lines show the ground state depletion probability $1 - P_{\text{GS}}$. The left panel reveals that the dynamics in the fitted and experimental THz pulses agree. Furthermore, while the ground state depletion probability and ionization probability do not coincide during

the pulse, they do when the pulse subsides. This indicates that excited states, that are completely ionized when the pulse has died out, are transiently occupied during the pulse. The dynamics are similar to those in Ref. [25], where exciton occupation probabilities in quantum-well structures subjected to THz radiation were investigated. The middle panel in Fig. 1(c) shows ionization probabilities after the pulse has died out (i.e., $t = 2 \text{ ps}$) for three different peak field strengths as functions of surrounding dielectric screening κ . We again observe that $1 - P_{\text{GS}}$ and P_{ion} coincide after the pulse. This is a clear indication that the process is adiabatic, and the same conclusion was reached in Ref. [33]. Comparing the ionization probability with the binding energies for the relevant dielectric screening shown in the inset, we see that the increasing ionization probability is well explained by the reduced binding energy. In fact, ionization rates depend exponentially on the binding energies [22,56]. Common dielectric surroundings include SiO_2 substrates ($\kappa \approx 2.4$) and hBN encapsulation ($\kappa \approx 4.5$).

The right panel of Fig. 1(c) shows ionization probabilities as functions of peak field strength \mathcal{E}_0 for MoS_2 in two different

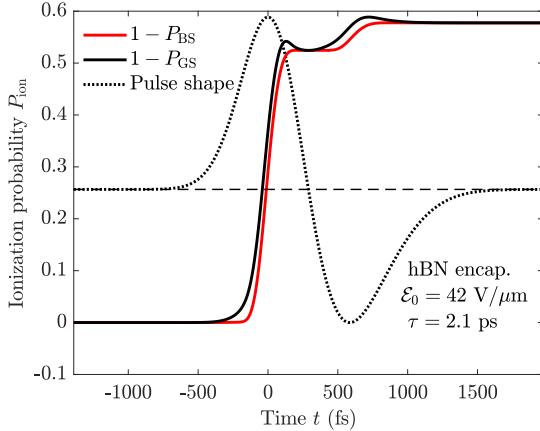


FIG. 2. Time-resolved ionization (red) and ground state depletion (black) probabilities for excitons in hBN-encapsulated MoS₂. The pulse shape is shown as the dotted line and is centered in time at its peak value of 42 V/μm with the dashed line indicating vanishing electric field level. The pulse duration is $\tau = 2.1$ ps.

dielectric surroundings. It is clear that the increased screening from encapsulating the TMD sheet in hBN, as opposed to simply placing it on an hBN substrate, causes a substantial increase in ionization probability. These results suggest that a single experimental THz pulse of the form used in Ref. [33] with a peak field strength of 42 V/μm would be able to ionize about 58% of the excitons in hBN-encapsulated MoS₂ where almost all of the ionization occurs over an interval of less than 0.5 ps (see Fig. 2). In their experiment, the authors of Ref. [33] use a sapphire substrate, which leads to an exciton binding energy of around 240 meV [33]. The authors find a broadening of the exciton absorption peak of about 10.8 meV for a peak field strength of 37 V/μm. In our calculations, this binding energy is reproduced by letting $\kappa \approx 4.1$. The middle panel of Fig. 1(c) reveals that about 14% of the excitons should be ionized in this case. This corroborates the assumption made by the authors that exciton ionization may be neglected compared to field-induced phonon broadening. The broadening induced by ionization alone may be estimated by using a static electric field of 37 V/μm. In this case, a full width of about 0.6 meV is found [20], further confirming that mechanisms other than exciton ionization dominate the broadening of the absorption peaks in this experiment. We note in passing that the results of Fig. 1(c) should not be compared directly to the absorption measurements in Ref. [33]. Intricate interplay between excitons and free charge carriers is important in realistic semiconductors and will be explored in Sec. IV.

To better understand the exciton dynamics in hBN-encapsulated MoS₂ subjected to a pulse of the experimental form in Ref. [33] with a peak field strength of 42 V/μm, we plot the time-resolved ionization rate in Fig. 2. It is evident that all ionization occurs over a remarkably short interval of about 0.5 ps. The reason for this is that the ionization rate depends exponentially on the field strength [20], and the

ionization rates at the tails of the THz pulse are therefore negligible.

The optimal material for a particular device is typically determined by requirements such as sensitivity to a certain wavelength. This is the case for, e.g., photodetectors, and it is therefore useful to have results for various materials that absorb light at different wavelengths. Figure 3 shows ionization probabilities in the four TMDs (a) MoS₂, (b) MoSe₂, (c) WS₂, and (d) WSe₂. The inset shows the exciton binding energies of these TMDs in the relevant range of dielectric surroundings. Common to all TMDs considered, hardly any ionization occurs if either the peak field strength is lower than 20 V/μm or the dielectric screening constant is close to unity (freely suspended). As the field strength and screening increase, a pronounced increase in ionization probability is observed. It is immediately clear that the tungsten based materials have larger ionization probabilities than molybdenum based ones in the relevant regions for device components. This is due to the lower exciton binding energies in the former, which suggests that it is easier to manipulate the free carrier density in these materials. If we consider the case with $\kappa = 3$ and $\mathcal{E}_0 = 40$ V/μm as an example, we see that when ordered from highest to lowest ionization probability, the four are WSe₂, followed by WS₂, MoS₂, and MoSe₂. This is in good agreement with the binding energies at $\kappa = 3$, for which we find $E_b^{(\text{MoSe}_2)} > E_b^{(\text{MoS}_2)} > E_b^{(\text{WS}_2)} > E_b^{(\text{WSe}_2)}$. Note that MoS₂ has a larger exciton binding energy than MoSe₂ for $\kappa \lesssim 2.5$ so that their binding energy curves cross. This is because MoS₂ has a lower 2D sheet polarizability than MoSe₂ [51]. However, as the surrounding dielectric screening is increased, the polarizability of the TMD sheet itself becomes less important and the larger reduced mass of the MoSe₂ excitons begins to dominate.

IV. FREE CARRIER DENSITY

To estimate the effect of a THz pulse on the free carrier concentration in a realistic TMD, one must take into account different loss mechanisms such as exciton recombination, exciton-exciton annihilation, and free carrier lifetimes, as well as impact ionization. To accurately include such effects, sophisticated theoretical modeling is often used [54]. In the present paper, the main focus is on obtaining an accurate prediction of ionization probabilities. However, it is interesting to see the effect that exciton ionization has on the free carrier concentration. To this end, we develop a simple model consisting of two coupled rate equations that describe the exciton n_x and free carrier n concentrations. Without external perturbations, we may write the coupled rate equations as

$$\frac{dn_x}{dt} = -\frac{n_x}{\tau_{\text{therm}}} + \gamma_c n^2 - \gamma_I n n_x, \quad (4)$$

$$\frac{dn}{dt} = \frac{n_x}{\tau_{\text{therm}}} - \gamma_c n^2 + \gamma_I n n_x. \quad (5)$$

Here, τ_{therm} is the exciton ionization rate due to thermal agitation, γ_c is the rate at which free electrons and holes combine to form excitons, and γ_I is the impact ionization rate, i.e., the rate at which excitons are ionized due to collisions with free carriers. For hBN-encapsulated WSe₂, a value of $\tau_{\text{therm}} \approx 100$ ps may be used [57]. The quantities γ_I and γ_c are

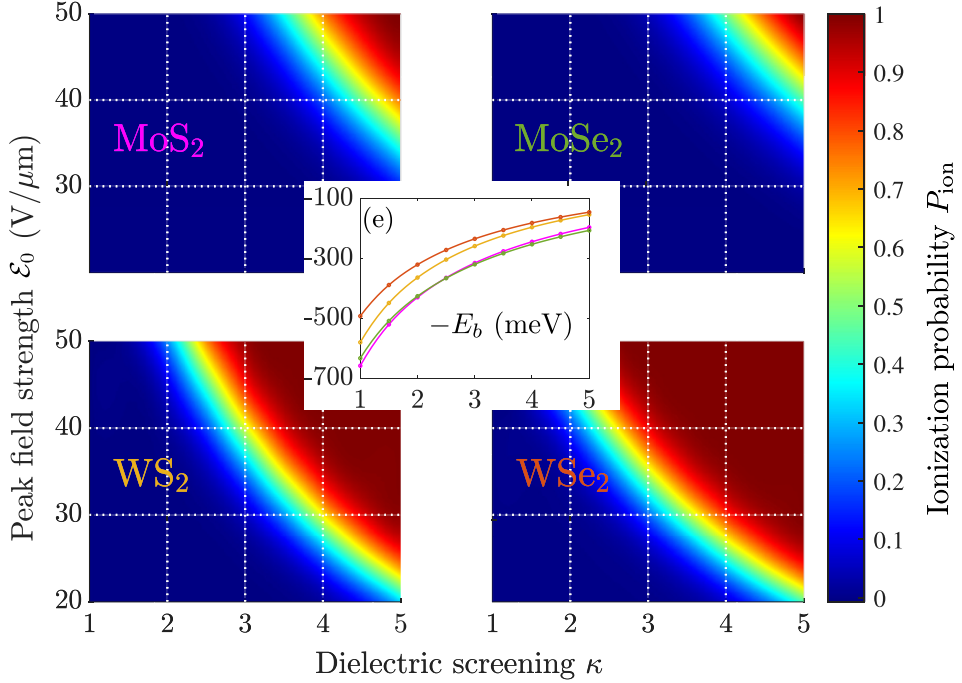


FIG. 3. Ionization probability as a function of peak field strength and surrounding dielectric screening for (a) MoS₂, (b) MoSe₂, (c) WS₂, and (d) WSe₂. Panel (e) shows the relevant binding energies. The colors of the TMD chemical composition in panels (a)–(d) correspond to the colors in panel (e).

estimated in Appendix B where we find $\gamma_I \approx 0.0043 \text{ cm}^2/\text{s}$ and $\gamma_c \approx 59 \text{ cm}^2/\text{s}$, respectively. Note that while a constant γ_I is used here, a THz field will accelerate free carriers which, in turn, increases impact ionization. As the acceleration depends on the field strength, γ_I will become time dependent. In our model, this may be simulated by changing the effective temperature. However, a slight change in γ_I does not alter the results much, and it will, therefore, be taken to be constant for simplicity.

In a realistic system, a laser pump is usually used to generate excitons. Furthermore, the excitons and free carriers have finite field-free lifetimes. To describe such a system, subjected to a THz pulse, one may write

$$\frac{dn_x}{dt} = G(t) + \left(\frac{d \log P_{\text{BS}}}{dt} - \frac{1}{\tau_x} - \frac{1}{\tau_{\text{therm}}} \right) n_x - \gamma_{ee} n_x^2 + \gamma_c n^2 - \gamma_I n n_x, \quad (6)$$

$$\frac{dn}{dt} = -\frac{n}{\tau_{fc}} + \left(\frac{1}{\tau_{\text{therm}}} - \frac{d \log P_{\text{BS}}}{dt} \right) n_x - \gamma_c n^2 + \gamma_I n n_x. \quad (7)$$

Here, $G(t)$ is the exciton generation rate, τ_x is the field-free exciton lifetime, γ_{ee} is the exciton-exciton annihilation rate, and τ_{fc} is the field-free free carrier lifetime. The logarithmic derivative of the total bound-state probability $P_{\text{BS}}(t)$ may be understood as a time-dependent ionization rate due to the applied THz pulse [53]. We use a linear interpolation of the

discrete bound-state probability found by the procedure in Appendix A to get a continuous P_{BS} . The coupled differential equations 6 and 7 may then be solved (starting from the equilibrium solutions) by a number of different methods. Here, we use the explicit Runge-Kutta (4,5) scheme that is built into MATLAB. Note that $d \log P_{\text{BS}}/dt$ depends on the field strength $\mathcal{E}(t)$ and is zero when $\mathcal{E} = 0$.

To describe the representative case of hBN-encapsulated WSe₂, we use $\tau_x \approx 90 \text{ ps}$ [36], $\gamma_{ee} \approx 0.05 \text{ cm}^2/\text{s}$ [18,37], and $\tau_{fc} \approx 40 \text{ ps}$ [58] together with the previously found quantities. We also assume a constant exciton generation rate $G = 2.5 \times 10^{24} \text{ s}^{-1} \text{ cm}^{-2}$ due to an external laser pump. The value is chosen such that we obtain the same equilibrium exciton density as used in Ref. [18]. We find initial equilibrium values of $n_x \approx 7 \times 10^{12} \text{ cm}^{-2}$ and $n \approx 3.5 \times 10^{10} \text{ cm}^{-2}$. The simulation results are shown in Fig. 4(a) with black and red curves representing the exciton and free carrier densities (left axis), respectively. The densities are initially assumed to be in statistical equilibrium, and a THz pulse reaching its peak field strength of $42 \text{ V}/\mu\text{m}$ at $t = 0$ is then turned on. This pulse is shown as the dotted black curve in Fig. 4(a) with absolute field strength shown on the right axis. A rapid increase in free carrier concentration from the initial $3.5 \times 10^{10} \text{ cm}^{-2}$ at equilibrium to about $1.8 \times 10^{12} \text{ cm}^{-2}$ can be observed. This is an increase in free carrier concentration by a factor of about 50 over a very short interval. After this sudden increase, the concentrations return to their equilibrium values almost instantaneously. It is evident that the densities are modified only

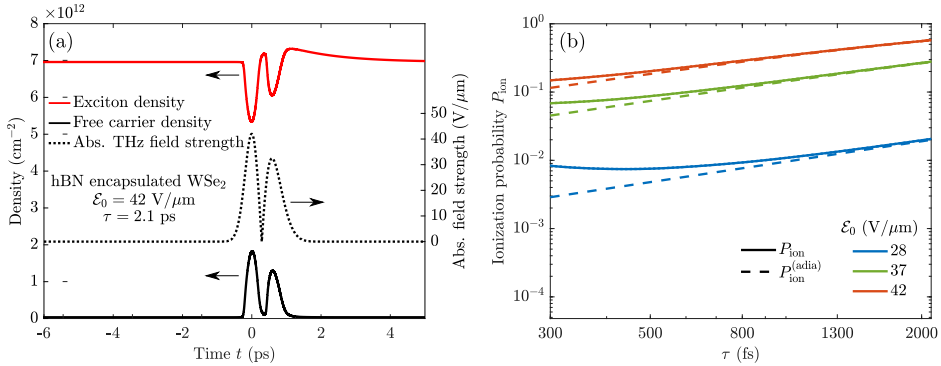


FIG. 4. (a) Exciton and free carrier densities in hBN-encapsulated WSe₂ obtained by solving the coupled rate equations (see Appendix B). The black and red curves indicate the exciton n_x and free carrier n densities (left axis), respectively. The densities are initially in equilibrium, that is $n_x \approx 7 \times 10^{12} \text{ cm}^{-2}$ and $n \approx 3.5 \times 10^{10} \text{ cm}^{-2}$. A THz pulse with a duration $\tau = 2.1 \text{ ps}$ reaching its peak field strength of $42 \text{ V}/\mu\text{m}$ at $t = 0$ is later turned on. The absolute THz field strength is shown as the black dotted curve (right axis). Realistic results are obtained by using a finite exciton generation rate and taking into account loss mechanisms from impurities (see Appendix B). (b) Ionization probability as a function of pulse duration for various peak field strengths, indicated by the different colors. The solid lines are the ionization P_{ion} probabilities computed by propagating the Wannier equation in time and projecting on the relevant bound states. The dashed lines are calculated using an adiabatic approach, utilizing the results from static electric fields. The adiabatic probabilities are given by $P_{\text{ion}}^{(\text{adia})} = 1 - e^{-\Gamma_1 \tau}$, where $\Gamma_1 = \{9.62, 154.24, 407.63\} \text{ ns}^{-1}$ for $\mathcal{E}_0 = \{28, 37, 42\} \text{ V}/\mu\text{m}$, respectively. See Appendix C for details.

when the THz pulse is present. This ability to dynamically control the charge carrier concentration is very promising for applications such as THz modulators based on monolayer TMDs [6,7]. It should also make it possible to measure exciton ionization probabilities by correlating them to free carrier absorption spectra.

V. SHORTER PULSES

So far we have only considered THz pulses with duration given by $\tau = 2.1 \text{ ps}$, closely resembling the experimental pulse used in Ref. [33]. For such relatively large τ the results are very accurately reproduced by adiabatic calculations, and it is therefore interesting to see how the results differ for shorter pulses. If the pulse varies sufficiently slowly in time, the adiabatic theorem allows us to obtain the ionization probability by treating time as a parameter in the time-dependent Hamiltonian. That is, one may increase the time parameter by small discrete steps, while repeatedly solving the resulting eigenvalue problem. This lets us trace the ground state energy and therefore the ionization probability. A detailed explanation of the procedure may be found in Appendix C. The results are summarized in Fig. 4(b), where we show the ionization probability of an exciton in MoS₂ encapsulated by hBN after the pulse has died out as a function of the pulse duration. The pulses considered are of the same shape as before but with a shorter duration. Different peak field strengths are indicated by line color. The solid lines show the ionization probabilities computed by propagating the Wannier equation in time (see Appendix A), while the dashed lines show adiabatic approximations (see Appendix C). We observe that for the longest pulses considered, the adiabatic calculation accurately reproduces the full time propagated results. Furthermore, we find that the ground state depletion probability and the ioniza-

tion probability are graphically indistinguishable for all pulse lengths shown in Fig. 4(b). This suggests that the excited states that are transiently occupied during the THz pulse are completely ionized once the pulse dies out. As the duration of the pulse decreases, we observe a deviation from the adiabatic results. This is to be expected, as the coupling between the states and the pulse should cease to be adiabatic for pulses that vary more rapidly with time. The results indicate that if the goal is to ionize as many excitons as possible, a pulse in the THz region is preferable over shorter pulses. The experimental THz pulse in Ref. [33] corresponds to the longest duration in Fig. 4(b) and therefore seems to be a good candidate for exciton ionization.

VI. SUMMARY

In summary, we have demonstrated using theoretical tools that realistic THz pulses may be used to efficiently ionize excitons in TMD monolayers, a desirable feature in many optoelectronic devices, such as photodetectors and THz modulators. We have shown that for the technologically important case of hBN-encapsulated MoS₂, a THz pulse with a peak field strength of $42 \text{ V}/\mu\text{m}$ (as applied in recent experiments [33]) will ionize about 58% of the photogenerated excitons. Reducing the peak field strength to $30 \text{ V}/\mu\text{m}$ already lowers the ionization probability to about 4.5%, revealing the extreme sensitivity to field strength. Similar behavior was demonstrated for MoSe₂, whereas exciton ionization probabilities in WS₂ and WSe₂ were shown to be considerably larger owing to their reduced exciton binding energies. In fact, a peak field of $30 \text{ V}/\mu\text{m}$ should ionize about 96% of the excitons in hBN-encapsulated WSe₂.

By solving the coupled rate equations for the exciton and free carrier concentrations in a realistic 2D semiconductor,

we have demonstrated that THz pulses boost the free carrier concentration considerably over a short time interval, providing dynamical control over both bound and free charge carriers. For the representative case of hBN-encapsulated WSe₂, we found an increase in free carrier concentration by about a factor 50. As the free carrier absorption is directly related to the number of free charge carriers, exciton ionization probabilities should be experimentally measurable in these materials by comparing free carrier absorption before and after the THz pulse or by collection via biased contacts. Finally, we have shown that reducing the duration of the pulse leads to ionization dynamics that are no longer adiabatic.

APPENDIX A: WANNIER EXCITONS IN THZ ELECTRIC FIELDS

To study exciton ionization induced by THz pulses, we include a time-dependent electric field term in the Wannier equation. Working in the length gauge under the dipole approximation and letting the field direction be along the x axis, we write

$$i\frac{\partial\psi(\mathbf{r},t)}{\partial t} = H(t)\psi(\mathbf{r},t), \quad (\text{A1})$$

with

$$H(t) = -\frac{1}{2\mu}\nabla^2 + V(\mathbf{r}) + \mathcal{E}(t)x, \quad (\text{A2})$$

where $\mathcal{E}(t)$ is the time-dependent field strength of the THz pulse. We will assume that only the excitonic ground state is occupied initially and then propagate Eq. (A1) in time while computing the ionization probability P_{ion} as

$$P_{\text{ion}}(t) = 1 - \sum_{m,n \text{ bound}} |\langle\varphi_{mn}(\mathbf{r})|\psi(\mathbf{r},t)\rangle|^2, \quad (\text{A3})$$

where we only count bound state solutions φ_{mn} of Eq. (1) (i.e., states with $E_{mn} < 0$). Note that $\sum_{m,n \text{ bound}} |\langle\varphi_{mn}(\mathbf{r})|\psi(\mathbf{r},t)\rangle|^2$ is equal to $P_{\text{BS}}(t)$ in the main text.

To perform numerical computations, the spatial region is truncated by placing the system inside a large radial box such that the wave function is forced to zero outside a radius R . This corresponds to introducing an infinite potential outside R . The wave function should be well described within this box as long as R is chosen large enough. Importantly, this allows us to write the wave function as a superposition of the *discrete* eigenstate solutions φ_{mn} to the unperturbed problem in Eq. (1) subject to $\varphi_{mn}(\mathbf{r}) = 0$ for $r \geq R$. We write

$$\psi(\mathbf{r},t) = \sum_{m=0}^M \sum_{n=0}^N c_{mn}(t) \varphi_{mn}(\mathbf{r}) e^{-iE_{mn}t}, \quad (\text{A4})$$

with time-dependent expansion coefficients. In practical calculations, one must make sure that the results are converged in M , N , and R . We have used $R = 5000$ a.u. for our calculations (M and N are discussed later). Substituting Eq. (A4) into Eq. (A1), the following expression may be derived

$$\frac{d}{dt} c_{mn}(t) = -i \sum_{m'n'} c_{m'n'}(t) \mathcal{E}(t) \langle\varphi_{mn}|x|\varphi_{m'n'}\rangle \times e^{-i(E_{m'n'} - E_{mn})t}. \quad (\text{A5})$$

Thus, the expansion coefficients may easily be propagated in time, and the occupation probability of state φ_{mn} obtained as $|c_{mn}|^2$. An adaptive step-size eight-order Dormand-Prince Runge-Kutta method with embedded fifth- and third-order methods for error control [59] has been used for time propagation.

The unperturbed states and energies have been obtained by expanding the eigenstates in a finite element (FE) basis

$$\varphi_{mn}(\mathbf{r}) = \sum_{k=1}^K \sum_{i=1}^p d_i^{(m,n,k)} f_i^{(k)}(r) \cos(m\theta), \quad (\text{A6})$$

where θ is the relative polar angle between the electron and hole, and k and i denote the radial segment and basis function, respectively. The procedure of using an FE approach to solve the Wannier equation is detailed in Ref. [20]. Nevertheless, a short explanation will now be given for completeness. Note that only the $\cos(m\theta)$ angular functions with $m \geq 0$ appear, as the electric field is taken along the x direction such that $x = r \cos \theta$. The radial functions $f_i^{(k)}$ are nonzero only on a specific radial segment $[r_{k-1}, r_k]$. On this segment, they are given by

$$\begin{aligned} f_i^{(k)}(r) = & \frac{1}{2}[1 - y_k(r)]\delta_{i,1} + \frac{1}{2}[1 + y_k(r)]\delta_{i,p} \\ & + \frac{1}{2}\{2P_i[y_k(r)] + (-1)^{i+1}[1 - y_k(r)] - [1 + y_k(r)]\} \\ & \times (1 - \delta_{i,1} - \delta_{i,p}), \end{aligned} \quad (\text{A7})$$

where δ is the Kronecker delta, P_i is the i th Legendre polynomial, and y_k maps the segment $[r_{k-1}, r_k]$ onto $[-1, 1]$

$$y_k(r) = \frac{2r - r_k - r_{k-1}}{r_k - r_{k-1}}. \quad (\text{A8})$$

This form ensures that all functions are zero at the segment boundaries with two exceptions, namely, the first and last function are equal to unity at the start and end of the segment, respectively. That is,

$$f_i^{(k)}(r_{k-1}) = f_i^{(k)}(r_k) = 0, \quad (\text{A9})$$

$$\text{except } f_1^{(k)}(r_{k-1}) = f_p^{(k)}(r_k) = 1. \quad (\text{A10})$$

This makes it simple to guarantee continuity of the wave function, even if the FE functions themselves are discontinuous, by requiring that $c_p^{(k-1)} = c_1^{(k)}$. This can be done by, e.g., grouping the two relevant functions into a single function so that they have the same expansion coefficient. Furthermore, forcing the wave function to zero at R is achieved by omitting the final function on the final segment. Substituting the expansion in Eq. (A6) into Eq. (1) and taking the inner product with $f_i^{(k')}\cos(m'\theta)$, one may construct a matrix eigenvalue problem that determines the states $\varphi_{m,n}$ in terms of the FE coefficients $d_i^{(m,n,k)}$. Once these coefficients are obtained, they may be used to propagate Eq. (A5) in time. With the above procedure, it is the limits K and p that determine the number of unperturbed states N for a given angular quantum number m . In our computations, we have made sure that the results are converged and have used $K = 80$, $p = 30$, and $M = 16$. We have furthermore excluded states in the pseudocontinuum with energy larger than 20 eV to improve numerical stability.

One of the advantages of using an FE expansion is that it is easy to implement exterior complex scaling (ECS) outside a particular radius R_0 chosen such that $R_0 < R$. In this region $r \geq R_0$, one lets the radial coordinate rotate into the complex plane

$$r \rightarrow \begin{cases} r & \text{for } r < R_0 \\ R_0 + (r - R_0)e^{i\phi} & \text{for } r > R_0, \end{cases} \quad (\text{A11})$$

by an angle ϕ (we use $\phi = 0.4$). This reduces the amount of spurious reflections from the boundary considerably, and greatly reduces the number of pseudocontinuous states necessary for convergences [52,60]. The ECS formalism is related to the uniform complex scaling (UCS) formalism, which is well explained in Ref. [61]. Here, one lets the radial coordinate rotate into the complex plane in the entire region ($R_0 = 0$), i.e., $r \rightarrow re^{i\phi}$. The UCS formalism is applicable whenever the potential is dilation analytic (i.e., it can be expanded in a Taylor series) [62]. ECS has been used in cases where UCS fails [63]. When they both are applicable, which is the case for the RK potential, they yield (formally) identical eigenvalues [64]. Under the transformation, the bound state energies remain real, while the continuous states are rotated into the complex plane, where they obtain a negative imaginary part [64]. This imaginary part turns oscillating continuous states into exponentially decaying states for $r > R_0$. The spectrum of complex eigenstates is still complete [62]. The exponential decay improves the numerical stability of the expansion in Eq. (A4) by reducing spurious reflections when we force the states to zero at $r = R$. While the two procedures should lead to identical results formally, we found the ECS approach to be more numerically stable when propagated in time. ECS is implemented in the above procedure by using the transformed Hamiltonian and integration path according to Eq. (A11) in inner products corresponding to segments with $r > R_0$. In our calculations, we have used $R_0 = 4937.5$ a.u. such that it coincides with the start of the final segment.

APPENDIX B: IMPACT IONIZATION AND EXCITON FORMATION RATES

The impact ionization rate γ_I may be estimated by [65]

$$\gamma_I = \int_0^\infty D(E)v(E)\sigma_I(E)dE, \quad (\text{B1})$$

where D is the energy distribution, v the free carrier velocity, and σ_I the exciton impact ionization cross section. In an effective mass approximation, we have $E = k^2/2m_e$ with the effective electron mass $m_e = 0.45$ [66]. We assume the energy distribution to be Maxwellian $D(E) = \exp(-E/k_B T)/k_B T$, where k_B is the Boltzmann constant and T the electron temperature. Note that the electron temperature is not necessarily the same as the surrounding temperature and that $\int_0^\infty D(E)dE = 1$. In Ref. [65] it was found that

$$\sigma_I \approx \frac{16}{k_0} \left(\frac{k_0^2}{k^2} - \frac{k_0^4}{k^4} \right) \theta(k - k_0), \quad (\text{B2})$$

which has a maximum of $4/k_0$, where k_0 is defined in terms of $E_b = k_0^2/2m_e$. Approximating the scattering cross section by

its maximum, it is found that

$$\gamma_I \approx \frac{1}{m_e} \left[2\sqrt{\frac{\pi}{z}} \Phi_c(\sqrt{z}) + 4e^{-z} \right], \quad (\text{B3})$$

where $z = E_b/k_B T$ and Φ_c is the complementary error function. Using an exciton binding energy of $E_b = 161.4$ meV and assuming the electron temperature is $T = 300$ K, a value of $\gamma_I \approx 0.0043$ cm²/s is found. It should be noted that using a slightly higher temperature does not have a large impact on the value of γ_I . To estimate the rate at which electrons and holes combine to form excitons γ_c , we will use the Saha equation, which describes the free carrier and exciton densities after statistical equilibration of their chemical potentials in the Boltzmann limit [67]

$$\frac{n^2}{n_x} = \frac{k_B T \mu}{2\pi} e^{-E_b/k_B T}. \quad (\text{B4})$$

The equilibrium solutions are obtained by setting the first order derivatives in Eqs. 4 and 5 equal to zero and supplementing with Eq. (B4) to determine γ_c . Here, we find $\gamma_c \approx 59$ cm²/s.

APPENDIX C: ADIABATIC IONIZATION PROBABILITY

Assuming that the system is initially in its (nondegenerate) ground state φ_{GS} , and that $\mathcal{E}(t)$ varies sufficiently slowly, the adiabatic theorem states that the system will remain in the eigenstate of $H(t)$ that evolves from the initial state φ_{GS} . This allows us to find the energy at all times by treating time as a parameter and tracing the relevant state. That is, we find the eigenstates of $H(t')$ at a time t'

$$H(t')\varphi_\lambda(\mathbf{r}; t') = E_\lambda(t')\varphi_\lambda(\mathbf{r}; t'), \quad (\text{C1})$$

where E and φ depend on t' as a parameter. Then we let t' take on values from the initial to the final t , all the while keeping track of the state that evolves from the ground state. Using the complex scaling procedure [20], we are then able to obtain both the real (Stark shift) and imaginary (ionization rate) part of the energy. The relevant (adiabatic) state is

$$\psi(\mathbf{r}, t) = \exp \left\{ -i \int_{-\infty}^t E(t') dt' \right\} \varphi_{GS}(\mathbf{r}; t). \quad (\text{C2})$$

As the pulse subsides, ψ will return to the ground state $c\varphi_{GS}(\mathbf{r}) \exp(-iE_{GS}t)$, where c is a complex number that arises from the integral in Eq. (C2), resulting in a norm less than unity. Defining the ionization rate as $\Gamma = -2\text{Im } E$, we obtain the adiabatic ionization probability

$$P_{\text{ion}}^{(\text{adia})}(t) = 1 - \exp \left\{ - \int_{-\infty}^t \Gamma(t') dt' \right\}. \quad (\text{C3})$$

Note that the pulse in Eq. (1) in the main text depends only on τ as the fraction t/τ . We therefore have

$$\Gamma(t; \tau, \mathcal{E}_0) = \Gamma\left(\frac{t}{\tau}; 1, \mathcal{E}_0\right) \quad (\text{C4})$$

and

$$\int_{-\infty}^\infty \Gamma(t') dt' = \tau \Gamma_1, \quad (\text{C5})$$

where

$$\Gamma_1 = \int_{-\infty}^{\infty} \Gamma(t'; 1, \mathcal{E}_0) dt'. \quad (\text{C6})$$

The adiabatic ionization probability after the pulse is therefore

$$P_{\text{ion}}^{(\text{adia})}(t \rightarrow \infty) = 1 - \exp(-\tau \Gamma_1). \quad (\text{C7})$$

- [1] J. R. Schaibley, H. Yu, G. Clark, P. Rivera, J. S. Ross, K. L. Seyler, W. Yao, and X. Xu, Valleytronics in 2D materials, *Nat. Rev. Mater.* **1**, 16055 (2016).
- [2] C. Gong, Y. Zhang, W. Chen, J. Chu, T. Lei, J. Pu, L. Dai, C. Wu, Y. Cheng, T. Zhai, L. Li, and J. Xiong, Electronic and optoelectronic applications based on 2D novel anisotropic transition metal dichalcogenides, *Adv. Sci.* **4**, 1700231 (2017).
- [3] Z. Yin, H. Li, H. Li, L. Jiang, Y. Shi, Y. Sun, G. Lu, Q. Zhang, X. Chen, and H. Zhang, Single-layer MoS₂ phototransistors, *ACS Nano* **6**, 74 (2012).
- [4] O. Lopez-Sanchez, D. Lembke, M. Kayci, A. Radenovic, and A. Kis, Ultrasensitive photodetectors based on monolayer MoS₂, *Nat. Nanotechnol.* **8**, 497 (2013).
- [5] H. Wang, C. Zhang, W. Chan, S. Tiwari, and F. Rana, Ultrafast response of monolayer molybdenum disulfide photodetectors, *Nat. Commun.* **6**, 8831 (2015).
- [6] Y. Cao, S. Gan, Z. Geng, J. Liu, Y. Yang, Q. Bao, and H. Chen, Optically tuned terahertz modulator based on annealed multilayer MoS₂, *Sci. Rep.* **6**, 22899 (2016).
- [7] Z. Fan, Z. Geng, W. Fang, X. Lv, Y. Su, S. Wang, J. Liu, and H. Chen, Characteristics of transition metal dichalcogenides in optical pumped modulator of terahertz wave, *AIP Adv.* **10**, 045304 (2020).
- [8] M. Bernardi, M. Palummo, and J. C. Grossman, Extraordinary sunlight absorption and one nanometer thick photovoltaics using two-dimensional monolayer materials, *Nano Lett.* **13**, 3664 (2013).
- [9] O. Lopez-Sanchez, E. Alarcon Llado, V. Koman, A. Fontcuberta I Morral, A. Radenovic, and A. Kis, Light generation and harvesting in a van der Waals heterostructure, *ACS Nano* **8**, 3042 (2014).
- [10] A. Ramasubramaniam, Large excitonic effects in monolayers of molybdenum and tungsten dichalcogenides, *Phys. Rev. B* **86**, 115409 (2012).
- [11] T. C. Berkelbach, M. S. Hybertsen, and D. R. Reichman, Theory of neutral and charged excitons in monolayer transition metal dichalcogenides, *Phys. Rev. B* **88**, 045318 (2013).
- [12] T. Olsen, S. Latini, F. Rasmussen, and K. S. Thygesen, Simple Screened Hydrogen Model of Excitons in Two-Dimensional Materials, *Phys. Rev. Lett.* **116**, 056401 (2016).
- [13] Q. H. Wang, K. Kalantar-Zadeh, A. Kis, J. N. Coleman, and M. S. Strano, Electronics and optoelectronics of two-dimensional transition metal dichalcogenides, *Nat. Nanotechnol.* **7**, 699 (2012).
- [14] D. Y. Qiu, F. H. da Jornada, and S. G. Louie, Optical Spectrum of MoS₂: Many-Body Effects and Diversity of Exciton States, *Phys. Rev. Lett.* **111**, 216805 (2013).
- [15] M. L. Trolle, G. Seifert, and T. G. Pedersen, Theory of excitonic second-harmonic generation in monolayer MoS₂, *Phys. Rev. B* **89**, 235410 (2014).
- [16] S. Hastrup, S. Latini, K. Bolotin, and K. S. Thygesen, Stark shift and electric-field-induced dissociation of excitons in monolayer MoS₂ and hBN/MoS₂ heterostructures, *Phys. Rev. B* **94**, 041401(R) (2016).
- [17] B. Scharf, T. Frank, M. Gmitra, J. Fabian, I. Žutić, and V. Perebeinos, Excitonic Stark effect in MoS₂ monolayers, *Phys. Rev. B* **94**, 245434 (2016).
- [18] M. Massicotte, F. Vialla, P. Schmidt, M. B. Lundberg, S. Latini, S. Hastrup, M. Danovich, D. Davydovskaya, K. Watanabe, T. Taniguchi, V. I. Fal'ko, K. S. Thygesen, T. G. Pedersen, and F. H. Koppens, Dissociation of two-dimensional excitons in monolayer WSe₂, *Nat. Commun.* **9**, 1633 (2018).
- [19] A. R. Klots, A. K. Newaz, B. Wang, D. Prasai, H. Krzyzanowska, J. Lin, D. Caudel, N. J. Ghimire, J. Yan, B. L. Ivanov, K. A. Velizhanin, A. Burger, D. G. Mandrus, N. H. Tolk, S. T. Pantelides, and K. I. Bolotin, Probing excitonic states in suspended two-dimensional semiconductors by photocurrent spectroscopy, *Sci. Rep.* **4**, 6608 (2014).
- [20] H. C. Kamban and T. G. Pedersen, Field-induced dissociation of two-dimensional excitons in transition metal dichalcogenides, *Phys. Rev. B* **100**, 045307 (2019).
- [21] T. G. Pedersen, S. Latini, K. S. Thygesen, H. Mera, and B. K. Nikolić, Exciton ionization in multilayer transition-metal dichalcogenides, *New J. Phys.* **18**, 073043 (2016).
- [22] H. C. Kamban and T. G. Pedersen, Interlayer excitons in van der Waals heterostructures: Binding energy, Stark shift, and field-induced dissociation, *Sci. Rep.* **10**, 5537 (2020).
- [23] R. R. Jones, D. You, and P. H. Bucksbaum, Ionization of Rydberg Atoms by Subpicosecond Half-Cycle Electromagnetic Pulses, *Phys. Rev. Lett.* **70**, 1236 (1993).
- [24] S. Li and R. R. Jones, Ionization of Excited Atoms by Intense Single-Cycle THz Pulses, *Phys. Rev. Lett.* **112**, 143006 (2014).
- [25] B. Ewers, N. S. Köster, R. Woscholski, M. Koch, S. Chatterjee, G. Khitrova, H. M. Gibbs, A. C. Klettke, M. Kira, and S. W. Koch, Ionization of coherent excitons by strong terahertz fields, *Phys. Rev. B* **85**, 075307 (2012).
- [26] M. Stein, C. Lammers, J. T. Steiner, P. H. Richter, S. W. Koch, M. Koch, and M. Kira, Exciton ionization by THz pulses in germanium, *J. Phys. B: At. Mol. Opt. Phys.* **51**, 154001 (2018).
- [27] Y. Murotani, M. Takayama, F. Sekiguchi, C. Kim, H. Akiyama, and R. Shimano, Terahertz field-induced ionization and perturbed free induction decay of excitons in bulk GaAs, *J. Phys. D: Appl. Phys.* **51**, 114001 (2018).
- [28] J. Klein, J. Wierzbowski, A. Regler, J. Becker, F. Heimbach, K. Müller, M. Kaniber, and J. J. Finley, Stark effect spectroscopy of mono- and few-layer MoS₂, *Nano Lett.* **16**, 1554 (2016).
- [29] T. G. Pedersen, Exciton Stark shift and electroabsorption in monolayer transition-metal dichalcogenides, *Phys. Rev. B* **94**, 125424 (2016).
- [30] L. S. R. Cavalcante, D. R. da Costa, G. A. Farias, D. R. Reichman, and A. Chaves, Stark shift of excitons and trions in two-dimensional materials, *Phys. Rev. B* **98**, 245309 (2018).
- [31] J. D. Dow and D. Redfield, Electroabsorption in semiconductors: The excitonic absorption edge, *Phys. Rev. B* **1**, 3358 (1970).

- [32] D. A. B. Miller, D. S. Chemla, T. C. Damen, A. C. Gossard, W. Wiegmann, T. H. Wood, and C. A. Burrus, Electric field dependence of optical absorption near the band gap of quantum-well structures, *Phys. Rev. B* **32**, 1043 (1985).
- [33] J. Shi, E. Baldini, S. A. Latini, S. A. Sato, Y. Zhang, B. C. Pein, P. C. Shen, J. Kong, A. Rubio, N. Gedik, and K. A. Nelson, Room temperature terahertz electroabsorption modulation by excitons in monolayer transition metal dichalcogenides, *Nano Lett.* **20**, 5214 (2020).
- [34] T. Ogawa, S. Watanabe, N. Minami, and R. Shimano, Room temperature terahertz electro-optic modulation by excitons in carbon nanotubes, *Appl. Phys. Lett.* **97**, 041111 (2010).
- [35] L. Yuan and L. Huang, Exciton dynamics and annihilation in WS₂ 2D semiconductors, *Nanoscale* **7**, 7402 (2015).
- [36] F. Cadiz, C. Robert, E. Courtade, M. Manca, L. Martinelli, T. Taniguchi, K. Watanabe, T. Amand, A. C. Rowe, D. Paget, B. Urbaszek, and X. Marie, Exciton diffusion in WSe₂ monolayers embedded in a van der Waals heterostructure, *Appl. Phys. Lett.* **112**, 152106 (2018).
- [37] S. Mouri, Y. Miyauchi, M. Toh, W. Zhao, G. Eda, and K. Matsuda, Nonlinear photoluminescence in atomically thin layered WSe₂ arising from diffusion-assisted exciton-exciton annihilation, *Phys. Rev. B* **90**, 155449 (2014).
- [38] H. Shi, R. Yan, S. Bertolazzi, J. Brivio, B. Gao, A. Kis, D. Jena, H. G. Xing, and L. Huang, Exciton dynamics in suspended monolayer and few-layer MoS₂ 2D crystals, *ACS Nano* **7**, 1072 (2013).
- [39] T. Korn, S. Heydrich, M. Hirmer, J. Schmutzler, and C. Schiller, Low-temperature photocarrier dynamics in monolayer MoS₂, *Appl. Phys. Lett.* **99**, 102109 (2011).
- [40] G. H. Wannier, The structure of electronic excitation levels in insulating crystals, *Phys. Rev.* **52**, 191 (1937).
- [41] F. L. Lederman and J. D. Dow, Theory of electroabsorption by anisotropic and layered semiconductors. I. Two-dimensional excitons in a uniform electric field, *Phys. Rev. B* **13**, 1633 (1976).
- [42] P. Cudazzo, C. Attaccalite, I. V. Tokatly, and A. Rubio, Strong Charge-Transfer Excitonic Effects and the Bose-Einstein Exciton Condensate in Graphane, *Phys. Rev. Lett.* **104**, 226804 (2010).
- [43] O. Pulci, P. Gori, M. Marsili, V. Garbuio, R. Del Sole, and F. Bechstedt, Strong excitons in novel two-dimensional crystals: Silicene and germanene, *Europhys. Lett.* **98**, 37004 (2012).
- [44] S. Latini, T. Olsen, and K. S. Thygesen, Excitons in van der Waals heterostructures: The important role of dielectric screening, *Phys. Rev. B* **92**, 245123 (2015).
- [45] M. L. Trolle, T. G. Pedersen, and V. Vénard, Model dielectric function for 2D semiconductors including substrate screening, *Sci. Rep.* **7**, 39844 (2017).
- [46] H. C. Kamban, T. G. Pedersen, and N. M. R. Peres, Anisotropic Stark shift, field-induced dissociation, and electroabsorption of excitons in phosphorene, *Phys. Rev. B* **102**, 115305 (2020).
- [47] P. Cudazzo, I. V. Tokatly, and A. Rubio, Dielectric screening in two-dimensional insulators: Implications for excitonic and impurity states in graphane, *Phys. Rev. B* **84**, 085406 (2011).
- [48] N. S. Rytova, The screened potential of a point charge in a thin film, *Moscow Univ. Phys. Bull.* **22**, 18 (1967).
- [49] L. V. Keldysh, Coulomb interaction in thin semiconductor and semimetal films, *JETP Lett.* **29**, 658 (1979).
- [50] M. Abramowitz and I. Stegun, eds., *Handbook of Mathematical Functions, With Formulas, Graphs, and Mathematical Tables* (Dover, New York, 1972).
- [51] M. Goryca, J. Li, A. V. Stier, T. Taniguchi, K. Watanabe, E. Courtade, S. Shree, C. Robert, B. Urbaszek, X. Marie, and S. A. Crooker, Revealing exciton masses and dielectric properties of monolayer semiconductors with high magnetic fields, *Nat. Commun.* **10**, 4172 (2019).
- [52] A. Scrinzi, Infinite-range exterior complex scaling as a perfect absorber in time-dependent problems, *Phys. Rev. A* **81**, 053845 (2010).
- [53] H. C. Kamban, S. S. Christensen, T. Søndergaard, and T. G. Pedersen, Finite-difference time-domain simulation of strong-field ionization: A perfectly matched layer approach, *Phys. Status Solidi B* **257**, 1900467 (2020).
- [54] F. Langer, C. P. Schmid, S. Schlauderer, M. Gmitra, J. Fabian, P. Nagler, C. Schüller, T. Korn, P. G. Hawkins, J. T. Steiner, U. Huttner, S. W. Koch, M. Kira, and R. Huber, Lightwave valleytronics in a monolayer of tungsten diselenide, *Nature (London)* **557**, 76 (2018).
- [55] B. C. Yang and F. Robicheaux, Field-ionization threshold and its induced ionization-window phenomenon for Rydberg atoms in a short single-cycle pulse, *Phys. Rev. A* **90**, 063413 (2014).
- [56] J. C. G. Henriques, H. C. Kamban, T. G. Pedersen, and N. M. R. Peres, Analytical quantitative semiclassical approach to the Lo Surdo-Stark effect and ionization in two-dimensional excitons, *Phys. Rev. B* **102**, 035402 (2020).
- [57] R. Perea-Causín, S. Brem, and E. Malic, Phonon-assisted exciton dissociation in transition metal dichalcogenides, *Nanoscale* **13**, 1884 (2021).
- [58] G. Aivazian, H. Yu, S. Wu, J. Yan, D. G. Mandrus, D. Cobden, W. Yao, and X. Xu, Many-body effects in nonlinear optical responses of 2D layered semiconductors, *2D Mater.* **4**, 025024 (2017).
- [59] W. H. Press, S. A. Teukolsky, W. T. Vetterling, and B. P. Flannery, *Numerical Recipes*, 3rd ed. (Cambridge University Press, New York, 2007).
- [60] J. Bengtsson, E. Lindroth, and S. Selstø, Solution of the time-dependent Schrödinger equation using uniform complex scaling, *Phys. Rev. A* **78**, 032502 (2008).
- [61] J. Bengtsson, *On the use of the uniform complex scaling-method for studying time- dependent systems* (Department of Physics, Stockholm University, 2012), p. 58.
- [62] N. Moiseyev, *Non-Hermitian Quantum Mechanics* (Cambridge University Press, Cambridge, 2011).
- [63] B. Simon, The definition of molecular resonance curves by the method of exterior complex scaling, *Phys. Lett. A* **71**, 211 (1979).
- [64] C. W. McCurdy, C. K. Stroud, and M. K. Wisinski, Solving the time-dependent Schrödinger equation using complex-coordinate contours, *Phys. Rev. A* **43**, 5980 (1991).
- [65] A. Dargys and J. Kundrotas, Impact ionization of excitons by hot carriers in quantum wells, *Semicond. Sci. Technol.* **13**, 1258 (1998).
- [66] S. Haastруп, M. Strange, M. Pandey, T. Deilmann, P. S. Schmidt, N. F. Hinsche, M. N. Gjerding, D. Torelli, P. M.

- Larsen, A. C. Riis-Jensen, J. Gath, K. W. Jacobsen, J. J. Mortensen, T. Olsen, and K. S. Thygesen, The Computational 2D Materials Database: High-throughput modeling and discovery of atomically thin crystals, [2D Mater.](#) **5**, 042002 (2018).
- [67] R. A. Kaindl, D. Hägele, M. A. Camahan, and D. S. Chemla, Transient terahertz spectroscopy of excitons and unbound carriers in quasi-two-dimensional electron-hole gases, [Phys. Rev. B](#) **79**, 045320 (2009).

ISSN (online): 2446-1636
ISBN (online): 978-87-7573-917-2

AALBORG UNIVERSITY PRESS